

JPRS-JST-90-031

15 JUNE 1990



**FOREIGN  
BROADCAST  
INFORMATION  
SERVICE**

# ***JPRS Report***

**DISTRIBUTION STATEMENT A**

Approved for public release  
Distribution Unlimited

# **Science & Technology**

***Japan***

40TH INTERNATIONAL SOCIETY OF ELECTROCHEMISTRY MEETING

REPRODUCED BY  
U.S. DEPARTMENT OF COMMERCE  
NATIONAL TECHNICAL INFORMATION SERVICE  
SPRINGFIELD, VA. 22161

**DTIC QUALITY INSPECTED 3**

22161

SPRINGFIELD, VA  
5285 PORT ROYAL RD  
ATTN: PROCESS 103  
NTIS

45  
22161

19980130 197

SCIENCE & TECHNOLOGY  
JAPAN

40TH INTERNATIONAL SOCIETY OF ELECTROCHEMISTRY MEETING

43070726 Kyoto 40th ISE MEETING EXTENDED ABSTRACTS in English  
Vols 1,11 17-22 Sep 89 pp 1-1348

[Selected "extended abstracts" presented at the 40th International Society of Electrochemistry Meeting held 17-22 Sep 89 in Kyoto, sponsored by the International Union of Pure and Applied Chemistry (IUPAC) and the Commemorative Association for the Japan World Exposition, and Organized by the Science Council of Japan and the Electrochemical Society of Japan]

CONTENTS

Contents Vol. I.....	1
Contents Vol II.....	22
Low Temperature Effects in Electrochemical Systems With High $T_c$ Superconductors [A. Pinkowski, J. Doneit, et al.].....	46
Complex Susceptibility of Single Crystal $YBa_2Cu_3O_y$ [H. Mazaki, H. Yasuoka, et al.].....	47
Effect of Synthesis Conditions on Microstructure and Superconducting Properties of Bulk $YBa_2Cu_3O_x$ by Quench and Melt Growth (QMG) Process [M. Morita, K. Doi, et al.].....	49
Glass Formation and Crystallization Process of Bi-Containing High- $T_c$ Superconductors [Tsutomu Minami].....	50

Chemical Properties of High Tc Oxide Superconductors Near Their Critical Temperatures [Y. Takasu, K. Hanyu, et al.].....	51
Ionic and Electronic Conductivity in Oxide Superconductors: Studies of the Prototype Systems "YBaCuO" and "(Bi,Pb)SrCaCuO" [W. Gopel, W. Carrillo-Cabrera, et al.].....	52
Dynamic Superconducting System by Using Novel Superconductor [Y. Murakami].....	53
Superconducting Properties of YBa <sub>2</sub> Cu <sub>3</sub> O <sub>7-x</sub> -Metal Composites [N. Imanaka, F. Saito, et al.].....	55
Silver Doping Into the High-Tc Oxide Superconductors [Y. Matsumoto, J. Hombo, et al.].....	57
Low Temperature Growth and Structure of YBa <sub>2</sub> Cu <sub>3</sub> O <sub>7-x</sub> Epitaxial Thin Film [Y. Bando].....	58
Effects of Structure on the Superconductivity of Bi-Sr-Ca-Cu-O Films [S. Nagai, N. Fujimura, et al.].....	60
The Sol-Gel Processing of Electroceramics [D. A. Payne].....	62
Texture and Photochromic Characteristics of ZnOx Thin Films [N. Fujimura, T. Nishihara, et al.].....	63
Formation of Yttria Stabilized Zirconia Film by Plasma MOCVD [Osamu Matsumoto, Nobuhiro Oka, et al.].....	65
Infrared-Sensitive SiC Fiber Thermistor [N. Muto, M. Miyayama, et al.].....	67
Characterization of Trap Centers in Semiconducting Ceramics by ICTS [T. Maeda, M. Takata].....	68
Evaluation of Some Amorphous Metal Electrodes for Alkaline Electrolysis: Standard Versus Novel Techniques [M. I. Ismail, M. A. Daous, et al.].....	70
Preparation of Cordierite Ceramics From Metal Alkoxides [M. Okuyama, T. Fukui, et al.].....	72
Electronic Materials Using the Energy Barrier Associated With Oxygen [Satoru Fujitsu, Kunihiro Koumoto, et al.].....	74

Hetero-Contact Effects of Atmosphere-Sensitive Ceramic Semiconductor [M. Miyayama, Y. Nakamura, et al.].....	75
Humidity Sensitivity of CaO Doped Yttria [K. Katayama, H. Ousawa, et al.].....	76
Microstructure and the Dielectric Properties in SrTiO <sub>3</sub> -Pb(fe,W)O <sub>3</sub> BL-Type Capacitors [M. Kuwabara].....	77
The Alkaline Fuel Cell Program for the European Space Vehicle HERMES (Its Possible "Spin-off" on Commercial Fuel Cell Technology) [K. Kordesch].....	79
High-Power Alkaline Fuel Cell System for Electric Vehicles (Hybrid System With Zinc-Bromine Battery) [K. Kordesch, J. Oliveira, et al.].....	81
In-situ Investigation of Fuel Cell Catalysts by SNIFTIRS and On- Line Mass Spectroscopy [W. Vielstich, B. Bittins-Cattaneo, et al.].....	83
Molecular Design of a Methanol Fuel Cell Electrode Based on Fundamental Studies of the Direct Oxidation of Methanol on Polycrystalline and Single Crystal Platinum Electrodes [C. Lamy, B. Beden, et al.].....	84
Electrocatalytic Oxidation of Alcohols on Non Precious Catalysts Such as Mixed Carbides of Tungsten and Molybdenum [G. Bornoel, G. Leclercq, et al.].....	87
The Electrocatalytic Oxidation of Some Organic Acids on Metal/Nafion Electrodes [O. Enea, D. Duprez].....	89
Development of Air-Cooled Phosphoric Acid Fuel Cell [Haruo Suzuki, Masahiro Ide, et al.].....	91
Improvements in Performances for Phosphoric Acid Fuel Cell Cathodes Using Thinner Electrode Substrates [M. Inoue, H. Fukui, et al.].....	93
Influence of Acid Occupation on Performance of PAFC Gas-Diffusion Cathodes [N. Giordano, E. Passalacqua, et al.].....	95
High-Performance Gas Diffusion Porous Electrode Starved of Electrolyte Solution [Z. W. Tian, Z. G. Lin, et al.].....	97
Polarization Study of Fuel Cell With Multi-Reference Electrodes [K. Mitsuda, T. Murhashi].....	98



Status of Advanced Fuel Cell Technology in Japan [Y. Kurihara].....	100
The Development of the Large-Scale Molten Carbonate Fuel Cell [Y. Yamamasu, M. Hotta, et al.].....	102
Molten Carbonate Fuel Cell Technology Improvement [T. Murahashi, T. Tanaka, et al.].....	104
Status of Advanced Fuel Cell Technology in Sweden [Lars A. Sjunnesson].....	106
Status of Advanced Fuel Cell Technology in Italy [F. Di Mario, R. Vellone].....	107
Status of the Advanced Fuel Cell Technology in the Netherlands [K. Joon, S. B. van der Molen].....	108
Electrode/Electrolyte Combined Tape for Molten Carbonate Fuel Cell [K. Hatoh, J. Niikura, et al.].....	110
A Study on Electrolyte Management of MCFC [Y. Akiyama, Y. Tonoike, et al.].....	111
The Effect of Pore Structure on Polarization Characteristics of MCFC Cathodes [S. Kuroe, Y. Twase, et al.].....	113
Solubilities of Metal Oxides in Molten Carbonate [K. Ota, S. Mitsushima, et al.].....	114
Electrochemical Behavior of Porous NiO in Molten Carbonate Fuel Cells Effect of Electrolyte Composition [H. Numata, T. Shimada, et al.].....	116
The Effect of Electrolyte Content on AC Impedance in Molten Carbonate Fuel Cell Electrodes [K. Yamashita, K. Murata].....	118
Characterization of Porous Electrodes for MCFC by Impedance Measurements [J. Niikura, K. Hatoh, et al.].....	120
Reaction Mechanism and Kinetics of Hydrogen Oxidation in Molten Carbonates [T. Nishina, I. Uchida].....	122
Electrode Modelling of Porous Anode of Sintered Au and Ni Spheres for MCFC [T. Nishina, T. Kudo, et al.].....	124

Cell Testing of Alternative Electrolytes for MCFC [Y. Miyazaki, K. Tanimoto, et al.].....	126
R&D on SOFC in Japan and Related Problems [Masayuki Dokiya].....	127
Planar Solid Oxide Fuel Cell: Nickel Cermet Anode [T. Kawada, N. Sakai, et al.].....	129
A Planar Type Solid Oxide Fuel Cell Technology [Shin-ichi Maruyama, Kazuo Koseki, et al.].....	131
Preparation of Planar Thin Film Solid Electrolyte Fuel Cells [H. Michibata, H. Tenmei, et al.].....	133
Solid Oxide Fuel Cell With Stabilized Zirconia and Doped Ceria Thin Film [K. Eguchi, T. Setoguchi, et al.].....	135
The Electrical Property and the Microstructure of ZrO <sub>2</sub> Based Solid Electrolytes [A. Yamashita, A. Nohtomi, et al.].....	137
A Proton Conductor Synthesized by the Thermal Reaction of Isopolytungstate [K. Nagata, Y. Taninaka, et al.].....	139
Planar Solid Oxide Fuel Cell: Chemical Thermodynamic Consideration on Materials [H. Yokokawa, N. Sakai, et al.].....	140
Planar Solid Oxide Fuel Cell: Ca Doped Lanthanum Chromite Separator [N. Sakai, T. Kawada, et al.].....	142
Planar Solid Oxide Fuel Cell: Lanthanum Manganate Based Cathode [M. Mori, R. Ishikawa, et al.].....	144
Planar Solid Oxide Fuel Cell: Cell Performance [T. Iwata, T. Kawada, et al.].....	146
Anodic and Cathodic Reactions on Lithium Electrodes in Aprotic Electrolytes [K. Wiesener, U. Eckoldt, et al.].....	148
Several Considerations of Lithium Anode Rechargeability [J. Yamaki].....	151
The Comparison of the Diffusion of the Dopants in Various Cathodes, TiO <sub>2</sub> , MoS <sub>2</sub> , Polyacetylene, Polyaniline, for Lithium Batteries [Z. Takehara, K. Kanamura, et al.].....	153

Lithium-Manganese Composite Oxides for Lithium Secondary Batteries [M. Yoshio, H. Nakamura, et al.].....	155
Electrochemistry of Manganese Dioxide in Lithium Nonaqueous Cell : Jahn-Teller Deformation of $\text{Li}_x\text{MnO}_{2-\delta}$ [Tsutomu Ohzuku, Keijiro Sawai, et al.].....	156
Rechargeability of Manganese Oxides in $\text{LiPF}_6$ Electrolyte [K. Yokoyama, Y. Uetani].....	157
Lithium Battery Technologies in Japan [Y. Matsuda].....	158
A Lithium Secondary Battery Using Lithium Containing Manganese Dioxide (CDMO) as the Cathode [T. Nohma, K. Teraji, et al.].....	160
Effect of Alkali Metal Cations on the Electrode Behavior of Lithium Batteries [K. Tanaka, S. Suzuki, et al.].....	162
Recent Developments in Rechargeable Lithium Batteries [M. Broussely, J. Labat].....	164
Amorphous $\text{FeVO}_4$ as a Cathode Active Material in Secondary Lithium Batteries [Michio Sugawara, Yukiteru Kaneko, et al.].....	166
$\text{Li}/\text{LiCr}_x\text{V}_y\text{S}_2$ Secondary Batteries [V. Manev, A. Nassalevska, et al.].....	168
Electrolytic Preparation of $\text{V}_2\text{O}_5$ and Its Charge-Discharge Character- istic as a Cathode Active Material of Lithium Secondary Battery [Y. Sato, T. Nomura, et al.].....	169
Structural and Kinetic Characteristics of Niobium Sulfide Electrode for a Secondary Lithium Battery [Naoaki Kumagai, Kazuo Tanno].....	171
Lithium-Carbon Anode as Lithium Secondary Batteries [O. Yamamoto, Y. Takeda, et al.].....	173
Electrochemical Intercalation of Alkali Metals Into Graphite and GIC's. An Application to Lithium Batteries, Part I [R. Yazami].....	175
Lithium Batteries Based on GIC's With Metal Fluorides (Part II) [R. Yazami, T. Nakajima].....	177
Lithium Surface Analyses by FAB Mass Spectrometry [M. Arakawa, S. Tobishima, et al.].....	179

Effects of Electrolytes on Electrodeposition of Lithium [H. Koshina, N. Eda, et al.].....	181
The AC Impedance Behavior at Lithium/Organic Electrolyte Interface [M. Morita, Y. Matsuda].....	183
Ionic Transport in Passivating Layers on Lithium Electrode [A. L. L'vov, E. S. Nimon, et al.].....	185
Electrochemical Behaviour of Graphite Fluorides in Propylene Carbonate [D. Devilliers, T. Nakajima, et al.].....	187
Discharge Characteristics of the Li/LiBF <sub>4</sub> -Quinoline/Carbon Systems as a Primary Cell [M. Dohzono, T. Yamada, et al.].....	188
Effects of Electrolyte Compositions on the Discharge Characteristics of the Positive Electrode of Li-Al/FeS <sub>2</sub> Thermal Batteries [H. Tsukamoto, M. Terasaki, et al.].....	190
Electrochemical Studies of LiAl in 1-Methyl-3-Ethylimidazolium Chloride-AlCl <sub>3</sub> Melt [Y. S. Fung, S. M. Chau].....	192
Ionically Conductive Plasma Polymer as an Electrolyte for Lithium Batteries [Z. Takehara, Z. Ogumi, et al.].....	194
Ionic Conductivity of Poly(Ethylene Oxide) (PEO)-Based Solid Electrolytes for Rechargeable Lithium Batteries [Y. Matsuda, M. Morita, et al.].....	196
Polymer Electrolyte Lithium Batteries [G. Vassort, M. Gauthier].....	198
Conductive Thin Films and Membranes: Their Scientific Foundations and Industrial Applications (Part 9) [Sardar K. Bahador].....	201
Electropolymerized Polyaniline as a Positive Electrode in a Lithium Secondary Cell - Morphology Changes and Their Effect in Charge-Discharge Characteristics - [K. Takei, K. Ishihara, et al.].....	203
Advances in Polymer Electrodes for Rechargeable Lithium Batteries [Bruno Scrosati].....	204
Charge-Discharge Characteristics of Polyaniline Electrodes in Various Nonaqueous Solutions [K. Nishio, M. Fujimoto, et al.].....	205

Electrochemical Analysis of Platinum-DNA Interactions: Relations to Anti-Cancer Activity of Platinum Complexes [V. Brabec].....	207
Electrochemical Behavior of Blue Copper Proteins From <i>Alcaligenes faecalis</i> S-6 [Yuzuru Iwasaki, Eiichi Tamiya, et al.].....	209
Voltammetric Responses of Cytochromes C <sub>3</sub> From Various Sulfate Reducing Bacteria [Y. Shigematsu, T. Sagara, et al.].....	211
Determination of Biological Species by Microelectrode Arrays [T. Matsue, A. Aoki, et al.].....	213
Electrochemistry of Modified Cytochrome C [I. Taniguchi, M. Tominaga, et al.].....	215
Spectroelectrochemical Study on Adsorption of Amp at Gold Electrode -- Uses of Specular Reflection, LOPTLC, and Magnetic Optical Rotation Methods -- [F. Kusu, K. Yuasa, et al.].....	217
Electrochemical Biosensing of Cu(II) and Zn(II) Ions Using the Immobilized Apoenzymes in the FIA System [I. Satoh].....	219
High Sensitive Immuno-Sensor With a Semi-Solid Electrolyte [H. Uchida, M. Hara, et al.].....	221
The Electrodeposition of Film of <i>H. Halobium</i> Purple Membrane (PM) Onto Poly(Vinyl Alcohol) (PVA). Fabrication of an Optically Transparent Gold (Au)/PVA/PM/PVA/Au Multi-Layer Sandwich Cell and Its Photoelectric Response [K. Uehara, K. Kawai, et al.].....	223
Amperometric Biosensors: Recent Advances [H. P. Bennetto, G. M. Delaney, et al.].....	224
Multi-Gate and Multi-Enzyme Sensors [F. Scheller, R. Hintsche, et al.].....	226
Electrochemical Immobilization of Enzymes and Current Response of GOD Electrodes [Wu Huihuang, Zheng Zhimin].....	227
Photochemical Control of Electrical Oscillations in Lipid Membranes [Hiroshi Nakanishi, Kanekazu Seki, et al.].....	228
Bioelectrochemical Immunoassay for Human Chorionic Gonadotrophin [Lu Mingxang, Chen Kungming].....	230

Electrochemical Preparation of Ultra-Thin Conductive Enzyme Membrane and Its Potential-Dependent Activity Control [M. Aizawa, Y. Ikariyama, et al.].....	231
Electrochemical Immobilization and Characterization of Enzyme GOD [H. H. Wu, Z. M. Zhen, et al.].....	232
Rectifying Function of Porphyrin-Flavin LB Monolayer-Junction on Gold Electrodes Derived from the Redox Properties of Proteins [Satoshi Ueyama, Satoru Isoda, et al.].....	233
Electrocatalytic Photolysis of Water at Photosystem II-Modified Carbon Paste Electrodes in the Presence of Electron Transfer Mediators [T. Ikeda, K. Amako, et al.].....	235
Platinum Electrode Potential in Wastewater Treatment [Alain Heduit, Daniel R. Thevenot].....	236
Prospects and Problems of Electrochemically Induced Cold Nuclear Fusion [J. W. Schultze, U. Konig, et al.].....	238
Neutron Evolution From Palladium Cathode in D <sub>2</sub> O-LiOD Solution [Tadahiko Mizuno, Tadashi Akimoto, et al.].....	239
Low Temperature Fusion of Deuterium in Electrochemical Processes [J. Zak, J. W. Strojek].....	241
Some Experiments and Analysis of Possible Cold Fusion [Noboru Oyama, Takeo Ohsaka, et al.].....	242
Electrochemical Properties of Metallic Hydrides [Derek Lewis, Kurt Skold].....	244
Search for Neutron Emission Associated With Electrolysis of Heavy Water on Pd and Ti Electrodes [A. Kira, S. Nakabayashi, et al.].....	245
Critical Analysis and Possible Explanation of Electrochemical Nuclear Fusion [G. Kreysa, M. Schutze, et al.].....	246
Electrochemical Study on Cold-Fusion Phenomenon [Sueki Baba, Kenji Kawamura, et al.].....	247
Characteristics of Pd Cathode in D <sub>2</sub> O [K. Ota, N. Kamiya, et al.].....	249
One Month Loadings of Palladium:Deuterium Content, Neutron Detection [R. Durand, R. Faure, et al.].....	250
In Search of Radioactive Emissions From the Pd Electrodes of the Pd-D and Pd-H Systems [H. Uchida, Y. Matsumura, et al.].....	251

# CONTENTS VOL.I

## PLENARY LECTURES

- a0 18-00-01-S Energy Demand and Supply in Japan  
T.MUKAIBO
- a0 18-00-02-S The Impact of Semiconductors on the Concepts of  
Electrochemistry  
H.GERISCHER
- a0 18-01-01-S Etching Phenomena in Electrochemical and Plasma Systems  
R.C.ALKIRE
- a0 19-01-01-S Scanning Tunneling and Scanning Electrochemical Microscopy  
A.J.BARD
- a0 19-01-02-S Electrochemistry at the Interface of Two Immiscible  
Electrolyte Solutions: Theory and Applications  
J.KORYTA
- a0 21-01-01-S Recent Developments in Electron Transfers, Solvation,  
and the Inverted Effect  
R.A.MARCUS
- a0 21-01-02-S Some Aspects of Functionalized Electrochemistry  
K.HONDA
- a0 22-01-01-S In-Situ Optical Studies of Electrocatalysts  
E.B.YEAGER

## I NEW MATERIALS

### I-1. High Temperature Materials and Engineering

- a1 18-09-01-K Novel Aspects of Graphite Intercalation by Fluorine and Fluorides and New B/C; C/N and B/C/N Materials Based on the Graphite Network  
J.KOUVETAKIS, T.SASAKI, B.SHEN, R.HAGIWARA, M.LERNER, K.KRISHNAN and N.BARTLETT
- a1 18-09-02-G Fluorination of Graphite Oxide  
T.NAKAJIMA, M.TOUMA and M.NAMBA
- a1 18-09-03-G The Preparation of Tungsten Carbide Film by Thermal CVD  
N.TOKUNAGA, Y.KITA and M.DOI
- a1 18-09-04-G CVD Tungsten Film for Solar Energy Conversion  
Y.CHONG, S.HONDA and N.WATANABE
- a1 18-09-05-K A New Process - PULSE CVI -  
K.SUGIYAMA
- a1 18-09-06-G Nitriding of Aluminum Oxide in a Microwave Discharge and Properties of Products  
H.UYAMA, T.KANAI and O.MATSUMOTO
- a1 18-09-07-G Effect of Additives on Combustion Synthesis of High Temperature Materials  
O.ODAWARA
- a1 18-09-08-G Studies on a New Combined Concentrating/Oven Type Solar Cooker  
P.RAMAIHAH, E.VIDYASAGARAN, M.RAGHAVAN, S.JOHN, N.SHANMUGAM and C.SOORIAMOORTHY
- a1 18-09-09-G Pebble Bed Solar Pond - A Feasibility Study  
M.RAGHAVAN, S.JOHN, E.VIDYASAGARAN, R.SELVARAJ and K.VASU
- a1 19-09-01-K The Effect of Acidity/Basicity on Cationic/Anionic Speciation in Non-Aqueous Solvents and Melts  
T.O'DONNELL
- a1 19-09-02-G Measurements of Basicity by Phosphorescence Spectrometry of Vanadate Ions in Molten Bisulfates and Pyrosulfates  
Y.KANEKO and H.KOJIMA
- a1 19-09-03-K Solid Electrolyte Sensors for Dissolved Elements in Molten Metals, Salts and Silicates  
Z.KOZUKA
- a1 19-09-04-G Investigation of Cathode Processes in Slag Melts with a Disk Rotating Electrode  
T.TZVETKOFF
- a1 19-09-05-G Redox Potential Studies in Borate and Silicate Melts by Linear Sweep Voltammetry  
K.SUZUMURA, K.KAWAMURA and T.YOKOKAWA
- a1 19-09-06-K Modified Carbon Anodes for Fluorine Production  
M.CHEMLA and D.DEVILLIERS
- a1 19-09-07-G Fluorine Cell with a Novel Electrode  
T.TOJO, Y.CHONG, T.IWASAKI, K.IKARI and N.WATANABE
- a1 19-09-08-K Preparation of Nitrogen Trifluoride by Molten Salt Electrolysis  
P.SARTORI and K.LATTASCH
- a1 19-09-09-G Effect of Water on Anodic Dissolution of Metal Electrode in a Molten  $\text{KF-HF-NH}_4\text{F}$  System  
A.TASAKA, M.HORI, M.OHASHI and K.KANEMITSU



- a1 19-09-10-G Development of Sodium/Selenium Tetrachloride Cells with Chloroaluminate Melts  
M.MATSUNAGA, M.MORIMITSU, T.ENDOH, M.SUEHIRO and K.HOSOKAWA
- a1 19-09-11-G Electrochemical Behaviour of Nickel Oxide in Molten Carbonate System  
G.XIE, Y.SAKAMURA, K.EMA and Y.ITO
- a1 19-09-12-G RRDE Studies of Molten Chloride Systems  
K.EMA, H.YABE, S.HIKINO and Y.ITO
- a1 19-09-13-G Corrosion of High Temperature Materials in Refluxing Mercury and Flowing Sodium  
T.SUZUKI and I.MUTOH
- a1 19-09-14-G Thermodynamic Considerations of Nuclear Pyrochemical Processing  
H.MORIYAMA, K.KINOSHITA, Y.ASAOKA and Y.ITO
- a1 19-09-15-G Chemical and Electrochemical Stability of SnO-based Anodes in Cryolite-Alumina Baths  
J.XUE and Z.QIU
- a1 21-09-01-K Quantum Chemistry of Metal-Molten Salt Interactions  
N.CHEN
- a1 21-09-02-G Structure and Dynamic Properties of Molten Alkali Hydroxides  
I.OKADA, S.OKAZAKI and N.OHTORI
- a1 21-09-03-G Surface Tension of LiCl-NaCl-AlCl<sub>3</sub> Ternary Melt  
T.EJIMA, Y.SATO, T.YAMAMURA and M.FUKASAWA
- a1 21-09-04-G X-Ray Diffraction Analysis of Molten PrCl<sub>3</sub>-MCl (M=Na and K) Mixtures  
K.IGARASHI and J.MOCHINAGA
- a1 21-09-05-G The Physical Properties and Structure of Molten NaCH<sub>3</sub>COO Hydrate  
A.KAJINAMI, K.MORIOKA, T.YANOMARU, S.DEKI and Y.KANAJI
- a1 21-09-06-K Electrodeposition from Molten Salt System  
A.BARABOSHKIN
- a1 21-09-07-G Electrodeposition of Tungsten from Zinc Halide-Sodium Halide Melts  
A.KATAGIRI, M.SUZUKI and Z.TAKEHARA
- a1 21-09-08-G Formation of a Surface Two-Component Alloy by Simultaneous Electrodeposition of Ions Dissolved in a Fused Electrolyte; Role of the Underpotential Deposition  
F.LANTELME, N.KUMAGAI and M.CHEMLA
- a1 21-09-09-G Cathodic Reaction of Zirconium in Alkali Chloride Melts  
M.IIZUKA, T.SHIMADA and Y.ITO
- a1 21-09-10-G Electrodeposition of Molybdenum from Molten Salts  
Z.ZOU, S.XIA and H.TONG
- a1 21-09-11-G Electrorefining of Refractory Metals in Molten LiCl-KCl  
T.TAKENAKA, K.ZHOU and M.NANJO
- a1 21-09-12-G Molten Salt Electrodeposition of Refractory Metal Carbides Mechanism and Nucleation Studies  
D.TOPOR and J.SELMAN
- a1 21-09-13-G Cathodic Reduction of Ti (II) and Ti (III) in Eutectic LiCl-KCl Melt  
M.KAWAKAMI, H.KUMA and K.ITO
- a1 21-09-14-G Nucleation and Growth of Liquid Magnesium when Deposited Cathodically from Molten Chlorides  
G.HAARBERG, S.JOHANSEN, J.MELAAS and R.TUNOLD
- a1 21-09-15-G Electrode Processes and Chemical Reactions of Hafnium in Halogenide Melts  
S.KUZNETSOV, S.KUZNETSOVA, E.POLYAKOV and P.STANGRIT

- a1 21-09-16-G Anodic Electrode Processes of Ta in Molten Chlorides  
L.POLYAKOVA, E.POLYAKOV and P.STANGRIT
- a1 22-09-01-K Materials and Materials Problems in Molten Salt Electrolysis Processes  
H.WENDT
- a1 22-09-02-G Chemical Stability of Molten Mixtures of Cryolite and Alkali Halides with Respect to Air and/or Carbon Dioxide  
O.HERSTAD
- a1 22-09-03-K Inert Anodes for Aluminium Electrolysis. The Corrosion Problem  
J.THONSTAD and H.WANG
- a1 22-09-04-G Effect of Cell Wall Structures on the Performance of Bipolar Electrode Cell in Fused Chloride System  
S.KONDA, T.NARITA and T.ISHIKAWA
- a1 22-09-05-K Application of Inert Cathode Materials in Aluminium Electrolysis at Lower Temperatures  
Z.QIU

## I-2. Material Problems for the Application of Oxide Superconductors

- a2 19-11-01-K Low Temperature Effects in Electrochemical Systems with High  $T_c$  Superconductors  
A.PINKOWSKI, J.DONEIT, K.JÜTTNER, W.LORENZ, G.SAEMAN-ISCHENKO and M.BREITER
- a2 19-11-02-G Complex Susceptibility of Single Crystal  $YBa_2Cu_3O_{7-x}$   
H.MAZAKI, H.YASUOKA, T.TERASHIMA, Y.BANDO, K.YAMAMOTO, K.HIRATA and K.IIJIMA
- a2 19-11-03-G Effect of Synthesis Conditions on Microstructure and Superconducting Properties of Bulk  $YBa_2Cu_3O_x$  by Quench and Melt Growth (QMG) Process  
M.MORITA, K.DOI, A.HAYASHI, K.MIYAMOTO, M.MURAKAMI and K.SAWANO
- a2 19-11-04-K Glass Formation and Crystallization Process of Bi-Containing High- $T_c$  Superconductors  
T.MINAMI
- a2 19-11-05-G Chemical Properties of High  $T_c$  Oxide Superconductors Near Their Critical Temperatures  
Y.TAKASU, K.HANYU, K.TAKEDA, Y.MATSUDA and K.YAHIKOZAWA
- a2 19-11-06-G Ionic and Electronic Conductivity in Oxide Superconductors : Studies of the Prototype Systems "YBaCuO" and "(Bi, Pb)SrCaCuO"  
W.GÖPEL, W.CARRILLO-CABRERA, H.WIEMHÖFER, C.ZIEGLER, T.BIEGER and N.VALVERDE
- a2 19-11-07-K Dynamic Superconducting System by Using Novel Superconductors  
Y.MURAKAMI
- a2 19-11-08-G Superconducting Properties of  $YBa_2Cu_3O_{7-x}$ -Metal Composites  
N.IMANAKA, F.SAITO, H.IMAI and G.ADACHI
- a2 19-11-09-G Silver Doping into the High- $T_c$  Oxide Superconductors  
Y.MATSUMOTO, J.HOMBO and Y.YAMAGUCHI
- a2 19-11-10-K Low Temperature Growth and Structure of  $YBa_2Cu_3O_{7-x}$  Epitaxial Thin Film  
Y.BANDO
- a2 19-11-11-G Effects of Structure on the Superconductivity of Bi-Sr-Ca-Cu-O Films  
S.NAGAI, N.FUJIMURA and T.ITO

### I-3. Electronic Materials in Electrochemical Technology

- a3 18-06-01-K Electrochemical Technology in Electronics  
L.ROMANKIW
- a3 18-06-02-G Thermodynamic and Kinetic Aspects of Underpotential Deposition  
D.SCHERSON
- a3 18-06-03-K Real-Time, Sub-Monolayer Monitoring of Electrochemical Processes Using SH-Acoustic Plate Mode Devices  
A.RICCO, S.MARTIN and G.FRYE
- a3 18-06-04-K Electrochemical Machining of Refractory Metals - Material Recycling and Waste Prevention  
L.BINDER
- a3 18-06-05-G The Mechanism of High Resolution in Azide/Novolak Photoresist Film by Developer Soak before Exposure  
S.ASAUMI and H.NAKANE
- a3 18-06-06-K Laser Induced Electrodeposition of Transition Metals on Silicon  
W.KAUTEK and W.PAATSCH
- a3 18-06-07-G Corrosion Study of Al(Cu) Exposed to Reactive Ion Etch  
V.BRUSIC, G.FRANKEL, C.HU, M.PLECHATY and J.LEWIS
- a3 18-06-08-K Activation Processes for Metallization of Polymers  
C.SAMBUCETTI, E.O'SULLIVAN and L.ROMANKIW
- a3 19-06-01-G Microstructure of Electrodeposited Nickel/Phosphorus Films  
U.HOFMANN and K.WEIL
- a3 19-06-02-G Double Layer Plating from Single Plating Bath  
F.MATSUI, I.NAKAYAMA, H.UCHIDA, T.OTAKA and T.KAWAKUBO
- a3 19-06-03-G Electrochemical Control of Defectiveness of Anode-Formed Dielectric on the Metal Surface  
E.SPERANSKAYA and A.MEIRMANOVA
- a3 19-06-04-G Properties of Electroless Rhodium Deposits  
K.OHTSUKA, K.OKUNO and E.TORIGAI
- a3 19-06-05-G Thermal Synthesis and Electrochemical Properties of Titanium Disulfide  
V.DUSHEIKO, Y.MIKHAILIK, N.PARKHOMENKO and T.TRIFONOVA
- a3 19-06-06-G Electrochemical Behaviour of  $(YBa_2Cu_3)C_{0.1}O_7$   
Z.STANKOVIC, M.SUSIC and M.PJESCIC
- a3 19-06-07-K Recent Development of Hybrid Microelectronics  
S.SHIBATA
- a3 19-06-08-G Electroless Deposition of  $RuO_2$  Conductive Films on Electroceramics  
N.BABA, T.YOSHINO and M.HIGASHIDA
- a3 19-06-09-G Electric Double-Layer Capacitors with Activated Carbon Fibers and Sprayed Aluminum Electrodes  
A.YOSHIDA, I.TANAHASHI and A.NISHINO
- a3 19-06-10-G Electrochemical Properties of Electric Double Layer Capacitors  
I.TANAHASHI, A.YOSHIDA and A.NISHINO
- a3 19-06-11-G Ways of Improving the Technology of Dielectric Formation in Manufacturing Aluminium Capacitors  
A.MEIRMANOVA and E.Speranskaya
- a3 19-06-12-G Effect of the Pulse Heating on Electroless Ni-Alloy Thin Films  
J.KAWAGUCHI, H.YAMAZAKI, I.SAITO and T.OSAKA

- a3 19-06-13-G A Study on Discharge Characteristics of Electroplated Cathodes for Plasma Display Panel  
H.SAWAI, I.KOIWA, K.FUJII, Y.TERA0, H.KOBAYASHI, M.IKEHATA and S.SHIBATA
- a3 19-06-14-G Film Formation Mechanism of Polymer Electrodeposition Applied to Micro-Color Filters in Full-Color LCD  
M.SUGINOYA, H.KAMAMORI and K.IWASA
- a3 19-06-15-G Poly(di(2-thienyl)naphthalenes): Anode-active and Electrochromic Polymers  
S.TANAKA and K.KAERIYAMA
- a3 19-06-16-K Modified Polymer Electrolytes for Ambient Temperature Applications  
J.PRZYLUSKI and W.WIECZOREK
- a3 19-06-17-G Anion-doped Polyaniline Films of Fractal Structure  
Y.MIKHAILIK, L.PISMENNAYA and V.PRISYAZHNYI
- a3 21-06-01-K Perpendicular Magnetic Recording Media by Electroless-Plating Method  
T.OSAKA and H.MATSUBARA
- a3 21-06-02-K Bias-Sputtered Cobalt-Chromium Films for Perpendicular-Recorded Computer Discs  
D.MAPPS and N.MAHVAN
- a3 21-06-03-G On the Microstructure of Electroless-Plated Cobalt Alloy Thin Films with Perpendicular Magnetic Anisotropy  
T.HOMMA, K.SAITO and T.OSAKA
- a3 21-06-04-G Magnetic Films of High Coercivity Prepared by Plating on Anodized Coatings of Aluminum  
S.KAWAI
- a3 21-06-05-G Some Electrical and Magnetic Characteristics of Electroless and Electrolytic Deposits  
J.POLUKAROV, M.IVANOV, G.GORJUNOV and V.KRUTSKICH
- a3 21-06-06-G High Corrosion-Resistive FeSi Multilayered Films for Magnetic Recording Heads  
C.WAKABAYASHI, N.ISHIWATA and T.MATSUMOTO
- a3 21-06-07-K Pulsed Electrodeposition of Invar Fe-Ni Alloys  
D.GRIMMETT, M.SCHWARTZ and K.NOBE
- a3 21-06-08-K Recent Trend on High Density Plated Disks  
F.GOTO, M.KIMURA, M.YANAGISAWA, Y.SUGANUMA and T.OSAKA
- a3 21-06-09-G The Role of Additives in the Plating of Magnetic Thin Films  
I.CROLL and G.WHITNEY
- a3 21-06-10-G Media Noise and Microstructure of Electroless Plated Disk  
T.MATSUNAGA, M.KANEKO, Y.MIYAMOTO, M.TAGAMI and T.TOMITA
- a3 21-06-11-G Chemically Textured Alumite Disk Substrates for Rigid Disks Assuring Low Flying Height of Heads  
N.TSUYA, T.TOKUSHIMA, Y.UMEHARA, M.SHIRAKI and Y.WAKUI
- a3 21-06-12-G Microstructure and Properties of Chemically Textured Magnetic Disc Substrates  
N.TSUYA, Y.OKA and Y.HIRAYAMA
- a3 21-06-13-K Structure-Property Relationship in Electroless Copper  
S.NAKAHARA
- a3 21-06-14-K Recent Trend Application of Electroless Copper Plating to Printed Circuit Boards  
H.HONMA
- a3 22-06-01-K Effect of Inclusions on the Properties of Plated Films for Electronic Applications  
Y.OKINAKA

- a3 22-06-02-K The Control of the Activity of Additives in Plating  
Electrolytes by Linear Sweep Voltammetry  
J.VANHUMBEECK and J.VAN PUymbROECK
- a3 22-06-03-G Electrochemical and XPS Studies of Dissolution and  
Passivation of Copper Surfaces  
V.BRUSIC, S.COHEN, F.KAUFMAN, G.FRANKEL and B.RUSH
- a3 22-06-04-G Application of Electroless Copper Plating to Molded Circuits  
K.YOSHINO, T.BENJAMIN and J.RYCHWALSKI
- a3 22-06-05-G Metallization of Alumina Ceramics by Electroless-Plating  
T.OSAKA, Y.TAMIYA, K.NAITO and K.SAKAGUCHI

#### I-4. Research and Development of Electroceramics

- a4 18-11-01-K The Sol-Gel Processing of Electroceramics  
D.PAYNE
- a4 18-11-02-G Texture and Photochromic Characteristics of  $\text{ZnO}_x$  Thin Films  
N.FUJIMURA, T.NISHIHARA and T.ITO
- a4 18-11-03-G Formation of Yttria Stabilized Zirconia Film by Plasma MOCVD  
O.MATSUMOTO, N.OKA, I.ONO and H.UYAMA
- a4 18-11-04-G Infrared-Sensitive SiC Fiber Thermistor  
N.MUTO, M.MIYAYAMA and H.YANAGIDA
- a4 18-11-05-G Characterization of Trap Centers in Semiconducting  
Ceramics by ICTS  
T.MAEDA and M.TAKATA
- a4 18-11-06-G Evaluation of Some Amorphous Metal Electrodes for  
Alkaline Electrolysis: Standard Versus Novel Techniques  
M.ISMAIL, M.DAOUS and G.KREYSA
- a4 18-11-07-G Preparation of Cordierite Ceramics from Metal Alkoxides  
M.OKUYAMA, T.FUKUI and C.SAKURAI
- a4 18-11-08-G Electronic Materials Using the Energy Barrier  
Associated with Oxygen  
S.FUJITSU, K.KOUMOTO and H.YANAGIDA
- a4 18-11-09-G Hetero-Contact Effects of Atmosphere-Sensitive Ceramic  
Semiconductor  
M.MIYAYAMA, Y.NAKAMURA and H.YANAGIDA
- a4-18-11-10-G Humidity Sensitivity of CaO Doped YTTRIA  
K.KATAYAMA, H.OUSAWA, T.AKIBA and H.YANAGIDA
- a4-18-11-11-G Microstructure and the Dielectric Properties in  
 $\text{SrTiO}_3\text{-Pb(Fe,W)O}_3$  BL-Type Capacitors  
M.KUWABARA

#### I-5. Materials and Processes for Information Recording, Display and Storage

- a5 21-10-01-K Electroluminescence in Organic Dye Films  
T.TSUTSUI, C.ADACHI and S.SAITO
- a5 21-10-02-G Electrochemical Deposition of  $\text{IrO}_2$  Thin Film on  
OTE and Its Electrochromic Properties  
T.YOSHINO, H.MASUDA, K.ARAI and N.BABA
- a5 21-10-03-G Effect of Post-Deposition Processes on the Corrosion  
Properties of Sputtered FeMn and FeMnCr Thin Films  
N.STAUD, C.HWANG and J.HOWARD

- a5 21-10-04-G Electrochemical Preparation of Phthalocyanine Layers on an Al Substrate Using Aqueous Surfactant Solutions  
K.HOSHINO, S.YOKOYAMA, T.SAJI and H.KOKADO
- a5 21-10-05-G Thermal and Electrical Properties of Naphthalocyanines  
M.SHIMURA, T.KAMIKUBO, Y.SHIMURA and S.OHTANI
- a5 21-10-06-K Prussian Blue Modified Electrodes and Applications as an Electrochromic Material  
K.ITAYA
- a5 21-10-07-G Performance Analysis of All-Solid-State Electrochromic Display Device with Inorganic Ion-Exchanger  
K.KUWABARA, M.OHNO and K.SUGIYAMA
- a5 21-10-08-G Electrochromism of Phthalocyanine Thin Film  
M.MASUI, Y.OHGO, A.HIGUCHI, F.KANEKO and M.TAKEUCHI
- a5 21-10-09-G A Polymer-Based Electrochromic Device  
A.CORRADINI, A.MARINANGELI and M.MASTRAGOSTINO

#### I-6. New Functional Materials by Electrochemical Methods -Syntheses and Applications

- a6 18-03-01-K Microelectrochemical Devices Based on Redox Polymers  
M.WRIGHTON, V.CAMMARATA, O.CHYAN, R.CROOKS, T.GARDNER, N.LEVENTIS, D.OFER, M.SCHLOH and D.TALHAM
- a6 18-03-02-K Pioneer Works about the Coupling between Electron and Proton Exchange and Transport Properties of Polymeric Semiconductors  
R.BUVET
- a6 18-03-03-G Conducting Polymer Thin Films Prepared by LB Technique and Electrochemical Polymerization  
M.ANDO, Y.WATANABE, T.IYODA, K.HONDA and T.SHIMIDZU
- a6 18-03-04-G Electrochemical Control of Layered Structure of Conducting Polymer Composite Film  
T.IYODA, H.TOYODA, K.HONDA and T.SHIMIDZU
- a6 18-03-05-G Electrochemical Preparation of Highly Conducting Polyaniline  
A.KITANI, K.YOSHIOKA and K.SASAKI
- a6 18-03-06-G Poly (Pyrrole-Metalloporphyrins) Film Modified Electrodes: Preparation and Electrocatalytic Applications  
F.BEDIOUI, P.MOISY, J.DEVYNCK and C.BIED-CHARRETON
- a6 18-03-07-G Electrochemical Properties of Polyaniline  
T.KABATA, T.OHSAWA, H.NISHIHARA, K.ARAMAKI, M.ONODA and K.YOSHINO
- a6 18-03-08-G Preparation, Structure and Electrochemical Properties of Highly Conductive Metallophthalocyanine Polymers  
M.FUTAMATA, S.HIGUCHI and S.TAKAHASHI
- a6 18-03-09-G One-Step Electrochemical Synthesis and Characterization of Poly(Aniline)/Nafion and Poly(3-Methylthiophene)/Nafion Composites  
G.BIDAN and B.EHUI
- a6 18-03-10-G Preparation of Ultra-Thin Solid Polymer Electrolyte Film by Using an RF Plasma Process  
Y.UCHIMOTO, Z.OGUMI and Z.TAKEHARA
- a6 18-03-11-G Scanning Tunneling Microscopy of Semiconductor/Liquid Interfaces under Potentiostatic Conditions  
K.ITAYA, E.TOMITA and N.MATSUDA
- a6 19-03-01-K Electrochemical Synthesis of Polypyrrole-Metal Oxide Particle Composite Films  
H.YONEYAMA, K.KAWAI and Y.SHOJI

- a6 19-03-02-G Separation of Molecules with Porous Anodic Aluminum Oxide Films  
K.WADA, S.ONO, T.YOSHINO, K.WADA, S.YABUSHITA and N.BABA
- a6 19-03-03-G Catalysis and Electrocatalysis by Electrodeposited Oxometallates  
B.KEITA and L.NADJO
- a6 19-03-04-G Surface Functionalization with Oxometallates in Polymeric Matrices  
L.NADJO and B.KEITA
- a6 19-03-05-G Solid State Voltammetry in Network Polymer Electrolytes  
M.WATANABE, M.LONGMIRE and R.MURRAY
- a6 19-03-06-G Polyaniline/Tungsten Oxide Electrochromic Glass  
T.ASAOKA, K.OKABAYASHI, K.ABE and T.YOSHIDA
- a6 19-03-07-G Sulphurization of Copper-Indium Thin Film Alloys: Substrate Effects  
J.HERRERO and J.ORTEGA
- a6 19-03-08-G Anodic Oxidation of Silicon in  $H_3PO_4$  and  $H_3BO_3$  Containing Solutions  
L.MILESHKO, I.SOROKIN and V.BONDARENKO

#### I-7. Molecular Design on Electrode Surfaces

- a7 19-03-01-K Transition Metal-Substituted Heteropolytungstates as Electrocatalysts  
J.TOTH, H.KIM and F.ANSON
- a7 19-03-02-G Molecular Design with Bilayer Polymer Membranes for Electrochemical and Photoelectrochemical Functions  
M.KANEKO
- a7 19-03-03-G Investigation of Charge-Transport Processes in Electroactive Thin Films Using a Quartz Crystal Microbalance Technique  
A.KELLY, S.YAMAMOTO, T.OHSAKA and N.OYAMA
- a7 19-03-04-G Odd-Even Effect on Electrochemistry of Viologen Polymers Complexed with Anionic Bilayer Membranes  
M.SHIMOMURA, K.UTSUGI, K.OKUYAMA, O.HATOZAKI and N.OYAMA
- a7 19-03-05-G Charge-Transport Rates in Thin Films of Poly (Alkyleneviologen)  
O.HATOZAKI, T.OHSAKA, N.OYAMA and M.SHIMOMURA
- a7 19-03-06-G Surface Properties and Electrochemistry of Well-Characterized, Electrode-Confined Redox Active Polymers and Block Copolymers  
D.ALBAGLI, G.BAZAN, R.SCHROCK and M.WRIGHTON
- a7 19-03-07-G Characterization of Alkylthiol Anchored Monolayer Film on Metal Electrode  
T.SAWAGUCHI, T.MATSUE and I.UCHIDA
- a7 19-03-08-G Development of Molecular Membrane Systems for Biomimetic Sensors  
Y.UMEZAWA, M.SUGAWARA, M.KATAOKA and K.ODASHIMA
- a7 19-03-09-K Design of Enzyme Layer on Electrodes for Biosensors  
T.OSA and J.ANZAI
- a7 19-03-10-G Promoter Modified Electrodes for Cytochrome c Electrochemistry  
I.TANIGUCHI
- a7 19-03-11-G Bioelectrocatalysis at Dehydrogenase-Modified Electrodes  
M.SENDA, T.IKEDA, K.MIKI, F.FUSHIMI and S.TODORIKI

- a7 21-03-01-K Electrodes Composed of Superconducting Ceramics  
J.McDEVITT, R.GOLLMAR, S.CHING, R.MURRAY, J.COLLMAN,  
G.YEE and W.LITTLE
- a7 21-03-02-G Conducting Polymer Films Formed by Electroreduction  
of Organic Halides  
H.NISHIHARA, M.TATEISHI, H.HARADA, S.KANEKO, T.SHIMURA,  
K.ARAMAKI and R.MURRAY
- a7 21-03-03-G Polypyrrole Having Quaternized Pyridine and Their Composites  
with Functional Anion  
T.IYODA, M.AIBA, T.SAIKA, K.HONDA and T.SHIMIDZU
- a7 21-03-04-G Spectroelectrochemical Studies on the Charge Transfer  
Complex Formation during Electron Transfer Process at the  
Interface of Metallocene Electrode Films  
Y.ANDO, N.OGINO, H.NISHIHARA and K.ARAMAKI
- a7 21-03-05-G Preparation and Characterization of the Polyaniline  
Functionalized with Rhenium Carbonyl  
M.SATO and M.WRIGHTON
- a7 21-03-06-G Electro-Oxidative Polymerization of Diphenyldisulfide  
on Electrode Surface  
K.YAMAMOTO, H.NISHIDE and E.TSUCHIDA
- a7 21-03-07-G Electrochemical Behavior of Polymer Film-Coated Electrodes  
Prepared by Electropolymerization of Poly-Amino Compounds  
N.OYAMA, M.SATO, T.OHSAKA and M.TASHIRO
- a7 21-03-08-G Quaternised Poly(4-Vinylpyridine) Coated Electrodes for  
Copper Ion Detection in the Presence of Ligands which  
Stabilise Cu(I)  
J.CASSIDY and K.TOKUDA
- a7 21-03-09-K Controlling the Supramolecular Structure of Electronically  
Conductive Polymers - An Electrochemical Method  
for Producing Better Materials  
C.MARTIN, L.VAN DYKE and Z.CAI
- a7 21-03-10-G Metal Ion Trapping by a Polypyrrole Film Containing  
Caten and Type Complexing Cavities  
G.BIDAN, B.DIVISIA-BLOHORN, J.KERN and J.SAUVAGE
- a7 21-03-11-K The Kinetics of Electropolymerization  
J.SCHULTZE
- a7 21-03-12-G Artificial Visual System with LB Film Modified Electrode  
K.NISHIYAMA and M.FUJIIHARA
- a7 21-03-13-G Artificial Photosynthetic Reaction Center Constructed with  
Monolayer Assembly  
M.FUJIIHARA, T.KAMEI and M.SAKOMURA
- a7 21-03-14-G Formation of Pigment Thin Films by Electrolysis of  
Surfactants with Ferrocenyl Moiety  
T.SAJI, Y.ISHII and M.GOTO
- a7 21-03-15-G Electropolymerization of a Vacuum-Evaporated Monomer Film  
A.YASUDA and J.SETO
- a7 21-03-16-G In Pursuit of Intelligent Polymeric Materials  
G.WALLACE
- a7 21-03-17-K Combined Ellipsometric and Electrochemical Studies of  
Hydrous Gold Oxide Layers and the Resulting Electroreduced  
Gold Overlayer  
M.VELA, R.SALVAREZZA, J.ZERBINO and A.ARVIA
- a7 21-03-18-G Recent Developments in the Application of Periodic  
Perturbing Potentials to Noble Metal Electrodes  
W.TRIACA, A.VISINTIN, J.CANULLO and A.ARVIA



## II HIGH TECHNOLOGY

### II-1. Advanced Fuel Cell

- b1 18-01-01-K The Alkaline Fuel Cell Program for the European Space Vehicle HERMES (Its Possible "Spin-off" on Commercial Fuel Cell Technology)  
K.KORDESCH
- b1 18-01-02-G High-Power Alkaline Fuel Cell System for Electric Vehicles (Hybrid System with Zinc-Bromine Battery)  
K.KORDESCH, J.OLIVEIRA, C.GRUBER and G.WINKLER
- b1 18-01-03-K In-Situ Investigation of Fuel Cell Catalysts by Sniftirs and On-Line Mass Spectroscopy  
W.VIELSTICH, B.BITTINS-CATTANEO and T.IWASITA
- b1 18-01-04-G Molecular Design of a Methanol Fuel Cell Electrode Based on Fundamental Studies of the Direct Oxidation of Methanol on Polycrystalline and Single Crystal Platinum Electrodes  
C.LAMY, B.BEDEN and J.LEGER
- b1 18-01-05-G Electrocatalytic Oxidation of Alcohols on Non Precious Catalysts such as Mixed Carbides of Tungsten and Molybdenum  
G.BRONOEL, E.MUSEUX, G.LECLERCQ, L.LECLERCQ, R.ROUGET and S.BESSE
- b1 18-01-06-G The Electrocatalytic Oxidation of Some Organic Acids on Metal/Nafion Electrodes  
O.ENE and D.DUPREZ
- b1 18-01-07-K Development of Alloy Electrocatalysts for Phosphoric Acid Fuel Cells (PAFC)  
P.STONEHART
- b1 18-01-08-G Development of Air-cooled Phosphoric Acid Fuel Cell  
H.SUZUKI, M.IDE, N.NISHIZAWA, O.TAJIMA and A.HAMADA
- b1 18-01-09-G Improvements in Performances for Phosphoric Acid Fuel Cell Cathodes Using Thinner Electrode Substrates  
M.INOUE, H.FUKUI, K.MIWA, M.WATANABE and P.STONEHART
- b1 18-01-10-G Characterization of Phosphoric Acid Fuel Cell Electrodes and Catalysts by Mathematical Modeling  
J.LEE, J.BUCHANAN, L.KECK, J.SELMAN and G.LIE
- b1 18-01-11-G Influence of Acid Occupation on Performance of PAFC Gas-Diffusion Cathodes  
N.GIORDANO, E.PASSALACQUA, V.RECUPERO, M.VIVALDI, E.TAYLOR and G.WILEMSKI
- b1 18-01-12-G High-Performance Gas Diffusion Porous Electrode Starved of Electrolyte Solution  
Z.TIAN, Z.LIN and J.YOU
- b1 18-01-13-G Polarization Study of Fuel Cell with Multi- Reference Electrodes  
K.MITSUDA and T.MURAHASHI
- b1 19-01-01-K Status of Advanced Fuel Cell Technology in Japan  
Y.KURIHARA
- b1 19-01-02-G The Development of the Large-Scale Molten Carbonate Fuel Cell  
Y.YAMAMASU, M.HOTTA and S.SATOU
- b1 19-01-03-G Molten Carbonate Fuel Cell Technology Improvement  
T.MURAHASHI, T.TANAKA, E.NISHIYAMA
- b1 19-01-04-K Status of Advanced Fuel Cell Technology in the United States  
G.HAGEY

- b1 19-01-05-K Direct Fuel Cells: Fundamental and Technological Aspects  
H.MARU
- b1 19-01-06-K Status of Advanced Fuel Cell Technology in Sweden  
L.SJUNNESSON
- b1 19-01-07-K Status of Advanced Fuel Cell Technology in Italy  
F.MARIO and R.VELLONE
- b1 19-01-08-K Status of the Advanced Fuel Cell Technology in The Netherlands  
K.JOON and S.Van der MOLEN
- b1 19-01-09-K Basic Properties and Parameters in Fuel Cell Development:  
Measurement Techniques and Relevance to Scale-Up  
J.SELMAN
- b1 19-01-10-G Electrode/Electrolyte Combined Tape for Molten Carbonate  
Fuel Cell  
K.HATOH, J.NIIKURA, N.TANIGUCHI, T.GAMO and T.IWAKI
- b1 19-01-11-G A Study on Electrolyte Management of MCFC  
Y.AKIYAMA, Y.TONOIKE, Y.ITOH, T.NAKAJIMA, M.NISHIOKA,  
Y.MIYAKE, S.MURAKAMI and T.SAITO
- b1 19-01-12-G The Effect of Pore Structure on Polarization Characteristics  
of MCFC Cathodes  
S.KUROE, Y.IWASE, H.OKADA, K.IWAMOTO, M.TAKEUCHI and T.MORI
- b1 19-01-13-G Solubilities of Metal Oxides in Molten Carbonate  
K.OTA, S.MITSUSHIMA, S.KATO and N.KAMIYA
- b1 19-01-14-G Electrochemical Behavior of Porous NiO in Molten Carbonate  
Fuel Cells Effect of Electrolyte Composition  
H.NUMATA, T.SHIMADA, M.TAMURA, I.OHNO and S.HARUYAMA
- b1 19-01-15-G The Effect of Electrolyte Content on AC Impedance in Molten  
Carbonate Fuel Cell Electrodes  
K.YAMASHITA and K.MURATA
- b1 19-01-16-G Characterization of Porous Electrodes for MCFC by Impedance  
Measurements  
J.NIIKURA, K.HATOH, N.TANIGUCHI, T.GAMO, T.NISHINA  
and I.UCHIDA
- b1 19-01-17-G Reaction Mechanism and Kinetics of Hydrogen Oxidation in  
Molten Carbonates  
T.NISHINA and I.UCHIDA
- b1 19-01-18-P Electrode Modelling of Porous Anode of Sintered Au and Ni  
Spheres for MCFC  
T.NISHINA, T.KUDO, I.UCHIDA and J.SELMAN
- b1 19-01-19-P Cell Testing of Alternative Electrolytes for MCFC  
Y.MIYAZAKI, K.TANIMOTO, M.YANAGIDA, S.TANASE, T.KOJIMA  
and T.KODAMA
- b1 21-01-01-K R&D on SOFC in Japan and Related Problems  
M.DOKIYA
- b1 21-01-02-G Planar Solid Oxide Fuel Cell: Nickel Cermet Anode  
T.KAWADA, N.SAKAI, H.YOKOKAWA, M.DOKIYA and M.MORI
- b1 21-01-03-G A Planar Type Solid Oxide Fuel Cell Technology  
S.MARUYAMA, K.KOSEKI and T.NAKANISHI
- b1 21-01-04-G Preparation of Planer Thin Film Solid Electrolyte Fuel Cells  
H.MICHIBATA, H.TENMEI, T.NAMIKAWA and Y.YAMAZAKI
- b1 21-01-05-G Solid Oxide Fuel Cell with Stabilized Zirconia and Doped  
Ceria Thin Film  
K.EGUCHI, T.SETOGUCHI, H.ITOH and H.ARAI
- b1 21-01-06-G The Electrical Property and the Microstructure of ZrO<sub>2</sub>  
Based Solid Electrolytes  
A.YAMASHITA, A.NOHTOMI, H.OHNO, T.NAGASAKI and N.IGAWA

- b1 21-01-07-G A Proton Conductor Synthesized by the Thermal Reaction of Isopolytungstate  
K.NAGATA, Y.TANINAKA, S.DEKI and Y.KANAJI
- b1 21-01-08-P Planar Solid Oxide Fuel Cell: Chemical Thermodynamic Considerations on Materials  
H.YOKOKAWA, N.SAKAI, T.KAWADA and M.DOKIYA
- b1 21-01-09-P Planar Solid Oxide Fuel Cell: Ca Doped Lanthanum Chromite Separator  
N.SAKAI, T.KAWADA, H.YOKOKAWA, M.DOKIYA and T.IWATA
- b1 21-01-10-P Planar Solid Oxide Fuel Cell: Lanthanum Manganate Based Cathode  
M.MORI, R.ISHIKAWA, N.SAKAI, T.KAWADA, H.YOKOKAWA and M.DOKIYA
- b1 21-01-11-P Planar Solid Oxide Fuel Cell: Cell Performance  
T.IWATA, T.KAWADA, N.SAKAI, H.YOKOKAWA and M.DOKIYA

## II-2. New Electrochemical Process

### - New Technologies for Industrial Electrolysis

- b2 18-10-01-G The Equilibrium Concentration of Silver Ions in  $\text{CuSO}_4\text{-H}_2\text{SO}_4$  Baths at 60°C  
J.HOTLOS and M.JASKULA
- b2 18-10-02-G Electroreduction of Nitrogen Oxides on Electrodes of Pt and Group IB Metals  
K.NISHIMURA, K.MACHIDA and M.ENYO
- b2 18-10-03-G Continuous Zn Electrowinning Using a  $\text{H}_2$  Gas-Diffusion Electrode  
N.FURUYA and N.MINEO
- b2 18-10-04-K Cathodic Behaviour of Oxide Electrodes  
J.BOODTS, G.FREGONARA and S.TRASATTI
- b2 18-10-05-G Investigation of the Film Formed by Cathodic Reduction of Chromate on Chlorate Cathodes  
G.LINDBERGH and D.SIMONSSON
- b2 18-10-06-G Voltammetric and ESCA Studies of the Chlorate Cell Cathodes  
Y.SELMI, R.FAURE and R.DURAND
- b2 18-10-07-K Electrochemical and Technological Aspects of a Solar Powered Advanced Water Electrolyzer  
J.DIVISEK
- b2 18-10-08-G Production of Acidic Hydrogen Peroxide Solution by Cathodic Oxygen Reduction  
H.TAKENAKA, Y.KAWAMI, I.UEHARA and N.WAKABAYASHI
- b2 18-10-09-G Ozone Generation by Water Electrolysis  
K.OTA, T.SUZUKI and N.KAMIYA
- b2 18-10-10-K New Electrochemical Processes Using High Overvoltage Anodes: Ozone Generation and Anodic Oxidation  
S.STUCKI
- b2 19-10-01-G Bipolar Electrolyzers for Chlor-Alkali Membrane Process  
H.ONO
- b2 19-10-02-G The Development of IEM Process and its Industrial Application in the Japanese Chlor-Alkali Industry  
K.YAMAGUCHI
- b2 19-10-03-G Expert System for Brine Electrolysis Cells  
L.ONICIU, S.AGACHI and A.IMRE

- b2 19-10-04-K Some Future Trends in Electrolysis Technology -Membrane Processes-  
S.YOSHIZAWA, Y.ITO and Z.OGUMI
- b2 19-10-05-G Hydrochloric Acid Electrolysis Using Solid Polymer Electrolytes  
I.UEHARA, Y.KAWAMI, N.WAKABAYASHI and H.TAKENAKA
- b2 19-10-06-G From the Catalyst Microparticles to the Pilot Plant: Development of a SPE Water Electrolyzer  
P.MILLET and R.DURAND
- b2 19-10-07-G Solid Polymer Electrolyte Water Electrolysis Using Perfluoro-Anion-Exchange Membrane  
M.MOTONE, Y.KAWAMI, I.UEHARA, N.WAKABAYASHI and H.TAKENAKA
- b2 19-10-08-G Preparation of Acids and Bases by Electrodialytic Water-Splitting Using Perfluorinated Ion Exchanger Membranes  
N.ISHIBASHI, M.TACHIBANA, S.INABA and T.IMATO
- b2 19-10-09-G Au/Nafion Anodes for the Electrooxidation of D-Glucose and Related Polyols  
O.ENEA
- b2 19-10-10-G Engineering and Kinetic Aspects of Electrolytic Xylitol and Sorbitol Production  
A.JOKIC, N.RISTIC, M.SPASOJEVIC, N.KRSTAJIC and M.JAKSIC
- b2 19-10-11-G Study on the Electro-Synthesis of p-Aminophenol from Nitrobenzene  
B.CHO and K.YUN
- b2 19-10-12-G Dissolution of Pt Anode in  $H_2SO_4$  Solution in the Presence of Acetonitrile  
N.KAMIYA, A.ANDO, K.NAGASATO and K.OTA
- b2 19-10-13-G An Electrochemical Method for the Growth Inhibition and/or Killing of Bacteria in Biological Fluids: URINE  
G.RAO
- b2 19-10-14-K Improved and New Materials for Aluminum Electrowinning  
H.ØYE
- b2 19-10-15-G Cell to Study Reaction Rates at the Interface of Molten Metal and Electrolyte  
R.KELLER, K.LARIMER and D.ANTHONY
- b2 19-10-16-G Kinetics of Titanium Dissolution in Alkali Melts  
T.TZVETKOFF and N.LINGORSKY
- b2 19-10-17-G Electrolytic Method for Simultaneous Separation and Purification of Rare Earth Elements Europium and Cerium in a Diaphragm Cell  
Q.ZHANG and M.WANG
- b2 19-10-18-G Advanced Materials for the Energy Efficient Production of Aluminum  
D.SADOWAY
- b2 19-10-19-G Electrochemical Fluorination - A Review  
W.CHILDS, F.KLINK, C.KOLPIN and L.CHRISTENSEN
- b2 19-10-20-K Electrode Materials in Electrosynthesis of Non-Organic Oxidants  
T.AGLADZE and Y.KOLOTYRKIN
- b2 21-10-01-G A Production Technology of Zn-Ni Alloy Electroplated Steel Sheets  
R.WAKE, M.SHIHONMATSU and Y.ANDO
- b2 21-10-02-G Study of an Undivided Filter-Press Electrochemical Reactor  
A.SAVALL, S.MOUYSSET and T.TZEDAKIS
- b2 21-10-03-G A Numerical Method of Calculating Secondary and Tertiary Current Distributions in Electrochemical Cells  
A.KATAGIRI

- b2 21-10-04-G Electrochemical Studies on Mass Transfer in a Gas-Liquid Two Phase Flow-Through-Electrode System  
M.KAMATA, K.SUGITA and F.UGINO
- b2 21-10-05-G Free Convection in Closed Electrochemical Systems  
F.BARK and F.ALAVYOON
- b2 21-10-06-G The Implications of Counter Electrode Gas Evolution on the Performance of Narrow Gap Parallel Plate Flow Electrolysers  
B.HAYATI and K.SCOTT
- b2 21-10-07-G Towards the Optimization of Mechanical Methods in Revealing the Surface Effects of Electrified Metal Surfaces  
T.HRYNIEWICZ

### II-3. Electrochemical Processing for Tailored Materials

- b3 18-05-01-K Outline on Plasma Processing  
R.ITATANI
- b3 18-05-02-K Plasma Deposition of Amorphous and Crystalline Silicon and Alloys  
C.TSAI
- b3 18-05-03-K The Influence of Pulse-Plating on the Microstructure of Copper Deposited from Sulfate Solution  
D.LANDOLT and O.CHENE
- b3 18-05-04-K Composition-Modulated Alloys Produced by Electrodeposition  
J.YAHALOM
- b3 18-05-05-G Electrochemical Deposition of Laminar Structures with Continuously Changing Composition of Layers  
A.DESPIC, S.SPAIC, V.JOVIC and T.TRISOVIC
- b3 18-05-06-G Crystallographic Structure of Plating Films and Amorphous Plating  
T.WATANABE
- b3 18-05-07-G Electrocatalytic Properties of Ultrafine Palladium Particles for Some Reactions Including Hydrogen  
Y.TAKASU, M.SUZUKI, Y.IWANAGA, Y.MATSUDA and K.YAHIKOZAWA
- b3 18-05-08-G MOVPE Growth of InGaAsP/InP Crystals for DFB Lasers Used in Optical Communication  
Y.IMAMURA
- b3 18-05-09-G Electrodeposition of Ga, As and Ga-As in Aqueous Solutions  
S.JANG, H.NUMATA, I.OHNO and S.HARUYAMA
- b3 18-05-10-G Synthesis of Advanced Materials by Electrochemical Processing in Nonaqueous Media  
D.SADOWAY
- b3 18-05-11-G In-Situ Surface Spectroscopy to Study the Photoelectrochemical Dissolution of Gallium Arsenide  
W.PLIETH, A.FELSKE and G.PFUHL
- b3 18-05-12-G Semiconductor Surface Modification for Electronic and Photochemical Applications  
H.LEWERENZ
- b3 18-05-13-G Anode Polarization under Non-Stationary Electrolysis  
A.RYBALKO and S.GALANIN
- b3 19-05-01-G Plasma-Photo Hybrid Processing of Electro-Functional Thin Films  
H.KOINUMA, M.NAKANO and K.TAKEUCHI
- b3 19-05-02-G Laser-Enhanced Deposition and Etching in Aqueous Media :  
A Review  
L.ROMANKIW

- b3 19-05-03-K In Situ Spectro-Ellipsometry Studies of Plasma and Electrochemical Deposition of Thin Film Electronic Materials  
R.COLLENS, Y.CONG, Y.KIM, R.MESSIER and K.VEDAM
- b3 19-05-04-K Microtopography of Electrochemical Surface Layers  
R.MULLER
- b3 19-05-05-G In Situ Observation of Electrode Surface by Using Photoacoustic and Photocurrent Spectroscopies  
A.FUJISHIMA, S.YOSHIHARA and A.ARUCHAMY
- b3 19-05-06-G LIFS Analysis of Spatial Distribution and Transport of Radicals in Processing Plasmas Used for Thin-Film Deposition  
K.TACHIBANA
- b3 19-05-07-G Laser Interferometry in Electrochemical Processing  
Y.FUKUNAKA and Y.KONDO
- b3 19-05-08-K Investigation of a Zinc Model Pore Electrode Using Photothermal Deflection Spectroscopy  
J.WEAVER, F.McLARNON and E.CAIRNS
- b3 19-05-09-G Electrochemical Measurement of Electrode Surface in Plasma  
S.ITO, H.SHIMADA, H.KIHIRA and T.MURATA
- b3 19-05-10-G Thermal Plasma Processing of Ceramic Coatings  
T.YOSHIDA
- b3 19-05-11-G Studies of Zinc-Nickel Alloy Plating  
T.CHAPMAN and M.MATHIAS
- b3 19-05-12-G Simulation of Low Pressure RF Plasma-Processing  
T.MAKABE
- b3 19-05-13-G Simulation of Shape Changes in Electrochemical Micro-Machining  
M.MATLOSZ, E.ROSSET and D.LANDOLT
- b3 19-05-14-G Future Perspectives  
N.MASUKO

#### II-4. Lithium Batteries

- b4 18-02-01-K Anodic and Cathodic Reactions on Lithium Electrodes in Aprotic Electrolytes  
K.WIESENER, U.ECKOLDT, D.RAHNER and E.BRACKMANN
- b4 18-02-03-K Several Considerations of Lithium Anode Rechargeability  
J.YAMAKI
- b4 18-02-04-G The Comparison of the Diffusion of the Dopants in Various Cathodes,  $\text{TiO}_2$ ,  $\text{MoS}_2$ , Polyacetylene, Polyaniline, for Lithium Batteries  
Z.TAKEHARA, K.KANAMURA, N.IMANISHI and S.YONEZAWA
- b4 18-02-05-K Rechargeability of  $\text{MnO}_2$  and  $\text{MnO}_2$  Cells  
A.KOZAWA
- b4 18-02-07-G Lithium-Manganese Composite Oxides for Lithium Secondary Batteries  
M.YOSHIO, H.NAKAMURA and H.KURIMOTO
- b4 18-02-08-K Electrochemistry of Manganese Dioxide in Lithium Nonaqueous Cell: Jahn-Teller Deformation of  $\text{Li}_x\text{MnO}_{2-\delta}$   
T.OHZUKU, K.SAWAI and T.HIRAI
- b4 18-02-09-G Rechargeability of Manganese Oxides in  $\text{LiPF}_6$  Electrolyte  
K.YOKOYAMA and Y.UETANI
- b4 19-02-01-K Lithium Battery Technologies in Japan  
Y.MATSUDA

- b4 19-02-02-G A Lithium Secondary Battery Using Lithium Containing Manganese Dioxide (CDMO) as the Cathode  
T.NOHMA, K.TERAJI, I.NAKANE, Y.FUJITA, H.WATANABE, Y.YAMAMOTO and N.FURUKAWA
- b4 19-02-03-G Effect of Alkali Metal Cations on the Electrode Behavior of Lithium Batteries  
K.TANAKA, S.SUZUKI, N.CHIBA, N.ISHIHARA and K.YODA
- b4 19-02-04-K Recent Developments in Rechargeable Lithium Batteries  
M.BROUSSELY and J.LABAT
- b4 19-02-05-G Amorphous  $\text{FeVO}_4$  as a Cathode Active Material in Secondary Lithium Batteries  
M.SUGAWARA, Y.KANEKO and K.MATSUKI
- b4 19-02-06-G  $\text{Li/LiCr}_x\text{V}_y\text{S}_2$  Secondary Batteries  
V.MANEV, A.NASSALEVSKA and A.MOMCHILOV
- b4 19-02-07-G Electrolytic Preparation of  $\text{V}_2\text{O}_5$  and Its Charge-Discharge Characteristic as a Cathode Active Material of Lithium Secondary Battery  
Y.SATO, T.NOMURA, H.TANAKA and K.KOBAYAKAWA
- b4 19-02-08-G Structural and Kinetic Characteristics of Niobium Sulfide Electrode for a Secondary Lithium Battery  
N.KUMAGAI and K.TANNO
- b4 19-02-09-K Lithium-Carbon Anode as Lithium Secondary Batteries  
O.YAMAMOTO, Y.TAKEDA, R.KANNO, S.OHASHI and T.ICHIKAWA
- b4 19-02-10-G Activity and Diffusivity of Lithium Intercalated in Graphite  
R.AGARWAL
- b4 19-02-11-G Electrochemical Intercalation of Alkali Metals into Graphite and GIC's. An Application to Lithium Batteries, Part I  
R.YAZAMI
- b4 19-02-12-G Lithium Batteries Based on GIC's with Metal Fluorides (Part II)  
R.YAZAMI and T.NAKAJIMA
- b4 19-02-13-G Lithium Surface Analyses by FAB Mass Spectrometry  
M.ARAKAWA, S.TOBISHIMA and J.YAMAKI
- b4 19-02-14-G Effects of Electrolytes on Electrodeposition of Lithium  
H.KOSHINA, N.EDA and A.MORITA
- b4 19-02-15-K Advances in Organic Electrolytes for Rechargeable Lithium Batteries  
V.KOCH, L.DOMINEY and J.GOLDMAN
- b4 19-02-16-G The AC Impedance Behavior at Lithium/Organic Electrolyte Interface  
M.MORITA and Y.MATSUDA
- b4 19-02-17-G Ionic Transport in Passivating Layers on Lithium Electrode  
A.L'VOV, E.NIMON, A.CHURIKOV, A.SENOTOV, A.CHUVASHKIN and I.PRIDATKO
- b4 21-02-01-G Electrochemical Behaviour of Graphite Fluorides in Propylene Carbonate  
D.DEVILLIERS, T.NAKAJIMA, B.TEISSEYRE and M.CHEMLA
- b4 21-02-02-G Discharge Characteristics of the  $\text{Li/LiBF}_4$ -Quinoline/Carbon Systems as a Primary Cell  
M.DOHZONO, T.YAMADA, Y.SHIMIZU and M.EGASHIRA
- b4 21-02-03-K The Use of Lithium Batteries in Biomedical Devices  
B.OWENS
- b4 21-02-04-G Thermodynamic Measurements on the  $\text{Li/SOCl}_2$  Couple, II  
H.BITTNER, B.CARTER and M.QUINZIO

- b4 21-02-05-G Effects of Electrolyte Compositions on the Discharge Characteristics of the Positive Electrode of Li-Al/FeS<sub>2</sub> Thermal Batteries  
H.TSUKAMOTO, M.TERASAKI and S.KASHIHARA
- b4 21-02-06-G Electrochemical Studies of LiAl in 1-Methyl-3-ethylimidazolium Chloride-AlCl<sub>3</sub> Melt  
Y.FUNG and S.CHAU
- b4 21-02-07-K Ambient Temperature Secondary Lithium Batteries for Space Applications  
S.SUBBARAO, D.SHEN, F.DELIGIANNIS, C.HUANG and G.HALPERT
- b4 21-02-08-K Ionically Conductive Plasma Polymer as an Electrolyte for Lithium Batteries  
Z.TAKEHARA, Z.OGUMI and Y.UCHIMOTO
- b4 21-02-09-G Ionic Conductivity of Poly (Ethylene Oxide) (PEO)-Based Solid Electrolytes for Rechargeable Lithium Batteries  
Y.MATSUDA, M.MORITA, M.MOTODA, H.TSUTSUMI, T.TAKAHASHI and H.ASHITAKA
- b4 21-02-10-K Polymer Electrolyte Lithium Batteries  
G.VASSORT and M.GAUTHIER
- b4 21-02-11-G Conductive Thin Films and Membranes: Their Scientific Foundations and Industrial Applications (Part 9)  
S.K.BAHADOR
- b4 21-02-12-G Application of Polypyrrole-Polyazulene Copolymer to Cathode of Rechargeable Lithium Battery  
T.OSAKA, K.NAOI, K.UEYAMA, T.NAKAJIMA and W.SMYRL
- b4 21-02-13-G Electropolymerized Polyaniline as a Positive Electrode in a Lithium Secondary Cell -Morphology Changes and Their Effect in Charge-Discharge Characteristics-  
K.TAKEI, K.ISHIHARA, T.IWAHORI and T.TANAKA
- b4 21-02-14-K Advances in Polymer Electrodes for Rechargeable Lithium Batteries  
B.SCROSATI
- b4 21-02-15-G Charge-Discharge Characteristics of Polyaniline Electrodes in Various Nonaqueous Solutions  
K.NISHIO, M.FUJIMOTO, N.YOSHINAGA, N.FURUKAWA, O.ANDO, H.ONO and T.SUZUKI

## II-5. Chemical Sensors

- b5 19-08-01-K Chemical Sensors with Catalytic Metal Gates  
I.LUNDSTRÖM
- b5 19-08-02-G Trimethylamine Gas-Sensing Characteristics of Semiconductor TiO<sub>2</sub> Sensor Doped with Noble Metal Sensitizers  
Y.TAKAO, Y.IWANAGA, Y.SHIMIZU and M.EGASHIRA
- b5 19-08-03-G Selective CO Sensing with Semiconductive Metal Oxides Supporting Ultrafine Gold Particles  
T.KOBAYASHI, M.HARUTA and H.SANO
- b5 19-08-04-G Hydrocarbon Sensing Characteristics of Tin Dioxide Based Sensors Depending on Sensor Types  
W.CHO and K.YUN
- b5 19-08-05-G Fast NO<sub>2</sub> Detection at Room Temperature with Annealed Phthalocyanine Thin Films  
Y.SADAOKA, T.JONES and W.GÖPEL



- b5 19-08-06-G Prototype Chemical Sensors for the Selective Protection of O<sub>2</sub> and NO<sub>2</sub> in Gases  
W.GÖPEL, K.SCHIERBAUM and H.WIEMHÖFER
- b5 19-08-07-K Electrochemical and Chemical Sensors Fabricated by Microelectronic Techniques  
C.LIU and M.NEUMAN
- b5 19-08-08-G Control of Alcohol Sensing Properties in SnO<sub>2</sub>-based Semiconductor Gas Sensor  
J.TAMAKI, S.MATSUSHIMA, T.MAEKAWA, N.MIURA and N.YAMAZOE
- b5 19-08-09-G Conducting Polymers as the Basis of Chemical Sensors  
G.WALLACE
- b5 19-08-10-G Electrode Reaction of Iodine for Hydrogen Fluoride Gas Sensor  
T.ISHIJI and K.TAKAHASHI
- b5 19-08-11-G Solid Electrolyte Oxygen Sensors with Perovskite-Type Oxide Electrode  
K.EGUCHI, T.INOUE and H.ARAI
- b5 19-08-12-G Dissolved Oxygen Sensing Properties Using Waterproof Type of Zirconia Oxygen Sensor  
T.KASHIMA, A.ASADA, M.NAKAZAWA and H.OSANAI
- b5 19-08-13-G Water Resistive Humidity Sensor Composed of Interpenetrating Polymer Networks  
Y.SAKAI, M.MATSUGUCHI, Y.SADAOKA and I.HIRAMATSU
- b5 19-08-14-G Humidity Sensor Using Microporous Polyethylene Film Grafted with Hydrophilic Polymer  
M.MATSUGUCHI, Y.SAKAI, Y.SADAOKA and M.KAMIGAKI
- b5 19-08-15-G Microhole Array Electrodes for Velocimeter and Flow-Independent Oxygen Sensor  
K.MORITA, M.OHABA, M.YOKOYAMA and K.SUGIYAMA
- b5 21-08-01-K Chemical Sensors Based on Electrodes Modified with Polymer Networks  
W.HEINEMAN, L.COURY Jr., C.GALIATSATOS, E.HUBER and S.SPONAUGLE
- b5 21-08-02-G Development of an Amperometric Glucose Sensor Using a Soluble Mediator  
K.YOKOYAMA, E.TAMIYA and I.KARUBE
- b5 21-08-03-G Dimethylferrocene as Redox Mediator in Amperometric Enzyme Electrodes  
U.LÖFLER, W.SCHUHMANN, H.WIEMHÖER, H.SCHMIDT and W.GÖPEL
- b5 21-08-04-G Anodic Polarization of Micro-Enzyme Electrode for the Improvement of Selectivity  
Y.IKARIYAMA, T.YUKIASHI and S.YAMAUCHI
- b5 21-08-05-G A Novel Immunoassay System Based on a Cascade Amplification Reactions  
A.SEKI, E.TAMIYA and I.KARUBE
- b5 21-08-06-G Enzyme Immunosensors for Human Immunoglobulin G Based on Polytyramine Modified Electrodes  
I.TSUJI and I.TANIGUCHI
- b5 21-08-07-K Clinical Application of Electrochemical Sensors: Problems Awaiting Solutions for Long-Term in Vivo Use of Glucose Sensor  
M.SHICHIRI
- b5 21-08-08-G Simultaneous Determination of Glucose and Sucrose with an Enzyme Electrode System  
F.MIZUTANI and M.ASAI
- b5 21-08-09-G Field Effect Transistors Sensitive to Sodium, Potassium, Calcium and Chloride Ions Based on Urushi Matrix Membrane  
S.WAKIDA, M.YAMANE, K.HIGASHI and K.HIIRO

- b5 21-08-10-G pH Sensitivity of Teflon® Film Prepared by Neutral Atomic Beam Sputtering  
T.ISHIZUKA, Y.KADOI, M.HARA, T.KATSUBE, S.YAMAGUCHI, N.UCHIDA and T.SHIMOMURA
- b5 21-08-11-G Coated Wire Perchlorate Ion Selective Electrode Based on Macrocyclic Schiff Base Complexes and Its Impedance Behaviour  
Y.MASUDA, J.LIU and E.SEKIDO
- b5 21-08-12-G Kinetic Considerations of Ion Selectivities of the Ion-Selective Electrodes Based on Neutral Carriers  
T.OKADA, H.SUGIHARA and K.HIRATANI
- b5 21-08-13-G Selective Coulometric Sensors of Uric Acid and L-Ascorbate Using Porous Carbon Felt  
S.UCHIYAMA and S.SUZUKI
- b5 21-08-14-G Miniature Clark-type Oxygen Electrode and Biosensors for Practical Applications  
H.SUZUKI, N.KOJIMA, A.SUGAMA, F.TAKEI and K.IKEGAMI
- b5 21-08-15-G Development of Ultra-Biosensors Using Carbon Fiber Electrodes  
E.TAMIYA, Y.SUGIURA, A.AKIYAMA and I.KARUBE

## II-6. Electrochemical Methods for Saving Energy and Materials

- b6 18-15-01-K Correlation of Hydrodynamics and Erosion Corrosion in High Velocity Particle Containing Liquids  
E.HEITZ, W.BLATT and T.KOHLEY
- b6 18-15-02-G Electrochemical Corrosion Studies of Aluminum-Copper Coatings  
J.ZAHAVI, M.ROTEL, H.HUANG, P.TOTTA and G.SCHWARTZ
- b6 18-15-03-G Corrosion Behavior of Steels in Various Hydroxylic Acids  
I.SEKINE, M.YUASA and T.HAYAKAWA
- b6 18-15-04-G On the Mechanism of the Dissolution and Passivation of KOVAL (Fe<sub>53.6</sub>Ni<sub>29</sub>Co<sub>17</sub>Mn<sub>0.4</sub>) in Acidic Aqueous and Alcoholic Solution  
F.GOBAL
- b6 18-15-05-G Aspects of Aluminium Corrosion in Acidic Chloride Solution  
C.BRETT
- b6 18-15-06-K Electrochemical Recovery and Recycling of Metals for Saving Materials  
R.KAMMEL
- b6 18-15-07-G Ad- and De-Sorption of Heavy Metals on an Ion Exchange Resin by Using an Electrochemical Device  
M.KATO, J.KUWANO, K.HASHIMOTO and S.TAKAHASHI
- b6 18-15-08-G Hydrogen Monitoring of Pressure Vessel Operated at High Temperature  
K.YAMAKAWA and S.ANDO
- b6 18-15-09-G Hot Corrosion of P/M Ni-base Superalloys  
I.TOMIZUKA, H.NUMATA, Y.KOIZUMI and M.YAMAZAKI
- b6 18-15-10-G In-Situ Technique for Prediction of Steel Failure in Sea Water  
M.ISMAIL and A.AL-ALI
- b6 19-15-01-K The Cathodic Processes Occurring during Localized Corrosion of Stainless Steel in Chlorinated Sea-water Environment  
M.IVES, Y.LU and J.LUO
- b6 19-15-02-G Electrochemical Determination of the Corrosion Rate in Cathodically Protected Systems  
Y.MEAS and J.FUJIOKA
- b6 19-15-03-G Study on Cathodic Reaction of Oxidizing Reagents on Passivated Nickel and Chromium in a Neutral Solution  
M.OKUYAMA and Y.ITOI

- b6 19-15-04-G Stochastic Process of Pit Generation of Al  
T.SHIBATA and M.SUDO
- b6 19-15-05-G Scanning Micro-Electrode Study for the Localized Corrosion  
of a Steel Weldment  
Y.TSURU, K.HOSOKAWA and K.AUST
- b6 19-15-06-G Corrosion Behavior of (Fe Ni)<sub>0.8</sub>B<sub>0.2</sub> Amorphous Alloys  
Partially Crystallized  
A.PIERNA, T.OTERO, J.BLANCO and J.GONZALEZ
- b6 19-15-07-G Inhibitory Effect of 2-Mercapto-ethanol on Corrosion of  
Copper Single Crystals in 0.1M H<sub>2</sub>SO<sub>4</sub>  
L.NANDEESH and B.SHESHADRI
- b6 19-15-08-K The Electrochemistry of Corrosion Inhibition by Organic  
Coatings  
J.SCANTLEBURY
- b6 19-15-09-G The Surface Enhanced Raman Scattering Study of Some Corrosion  
Inhibitors Adsorbed on Iron in an Acid Solution  
K.ARAMAKI, J.UEHARA and H.NISHIHARA
- b6 19-15-10-G Initial Processes of Fluctuations in Electrochemical  
Nucleation  
R.AOGAKI and J.SHINOZUKA
- b6 19-15-11-G Initial Processes of Fluctuations in Pitting Corrosion  
R.AOGAKI and M.KURUSU
- b6 19-15-12-G Effect of Heat Treatment on the Corrosion Behaviour  
of  $\delta$  Alumina Fibre/Al-4% Cu Composite  
W.METWALLY and S.MOUSTAFA
- b6 19-15-13-G Corrosion Behaviour of Some Graphite/Aluminium Alloys  
Composites  
W.METWALLY and S.MOUSTAFA
- b6 19-15-14-G Theoretical Analysis of the Steady-State Properties of Passive  
Films on Metal Surfaces  
D.MACDONALD and M.URQUIDI-MACDONALD
- b6 19-15-15-G Growth of Anodic Films on Ferrous Alloys  
H.BROOKES and F.GRAHAM
- b6 19-15-16-G Pitting Potential and Critical Pitting Temperature.  
Analogies and Particularities  
P.LE GUEVEL, N.JALLERAT K.VU QUANG and J.BAVAY
- b6 19-15-17-G Electrochemical Investigation of the Corrosion Resistance  
of Zn and Zn-Ni Alloy Coatings  
B.AMANI, E.CHASSAING and K.VU QUANG
- b6 19-15-18-G The Effect of Some Substituents in the Molecule of Five-Atomic  
N-Containing Heterocycles on their Inhibitor Activity  
S.RAICHEVA, E.SOKOLOVA and A.POPOVA

# CONTENTS VOL.II

## III FUNDAMENTALS

### III-1. Photoelectrochemistry and Spectroelectrochemistry

- c1 18-07-01-K Improved Concepts for Charge Transfer Processes at Semiconductor Electrodes  
R.MEMMING
- c1 18-07-02-K Quantization and Related Hot Electron Effects in Superlattice and Quantum Well Photoelectrodes and Semiconductor Colloids  
A.NOZIK
- c1 18-07-03-G Photo - and Electro-Chromic Properties of  $\text{MoO}_3$  Thin Films  
A.FUJISHIMA, J.YAO and B.LOO
- c1 18-07-04-P Preparation and Electrode Properties of  $\text{SnO}_2/\text{Sb}$  and  $\text{TiO}_2/\text{Sb}$ -Thin Films for Solar Energy Conversion  
W.BADAWY
- c1 18-07-05-P Electronic State-Densities of Ions in Non-Aqueous Electrolytes Determined by Electrochemical Tunneling Spectroscopy  
H.MORISAKI, A.NISHIKAWA, H.ONO and K.YAZAWA
- c1 18-07-06-P Catalytic Activity of Photoelectrodes: An In-Situ-Determination of the Overvoltage  
H.KUEHNE and J.SCHEFOLD
- c1 18-07-07-P Si Photoelectrochemical Cells in Nonaqueous Solution  
H.KOBAYASHI, N.TAKEDA, A.CHIGAMI and H.TSUBOMURA
- c1 18-07-08-P Photo- and Spectroelectrochemical Studies on Copper Electrodes in Aqueous Electrolytes Containing Inhibitors  
A.ARUCHAMY, A.IBRAHIM, B.LOO and A.FUJISHIMA
- c1 18-07-09-P Comparison of Surface Reactivities of InP and GaAs Compounds in Electrochemical Devices  
A.ETCHEBERRY, J.GAUTRON and J.SCULFORT
- c1 18-07-10-P Electrodeposition of Thin Copper Layer on InP Surfaces  
A.ETCHEBERRY, J.GAUTRON, A.MARBEUF, G.TOURILLON, J.VIGNERON and J.SCULFORT
- c1 18-07-11-P Anodic Dissolution of InP in Presence of Injecting Species  
A.ETCHEBERRY, J.GAUTRON, B.FOTOUHI, S.PELLETIER and J.SCULFORT
- c1 18-07-12-P Photoelectro- and Electrochemical Reduction of Carbon Dioxide  
S.IKEDA, H.NODA, M.MAEDA and K.ITO
- c1 18-07-13-P Photoelectrochemistry and Auger Electron Spectroscopy of  $\text{TiO}_2$  with  $\text{RuO}_2$  Overlayers  
R.ATANASOSKI, L.ATANASOSKA, M.KOZLOWSKI and W.SMYRL
- c1 18-07-14-P Morphology and Photoelectrochemical Properties of Semiconducting Thin Films Prepared from  $\text{TiO}_2$  Particle Precursors  
O.ENE, J.MOSER and M.GRÄTZEL
- c1 18-07-15-P Photocatalysis of Microcrystalline  $\text{TiO}_2$  and  $\text{Fe}_2\text{O}_3$  Incorporated in Clay Interlayers  
H.YONEYAMA, S.NIPPA and H.MIYOSHI
- c1 18-07-16-P Energy Transfer in Polyoxotungstoeuropate Lattice as Molecular Analogue of Metal Oxide Electrode  
T.YAMASE, H.NARUKE and Y.SASAKI
- c1 18-07-17-P Photoluminescence as a Probe of Surface Reactivity of  $\text{TiO}_2$  Catalysts under UV Irradiation  
M.ANPO, M.TOMONARI, P.PICHAT, H.COURBON and J.DISDIER

- c1 18-07-18-P Picosecond Dynamics of Photocatalytic Reactions with Powdered Semiconductors Studied by Transient Absorption  
K.HASHIMOTO and T.SAKATA
- c1 18-07-19-P Estimation of Photocatalytic Activity of Semiconductor Powders Based on 'Photo-Sinking Phenomenon'  
K.PATEL, S.YAMAGATA, B.LOO and A.FUJISHIMA
- c1 18-07-20-P Improved Efficiency of Photocatalytic Degradation of Organic Compound in Semiconductor Suspension  
K.TANAKA, K.HARADA and T.HISANAGA
- c1 18-07-21-P Basic Characteristics of Optical Waveguide Systems for Monitoring Surface Chemistry  
K.ITOH and A.FUJISHIMA
- c1 18-07-22-P Anodic Oxide Films on Niobium. A Spectroelectrochemical Study of the Initial Stages of Film Formation  
F.Di QUARTO, S.PIAZZA and C.SUNSERI
- c1 18-07-23-P Electrochemical and Spectroscopic Study on the Valence Electronic Structure of Metal Complexes  
T.MATSUMURA-INOUE, M.HAGA and K.KURODA
- c1 18-07-24-P Surface Enhanced Raman Scattering Study of Flavin Adenine Dinucleotide and Flavoproteins  
I.TANIGUCHI
- c1 18-07-25-P Evaluation of Adsorption Parameters of Organic Compounds by Use of Spectroellipsometric Method on Electrodes  
U.PALM, T.SILK and T.RAUD
- c1 18-07-26-P In-Situ Infrared Spectroscopy as Applied to the Study of Molecules Irreversibly Adsorbed on Electrode Surfaces  
T.SASAKI, I.BAE and D.SCHERSON
- c1 18-07-27-P The Hysteresis between the Electrochemical Doping and Undoping of Poly (3-Methyl-thiophene) Studied by Ellipsometry  
F.CHAO, M.COSTA, P.LANG and J.BAUDOIN
- c1 19-07-02-K A Novel Approach to High-Efficiency and Low-Cost Solar Cells by Use of Semiconductors Coated with Ultrafine Metal Islands  
Y.NAKATO, H.USHIKA, K.KAI and H.TSUBOMURA
- c1 19-07-03-K Passivation of Recombination Centers on Isotropic and Anisotropic Materials through (Photo)Electrochemical Etching  
R.TENNE
- c1 19-07-04-G New Mechanism of Photoinduced Electron Transfer on Semiconductor Surfaces  
T.SAKATA and K.HASHIMOTO
- c1 19-07-05-G (Photo-)Electrochemical Investigation on the Mechanisms of Etching and Photoetching Reactions at Gallium Phosphide Single Crystals  
H.GOOSSENS, F.VANDEN KERCHOVE and W.GOMES
- c1 19-07-06-G Photoelectrochemical Processes at the Silicon/Aqueous Electrolyte Interface  
H.LEWERENZ
- c1 19-07-07-K Solid-State Electrochromic Devices  
B.SCROSATI
- c1 19-07-08-K Preparation of  $Pb_3O_4$  by Anodic Oxidation of Lead and a Study of Its Photoelectrochemical Properties and Its Use in Solar Chargeable Battery  
M.SHARON, P.VELUCHAMY, C.NATARAJAN and D.KUMAR
- c1 19-07-09-G Photoelectrochemical and Electrochemical Properties of Copper Oxide Layers  
U.COLLISI and H.STREHLOW

- c1 19-07-10-P In-Situ Photoluminescence Studies of the Mechanism of the Photooxidation Reaction of Water at an n-TiO<sub>2</sub> Electrode  
Y.NAKATO, H.AKANUMA and H.TSUBOMURA
- c1 19-07-11-P Photoelectrochemical Characterization of Compound Semiconductors by Fiber Optical Laser Spot Microscopy  
P.CARLSSON, B.HOLMSTRÖM, K.UOSAKI and H.KITA
- c1 19-07-12-P Electrode Kinetics in Semiconductor Electrodes  
G.NOGAMI
- c1 19-07-13-P Mechanism of EL at Semiconductors such as SiC: Observation of Fast EL Rise Time Transients by Hole Injection During Persulfate Reduction  
A.MANIVANNAN, K.HASHIMOTO, T.SAKATA and A.FUJISHIMA
- c1 19-07-14-P Photoelectrochemical Oxidation of Alcohols on Semiconductors  
T.KATO, M.YOKOMAKU, Y.BUTSUGAN and A.FUJISHIMA
- c1 19-07-15-P Anodic Oxidation of Silicon in H<sub>3</sub>PO<sub>4</sub> and H<sub>3</sub>BO<sub>3</sub> Containing Solutions  
L.MILESHKO, I.SOROKIN, V.BONDARENKO
- c1 19-07-17-P Photocatalytic Synthesis of Cyclic Imino Acids  
B.OHTANI, S.TSURU, K.IZAWA, S.NISHIMOTO and T.KAGIYA
- c1 19-07-18-P On Electroluminescence Accompanied with Anodic Salt Film Formation on Hg in Organic and Inorganic Aqueous Solutions  
K.TACHIBANA, E.SHIMADA and O.NOMURA
- c1 19-07-19-P n-CuIn<sub>11</sub>S<sub>17</sub> : A New and Novel Semiconductor for Photoelectrochemical Cells  
K.BASAVASWARAN, Y.UENO, T.SUGIURA and H.MINOURA
- c1 19-07-20-P Phenomena of Weak Electroluminescence of Iron and Other Metal Electrodes and its Application Potentiality in Electrochemistry Research  
S.CAI, L.GAO, L.SU, L.CHEN and A.FUJISHIMA
- c1 19-07-21-P Photovoltaic Properties of Electrochemically-Doped Polymer and Polymer/Dye Systems  
Y.SHIROTA, N.NOMA and H.YASUI
- c1 19-07-22-P Spectroelectrochemical Measurements of Ion Transport at Polymer/Electrolyte Solution Interfaces  
K.SHIMAZU, K.MURAKOSHI and H.KITA
- c1 19-07-23-P Oxidative and Reductive Quenching of the Photo-Excited Tris(2,2'-Bipyrazine) Ruthenium(II) in the Photoelectrochemical System  
S.NISHIDA, Y.HARIMA and K.YAMASHITA
- c1 19-07-24-P Oxidation and Reduction Potentials and Electron Transfer Interactions in Photoexcited States  
T.KUBOTA, B.UNO, K.KANO and T.KAWAKITA
- c1 19-07-25-P Development of Optically Transparent Reticulated Vitreous Carbon Electrode  
Z.ZENG, Y.HU and L.WANG
- c1 19-07-26-P Spectroelectrochemical Studies on the Production of the Ascorbic Acid Radical  
H.KOBAYASHI, H.AKAMINE, T.OHNO and S.MIZUSAWA
- c1 19-07-27-P Simulation of the CV and Probe Beam Deflection Signal of a Redox Polymer Coated Electrodes  
O.HAAS, E.DEISS and C.DAUL
- c1 19-07-28-P Reduction of Methylviologen at a Gold Electrode with and without Sodium Dodecyl Sulfate -In situ Study by Uv-Visible Absorption and Raman Scattering Spectroscopy-  
C.NISHIHARA

- c1 19-07-29-P Study of Al Anodic Film by Positron Annihilation Lifetime Spectroscopy  
S.ZHOU, H.WU, S.YAO and Y.ZHANG
- c1 19-07-30-P Kinetic Studies of Cis-Trans Isomerization of Stilbene Anion Radicals with a Quantitative-Electrolysis ESR Method  
A.NAITO, K.NOZAKI, T.HO, H.HATANO and S.OKAZAKI
- c1 21-07-01-K Electron Transfer Reactions on Semiconducting Colloids and Membranes  
M.GRÄTZEL
- c1 21-07-02-G Electron Transfer at Ultrafine Semiconductor Particles in Solution and Its Size Effect  
Y.NOSAKA, N.OHTA and H.MIYAMA
- c1 21-07-03-G Novel Series of Photocatalysts with Layered Structure of Niobate  
K.DOMEN, J.YOSHIMURA, A.TANAKA and T.ONISHI
- c1 21-07-04-K Photoelectrochemical and Surface Chemical Processes at Thin Film Molecular Semiconductor Materials: From Abrupt Heterojunctions to Chemical Sensors  
N.ARMSTRONG
- c1 21-07-05-G Energy Transfer and Electron Transfer in Langmuir-Blodgett Films  
Y.NISHIYAMA, K.KASATANI, H.SHINOHARA and H.SATO
- c1 21-07-06-G Photocatalytical Properties of Water Soluble Metallo (Ru-II, Sn-IV, Mg-II) meso-Tetraanilinoporphyrin  
W.SZULBINSKI and J.STROJEK
- c1 21-07-07-K Spectroelectrochemistry: Designs, Properties and Applications of the Long Optical Pathlength Thin-Layer Cell  
Y.GUI, G.HANCE and T.KUWANA
- c1 21-07-08-K In-Situ Spectroelectrochemical Studies on Chemically Modified Electrodes  
Z.TIAN, C.ZHONG and Z.TIAN
- c1 21-07-09-P Analysis of the Early Stage of Transient Photovoltages at Semiconductor-Electrolyte Interface  
H.KIM, T.SAKATA and K.HASHIMOTO
- c1 21-07-10-P Study of the Grain Structure of Polycrystalline CdSe by Photoelectrochemical Etching Technique  
T.SUGIURA, M.HIDA, H.MINOURA and Y.UENO
- c1 21-07-11-P The Surface Density of a TiO<sub>2</sub> Single Crystal and Observation of Adsorbed Molecule by Scanning Tunneling Microscopy and Tunneling Spectroscopy  
K.SAKAMAKI, K.ITOH and A.FUJISHIMA
- c1 21-07-12-P Structure of the Interface and Photoelectrochemical Properties of an Si Electrode in the Case of Charge Carrier Degeneration Near the Surface  
A.GORODYSKII, G.KOLBASOV, N.TARANENKO and L.KAZAROVA
- c1 21-07-13-P Time Resolved EER Spectroscopy by Nano Second-Pulse Laser Excitation  
S.NAKABAYASHI and A.KIRA
- c1 21-07-14-P Semiconducting Metal Oxide Photoanodes : Their Probed Characteristics and Implications (Pt.30)  
S.K.BAHADOR
- c1 21-07-15-P The Photoelectrochemical Reduction of Carbon Dioxide on Heterojunction Photoelectrode  
B.CHUN YU, P.WEI, J.LIU and S.ZHAO
- c1 21-07-16-P Photoelectrocatalytic Synthesis of Organic Compounds on n-Silicon Oxide-Film-Coated Photoanodes  
A.KULAK, S.POZNYAK, I.MAKUTA and D.SVIRIDOV

- c1 21-07-17-P Photoelectrochemical Processes on the Semiconductor/Solid Electrolyte Interface  
E.NIMON, A.L'VOV, A.ROKAKH and L.MATASOVA
- c1 21-07-18-P Photodegradation of Surfactants by Semiconductor in the Protection of the Environment  
H.HIDAKA and S.SUENAGA, E.PELIZZETTI, N.SERPONE and M.GRÄTZEL
- c1 21-07-19-P Transient Technique for Evaluation of Photovoltaic and Solar Materials: Response to Heat and DC Pulse  
M.ISMAIL, W.BLOSS, G.BAUER and N.SCHOCK
- c1 21-07-20-P Photodeposition of Prussian Blue on  $\text{TiO}_2$  Particles  
H.TADA, Y.SAITO and H.KAWAHARA
- c1 21-07-21-P Influence of Hydroxyl Group of  $\text{TiO}_2$  Surface on Photocatalytic Reactions  
K.KOBAYAKAWA, M.IKEDA, Y.SATO and A.FUJISHIMA
- c1 21-07-22-P Study of Photo-Assisted Fuel Cell Using Powdered Photocatalysts  
H.HARADA
- c1 21-07-23-P Photoelectrochemical Behavior of Copper-Phthalocyanine Thin Films in Liquid Electrolytes  
M.TAKEUCHI, T.SHINOHARA, F.KANEKO and M.MASUI
- c1 21-07-24-P Study on the Interaction of  $\text{O}_2$  and Metal Tetraphenylporphyrins in DMSO Solution by Thin-Layer Spectroelectrochemical Method  
C.HUANG, F.GUO, Q.WANG and X.CAO
- c1 21-07-25-P Correlation Photoacoustics Study on Corrosion of Film Coated Metal  
R.TAKAUE, M.MATSUNAGA, K.KANTOU and K.HOSOKAWA
- c1 21-07-26-P Studies with a Thin Layer Spectroelectrochemical Cell  
A.OLIVEIRA BRETT
- c1 21-07-27-P Modulated UV-V Reflectance Spectroscopy of the Adsorption of Phenol on Gold  
R.LEZNA, N.De TACCONI, S.CENTENO and A.ARVIA
- c1 21-07-28-P Electrochemical and Spectroelectrochemical Studies of Metal Cyano Complexes  
I.TANIGUCHI, K.YAGI, M.OKAMOTO and K.YASUKOUCHI
- c1 21-07-29-P Factor Analysis of Spectroelectrochemical Data of Conducting Polymers  
J.KANKARE, J.LUKKARI, T.PAJUNEN and C.VISY
- c1 21-07-30-P Adsorption of Acrylonitrile on Ag Studied by SERS  
H.SHINDO and H.NOZOYE
- c1 21-07-31-P Resonance Raman Spectroscopic Studies of Electrogenenerated Species in Solution  
M.OYAMA, K.NOZAKI and S.OKAZAKI
- c1 21-07-32-P In Situ X-Ray Diffraction Electrochemical Studies  
C.CHEN and Z.HUANG
- c1 22-07-01-K The Influence of Surface Structure and Interfacial Potential on the Orientation and Extent of Adsorption of  $\text{HSO}_4^-$  and  $\text{SO}_4^{2-}$  on Pt and Au Single Crystal Electrodes  
N.ANASTASIJEVIC, A.BEWICK and R.NICHOLS
- c1 22-07-02-G Electrochemically Modulated Infrared Spectroscopy of  $\text{Fe}(\text{CN})_6^{3-/4-}$  Redox Couple  
K.KUNIMATSU, Y.SHIGEMATSU, K.UOSAKI and H.KITA
- c1 22-07-03-G Potential Dependent In-Situ Raman Spectroscopy of Ions at the Pt-Electrolyte Interface  
B.PETTINGER and A.FRIEDRICH
- c1 22-07-04-G STM and IR Investigation of Semiconductor/Electrolyte Interfaces  
K.UOSAKI, Y.SHIGEMATSU and H.KITA



- c1 22-07-05-G Photoelectrochemical Investigations of Metal-Solution Interface under Electropolishing  
A.SZÜCS, Z.GERTNER and M.NOVAK
- c1 22-07-06-G Application of Electromodulated Infrared Reflectance Spectroscopy to Electrocatalysis : A Detailed Study of the Reaction Mechanisms of Formic Acid Oxidation at Rhodium Electrodes  
C.LAMY, B.BEDEN, F.HAHN and M.CHOY de MARTINEZ
- c1 22-07-07-G Scanning Tunneling Microscopy at Potential Controlled Electrodes  
H.SIEGENTHALER and R.CHRISTOPH

### III-2. Electroorganic Chemistry

- c2 18-04-01-K CC-Bond Formation and Functionalization at the Electrode - Recent Results on the Use of the Kolbe-Electrolysis and the Nickel Hydroxide Electrode  
H.SCHÄFER, A.WEIPER, L.FELDHUES, G.DRALLE and R.SCHNEIDER
- c2 18-04-02-G Reactions of Highly-Reactive Electrogenenerated Anionic Species with Onium Counterions in Anhydrous Media  
T.NONAKA, M.BAIZER and T.FUCHIGAMI
- c2 18-04-03-G Structure and Product-Selectivity in Electrochemical Trifluoromethylation of Olefins  
K.UNEYAMA, H.NANBU, S.WATANABE and K.KITAGAWA
- c2 18-04-04-G Contributions to the Electrochemistry of Aromatic Nitrocompounds  
P.ZUMAN, Z.FIJALEK, D.DUMANOVIC, D.SUZNJEVIC and M.PUGIA
- c2 18-04-05-G Electrocatalytic Oxidation of Alcohols on TEMPO Modified Carbon Felt Electrode  
T.OSA, Y.KASHIWAGI and J.BOBBITT
- c2 18-04-06-K Aspects of Synthetic Organic Electrochemistry  
R.LITTLE, C.SOWELL, H.BODE and R.WOLIN
- c2 19-04-01-G Electrochemistry of Nitroazoles  
D.DUMANOVIC, D.SUZNJEVIC and P.ZUMAN
- c2 19-04-02-G Investigations on the Construction of Modified Electrodes for Preparative Electrolyses  
H.SCHÄFER and H.RIERING
- c2 19-04-03-G Improvement of the Dehalogenation of Dichloroacetic Acid by Electrocatalysis  
S.DAPPERHELD
- c2 19-04-04-G Electroreductive Intramolecular Cyclization of Carbonyl Compounds  
T.SHONO, N.KISE, N.UEMATSU and S.MORIMOTO
- c2 19-04-05-G Reduction and Oxidation Potentials of ( $\eta$ -Cyclopentadienyl) (Substituted 1,2-Dichalcogenato) Metal Complexes - Effects of the Dichalcogenate and Metal  
M.KAJITANI, K.SHIMIZU, K.HIRAKATA, H.USHIJIMA, T.AKIYAMA, G.SATÔ and A.SUGIMORI
- c2 19-04-06-G Electrooxidation of (Cyclo)-Aliphatic Ethers and Ketones in Aqueous Electrolytes  
F.BECK, B.WERMECKES and S.YE
- c2 19-04-07-K Use of Sacrificial Anodes in Electroreductive Organic Synthesis  
J.NEDELEC and J.PERICHON
- c2 19-04-08-G Electroreductive Polymerization of Dichlorosilanes  
M.UMEZAWA, M.TAKEDA, H.ICHIKAWA, T.ISHIKAWA and T.NONAKA

- c2 19-04-09-G Electrochemical Reduction of 1,1,2-Trichlorotrifluoroethane:  
Mediating Effect of the Ammonium Cation  
A.SAVALL, R.ABDELHEDI, S.DALBÉRA and M.BOUQUERRA
- c2 19-04-10-G Electrochemical Carboxylation of Some Sulfur-Containing  
Olefines  
M.YASUZAWA and A.KUNUGI
- c2 19-04-11-G Electroreductive Coupling of Activated Halides with Acid  
Anhydrides  
I.NISHIGUCHI, T.OKI, T.HIRASHIMA and J.SHIOKAWA
- c2 19-04-12-G Electrochemical Bioreactor Based on Regeneration of  $\text{NAD}^+/\text{NADH}$   
T.MATSUE, H.CHANG, H.YAMADA and I.UCHIDA
- c2 19-04-13-G Electrochemical Reduction of  $\alpha$ -Substituted Cyclic Amine  
Derivatives  
T.SHONO, J.TERAUCHI, K.KITAYAMA and Y.MATSUMURA
- c2 19-04-14-G Electroreduction of Aromatic Nitrosulphadienes for Prediction  
of their Reactivity in Nucleophilic Reactions  
V.BERESTOVITSKAIA, O.YAKOVLEVA and V.LATYPOVA
- c2 19-04-15-G Co(I)-Mediated Electroreduction of Halo-Carbonyl Compounds  
T.INOKUCHI, M.TSUJI and S.TORII
- c2 19-04-16-G An Electrochemical Carbon-Carbon Bond Formation between  
Carbonyl Compounds and Allylic Halides-The Use  
of a Reactive-Metal Electrode  
M.TOKUDA, K.ENDATE, M.UCHIDA and H.SUGINOME
- c2 19-04-17-G Cathodic Carbonylation of Alkyl Halides  
K.YOSHIDA, M.KOBAYASHI and S.AMANO
- c2 19-04-18-K The Polarographic Reductions of 4-Formyl-, 4-Acetyl- and  
4-Cyano-3-Substitutedsydnones  
H.TIEN and L.WANG
- c2 21-04-01-G Design of the Metal Redox Systems for Reductive Carbon-  
Carbon Bond Making in a One-Compartment Cell  
H.TANAKA, T.NAKAHARA and S.TORII
- c2 21-04-02-G Electrolytic Reactions of Fluoro Organic Compounds  
T.FUCHIGAMI, S.ICHIKAWA, A.KONNO and T.NONAKA
- c2 21-04-03-G Inorganic Mediators in the Non-Dimerizant Electroreduction  
of Acrylonitrile  
L.ONICIU, D.LÖWY, M.JITARU and B.TOMA
- c2 21-04-04-G Mechanistic Analysis of Organic Electrode Reactions  
by Impedance Voltammetry  
M.SLUYTERS-REHBACH, M.RUEDA and J.SLUYTERS
- c2 21-04-05-G Selective Oxidation of Allyl Alcohol to Aldehyde on an  
SPE-MnO<sub>2</sub> Composite Electrode  
Z.OGUMI, C.ZHEN and Z.TAKEHARA
- c2 21-04-06-G  $\text{Mn}^{+3}$ -Mediated Carbon-Carbon Bond Formation between Dienes  
and Active Methylene Compounds by Electrooxidation  
R.SHUNDO, Y.MATSUBARA, I.NISHIGUCHI and T.HIRASHIMA
- c2 21-04-07-G Synthesis of Nucleoside Skeletons by Electrooxidation  
as a Key Reaction  
S.TORII, H.OKUMOTO and S.HIKASA
- c2 21-04-08-G Preparation of Perfluoroalkanedisulfonic Acids by  
Electrochemical Perfluorination  
P.SARTORI and R.HERKELMANN
- c2 21-04-09-G Electroreductive and Electrooxidative Dissociation of Adducts  
between ( $\eta$ -Cyclopentadienyl)(Substituted 1,2-  
Ethylenedithiolato) Cobalt(III) and Phosphines and Phosphites  
K.SHIMIZU, M.KAJITANI, Y.HOSHINO, T.AKIYAMA, G.SATO and  
A.SUGIMORI

- c2 21-04-10-G Electrocatalytic Oxidation of Methanol Using Nickel Cyclam Modified Electrodes  
I.TANIGUCHI, H.YAMAGUCHI and K.YASUKOUCHI
- c2 21-04-11-G Duet Electrosynthesis of p-Benzoquinone from Benzene  
S.ITO, A.KUNAI and K.SASAKI
- c2 21-04-12-G A Study of Electrochemical Kinetics of Lead-Lead Methylsulfonate System  
W.HSUEH and C.WAN
- c2 21-04-13-G Electro-Initiated Oxygenation  
J.YOSHIDA, S.NAKATANI and S.ISOE
- c2 21-04-14-G Electrochemical Synthesis of Iron Subgroup Metallocenic Compounds  
V.SHIROKII, T.KONOVALOVA, A.SUTORMIN, A.MOSIN, A.RYABTSEV, N.MAIER and Y.OL'DEKOP
- c2 21-04-15-G Electrooxidative Methoxylation of Benzyl Sulfides  
M.KIMURA, Y.YAMAMOTO and Y.SAWAKI
- c2 21-04-16-G The Oxidation Mechanism of Organic Compounds at Platinum Electrodes  
G.NOGAMI and J.KENNEDY
- c2 21-04-17-G Electrochemical Characteristic of Metallo-Tetraphenyl-Porphyrin Silane Films  
X.WEN and B.CHUN YU
- c2 21-04-18-G Oxidation of Formic Acid on Platinum Single Crystal Electrodes and the Effects of Anion Adsorption  
A.TRIPKOVIC and R.ADZIC
- c2 21-04-19-K Natural Products Syntheses by Means of Electrochemical Method  
S.YAMAMURA, Y.SHIZURI, S.SHIGEMORI, M.OHKUBO, S.MAKI and Y.OKUNO
- c2 22-04-01-G Electrochemical Functionalization of Organic Substrates by Small Molecules ( $\text{CO}_2$ ,  $\text{SO}_2$ ,  $\text{NO}$ )  
V.POKHODENKO, V.KOSHECHKO, V.TITOV, D.SEDNEV and S.SHPILNY
- c2 22-04-02-G New Electron Transfer Mediators in Electrocatalytic Reduction of  $\text{CO}$ ,  $\text{CO}_2$  and  $\text{CS}_2$   
V.POKHODENKO, V.KOSHECHKO, V.ATAMANYUK, V.TITOV, M.MININA, O.LAZURSKY and D.SEDNEV
- c2 22-04-03-G New Heteroaromatic Polymer Films Prepared by Electropolymerization of Fused Pyrroles  
T.OHSAKA, H.MIYAMOTO, N.OYAMA, S.TANAKA, A.KIYOMINE, T.KUMAGAI and T.MIYASHI
- c2 22-04-04-G Photo-Electroorganic Chemistry in Particulate Systems  
S.YANAGIDA, T.SHIRAGAMI, H.KIZUMOTO, H.KAWAKAMI and C.PAC
- c2 22-04-05-G Oxidation of Formaldehyde and Glycerol on Rotating Disc Gold Single Crystal Electrodes in Alkaline Solutions  
M.AVRAMOV-IVIC and R.ADZIC
- c2 22-04-06-G Electrooxidation of Alcohols by a Double Mediatory System of N-Oxyl/Halogen Redoxes  
T.INOKUCHI, S.MATSUMOTO, T.NISHIYAMA and S.TORII
- c2 22-04-07-G Electrochemical Behaviour of 6, 6'-Disubstituted Fulvenes in Nonaqueous Solvents  
M.YAROSH, T.KONOVALOVA, V.SHIROKII, A.RYABTSEV, N.MAIER and Y.OL'DEKOP
- c2 22-04-08-G Electrochemical Perfluoroalkylation of Organic Compounds  
V.KOSHECHKO, L.KIPRIANOVA and L.FILELEEEVA
- c2 22-04-09-G Electrochemical Oxidation of Aromatic Selenium Ethers  
V.ZHOUIKOV, V.LATYPOVA and D.FATTAHOVA

### III-3. Bioelectrochemistry

- c3 18-12-01-K Electrochemical Analysis of Platinum-DNA Interactions:  
Relations to Anti-Cancer Activity of Platinum Complexes  
V.BRABEC
- c3 18-12-02-G Electrochemical Behavior of Blue Copper Proteins  
from *Alcaligenes Faecalis* S-6  
Y.IWASAKI, E.TAMIYA, T.BEPPU and I.KARUBE
- c3 18-12-03-G Voltammetric Responses of Cytochromes  $c_3$  from Various Sulfate  
Reducing Bacteria  
Y.SHIGEMATSU, T.SAGARA, H.AKUTSU and K.NIKI
- c3 18-12-04-G Determination of Biological Species by Microelectrode Arrays  
T.MATSUE, A.AOKI, E.ANDO, M.NARUMI and I.UCHIDA
- c3 18-12-05-K SERS of Biological Molecules  
E.KOGLIN
- c3 18-12-06-G Electrochemistry of Modified Cytochrome  $c$   
I.TANIGUCHI, M.TOMINAGA, K.YOSHIDA and K.YASUKOUCHI
- c3 18-12-07-G Electrochemistry and Spectroelectrochemistry of (TPP)Co(Et)  
and [(N-EtTPP)Co]<sup>+</sup> in Nonaqueous Media  
A.ENDO, B.HAN and K.KADISH
- c3 18-12-08-G Phthalocyanines in Molecular Electronic Devices  
B.SIMIC-GLAVASKI
- c3 18-12-09-G Spectroelectrochemical Study on Adsorption of AMP at a Gold  
Electrode -Uses of Specular Reflection, LOPTLC, and Magnetic  
Optical Rotation Methods-  
F.KUSU, K.YUASA, T.MISHIMA, H.TAKAYAMA and K.TAKAMURA
- c3 19-12-01-K From in Vitro to in Vivo Sensors : Application to Subcutaneous  
Glucose Sensors  
R.STERNBERG, J.PAUGAM, G.VELHO, G.REACH, D.BINDRA, M.BARRAU,  
G.WILSON and D.THEVENOT
- c3 19-12-02-G Electrochemical Biosensing of Cu(II) and Zn(II) Ions  
Using the Immobilized Apoenzymes in the FIA System  
I.SATO
- c3 19-12-03-G High Sensitive Immuno-Sensor with a Semi-Solid Electrolyte  
H.UCHIDA, M.HARA and T.KATSUBE
- c3 19-12-04-K Mechanistic Studies of the TTF-TCNQ Enzyme Electrode  
B.HILL C.SCOLARI and G.WILSON
- c3 19-12-05-G The Electrodeposition of Film of H. Halobium purple  
Membrane (PM) onto Poly(Vinyl Alcohol) (PVA).  
Fabrication of an Optically Transparent  
Gold(Au)/PVA/PM/PVA/Au Multi-Layer Sandwich Cell and  
Its Photoelectric Response  
K.UEHARA, K.KAWAI, T.KOUYAMA and M.TANAKA
- c3 19-12-06-G Amperometric Biosensors: Recent Advances  
H.BENNETTO, G.DELANEY, S.FORD, A.KOSHY, J.MASON, J.STIRLING,  
R.SUTTON and C.THURSTON
- c3 19-12-07-K Multi-Gate and Multi-Enzyme Sensors  
F.SCHELLER, R.HINTSCHE, I.DRANSFELD, W.MORITZ and M.PHAM
- c3 19-12-08-G Electrochemical Immobilization of Enzymes and Current Response  
of GOD Electrodes  
H.WU and Z.ZHENG
- c3 19-12-10-G Photochemical Control of Electrical Oscillations in Lipid  
Membranes  
H.NAKANISHI, K.SEKI and Y.MORI

- c3 19-12-11-G Bioelectrochemical Immunoassay for Human Chorionic Gonadotrophin  
M.LU and K.CHEN
- c3 19-12-12-K Electrochemical Preparation of Ultra-Thin Conductive Enzyme Membrane and Its Potential-Dependent Activity Control  
M.AIZAWA, Y.IKARIYAMA, S.YABUKI and H.SHINOHARA
- c3 19-12-13-G Electrochemical Immobilization and Characterization of Enzyme GOD  
H.WU, Z.ZHEN and S.ZHOU
- c3 19-12-14-G Rectifying Function of Porphyrin-Flavin LB Monolayer-Junction on Gold Electrodes Derived from the Redox Properties of Proteins  
S.UHEYAMA, S.ISODA and M.MAEDA
- c3 19-12-15-G Electrocatalytic Photolysis of Water at Photosystem II-Modified Carbon Paste Electrodes in the Presence of Electron Transfer Mediators  
T.IKEDA, K.AMAKO, M.SENDA, T.SHIRAIISHI and K.ASADA
- c3 19-12-16-G Platinum Electrode Potential in Wastewater Treatment  
A.HÉDUIT and D.THÉVENOT

#### III-4. New Trends in Electrode Kinetics

- c4 22-08-01-K Modern Aspects of Solvent Reorganization in Charge Transfer Processes  
L.KRISHTALIK
- c4 22-08-02-K Study of Electrode Processes and Investigation of Adsorbates by on line Mass Spectrometry  
N.ANASTASIJEVIC, H.BALTRUSCHAT, G.HAMBITZER, T.HARTUNG and J.HEITBAUM
- c4 22-08-03-K Single Crystal Surfaces and Anisotropic Effect in Electrocatalytic Reactions  
J.CLAVILIER
- c4 22-08-04-K Detection of Radicals in Electrode Processes  
J.BOCKRIS, K.CHANDRASEKARAN and J.WASS

#### III-5. Ions in Solution

- c5 18-08-01-K Structure of Nonaqueous Solvents and Solvated Ions  
H.OHTAKI
- c5 18-08-02-K Ionic Solvation in Water-Methanol Mixtures  
Y.TAMURA, G.PALINKAS and K.HEINZINGER
- c5 18-08-03-K Application of the Quasi-Lattice Quasi-Chemical and the Kirkwood-Buff Theories to the Selective Solvation of Ions in Mixed Solvents  
Y.MARCUS
- c5 18-08-04-K Dynamic Aspect of Reactions Involving Metal Ions in Solution  
M.TANAKA
- c5 18-08-05-G Preferential Solvation of Ions in Mixed Solvent Systems  
H.NOMURA, F.KAWAIZUMI and H.HIRAKAWA
- c5 18-08-06-G The Effects of Solute-Solvent Interaction on Intramolecular Structure of a Water Molecule in Hydrated and Incompletely Hydrated LiCl Solutions  
K.ICHIKAWA and Y.KAMEDA

## **IV FUNDAMENTAL AND APPLIED ELECTRO- CHEMISTRY IN RELATION TO "SCIENTIFIC DIVISIONS OF ISE"**

### **IV-1,3,4. Fundamental Interfacial Electrochemistry Analytical Electrochemistry Molecular Electrochemistry**

#### **Voltammetry of Organic Compounds**

- d1 18-16-01-G Phase-Selective Second Harmonic Voltammetry and Ultraviolet Photoelectron Spectroscopy for Evaluation of Electronic Structures of Cyanine and Merocyanine Dyes  
T.TANI, K.OHZEKI, S.OHTA, K.SEKI, T.TANG, H.YAMAMOTO and H.INOKUCHI
- d1 18-16-02-G Some Aspects of Carbenes Electrogenation  
V.PETROSYAN
- d1 18-16-03-P Stabilization of Electrogenated Anion Radical Intermediates by Inclusion Complex Formation with Cyclodextrins in Aqueous Solution  
K.KANO, K.MORI, B.UNO and T.KUBOTA
- d1 18-16-04-P Origin of the Retardation of the Electrochemical Reduction of Viologens Captured by Sodium Dodecyl Sulfate Micelles  
K.SUGA and M.FUJIHIRA
- d1 18-16-05-P Electrocatalytic Oxidation of Ethylene-Glycol in Alkaline Medium on Platinum-Palladium Alloy Electrodes  
F.KADIRGAN, I.DUMAN and N.DALBAY
- d1 18-16-06-P Voltammetry of the Five-Member Polyheteroatomic Cations  
V.TSVENIASHVILI, R.CHARASHVILI and N.CHAVTASI
- d1 18-16-07-P New Method of Investigation of Adsorption of Organic Substances at Metal/Solution Interface  
J.JAPARIDZE and M.KHOKHASHVILI
- d1 18-16-08-P Adsorption Kinetics of Organic Compounds at a Hanging Mercury Drop Electrode  
H.SAWAMOTO and K.GAMOH
- d1 18-16-09-P Oxidation of Glucose on Single Crystal Pt-Electrodes  
K.POPOVIC, A.TRIPKOVIC, N.MARKOVIC and R.ADZIC
- d1 18-16-10-P Electrochemistry of Nitroazoles. Polarography in the Synthesis of Nitroimidazoles and Nitropyrzoles  
D.DUMANOVIC, D.SUZNJEVIC, M.ERCEG, D.KOSANOVIC and J.JOVANOVIC

#### **Electrochemical Analysis**

- d1 19-13-01-K Some New Aspects of Electrochemistry at the Liquid-Liquid Interface  
E.WANG

- d1 19-13-02-G Electrochemical Detectors Using Micro Working Electrode  
for Micro HPLC and FIA  
M.GOTO, H.MIYAHARA, H.MORI and D.ISHII
- d1 19-13-03-P Development and Application of the Polymer Based Ion-Selective  
Electrodes for Use in Nonaqueous Solutions  
T.NAKAMURA and K.IZUTSU
- d1 19-13-04-P Some New Aspects of Liquid Chromatography/Electrochemistry  
E.WANG, H.JI and W.HOU
- d1 19-13-05-P Ion-Selective Electrode(ISE) Based on Polarizable Oil/Water  
Interface. Potentiometric ISE and Amperometric ISE  
M.SENDA, T.OSAKAI, Y.YAMAMOTO and T.NUNO
- d1 19-13-06-P The Application of Square Wave Voltammetry for Electrochemical  
Detection of Ascorbic Acid in Flow Injection Analysis  
Y.FUNG and S.MO
- d1 19-13-07-P A New Approach to Coulometric Technique for Flow-System  
Z.TIAN and L.BAO
- d1 19-13-08-P Determination of Sub-nmol Hydrogen Peroxide and Lipid  
Hydroperoxide by Electrochemiluminescence of Luminol in  
Aqueous Solution  
S.CHAPMAN
- d1 19-13-09-P Environmental Pollution Monitoring by Transient In-Situ  
Technique  
M.ISMAIL and K.KIRCHNER
- d1 19-13-10-P Novel Techniques for Monitoring Water Quality  
U.DAWOUD and M.ISMAIL
- d1 19-13-11-P New Device for Analysis and Quality Monitoring  
M.ISMAIL
- d1 19-13-12-P Quality Control and Monitoring of Food Products: Honey  
M.ISMAIL, M.GASHGARI and I.ABDUL-RAHMAN
- d1 19-13-13-P Combined Physical Electrochemical and Microscopic Studies on  
Urine  
M.ISMAIL and H.EL-MOGAZY
- d1 19-13-14-P Voltammetric Study of Metallothionein  
K.TANAKA and R.TAMAMUSHI
- d1 19-13-15-P Electrochemical Analysis of Mediated Electron Transfer of  
Flavoenzymes  
I.TANIGUCHI, S.TOMIMURA and K.YASUKOUCHI
- d1 19-13-16-P Chemically Amplified Enzyme Electrodes by Substrate Recycling  
T.YAO, H.YAMAMOTO and T.WASA

#### Solution Chemistry

- d1 19-13-17-G Adsorption Investigation of 1-Hydroxy-ethane-1,1-diphosphonic  
Acid with Divalent Cations by Radiotracer Method  
E.KALMAN, F.KARMAN, J.KONYA and L.VARALLYAI
- d1 19-13-18-P The Complexing of the Chloride Ion in Acetylacetone and  
Acetonitrile with Water and Alcohols  
I.SAKAMOTO and S.OKAZAKI
- d1 19-13-19-P Acetamide-Electrolyte Molten Mixtures: High Dielectric  
Constant Systems  
G.BERCHIESI and G.VITALI
- d1 19-13-20-P Evaluation and Prediction of Physicochemical Characteristics  
of Aqueous Glycerol  
M.AJLAN and M.ISMAIL

- d1 19-13-21-P On the Limiting Conductance of Small Ions in Water and Non-Aqueous Media  
C.MARSCHOFF
- d1 19-13-22-P Triple Ion Formation by the Hydrogen Bonding in Protophobic Solvents  
S.HOJO, A.WATANABE, T.MIZOBUCHI and Y.IMAI
- d1 19-13-23-P Physical and Chemical Properties of Liquid Phase in Highly Concentrated Solid-Liquid Dispersion System  
S.DEKI, M.MIZUHATA, A.KAJINAMI and Y.KANAJI

#### Thermodynamics

- d1 19-13-24-G Contributions to EMF from Heat and Internal Energy Changes in a Thermocell  
S.RATKJE, T.IKESHOJI and K.SYVERUD
- d1 19-13-25-G Three Components of the Liquid Junction Potential between Different Solvents: Their Characteristics and Estimation  
K.IZUTSU and T.NAKAMURA
- d1 19-13-26-P On the Concept of Equilibrium Potential in Electrochemistry  
P.RADHAKRISHNAMURTY
- d1 19-13-27-P Efficiency Calculations for Thermoelectric Converters with Identical Electrodes  
T.IKESHOJI and S.RATKJE
- d1 19-13-28-P Thermodynamics vs. Kinetics of Charge Transfer Processes at Semiconductor Electrodes  
D.MEISSNER
- d1 19-13-29-P The Role of Majority Carriers in Electrode Reactions at an Illuminated Semiconductor Electrode  
R.SHIRATSUCHI and G.NOGAMI
- d1 19-13-30-P Cyclic Voltammetric Determination of the Redox Potential of Lanthanide Ions at High Temperatures and Pressures  
B.BILAL
- d1 19-13-31-P Equilibrium and Kinetic Properties of the Complexation Reactions of Copper (II) with Aspartic Acid  
M.FORESTI and L.NYHOLM
- d1 19-13-32-P Molar Volumes of  $[M^{III}(\text{acac})_3]$  (M=Fe,Co,Ru) in Acetonitrile Solutions  
H.IKEUCHI, Y.FURUSHIMA, S.OHKUBO, R.SHIMIZU and G.SATÔ

#### Spectroelectrochemistry

- d1 19-16-01-K Transparent Sprayed  $\text{SnO}_2$  Films Structure and Electrochemical Properties  
J.BRUNEAUX, H.CACHET and M.FROMENT
- d1 19-16-02-P Observation of Electrochemically Roughened Silver Electrode Surfaces by Scanning Tunneling Microscopy  
I.OHTSUKA and T.IWASAKI
- d1 19-16-03-P Electroluminescence at the Tb(III)-Doped Oxide-Covered Zirconium Electrode  
K.HAAPAKKA, J.KANKARE and K.LIPIÄINEN



- d1 19-16-04-P The Evaluation of Surface Diffusion of Metal Atoms through Combined SEM, STM and Electrochemical Data  
L.VÁSQUEZ, A.BARTOLOME, A.BARÓ, C.ALONSO, R.SALVAREZZA and A.ARVIA
- d1 19-16-05-P The Evaluation of Surface Diffusion Coefficients of Gold and Platinum Atoms at Electrochemical Interfaces from Combined STM-SEM Imaging and Electrochemical Techniques  
C.ALONSO, R.SALVAREZZA, J.VARA, A.ARVIA, L.VASQUEZ, A.BARTOLOME and A.BARO
- d1 19-16-06-P Adsorption of  $\text{HSO}_4^-$  and  $\text{SO}_4^{2-}$  on Platinum Electrode Studied by In-Situ FT-IRRS  
K.KUNIMATSU, M.SAMANT and H.SEKI

#### Electrode/Electrolyte Interphase

- d1 19-16-07-P Interphase Characterization at the Cu-Ni/Electrolyte Contact  
I.MILOSEV and M.HUKOVIC
- d1 19-16-08-P Intercalation of Alkylamines and Phospholipid in Layered Inorganic Compounds  
Y.KANZAKI and M.ABE
- d1 19-16-09-P A Study of the Electrochemical Behaviour of Palladium Electrodes at High Positive Potentials  
A.BOLZAN and A.ARVIA
- d1 19-16-10-P The Complex Mechanism of Silver (I) Oxide Layer Electroformation on Polycrystalline Silver  
C.ALONSO, R.SALVAREZZA, J.VARA and A.ARVIA
- d1 19-16-11-P The Influence of the Forming Electrolyte on Anodic Zirconium Oxide Films  
E.PATRITO, R.TORRESI, E.LEIVA and V.MACAGNO
- d1 19-16-12-P The Kinetics of Formation of an Anodic Film on Bismuth in Phosphoric Acid at Large Underpotential  
G.WRIGHT and C.WAI

#### Liquid/Liquid Interface

- d1 21-11-03-K The Double Layer Capacity at the Polymer/Water Interface  
R.ARMSTRONG
- d1 21-11-05-G Relation between ISE Potential and Charge Transfer at Liquid/Membrane Interface  
S.KIHARA, M.SUZUKI, Z.YOSHIDA and M.MATSUI
- d1 21-11-06-G Differential Capacity of Liquid-Liquid Interfaces in the Presence of 1:1, 2:1 and 2:2 Electrolytes in the Aqueous Phase  
F.SILVA, C.SILVA, C.PEREIRA and J.EIRO
- d1 21-11-07-G Voltammetric Investigation into the Thermodynamics and Kinetics of Interfacial Ion Transfer of Ni(II) Complexes of Aromatic and Aliphatic Diamines  
A.BARUZZI and H.WENDT
- d1 21-11-08-G Structure of and Ion Transfer through the Phospholipid Monolayers at the Polarized Oil-Water Interface  
T.KAKIUCHI, M.KOTANI, M.NAKANISHI and M.SENDA

### Voltammetry-Fundamental

- d1 21-11-09-K New Trends in Electrode Kinetics Using Faradaic Rectification Method  
H.AGARWAL
- d1 21-11-10-G Voltammetric Study of Osmium Electrodes in Acid Solutions  
F.COLOM and J.PEINADO
- d1 21-11-11-P Linear Dependence of Reversible Half-Wave Potential on the Ligand Composition of Mixed-Ligand Ruthenium Chelates  
Y.HOSHINO, A.ENDO, T.MARUYAMA, F.OKUYAMA, K.SHIMIZU and G.SATÔ
- d1 21-11-12-P Comparative Voltammetric Behaviour of H- and O- Atoms on Pt Electrode in Liquid and Frozen Acid Solutions  
M.FLORIT, M.MARTINS and A.ARVIA
- d1 21-11-13-P Non Straight Correlation between I (V) Curves and Impedance Diagrams in the Case of Nickel in Sulphuric Media  
M.PETIT and M.CID
- d1 21-11-14-P Simulation of Electrochemical Processes under Periodical Perturbing Potentials  
C.ELSNER, S.MARCHIANO and A.ARVIA
- d1 21-11-15-P Double-Layer Impedance of a Platinum Electrode in Sulfuric Acid and Potassium Hydroxide Solutions  
H.MATSUI, A.KUNUGI and M.YASUZAWA
- d1 21-11-16-P Electrochemical Uses of the Quartz Oscillator  
K.HEUSLER
- d1 21-11-17-P Detection of EC' Reaction for Reversible and Irreversible Redox Species at Interdigitated Array Electrodes  
O.NIWA, M.MORITA and H.TABEI
- d1 21-11-18-P Electrochemical Behavior of GRC Electrodes for Voltammetry  
H.KANEKO, A.NEGISHI and K.AOKI
- d1 21-11-19-P Electrochemical Behaviour of Cu(II) in Valerate and Isovalerate Media  
K.CHOUDHARY, S.BAGHEL and K.ZUTSHI
- d1 21-11-20-P How Do I Know My Impedance Measurements are Correct?  
D.MACDONALD and M.URQUIDI-MACDONALD
- d1 21-11-21-P Double Layer Properties of Au(100) in the 0.1 M NaOH in the Presence of Glycerol  
M.AVRAMOV-IVIC, V.JOVIC and N.ANASTASIJEVIC

### Adsorption

- d1 21-12-01-K Chronocoulometric Procedures for Adsorption Studies of Electroactive and Electroinactive Surfactants  
R.GUIDELLI
- d1 21-12-02-K Electrocatalysis - Problems and Applications  
V.KAZARINOV
- d1 21-12-03-G The Effects of Molecular Structure on the Electrooxidation of D-Glucose and of Linear Polyols on Ni Electrodes  
O.ENEÀ
- d1 21-12-04-G The Adsorption Properties of Dioxide Iridium Electrodes  
O.PETRII, A.VITINS and T.SAFONOVA
- d1 21-12-05-G Competitive Adsorption of Nitrate and Fluoride Ions at the Mercury Electrode  
H.HURWITZ, B.BICAMUMPAKA and A.JENARD

- d1 21-12-06-P Adsorption of Ions at Single Crystal Planes of Bismuth Electrodes  
U.PALM, E.LUST, K.LUST and M.SALVE
- d1 21-12-07-P Electroless Process: Discussion of Hypophosphite Adsorption and Oxidation  
L.ABRANTES and J.CORREIA
- d1 21-12-08-P Nature of the Strong Adsorption Products of Monocarbon Compounds on Platinized Platinum  
V.KAZARINOV

#### Electrocatalysis

- d1 21-12-09-K Underpotential Deposition of Metals  
A.DESPIC
- d1 21-12-10-G Electrocatalysis of Hydrogen Evolution in the Light of the Brewer-Engel Valence-Bond Theory and d-d Electronic Correlations  
M.JAKSIC
- d1 21-12-11-G Electrocatalysis Problems in Advanced Water Electrolysis  
V.KAZARINOV and A.PSHENICHNIKOV
- d1 21-12-12-P A Jellium Model for Underpotential Deposition  
W.SCHMICKLER and E.LEIVA
- d1 21-12-13-P Electrocatalytic Reactions on a Platinized Electrode Modified by Thallium Adatoms  
V.ANDREEV, A.ZHUCHKOV, V.KAZARINOV and R.ADZIC
- d1 21-12-14-P Method of Analysis of the Kinetics of the Solution Solid Phase Interface Electrode Reactions Conjugate to the Diffusion in the Solid Phase of Variable Composition  
B.EZHOV
- d1 21-12-15-P Significance of Copper Electrode in Electroreduction of  $\text{CO}_2$  and CO Demonstrated by Surface Alloy Electrodes Au-Cu and Ag-Cu  
Y.HORI and A.MURATA
- d1 21-12-16-P Selectivity of Reaction Products in Electroreduction of  $\text{CO}_2$  and CO on Copper Electrodes Modified by In-Situ Electrodeposition of Various Metals  
Y.HORI, Y.YOSHINAMI, S.ITO, A.MURATA and O.KOGA
- d1 21-12-17-P Reaction Mechanism of Hydrocarbon Formation in Electroreduction of  $\text{CO}_2$  and CO on Copper Electrode  
Y.HORI, A.MURATA and R.TAKAHASHI
- d1 21-12-18-P Carbon Dioxide Reduction at Low Temperature on Various Metal Electrodes  
M.AZUMA, K.HASHIMOTO, M.HIRAMOTO, M.WATANABE and T.SAKATA
- d1 21-12-19-P Determination of Adsorption Heats of Hydrogen on Pt Electrodes at Different Grades of Activation  
J.Doña and J.GONZALEZ-VELASCO
- d1 21-12-20-P A Temperature Study of the Oxidation of Reduced  $\text{CO}_2$  on Activated Pt Electrodes  
M.MARCOS, J.VARA, J.GONZALEZ-VELASCO, M.GIORDANO and A.ARVIA
- d1 21-12-21-P A Study of the Adsorption Rate of Glyoxalate on Pt Electrodes in Basic Media  
P.OCON and J.GONZALEZ-VELASCO
- d1 21-12-22-P Electrochemistry of Rare Earth Cations on Modified Electrodes  
P.UGO, B.BALLARIN, S.DANIELE and G.MAZZOCCHIN

- d1 21-12-23-P Nitrogen Fixation Using a Gas-Diffusion Electrode  
N.FURUYA and H.YOSHIBA
- d1 21-12-24-P The Hydrous Oxide Mediator Mechanism for Electrocatalysis  
at the Metal/Aqueous Solution Interface  
L.BURKE, K.O'DWYER, W.O'LEARY and T.RYAN
- d1 21-12-25-P Electroreduction of the Oxyanions of the V-VII Groups  
Elements and Position of the Element in Periodic System  
R.KVARATSKHELIYA, T.MACHAVARIANI and G.KVARATSKHELIYA

#### Microelectrodes

- d1 21-13-01-P Fundamentals and Applications of Rapid-Response Voltammetry  
with Ultra-Microelectrode in Analytical Chemistry  
K.NOZAKI, S.NOMURA and S.OKAZAKI
- d1 21-13-02-P Voltammetry and Chronoamperometry at Interdigitated  
Array Electrode with Hollows and Protrusions  
M.MORITA, O.NIWA, H.TABEI and K.AOKI
- d1 21-13-03-P Microhole Array Electrodes as Detectors for HPLC  
K.TOKUDA, K.MORITA, Y.SHIMIZU and T.OKAMOTO
- d1 21-13-04-P Fabrication and Application of Microelectrodes to in-Vivo  
Voltammetry  
T.ABE, T.ITABASHI, T.MATSUE and I.UCHIDA
- d1 21-13-05-P Microhole Array Electrode for Biosensor  
Y.SHIMIZU and K.MORITA

#### IV-2. Electrode and Electrolyte Materials

- d2 18-13-01-P Oxygen Evolution Reaction on Ni-Co Oxide Electrodes Containing  
the Third Elements -Electrode Preparation and Catalytic  
Activity-  
K.TACHIBANA, K.KOBAYASHI and A.TSURUNO
- d2 18-13-02-P Characterization of DSA Type Oxygen Evolving Electrodes  
G.VERCESI, C.COMNINELLIS and E.PLATTNER
- d2 18-13-03-P Examining DSA's Coating by Transmission Microscope  
D.TANG and X.LIN
- d2 18-13-04-P Electrochemical Behavior of Nonstoichiometric Titanium Oxide  
Electrodes  
K.BOROWIEC, J.PRZYLUSKI and K.KOLBRECKA
- d2 18-13-05-P Physico-Chemical Behaviour of Ferric Hydroxides and Hydroxo  
Complexes and Their Effect on the Anodic Oxygen Evolution  
Kinetics on the Nickel Hydroxide Electrode in Alkaline  
Electrolytes  
A.KAMNEV, B.EZHOV and O.MALANDIN
- d2 18-13-06-P Mechanism of the Influence of Co, Li and Fe Hydroxides  
on the Nickel Hydroxide Electrode  
B.EZHOV and O.MALANDIN
- d2 18-13-07-P The Dielectric Breakdown of Sodium  $\beta''$ -Alumina  
M.NISHIMURA, S.NISHIMURA, M.YOSHIKAWA, A.KOBAYASHI and  
M.OHSHIMA
- d2 18-13-08-P Mechanism of Electrochemical Consumption of Graphite Anodes  
in Alkali Nitrate Solutions  
M.RABAH, N.NASSIF and A.ABDUL AZIM

- d2 18-13-09-P Electrochemical Properties of Glassy Carbon Modified by  $N^{+}$ - and  $O^{+}$ -Ion Implantation  
K.TAKAHASHI, Y.ABE, A.SEKIGUCHI and M.IWAKI
- d2 18-13-10-P Electrocatalytic Aspects of Some Amorphous Electrode Materials for Alkaline Water Electrolysis  
M.ISMAIL, M.TALBALLA and M.DAOUS
- d2 18-13-11-P Preparation of W-C Thin Films by RF Sputtering and their Electrocatalytic Property for the Methanol Oxidation  
K.MACHIDA, K.KODAIRA and M.ENYO
- d2 18-13-12-P Nonstoichiometry of  $Ca_{1-x}Ce_xMnO_{3+\delta}$  and Its Properties as an Active Material for Alkaline Battery  
T.ESAKA and H.IWAHARA
- d2 18-13-13-P Evaluation of Some Lead Oxides Used in the Manufacture of Lead Acid Battery Electrodes  
A.SABA and S.AFIFI
- d2 18-13-14-P Sorption Electrode Properties on the Basis of  $LaNi_5H_n$  in the Dependence on Conditions of Active Hydride Surface  
R.BAISHEVA, R.IBRASHEVA, T.SOLOMINA, G.FEDOROV and K.ZHUBANOV
- d2 18-13-15-P Influence of the Catalytic Surface Forming  $LaNi_5H_n$  in the Electroreduction Process on Adsorption of Nitrobenzene  
R.IBRASHEVA, R.BAISHEVA, G.FEDOROV, T.SOLOMINA and K.ZHUBANOV
- d2 18-13-17-P Dissolution Behaviour of Aluminium Covered with Anodic Oxide Film in Trichloroacetic Acid Solution Using Impedance Measurements  
M.EL-BASIOUNY, A.BABAQI and R.ABDULLA
- d2 21-13-06-K Electrochemistry of Polymer Layers  
F.BECK
- d2 21-13-07-P Photoelectrochemical and Impedance Studies of Thin Electropolymerized Polypyrrole Films in Aqueous Solution  
F.BÜCHI and H.SIEGENTHALER
- d2 21-13-08-P Effect of Heat Treatment on Carbon Supported Metalloporphyrins and Naphtalocyanines for Air Electrodes in Alkaline Media  
G.BRONOEL, M.SAVY, F.COOWAR, J.RIGA, J.VERBIST, R.ROUGET and S.BESSE
- d2 21-13-09-P Properties of Organic Electrolytes for Electric Double Layer Capacitors  
K.HIRATSUKA, T.MORIMOTO, Y.SANADA and K.KURIHARA
- d2 21-13-10-P Transient Technique for Evaluation of Polymer Coatings  
M.GASHGARI, M.AJLAN and M.ISMAIL
- d2 21-13-11-P CV-Characteristics and Impedance of the Conjugated Polymers Doped with Reversible Redox Systems  
V.KUTZ, O.ZHALKO-TITARENKO and O.LAZURSKY
- d2 21-13-13-P Electrochemistry at Fractal Electrodes : Relation between Self-Similarity and Frequency Response  
M.KEDDAM and H.TAKENOUTI
- d2 21-13-14-P The Electrochromism and the Electrode Impedance of Conductive Polymer Films  
M.KEDDAM, M.MUSIANI and H.TAKENOUTI
- d2 21-13-15-P Electrochromic Properties of Polyaniline Films Doped with Methylene Blue-Bound Nafion  
S.KUWABATA, K.MITSUI and H.YONEYAMA
- d2 21-13-16-P The Investigation of Charge Transport through Thin Films of Osmium Containing Polymers  
R.FORSTER, A.KELLY and J.VOS

#### IV-5. Electrochemical Energy Conversion

- d5 18-14-01-P Free Convection in the Lead-Acid Battery  
A.EKLUND, D.SIMONSSON, F.ALAVYOON, R.KARLSSON and F.BARK
- d5 18-14-02-P Mathematical Modelling of the Electrode Processes in the  
Pb/PbSO<sub>4</sub> and Pb/PbO<sub>2</sub> Systems  
S.STERNBERG, V.BRANZOI and L.APATEANU
- d5 18-14-03-P Lead Oxide for Electrodes from Acid Lead Battery Scrap  
M.RABAH, I.MORSI and S.EL-TAWIL
- d5 18-14-04-P A New Sensor for the State of Discharge in Lead Acid Batteries  
F.BECK and H.KROHN
- d5 18-14-05-P Modeling on Porous Sulfur Electrode of Sodium-Sulfur Cell  
H.KAWAMOTO
- d5 18-14-06-P Safety Design of a Sodium-Sulfur Cell  
M.OHSHIMA, M.NAKAMURA and A.KOBAYASHI
- d5 18-14-07-P Cycling Behavior of Zinc-Bromine Battery at High  
Discharge Current Density  
S.HIGUCHI, T.FUJIEDA, S.TAKAHASHI, K.JINNAI and T.FUJII
- d5 18-14-08-P Evaluation of Microporous Separators for Zinc Bromine Batteries  
K.KAWAHARA, T.SAEKI, K.ABE and T.YOSHIDA
- d5 18-14-09-P Numerical Analysis on Shunt Current in Flow Batteries  
K.KANARI, K.NOZAKI and H.KANEKO
- d5 18-14-10-P Redox Reactions of Vanadium Ions on GRC and Carbon Fiber  
Electrodes  
H.KANEKO, T.AOKI and K.NOZAKI
- d5 18-14-11-P Regeneration of Ni-Cd Accumulators by Hydrogen Peroxide  
M.CENEK, J.KAZELLE and V.HODINAR
- d5 18-14-12-P Cadmium Electrode with Oxalic Acid for Alkaline Accumulators  
M.CENEK, B.WILCZEK and V.HODINAR
- d5 18-14-13-P The Influence of the Preparation Conditions on the Discharge  
Efficiency, Self Discharge and Secondary Discharge of Nickel  
Hydroxide Electrodes Chemically Precipitated on Different  
Substrates  
M.VAZQUEZ, R.CARBONIO and V.MACAGNO
- d5 18-14-14-P Pasted Zinc Electrodes for Alkaline Secondary Batteries  
M.NOAGAMI, M.TADOKORO, K.INOUE and N.FURUKAWA
- d5 18-14-15-P Advanced Batteries with Zinc Anodes  
L.BINDER, A.HAYNES and K.KORDESCH
- d5 18-14-16-P New Type of Iron Electrode for Ni-Fe Traction Accumulator  
M.CENEK, J.KAZELLE, B.WILCZEK and V.HODINAR
- d5 18-14-17-P Effect of the Additives on Character of Iron Electrode  
S.ZHU and Z.SHAN
- d5 18-14-18-P Charging Efficiency of Zinc Electrode for Nickel-Zinc Battery  
H.YASUDA and S.KASHIHARA
- d5 18-14-19-P On the Influence of Hafnium Chloride on the Electrochemical  
Behaviours of Silver-Silver Oxide Electrode  
Y.YAMAMOTO, K.FUMINO and Y.YAMAKAWA
- d5 19-14-01-G Rare Earth-Nickel Alloys for Nickel/Metal Hydride Battery  
T.SAKAI, H.MIYAMURA, N.KURIYAMA, A.KATO, K.OGURO, H.ISHIKAWA  
and C.IWAKURA
- d5 19-14-02-P New Protonic Conductor and Its Application to Nickel/Metal  
Hydride Battery  
N.KURIYAMA, T.SAKAI, H.MIYAMURA and H.ISHIKAWA

- d5 19-14-03-P Electrochemical Hydrogen Absorption Behavior of Lanthanum-Nickel Alloy Thin Films  
H.MIYAMURA, T.SAKAI, N.KURIYAMA, K.OGURO, A.KATO and H.ISHIKAWA
- d5 19-14-04-P  $C_{14}/C_{15}$  Type Laves Phase Alloy Electrode for Ni-H<sub>2</sub> Battery  
T.GAMO, Y.MORIWAKI and T.IWAKI
- d5 19-14-05-P An Advanced Secondary Battery Employing a Hydrogen Absorbing Alloy Electrode  
M.NOGAMI, S.KAMEOKA, I.YONEZU, K.INOUE, T.MATSUMOTO and N.FURUKAWA
- d5 19-14-06-P Studies on the Cycle Life of Metal Hydride Electrodes for Ni/H<sub>2</sub> Secondary Batteries  
M.YAMAMOTO, K.KANNO, Y.SATOH, H.HAYASHIDA and M.SUZUKI
- d5 19-14-07-P Hydrogen Absorption in Sodium Tungsten Bronze  
Y.MURANUSHI, T.MIURA and T.KISHI
- d5 19-14-08-G Recent R&D Trend of Metal-Active Materials for Batteries  
K.MIYAZAKI
- d5 19-14-09-G The Investigation of Polyaniline as Electrode Material in Secondary Batteries  
B.WANG, C.LI, G.LI and F.WANG
- d5 19-14-10-G Al/Polyaniline Secondary Batteries Operated at Room Temperature  
N.KOURA and H.EJIRI
- d5 19-14-11-G The Usage Perspectives of Monomeric and Polymeric Active Organic Materials in the Chemical Recharged Batteries  
V.BARSUKOV, S.DUNOVSKY, A.GORODYSKY and V.DMITRENKO
- d5 19-14-12-P Battery Tester for Accumulators Used in Battery Trucks and Invalid Carriages  
J.KAZELLE and M.CENEK
- d5 19-14-13-P Mechanism of Self-Discharge in Conductive Polymer Electrodes  
K.SHINOZAKI, A.KABUMOTO, K.WATANABE, H.UMEMURA and N.NISHIKAWA
- d5 19-14-14-K Global Perspectives of Fuel Cell Technologies and Their Applications  
S.SRINIVASAN, M.ENAYETULLAH and A.APPLEBY
- d5 19-14-15-G Evaluation of Electrocatalytic Activity and Corrosion Resistivity of Ni-Pd-P Deposited Anode for Fuel Cell  
M.YAMASHITA, H.TAKEMURA, H.INUI and Y.UETANI
- d5 19-14-16-P Influence of Ultra-Dispersion of Pt Electrocatalysts on the Activity at the Direct Methanol Fuel Cell Reactions  
M.WATANABE and P.STONEHART
- d5 19-14-17-P Solid Polymer Electrolyte (SPE) Electrodes as Methanol Fuel Cell Anodes  
A.ARAMATA
- d5 19-14-18-P Enhancement in Methanol Oxidation by Molybdenum Modification of Pt and Pt-SPE Electrodes  
H.NAKAJIMA, J.WANG and H.KITA
- d5 19-14-19-P Electro-Oxidation of Methanol on Pt Electrodes Modified by Metal Oxides and Noble Metals  
T.OHMORI and M.ENYO
- d5 19-14-20-P Oxidation of Formaldehyde on Copper Electrode Modified by Foreign Metals  
M.MATSUOKA, S.WATANABE, Y.FUKUMOTO and C.IWAKURA
- d5 19-14-21-P On the Electrochemical Behaviours and the Synthesis of  $Na_{1+x}Zr_2Si_xP_{3-x}O_{12}$  ( $0 \leq x \leq 3$ )  
Y.YAMAMOTO, M.ADACHI, S.HONDA, O.NAKAMURA and Y.SAITO

- d5 19-14-22-P Solid State Rechargeable Battery Using Paper Form Copper Ion Conductive Solid Electrolyte and Copper Chevrel Electrodes  
T.SOTOMURA, Y.MORIWAKI, S.KONDO and T.IWAKI
- d5 19-14-23-P Paper Form Copper Ion Conductive Solid Electrolyte  
N.YASUDA, M.NAGATA, S.KONDO and T.SOTOMURA
- d5 19-14-24-P Oxygen Electrode Reaction on Iridium-Oxide Coated Platinum  
R.NOTOYA
- d5 19-14-26-P Computer Analysis of Natural Convection in Thermoelectric Converters with a Redox-Couple in Solution  
T.IKESHOJI, S.KIMURA and M.YONEYA
- d5 19-14-27-P Molecular Structure - Electroactivity Correlations in the Gas Phase Processes  
O.ENEAA
- d5 19-14-28-P Electrochemical Oxidation of CO at Au- and Pt-SPE Electrodes with and without Sn Modification  
K.FUJIKAWA, K.MURAOKA and M.ISHIKO
- d5 19-14-29-P Improvement of Thermoelectric Conversion Characteristics of Porous SiC Ceramics by Microstructure Control  
- Effects of Powder Compaction Pressure and Sintering Time -  
C.PAI, K.KOUMOTO and H.YANAGIDA
- d5 19-14-30-P Transition Metal Chalcogenides and Lamellar Compound  
Their Science and Technology (part 6)  
S.K.BAHADOR

#### IV-6. Corrosion, Electrodeposition and Surface Treatment

- d6 21-14-01-K Characterization of Electrodeposited Metal Layers with Ellipsometry  
W.VISSCHER
- d6 21-14-02-K Recent Progress in the Electrodeposition of Refractory Carbides from Molten Salts  
K.STERN and D.ROLISON
- d6 21-14-03-P Electrodeposition of Precious Metals with Asymmetric AC  
K.HOSOKAWA, A.ABLIMIT, H.ENDOH, S.HAMAGUCHI, Y.TSURU and M.MATSUNAGA
- d6 21-14-04-P Surface Analysis of Iridescent Electrodeposition Chromium Films  
F.GE, S.XU and S.ZHOU
- d6 21-14-05-P Role of Individual Groups in Anthranilic Acid on Copper and Cadmium Electrodeposits  
M.IQBAL and S.NAGESWAR
- d6 21-14-06-P Formation of Zinc Electrodeposits with Highly Preferred Orientation  
S.ZHOU, Y.ZHANG and X.CHEN
- d6 21-14-07-P Effect of Quaternary Ammonium Salts on the Electrodeposition of Zinc and Its Alloys  
M.KUME and M.NISHIMURA
- d6 21-14-08-P Gallium Thin Film Electrodeposition onto Titanium from Aqueous Bath  
J.ORTEGA
- d6 21-14-09-P Electrodeposition of Technetium and Concurrent Processes in Electrolysis of Acid Solutions of Pertechnetates  
V.KUDRYAVTSEV, S.BAGAEV, E.ZAKHAROV and K.PEDAN
- d6 21-14-10-P Electrocrystallization of Silver from Thiocyanate Solution  
I.KOSENKO, V.TROFIMENKO and Y.LOSHKARYOV



- d6 21-14-11-P Electrolytic Crystal Growth of Copper on Cu-Zr Metallic Glasses  
M.KUMAR and S.NAGESWAR
- d6 21-14-12-P Kinetics and Mass Transfer in Permalloy Electrodeposition  
J.JU, H.KIM and K.YUN
- d6 21-14-13-P Development of Plating Bath for Decorative Fe-Ni Alloys  
S.MAYANNA, A.RAMACHANDRAN and T.VENKATESHA
- d6 21-14-14-P Study on Electrodeposition of Ni-Fe Alloy  
P.LI, J.XU and S.Zhou
- d6 21-14-15-P Study on Electrodeposition of CdSe Films  
S.ZHOU, D.LIU and Y.ZHANG
- d6 21-14-16-P Formation of Alloys during Aluminium Deposition from "Low" Temperature Melts  
B.RADOVIC, M.PAVLOVIC and J.JOVICEVIC
- d6 21-14-17-P Interdependence of Individual Partial Reactions in Electroless Nickel Plating  
M.MATSUOKA, S.MAEGAWA and C.IWAKURA
- d6 21-14-18-P Electroless Plating Process by Nickel and Nickel Alloys  
T.KHOPERIA and A.ULANOVA
- d6 21-14-19-P Electrodeposition of Ni-Al<sub>2</sub>O<sub>3</sub>-PTFE Composite Materials from Watts Type Bath  
H.HAYASHI, I.KAWAHARA and I.TARI
- d6 21-14-20-P Electrodeposition of Silver Dispersion Coatings for Contact Applications  
N.FURUKAWA, A.OIDO, Y.FUKUMOTO and C.IWAKURA
- d6 21-14-21-P Underpotential Deposition of Heavy Metal Adatoms on Platinum Single Crystal Stepped Surfaces  
N.MARKOVIC and R.ADZIC
- d6 21-14-22-P Electrochemical, Optical and Theoretical Studies of Nucleation and Growth  
M.SLUYTERS-REHBACH, J.WIJENBERG, E.BOSCO, W.KRUIJT, P.BOBBERT and J.SLUYTERS
- d6 21-14-23-P A.C. Impedance of Electrocrystallization Processes for Metals with High and Low Exchange Current Densities  
B.TOPERIC, B.RADOVIC, V.JOVIC, M.PAVLOVIC and J.JOVICEVIC
- d6 21-14-24-P Analysis of Mass Transfer Limited Electrodeposition to Blind Holes  
A.PEARLSTEIN and S.NOBE
- d6 21-14-25-P Electrodeposition at the Interface between Aqueous Solution and Non-Aqueous Solvent  
T.FUJIEDA, S.HIGUCHI and S.TAKAHASHI
- d6 21-14-26-P Evaluation of Surface Finishing Surfactants Using Response to DC Pulse and Transient Heat Transfer Technique  
M.ISMAIL and H.HINZ
- d6 21-14-28-K Transfer of Ions and Electrons at Anodic Cadmium Sulfide Films  
M.KREBS and K.HEUSLER
- d6 21-14-29-P Electroreduction of Anodic Oxide Films on Cobalt in Neutral Solution  
J.VILCHE, S.BIAGGIO, C.GERVASI and A.ARVIA
- d6 21-14-30-P Surface Oxidation Behaviour of Amorphous and Crystallized Cu-Ti Alloys  
M.HUKOVIC, D.BOSKOVIC and I.MILOSEV
- d6 21-14-31-P Kinetics of Thin-Film Aluminum-Tantalum Anodization Studied with Electron Microscopy  
V.SURGANOV and A.MOZALEV

- d6 21-14-32-P Study of Anodic Film on Aluminium by Positron Annihilation  
Lifetime Spectroscopy  
S.YAO, J.FANG and S.ZHOU
- d6 21-14-33-P Anodic Oxide Dissolution during Aluminum Anodization  
in Organic and Inorganic Acids Solutions  
V.SURGANOV and A.POZNYAK
- d6 21-14-34-P On the Nature of Activation of Surface Skeleton Nickel  
Catalysts Produced by Different Methods  
N.KOROVIN, E.UDRIS, O.SAVELJEVA, N.KOZLOVA and I.TAZAGULOVA
- d6 21-14-35-P Electrochemical Behaviours of Laser Surface Alloying for  
Low Alloy Steel  
S.SONG, W.WANG and Z.FANG
- d6 21-14-36-P Ion Beam Irradiation onto the Electrode Surface  
K.MORITANI, K.YOSHIDA, T.SHIMADA and Y.ITO
- d6 21-14-37-P A Study of Vanadium Phases Analysis of the Steel  
Welded by Gleeble 1500 by Electrolysis  
S.FENG

## V SPECIAL SESSION

### V-1. Electrochemical Aspects of Cold Fusion

- e1 22-01-00-1 (Introductory Remarks) Prospects and Problems  
of Electrochemically Induced Cold Nuclear Fusion  
J.SCHULTZE, U.KONIG, A.HOCHFELD, C.van CALKER and W.KIES
- e1 22-01-01-G Heat, Tritium and Neutrons from the Palladium - D<sub>2</sub>O Systems  
J.BOCKRIS, K.WOLF, R.KAINTHLA, O.VELEV and N.PACKHAM
- e1 22-01-02-G Neutron Evolution from Palladium Cathode in D<sub>2</sub>O-LiOD Solution  
T.MIZUNO, T.AKIMOTO and N.SATO
- e1 22-01-04-G Low Temperature Fusion of Deuterium in Electrochemical  
Processes  
J.ZAK and J.STROJEK
- e1 22-01-05-G Some Experiments and Analysis of Possible Cold Fusion  
N.OYAMA, T.OHSAKA, O.HATOZAKI, N.YAMAMOTO, Y.KURASAWA,  
S.KASAHARA, S.TAKEOKA, Y.IMAI, Y.OYAMA, T.NAKAMURA,  
T.SHIBATA, M.IMAMURA, Y.UWAMINO and S.SHIBATA
- e1 22-01-06-G Electrochemical Properties of Metallic Hydrides  
D.LEWIS and K.SKOLD
- e1 22-01-07-G Search for Neutron Emission Associated with Electrolysis of  
Heavy Water on Pd and Ti Electrodes  
A.KIRA, S.NAKABAYASHI, S.YAMAGATA, M.ARATANI, M.MINAMI,  
K.YOSHIDA, M.YANOKURA, T.SUZUKI, T.ICHIHARA, H.KUMAGAI and  
I.TANIHATA
- e1 22-01-08-G Critical Analysis and Possible Explanation of Electrochemical  
Nuclear Fusion  
G.KREYSA, M.SCHUTZE, G.MARX, W.PLIETH, B.ZEITNITZ,  
W.HEERINGA and H.KLAGES
- e1 22-01-09-G Electrochemical Study on Cold-Fusion Phenomenon  
S.BABA, K.KAWAMURA and N.TANIGUCHI
- e1 22-01-10-G Characteristics of Pd Cathode in D<sub>2</sub>O  
K.OTA, N.KAMIYA, F.SHIRAIISHI, Y.ISHIZUKA, M.YAMAGUCHI,  
H.MATSUI, S.WATANABE and H.TANACA

- e1 22-01-11-G One Month Loadings of Palladium: Deuterium Content, Neutron  
Detection  
R.DURAND, R.FAURE and D.ABERDAM
- e1 22-01-12-K Electrochemically-Induced Nuclear Fusion of Deuterium  
(Tentative)  
M.FLEISCHMANN and B.PONS
- e1 22-01-13-G In Search of Radioactive Emissions from the Pd Electrodes  
of the Pd-D and Pd-H Systems  
H.UCHIDA, Y.MATSUMURA, T.HAYASHI, Y.OHTANI and M.KAWACHI

19-11-01-K

LOW TEMPERATURE EFFECTS IN ELECTROCHEMICAL SYSTEMS  
WITH HIGH  $T_c$  SUPERCONDUCTORS

A. Pinkowski, J. Doneit, K. Jüttner and W. J. Lorenz  
 Institut für Physikalische Chemie und Elektrochemie, Uni-  
 versität Karlsruhe, Karlsruhe, FRG

G. Saemann-Ischenko  
 Physikalisches Institut, Universität Erlangen-Nürnberg,  
 Erlangen, FRG

M. W. Breiter  
 Institut für Technische Elektrochemie, Technische Univer-  
 sität Wien, Wien, Austria

Low temperature electrochemical measurements were carried out on interfaces between different polycrystalline high  $T_c$  superconductors (  $YBa_2Cu_3O_{7-\delta}$  with  $0 \leq \delta \leq 0.5$ ,  $YBa_2Cu_{3(1-x)}Zn_{3x}O_{7-\delta}$  with  $0 \leq x \leq 0.06$ ,  $Tl_2Ba_2Ca_2Cu_3O_{10}$ ,  $Tl_2Ba_2CaCu_2O_8$ ,  $Tl_2Ba_2Ca_2Cu_3O_{10}$  ) and Ag beta" alumina as solid electrolyte. By using a special transient technique, cell currents were measured as a function of time at constant potential. The transient currents approach values which change only slightly with time after about 10 sec. The latter currents display a significant increase around  $T_c$ . The increase cannot be explained by a specific property of the solid electrolyte. This effect should be correlated to Cooper pairs changing the structure of the electrochemical double layer and possibly penetrating the energy barrier at the interface HTSC/solid electrolyte. The results are interpreted as an enhancement of the kinetics at the electrode or a proximity effect.

19-11-02-G

COMPLEX SUSCEPTIBILITY OF SINGLE CRYSTAL  $\text{YBa}_2\text{Cu}_3\text{O}_y$ 

H. Mazaki, H. Yasuoka

Department of Mathematics and Physics, The National Defense Academy,  
Yokosuka 239

T. Terashima, Y. Bando

Institute for Chemical Research, Kyoto University, Uji 611

K. Yamamoto, K. Hirata, K. Iijima

Research Institute for Production Development, Kyoto 606

The superconducting transition of single crystal  $\text{YBa}_2\text{Cu}_3\text{O}_y$  (YBCO) has been measured in terms of complex susceptibility. The samples used are thin films and a bulk crystal. The films were prepared by the activated reactive evaporation technique [1]. The substrate (single-crystal  $\text{SrTiO}_3$ ) temperature during the metal evaporation was kept at  $530\text{--}700^\circ\text{C}$ . We empirically found that YBCO(001) epitaxially grown on  $\text{SrTiO}_3(100)$  can have particularly good quality. The X-ray diffraction patterns of as-grown films indicate that they consist of the single-phase YBCO whose (001) plane is parallel to the substrate. Examination by means of low energy electron (74 eV) deflection observation showed that the films are well crystallized, even at the top surface of the film. In fact, an ultrathin film (100 Å) thus prepared showed a superconducting transition at 82 K. The maximum thickness of the films used in the present experiment was 6000 Å.

A bulk single crystal was made by slow cooling from the mixture of  $\text{Y}_2\text{O}_3$ ,  $\text{BaCO}_3$ , and  $\text{CuO}$ . The specimen was annealed in the 100-atm oxygen atmosphere at  $500^\circ\text{C}$  for 10 h. The bulk single crystal thus prepared is  $0.8 \times 2 \times 2 \text{ mm}^3$ .

The measuring system of complex susceptibility  $\chi = \chi' - i\chi''$  mainly consists of the Hartshorn bridge and the temperature control system. A null adjustment of the bridge was made at the sample temperature of 105 K. Phase setting of the lock-in analyzer was made so as to give variation only to the in-phase signal, but not to the out-of-phase signal, against the change in the bridge inductance. Temperature was measured with a calibrated carbon-glass thermometer [2].

In Fig. 1, we show a typical result of  $\chi$  for a film with 1000 Å thickness, where the ac field  $h(t) = h_0 \sin 2\pi f t$  was applied perpendicular to the film plane (c planes). The Meissner effect was confirmed from the measurement of  $\chi'$ .  $\chi''$  forms a single

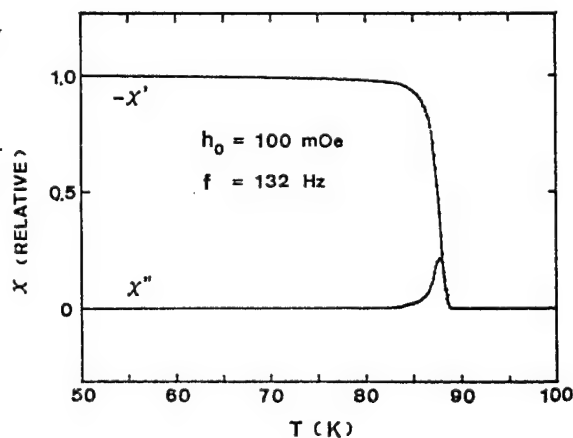


Fig. 1. Real and imaginary components of  $\chi$  for a YBCO(001) film (1000 Å). The applied magnetic field is perpendicular to the c planes.

peak, indicating that the structural uniformity of the specimen is satisfactory. However, we have found that the offset temperature of resistive transition is often higher than the onset temperature of  $\chi'$  by several degrees. And this difference becomes larger when the magnetic field amplitude  $h_0$  increases. It is well known that even very small external magnetic field ( $<1$  Oe) perpendicular to a film plane can penetrate into it, and in this situation the sample should be in a vortex state.

To examine the above possibility, we measured the  $h_0$  dependence of  $\chi$  for several films. As a typical result, we show  $-\chi'$  for the 1000-Å film, where the magnetic field with two different values of  $h_0$  was applied perpendicular to the c planes (Fig. 2). In the figure, when  $h_0$  increases, the transition curves of  $-\chi'$  always shifts to lower temperatures and this tendency was the same even for a 6000-Å film. This may indicate that due to an extremely large demagnetization factor the effective field becomes over the lower critical field and the sample is in the vortex state.

In the case of the bulk specimen, the observed  $\chi''$  which represents the eddy current loss exhibits different features for parallel and perpendicular to the c planes. This feature can be qualitatively understood by the different mobility of shielding current in the direction perpendicular and parallel to the c planes.

Summarizing, we have measured  $\chi$  for single crystal YBCO films and a bulk specimen. For the films,  $-\chi'$  exhibits a parallel shift to lower temperatures when  $h_0$  increases. This indicates the existence of the vortex state. Anisotropic nature of a bulk YBCO was observed in the imaginary component of  $\chi$ , indicating the different mobility of shielding current in the parallel and perpendicular directions to the c planes.

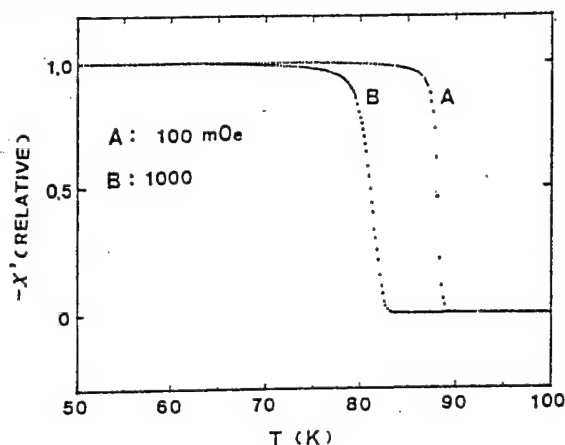


Fig. 2.  $h_0$  dependence of real component of  $\chi$  for a YBCO(001) film (1000 Å). The applied field is perpendicular to the c planes.

[1] T. Terashima, K. Iijima, K. Yamamoto, Y. Bando, H. Mazaki; Jpn. J. Appl. Phys., Vol. 27 (1988) L91.

[2] T. Ishida, H. Mazaki; J. Appl. Phys., Vol. 52 (1981) 6798.

19-11-03-G

EFFECT OF SYNTHESIS CONDITIONS ON MICROSTRUCTURE AND SUPERCONDUCTING PROPERTIES OF BULK  $\text{YBa}_2\text{Cu}_3\text{O}_x$  BY QUENCH AND MELT GROWTH (QMG) PROCESS

M. Morita, K. Doi, A. Hayashi, K. Miyamoto, M. Murakami and K. Sawano  
R & D Labs - I, Nippon Steel Corporation  
1618 Ida, Nakahara, Kawasaki 211 Japan

Quench and Melt Growth (QMG) process is of interest to synthesize a bulk YBCO superconductor with high critical current density ( $J_c$ ). This process consists of quenching molten stoichiometric  $\text{YBa}_2\text{Cu}_3\text{O}_x$  (123) from about  $1400^\circ\text{C}$ , partial melting at about  $1200^\circ\text{C}$  and slow cooling. The bulk obtained by this process includes highly oriented 123 crystals with  $\text{Y}_2\text{BaCuO}_5$  (211) inclusions, cracks and streaks. The 123 crystals form by a peritectic reaction of 211 and liquid. As well as other processes, the synthesis conditions strongly affect the superconducting properties and microstructure of the bulk. Each step of the QMG process were examined to improve the quality of the resultant 123 crystals.

As-quenched samples consist of yttria,  $\text{BaCuO}_2$  and an unknown phase. The yttria grains are spherical and about  $10\text{ }\mu\text{m}$  in size. The size of yttria grains seemed to decrease with increasing temperature. During partial melting, crystalline phases changed to 211, BC and the unknown phase. The 211 grains were needle-shaped and considered to nucleate around the yttria grains. The difference in size and distribution of the 211 needles is not obvious by changing partial melting conditions. After slow cooling at about  $1000^\circ\text{C}$ , 123 crystals grew up to several mm and contained fine 211 grains inside. The size of the 211 inclusions in the final microstructure seemed to reflect the size of the 211 needles during partial melting. 123 crystals grown from  $1200^\circ\text{C}$  partial melting included larger number of coarsened 211 grains than  $1100^\circ\text{C}$ . The distribution of the 211 grains in the 123 crystals is also different.  $1100^\circ\text{C}$  partial melting seemed produce more homogeneously distributed 211 inclusions than  $1200^\circ\text{C}$ . These indicate the more rapid growth and slower nucleation rate at  $1200^\circ\text{C}$  than at  $1100^\circ\text{C}$  due to the difference in the energy of the nucleation. The final 123 crystal size seemed to become smaller by  $1050^\circ\text{C}$  partial melting compared to  $1200^\circ\text{C}$  and  $1100^\circ\text{C}$  partial melting. The partial melting conditions seem to have an influence on the subsequent nucleation of 123. Atmosphere of the process strongly affect the superconducting properties mainly related to oxygen content in the crystals. The crystal cooled in air exhibited about 80K of  $T_c$  and  $600\text{ A/cm}^2$  of  $J_c$ , while post-annealing in oxygen improved them to 92K and  $10^4\text{ A/cm}^2$ , respectively. This is caused by the relatively slow oxygen diffusion in this high density sample. Twinning were often observed along cracks and streaks in the bulk. However, the rate of oxygen diffusion into the bulk is faster than a densely sintered 123 body. Cracks, streaks and 211 inclusions may act as oxygen diffusion paths. As described above, many factors have influences on the process. More work is necessary to understand the formation mechanism of the 123 crystals and to optimize the process.

19-11-04-K

GLASS FORMATION AND CRYSTALLIZATION PROCESS OF Bi-CONTAINING HIGH- $T_c$  SUPERCONDUCTORS

Tsutomu MINAMI

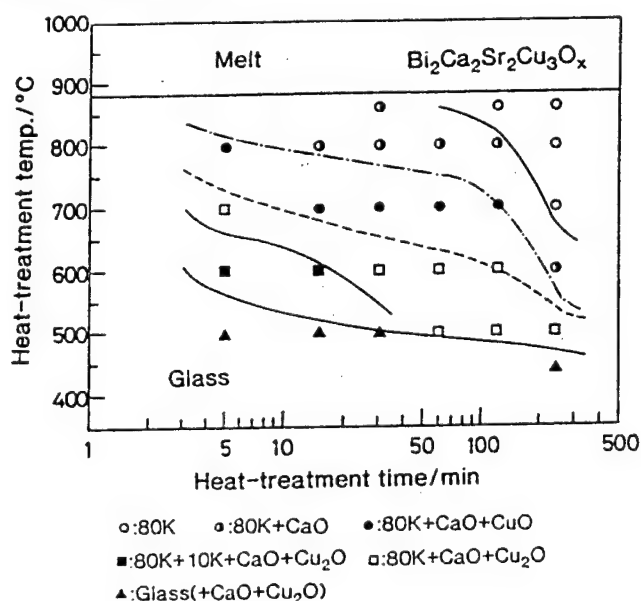
Department of Applied Chemistry, University of Osaka Prefecture, Sakai,  
Osaka 591, Japan

Among several kinds of high- $T_c$  superconductors, compounds in the system Bi-Ca-Sr-Cu-O have been found independently by several groups to form glasses [1-4]. These glasses can, of course, be transformed by appropriate heat-treatment to superconductors, which have a critical temperature over 80K. Glass formation is thus expected to be a first step to prepare fibers of superconductors through glass, since glasses have a feature of easy shaping like fibers, plates, pipes, and so on.

A wide composition region was found to form glass in this system. The crystalline phases produced by the heat-treatment of the glasses have been reported differently from reference to reference. Such a difference was found to result from the difference in the heat-treatment time at a given temperature. As an example of crystalline phases produced by the heat-treatment the result for the  $\text{Bi}_2\text{Ca}_2\text{Sr}_2\text{Cu}_3\text{O}_x$  is shown in Fig. 1. It is obvious from this figure that the crystalline phases are different with the heat-treatment time at any temperature. For example, at 500 C, which is 60 C higher than the crystallization temperature of this glass in DTA, crystalline  $\text{Cu}_2\text{O}$  appears in short time in addition to CaO; a trace of CaO remained in the as-quenched glass. When the time was prolonged than 60 min, the 80K phase appears. The single phase of 80K is produced in the region of high temperature and long heat-treatment as shown by open circles. This kind of maps has been obtained for the other typical compounds,  $\text{Bi}_2\text{CaSr}_2\text{O}_x$  and  $\text{BiCaSrCu}_2\text{O}_x$ .

The  $T_c$  of the heat-treated samples was observed at around 85K. The 110K phase was not formed from the Bi-Ca-Sr-Cu-O glasses, even for the composition  $\text{Bi}_2\text{Ca}_2\text{Sr}_2\text{Cu}_3\text{O}_x$ . The addition of Pb for the replacement of Bi by 10% increased the  $T_c$  up to about 110K.

- [1] D.J. Hinks et al.; Appl. Phys. Lett., 53 (1988)423.  
[2] T. Komatsu et al.; Jpn. J. Appl. Phys., 27 (1988)L550.  
[3] T. Minami et al.; Jpn. J. Appl. Phys., 27 (1988)L777.  
[4] A. Inoue et al.; Jpn. J. Appl. Phys., 27 (1988)L941.





19-11-05-G

CHEMICAL PROPERTIES OF HIGH  $T_c$  OXIDE SUPERCONDUCTORS NEAR  
THEIR CRITICAL TEMPERATURES

Y. Takasu,\* K. Hanyu,\* K. Takeda,<sup>o</sup> Y. Matsuda,<sup>o</sup> K. Yahikozawa\*

\* Department of Fine Materials Engineering, Faculty of Textile Science and Technology, Shinshu University, 3-1-5 Tokida, Ueda-shi, Nagano 386, Japan

<sup>o</sup> Department of Industrial Chemistry, Faculty of Engineering, Yamaguchi University, 2557 Tokiwadai, Ube-shi, Yamaguchi 755, Japan

The high  $T_c$  oxide superconductor YBaCuO system has a perovskite structure, and many investigators suggest that the plane consisting of  $\text{Cu}3d_{x^2-y^2}$  and  $\text{O}2p$  orbitals must contribute to its superconduction. On the other hand, Dowden and his coworkers have insisted that the  $3d_{x^2-y^2}$  orbitals of 3d-transition metal oxides can play an important role for the catalytic exchange of  $\text{H}_2\text{-D}_2$  on their surfaces.<sup>1)</sup> It can be possible, therefore, that the catalytic activity for the  $\text{H}_2\text{-D}_2$  exchange reaction over YBaCuO system shows catastrophic behavior around its  $T_c$ . This report will present an experimental approach to reveal whether such phenomenon does exist or not.

The YBaCuO oxide was prepared by calcination of  $\text{Y}_2\text{O}_3$ ,  $\text{BaCO}_3$ , and  $\text{CuO}$ . X-ray diffraction analysis, iodometry, and four-probe electric resistivity measurement showed the oxide to be orthorhombic  $\text{YBa}_2\text{Cu}_3\text{O}_{6.90}$  with  $T_{c,\text{end}} = 85$  K. The most important point for the catalytic activity measurement at low temperature is to construct an ultra-high vacuum system which can avoid any effects of residual water, CO, and any other contaminants, so that we have constructed a stainless steel UHV catalytic reaction apparatus capable to be evacuated lower than  $5 \times 10^{-10}$  Torr. After setting a few pieces of YBaCuO oxide (40 mg) in the reaction cell part, we baked the apparatus at 200 °C and then cooled. Next, the YBaCuO oxide was crushed to powder in vacuum with a stainless hammer at 77 K. Figure 1 shows the catalytic activity of the YBaCuO oxide for the  $\text{H}_2\text{-D}_2$  exchange reaction at various temperatures. With decreasing the reaction temperature, the first order reaction constant  $k$  decreased, but abruptly increased at just below the  $T_c$  followed by further decrease in the activity. The anomalous behavior of this activity should suggest that  $\text{Cu}3d_{x^2-y^2}$  orbital mainly contribute to the superconductivity of the oxide.

#### Reference

- 1) D. A. Dowden, N. McKenzie, B. M. W. Trapnell, Proc. Roy. Soc. London, Ser. A. 237, 245 (1956).

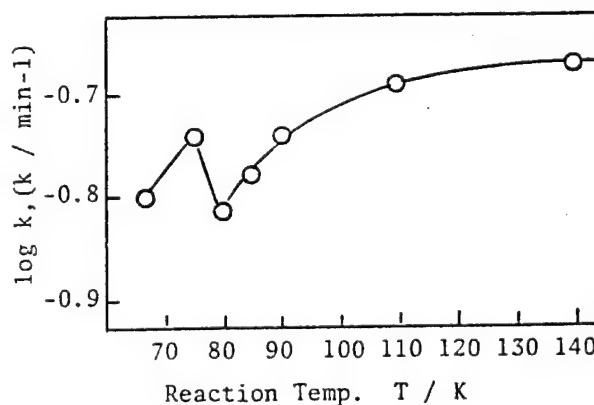


Fig.1 Catalytic activity of  $\text{YBa}_2\text{Cu}_3\text{O}_{6.90}$  for  $\text{H}_2\text{-D}_2$  reaction. ( $\text{H}_2+\text{D}_2 = 1.5 \times 10^{-3}$  Torr)

19-11-06-G

IONIC AND ELECTRONIC CONDUCTIVITY IN OXIDE SUPERCONDUCTORS:  
STUDIES OF THE PROTOTYPE SYSTEMS "YBaCuO" AND "(Bi,Pb)SrCaCuO"

W.Göpel, W.Carrillo-Cabrera, H.D.Wiemhöfer, Ch.Ziegler,  
Th.Bieger, and N.Valverde  
Institute of Physical and Theoretical Chemistry, University of  
Tübingen, Auf der Morgenstelle 8, D-7400 Tübingen, FRG

Both, the ionic and electronic conductivity of oxygen ions was determined in  $\text{YBa}_2\text{Cu}_3\text{O}_{7-x}$ -samples and in Bi-based oxide superconductors at constant partial pressures of oxygen as a function of temperature.

The  $\text{YBa}_2\text{Cu}_3\text{O}_{7-x}$  samples were sintered in air at different temperatures between 875 and 900°C, followed by a further annealing at 425°C for 5-10 h. Related to increasing sintering temperatures, the samples exhibit increasing grain sizes between 1 and 10  $\mu\text{m}$ .

The ionic conductivity was measured by applying a four-probe DC-technique. The electrodes, consisting of the phase sequence  $\text{M}/\text{YBa}_2\text{Cu}_3\text{O}_{7-x}/\text{ZrO}_2(+10\% \text{Y}_2\text{O}_3)$  with  $\text{M}=\text{Pt}$  or  $\text{Au}$  were blocking for electrons.

The oxygen-ion conductivity of  $\text{YBa}_2\text{Cu}_3\text{O}_{7-x}$  changes in air in the temperature range between 300 and 500°C with increasing temperature from  $10^{-5}$  to  $1 \text{ (Ohm cm)}^{-1}$ . From an Arrhenius plot "activation" energies of 2.5-2.7 eV are determined for temperatures above 390°C and slightly lower values of 2.2 eV below 370°C. Comparable values were obtained for Bi-based samples.

For  $\text{YBa}_2\text{Cu}_3\text{O}_{7-x}$ , the ionic conductivity vs. temperature curves shift to lower values with increasing sintering temperature. This can be explained by changes of the nonstoichiometry in the metal sublattice and by contributions from grain boundary transport of ions.

The electronic conductivity vs. temperature curves show the opposite behavior with respect to the influence of sintering temperature and grain size: For larger grain sizes we observe higher electronic conductivity.

The electronic and ionic conductivities are discussed in terms of competing contributions from the bulk and the grain boundaries.

a2

19-11-07-K

DYNAMIC SUPERCONDUCTING SYSTEM BY USING NOVEL SUPERCONDUCTOR

Y. Murakami

Laboratory for Applied Superconductivity, Faculty of Engineering, Osaka University 565 Suita, Japan

Introduction

We have been mainly concerned with small scale SMESs (Superconducting Magnet Energy Storage). Their utilizations are proposed as follows.

(1) Stabilization of Electrical Power Systems by the simultaneous control of active(P) and reactive(Q) power of SMES. Storage capacity: 50 MJ or so.

(2) The same purpose as (1) by using the storage in the field winding of superconducting generator. Storage capacity: Several tens MJ.

(3) The high density storage comparable to batteries. Storage density: Several tens MJ per cubic meter.

The features of these storages are: 1) high density of storage, 2) quick response and fast charge and discharge of the stored energy, and furthermore 3) the operations of power converter and transformer in the same cold environment with the superconducting magnet. Let this system be called Dynamic Superconducting Magnet System and this proposal can be enabled by using the high temperature superconductors.

High Density Storage

The stress in circumferential direction due to magnetic field is proportional to the diameter of solenoidal coil. Hence the small diameter of coil is acceptable for the large density of magnetic field. We propose the configuration as shown by Fig.1, in which long cylindrical coils of small diameter are piled up. The small leakage of magnetic fields can be expected by the alternative directions of magnetomotive forces of the adjacent coils.

The energy density  $48 \text{ MJ/m}^3$  can be obtained by the configuration:  $5 \times 5$  solenoids in the sectional area  $1.0 \text{ m}(\text{width}) \times 1.0 \text{ m}(\text{length})$ , with magnetic field 17 T.

Operation of Total System in the Same Cold Environment

The semiconductor power devices demonstrate excellent characteristics in the liquid nitrogen temperature, which environment is adequate for high temperature superconductors. The average switching loss in repeated pulse drives of a MOSFET shows that the loss in 80 K becomes  $1/4$  that in the room temperature, which is shown by Fig.2.

In the future the superconductor power transistors or thyristors can be expected.

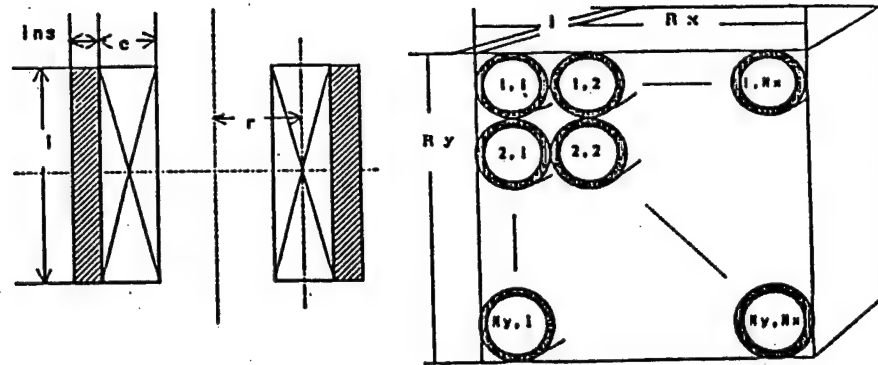


Fig.1 Configuration of high density energy storage

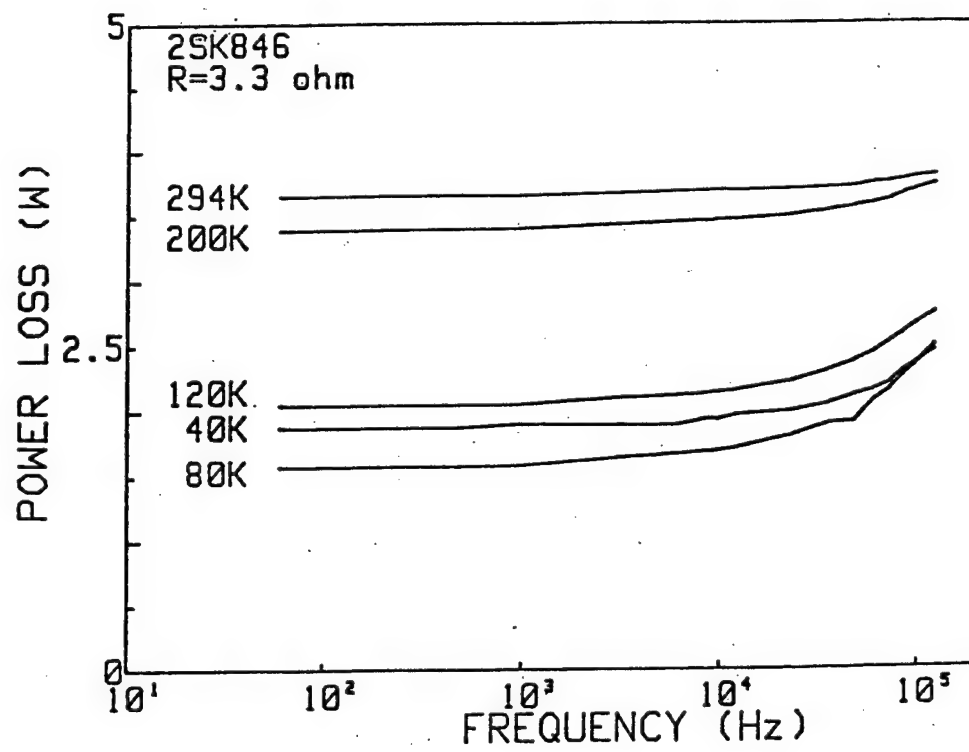


Fig.2 Average switching loss of repeated pulse drive

19-11-08-G

SUPERCONDUCTING PROPERTIES OF  $\text{YBa}_2\text{Cu}_3\text{O}_{7-x}$ -METAL COMPOSITES

N. Imanaka, F. Saito, H. Imai, G. Adachi  
 Department of Applied Chemistry, Faculty of Engineering, Osaka  
 University, Yamadaoka 2-1, Suita, Osaka 565 JAPAN

Metal powder was mixed with a Y-Ba-Cu-O superconductor in order to suppress the nonsuperconducting phase formation and to fill the pores. The effect of the metal addition on the superconducting characteristics was investigated. The mixture of  $\text{Y}_2\text{O}_3$ ,  $\text{BaCO}_3$ , and  $\text{CuO}$  (by molar ratio 0.5:2:3) was pelletized and heated at  $940^\circ\text{C}$  for 5 h in an oxygen flowing atmosphere. The preheated pellets were ground and further mixed with an appropriate amount of Ag powder (purity: 99.9%,  $<44\mu\text{m}$ ). The  $\text{YBa}_2\text{Cu}_3\text{O}_{7-x}$ -metal composites were obtained by sintering the  $\text{YBa}_2\text{Cu}_3\text{O}_{7-x}$ -metal mixture at  $900^\circ\text{C}$  for 5 h in the same  $\text{O}_2$  flowing atmosphere. The electrical resistivity measurement was carried out by a four-probe method. Silver paste was utilized so as to obtain a good contact between lead wires and the sample.  $J_c$  was determined by the existence of a 1  $\mu\text{V}$  potential between the inner wires of the four probes. The distance between them was approximately 4 mm. The temperature was measured with an Au(0.07at%Fe)-Chromel thermocouple. The  $T_c^{\text{zero}}$  dependences on the Ag content is plotted in Fig. 1.  $T_c^{\text{zero}}$  for  $\text{YBa}_2\text{Cu}_3\text{O}_{7-x}$  without Ag, which is denoted as a  $\text{YBa}_2\text{Cu}_3\text{O}_{7-x}$  standard, was 90.5 K. For the  $\text{YBa}_2\text{Cu}_3\text{O}_{7-x}$ -Ag composites,  $T_c^{\text{zero}}$  was almost constant around 91 K. The Ag powder addition to the  $\text{YBa}_2\text{Cu}_3\text{O}_{7-x}$  sintered sample had no obvious effect on the  $T_c^{\text{zero}}$ . Figure 2 shows the  $J_c$  variation with the Ag amount for the  $\text{YBa}_2\text{Cu}_3\text{O}_{7-x}$ -Ag composites. The  $J_c$  for the standard was  $153 \text{ A/cm}^2$ . By the Ag addition to the  $\text{YBa}_2\text{Cu}_3\text{O}_{7-x}$  sample,  $J_c$  greatly increased to  $352 \text{ A/cm}^2$  for  $\text{YBa}_2\text{Cu}_3\text{O}_{7-x}$ -Ag(1wt%), and a maximum  $J_c$  of  $375 \text{ A/cm}^2$  was obtained at the Ag 3wt% addition. This  $J_c$  value was approximately two times as high as that of the standard. The  $T_c^{\text{zero}}$  deviation with the magnetic flux density is presented in Fig. 3 for both the standard and the  $\text{YBa}_2\text{Cu}_3\text{O}_{7-x}$ -Ag(3wt%) composite. For the  $\text{YBa}_2\text{Cu}_3\text{O}_{7-x}$  standard,  $T_c^{\text{zero}}$  was considerably decreased by the magnetic field application.

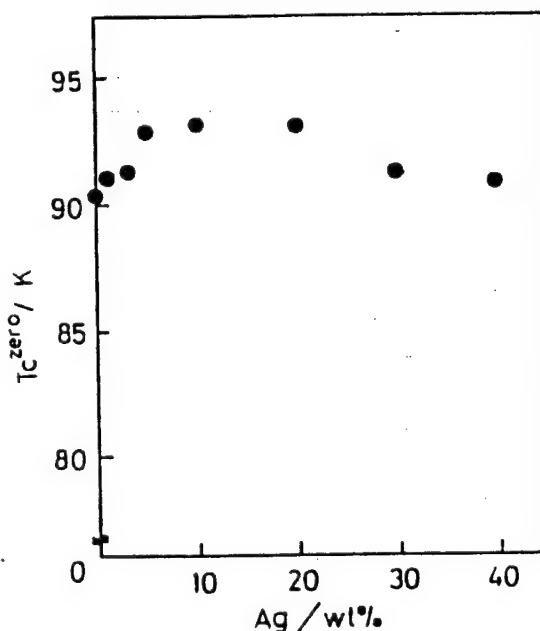


Fig. 1. The variation of  $T_c^{\text{zero}}$  with the mixed Ag wt% for the  $\text{YBa}_2\text{Cu}_3\text{O}_{7-x}$ -Ag composites

$T_c^{\text{zero}}$  for the magnetic flux density between 1500 and 5000 G was near 80 K and that for 6700 G was 77 K. The  $T_c^{\text{zero}}$  decrease with the magnetic flux density for the  $\text{YBa}_2\text{Cu}_3\text{O}_{7-x}\text{-Ag}(3\text{wt}\%)$  composite was not so large as that for the standard.  $T_c^{\text{zero}}$  was still higher than 85 K even at the magnetic flux density of 6700 G. The addition of silver to the  $\text{YBa}_2\text{Cu}_3\text{O}_{7-x}$  sample greatly redresses the problem of the weak link between the grains.

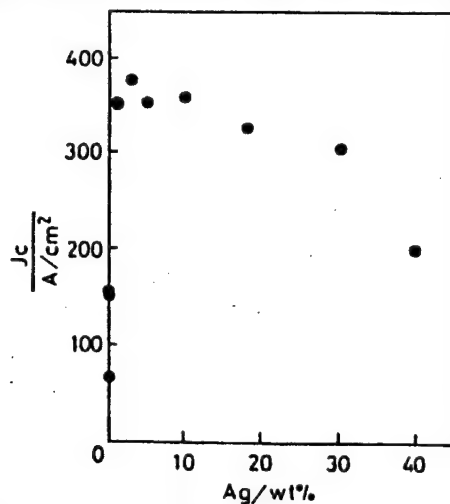


Fig. 2. The variation of  $J_c$  with the mixed Ag wt% for the  $\text{YBa}_2\text{Cu}_3\text{O}_{7-x}\text{-Ag}$  composites

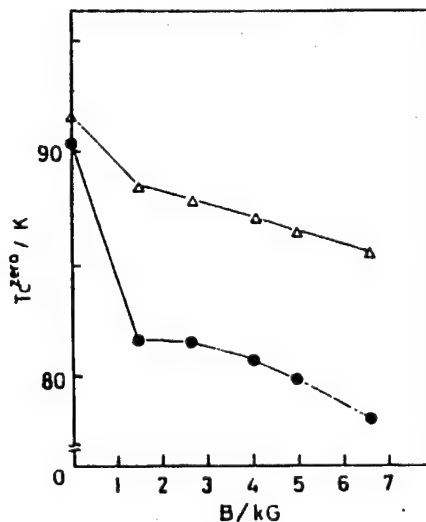


Fig. 3. The  $T_c^{\text{zero}}$  deviation with the magnetic flux density (77K)

- $\text{YBa}_2\text{Cu}_3\text{O}_{7-x}$  standard sample
- △  $\text{YBa}_2\text{Cu}_3\text{O}_{7-x}\text{-Ag}(3\text{ wt}\%)$  composites

(1) N. Imanaka, F. Saito, H. Imai, G. Adachi; Jpn. J. Appl. Phys., 28, (4), (1989), in press.

19-11-09-G

SILVER DOPING INTO THE HIGH-T<sub>c</sub> OXIDE SUPERCONDUCTORS

Y. Matsumoto, J. Hombo, Y. Yamaguchi  
 Department of Applied Chemistry, Faculty of Engineering  
 Kumamoto University, Kurokami 2-39-1, Kumamoto 860

The Ag doping effects on the superconducting properties, the structural and morphological properties of the high T<sub>c</sub> oxide superconductors such as Y-Ba-Cu-O, Bi-(Pb)-Sr-Ca-Cu-O, and Tl-Ba-Ca-Cu-O systems were studied. The crystallization and the c-axis orientation were promoted by the Ag doping, especially for the Y-Ba-Cu-O and the Bi-(Pb)-Sr-Ca-Cu-O systems, although Ag was scarcely substituted for all the cations in the lattice. The resistivities at room temperature decreased by the Ag doping for all the oxide systems. The typical resistivity-temperature curves are shown in Fig. 1 for the Tl-Ba-Ca-Cu-O system. A little high temperature shift of the T<sub>c</sub> and the increase of the J<sub>c</sub> by the Ag doping were observed. The above effects by the Ag doping will indicate that Ag promotes the joining between the grains consist of the high T<sub>c</sub> single phase in the ceramics. By this effect, the T<sub>c</sub> of 104 K was observed for the Bi-Pb-Sr-Ca-Cu-O system, even when the ceramics consist of the 80 K phase and a little amount of the 110 K phase. Moreover, the single phase of the 110 K phase was obtained in this ceramics sintered in air for 140 hours, if Ag was partially substituted for Ca. Thus, Ag is a very attractive dopant in the improvement of the superconducting properties of the high T<sub>c</sub> oxide superconductors.

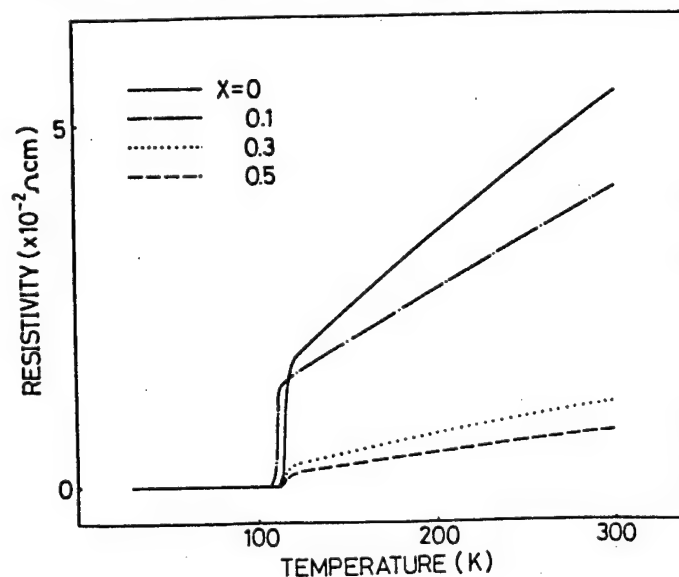


Fig. 1 Resistivity as a function of temperature for Tl<sub>2</sub>Ba<sub>2</sub>Ca<sub>2</sub>Cu<sub>3</sub>O<sub>y</sub>.Ag<sub>x</sub>

19-11-10-K

LOW TEMPERATURE GROWTH AND STRUCTURE OF  $\text{YBa}_2\text{Cu}_3\text{O}_{7-x}$  EPITAXIAL THIN FILM

Y. Bando

Institute for Chemical Research, Kyoto University, Uji, Kyoto-fu 611, Japan

Many studies have been made on the fabrication of the high-quality thin films of  $\text{YBa}_2\text{Cu}_3\text{O}_{7-x}$  (YBCO). Particularly, in-situ growth of the epitaxial thin film at low temperatures is apparently needed to fabricate the superconducting thin film device such as Josephson tunnel junction and the high- $T_c$  thin film with a thickness below 2000Å because the interdiffusion between the film and another oxide at high temperatures is crucial. This paper presents the recent information on the crystal growth, structure and properties of the single-crystal thin films of YBCO, prepared at low temperature. A high quality film also provides a sample for elucidating the fundamental superconducting physics.

In-situ growth of YBCO at low temperatures has been achieved by reactive evaporation with activated oxygen, reactive sputtering and laser evaporation. We succeeded in fabricating, for the first time, the single-crystal thin film of YBCO below 600°C by activated reactive evaporation [1]. The films grown on  $\text{SrTiO}_3(100)$  are the single-crystal with the c-axis perpendicular to the substrate surface and have the superior superconduction properties such as the high- $T_c$  of 86~90K, the  $J_c$  (at 77K) of  $4 \times 10^6 \text{ A/cm}^2$ , the high  $H_{c2}$  and the low resistivity of  $63 \mu\Omega \cdot \text{cm}$  at  $T_c(\text{onset})$ . Studies on the angular resolved ultraviolet photoemission spectroscopy and the magnetoresistance using the single-crystal thin films have brought some new physical information.

The film was deposited on a single-crystal at around 600°C with incorporation of oxygen by coevaporating three metals from the separate sources using deposition system, as shown in Fig. 1. The oxygen pressure at the substrate can be kept at  $10^{-1} \sim 10^{-2}$  Torr by flowing oxygen gas near the substrate, and the background pressure remained  $10^{-5}$  Torr. Oxygen plasma was generated by RF discharge. The typical overall deposition rate is 4Å/s. The as-grown films were oxidized below the growth temperature in oxygen gas above 200 Torr in the deposition chamber.

X-ray examination of the 1000Å-thick film revealed that the c-axis of YBCO was perfectly perpendicular to the  $\text{SrTiO}_3(100)$  face and the film consisted of microdomains whose structure was orthorhombic. An orienta-

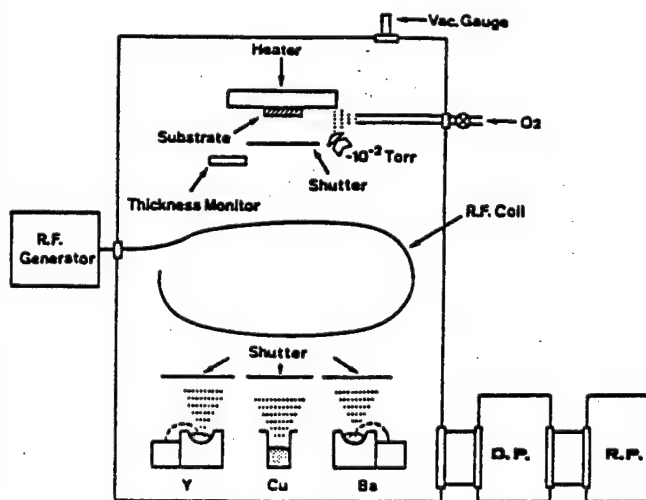


Fig. 1 Deposition system



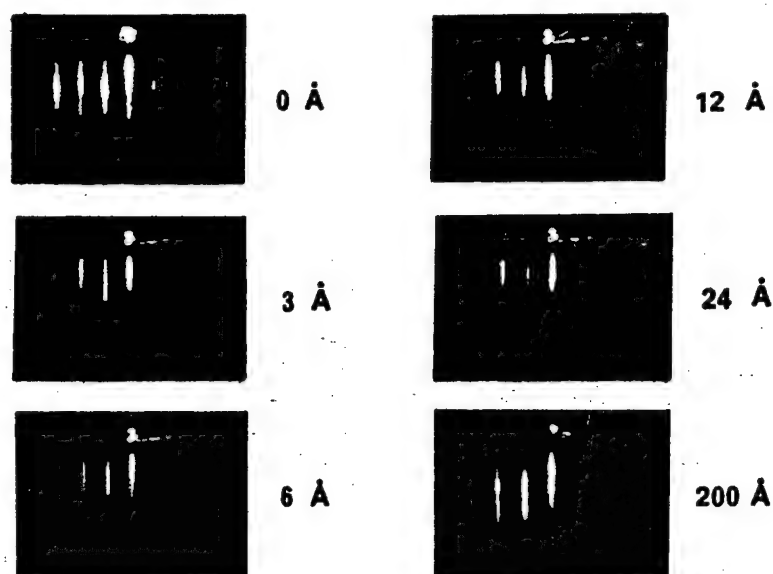


Fig. 2 In-situ RHEED patterns observed during growth of YBCO on (100)  $\text{SrTiO}_3$

tion relationship of a-axis at right angles may be formed between adjacent domains. The surface properties have been investigated by means of RHEED, low energy electron diffraction (LEED) and Auger electron spectroscopy (AES). We could not observe any other elements except Y, Ba, Cu and O by AES measurement for a film exposed to air. The peak due to carbon or both carbon and chlorine were frequently observed for our films. However, the carbon contaminant could be removed by heating the film in an oxygen atmosphere. A sharp LEED pattern of (1x1) from the (001) face of YBCO with a low background guaranteed the good crystalline order at the surface of film. We can prepare a 100Å-thick film with  $T_c(R=0)=82\text{K}$ . This suggests that the growth of YBCO occurs in the layer-by-layer manner. The in-situ RHEED observation during deposition is one of the most effective method for investigating the growth manner.

Figure 2 shows in-situ RHEED patterns of a growing film on  $\text{SrTiO}_3(100)$ , where the electron beam is parallel to the [100] direction of  $\text{SrTiO}_3$ . The thickness is monitored by a quartz oscillating sensor located near the substrate. One atomic layer of YBCO crystal corresponds to a thickness of about 2Å. The pattern at an initial stage of 3Å is the sharp streaks which remain until 200Å. This suggests that the deposit of YBCO on  $\text{SrTiO}_3$  occurs in the layer-by-layer growth manner. RHEED observation was also demonstrated that deposition on  $\text{MgO}(100)$  occur in the same growth manner. The in-plane lattice spacing of YBCO at an initial deposition has the same value as  $\text{MgO}$ . When the thickness came to above 12Å, the spacing drastically converted to the value of tetragonal YBCO.

[1] T. Terashima, K. Iijima, K. Yamamoto, Y. Bando; H. Mazaki. Jpn. J. Appl. Phys., Vol. 27 (1988) L91.

19-11-11-G

## EFFECTS OF STRUCTURE ON THE SUPERCONDUCTIVITY OF Bi-Sr-Ca-Cu-O FILMS.

S. Nagai\*, N. Fujimura, T. Ito

\*Graduate school, University of Osaka prefecture,  
College of Engineering, University of Osaka Prefecture,  
Mozu-umemachi. Sakai, Osaka, 591, Japan

Recently, Maeda et al. discovered a new superconducting Bi-Sr-Ca-Cu-O system without rare-earth (R.E.) elements.<sup>(1)</sup> This system is superior to the R.E.-Ba-Cu-O system such as Y-Ba-Cu-O system, in the superconducting transition temperature,  $T_c$ . The Bi-Sr-Ca-Cu-O films are expected to have great advantages for the device application. In this system, two different superconducting phases with  $T_c \sim 80\text{K}$  and  $T_c \sim 110\text{K}$  have been found. The superconducting phase with  $T_c \sim 80\text{K}$  has a stoichiometric composition of  $\text{Bi}_2\text{Sr}_2\text{Ca}_1\text{Cu}_2\text{O}_x$ . The phase with  $T_c \sim 110\text{K}$  has a stoichiometric composition of  $\text{Bi}_2\text{Sr}_2\text{Ca}_2\text{Cu}_3\text{O}_x$ . Moreover, there is a  $\text{Bi}_2\text{Sr}_2\text{Cu}_1\text{O}_x$  phase showing semiconductor-like behavior in the temperature dependences of resistivity. In this paper, we report the effect of substrate temperature on deposition ( $T_s$ ) and annealing time on the structure, composition and superconductivity of the Bi-Sr-Ca-Cu-O films.

Bi-Sr-Ca-Cu-O thin films were deposited by a rf magnetron sputtering onto the (100) MgO single crystal substrate kept at  $250^\circ\text{C}$  and  $400^\circ\text{C}$ . The powder of Bi-Sr-Ca-Cu-O was used as the target with a diameter of 77 mm. The powder was made by calcining, sintering and grinding the mixture of  $\text{Bi}_2\text{O}_3$ ,  $\text{SrCO}_3$ ,  $\text{CaCO}_3$  and CuO powders. Calcining and sintering were performed at  $800^\circ\text{C}$  for 10 h and  $870^\circ\text{C}$  for 10 h, respectively. Nominal target composition of Bi:Sr:Ca:Cu was 1.3:1.0:1.0:2.0. The applied rf power was 100 W. The mixture of argon and oxygen (1:1) was used as the sputtering gas, and the pressure was kept 1.33 Pa during the deposition. The grown films were always annealed at  $870^\circ\text{C}$  in air. The composition of samples was determined by X-ray photoemission spectroscopy (XPS). The XPS measurement was performed after 5 min etching with argon ion beam (4 KV, 25 mA) in  $2 \times 10^{-5}$  Pa to remove the contamination at the surface. The structures of the samples were studied by X-ray diffraction (XRD) method. The surface condition of the samples were observed using a scanning electron microscopy (SEM). The resistivity was measured by a standard four-probe method.

The films deposited below  $400^\circ\text{C}$  are amorphous and insulating. The composition of Bi-Sr-Ca-Cu-O film deposited at  $250^\circ\text{C}$  and  $400^\circ\text{C}$  were 2.0:2.4:1.9:5.0 and 2.0:3.1:2.4:6.2, respectively. Figure 1 shows the temperature dependences of resistivity for different  $T_s$  and annealing time. In the sample deposited at  $400^\circ\text{C}$  and annealed for 0.5 h (Sample A) and the sample deposited at  $250^\circ\text{C}$  and annealed for 1.0 h (Sample C), resistivity reaches zero at 80 K and 60 K, respectively. In the sample deposited at  $250^\circ\text{C}$  and then annealed for 0.5 h (Sample B) and for 5 h (Sample D), resistivity does not reach zero at 60 K. A slight resistivity drop at 115 K is observed for sample D. XRD analysis identified most of their structure

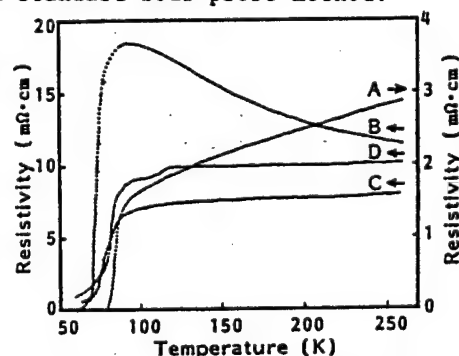


Fig.1. Temperature dependence of resistivity for Bi-Sr-Ca-Cu-O films.

consist of the  $\text{Bi}_2\text{Sr}_2\text{Ca}_1\text{Cu}_2\text{O}_x$  phase (80 K phase), with a highly c-axis oriented structure. The results of XRD analysis indicate that sample B contains small amount of  $\text{Bi}_2\text{Sr}_2\text{Cu}_1\text{O}_x$  phase (semiconductor-like phase), sample A, C and D hardly contain semiconductor-like phase, and sample D contains a small amount of  $\text{Bi}_2\text{Sr}_2\text{Ca}_2\text{Cu}_3\text{O}_x$  phase (110 K phase). Figure 2 shows the surface morphologies observed in SEM. Sample B, C and D, particularly B and D have lower density and more cavities comparing to sample A. Moreover, sample D has a needle-like structure. The low density may enhance the transportation problems at grain-boundary junctions, resulting in the degradation of the superconductivity.

Figure 3 shows composition of targets, as deposited films and annealed films (0.5 h). On deposition, a large amount of Bi and a small amount of Ca are lost. As Ts become high, the decrement of Bi becomes larger. On annealing, a large amount of Cu is lost, particularly in the sample with high Ts. The annealed sample B is with composition of 2.0:2.0:1.6:3.6, and consists of a large amount of  $\text{Bi}_2\text{Sr}_2\text{Ca}_1\text{Cu}_2\text{O}_x$  phase (80 K phase) and a small amount of  $\text{Bi}_2\text{Sr}_2\text{Cu}_1\text{O}_x$  phase (semiconductor-like phase). This means that sample B contains excess Ca and Cu atoms. The existence of this excess Ca and Cu also results in degradation of superconductivity. The annealed sample A is with composition of 2.0:2.1:1.4:2.8 and most of structure consists of  $\text{Bi}_2\text{Sr}_2\text{Ca}_1\text{Cu}_2\text{O}_x$  phase (80 K phase). Even sample A, with a good superconductivity has a small amount of excess Ca and Cu atoms, probably as  $\text{Ca}_2\text{CuO}_3$  and CuO.

In conclusion, annealing for a long period is effective to produce the high- $T_c$  phase, however, it causes surface roughness and growth of needle-like structure, resulting in the degradation of the superconductivity. Samples deposited at higher Ts shows better superconductivity, than those deposited at lower Ts.

#### References

- (1) H.Maeda, Y.Tanaka, M.Fukutomi and T.Asano: Jpn. J. Appl. Phys. 27 (1988) L209

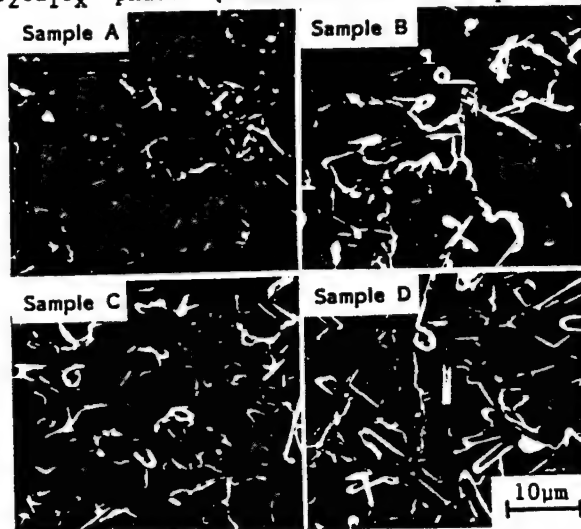


Fig.2. SEM photographs for annealed samples.

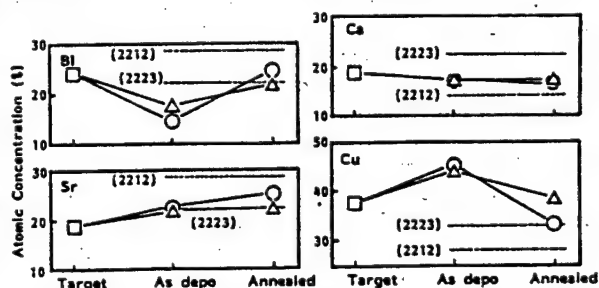


Fig.3. Atomic concentration (A.C.) measured by XPS. Square shows the A.C. of the target. Triangle and circle show the A.C. of the samples Ts 250°C and 400°C, respectively. Dotted lines show the A.C. of  $\text{Bi}_2\text{Sr}_2\text{Ca}_2\text{Cu}_3\text{O}_x$  phase (2223) and  $\text{Bi}_2\text{Sr}_2\text{Ca}_1\text{Cu}_2\text{O}_x$  phase (2212).

18-11-01-K

THE SOL-GEL PROCESSING OF ELECTROCERAMICS

D. A. Payne  
Department of Materials Science and Engineering,  
University of Illinois at Urbana-Champaign  
Urbana, IL, 61801, USA

Recent developments in the sol-gel processing of electrical ceramics are reported. Particular attention is paid to the low temperature synthesis of dielectric materials by polymeric alkoxide precursors. Examples are given for  $\text{LiNbO}_3$  and  $\text{PbTiO}_3$  based systems. Factors governing the chemical synthesis and structure-property relations are discussed. Emphasis is placed on a novel processing route, which avoids powders, for the fabrication of thin-layer dielectrics (0.1 - 1.0  $\mu\text{m}$ ) on semiconductors. The processing temperatures are sufficiently reduced for the integration of devices on silicon or gallium arsenide. Data are reported for the evolution of structure, through hydrolysis and condensation reactions, and thermal treatments. NMR and FTIR measurements were used to monitor the molecular nature of the precursors through the sol-gel transition. Crystallization behavior was characterized by non-isothermal DSC analysis. Data are reported for the electrical and optical properties of the thin-layer dielectrics. Emphasis is placed on the non-linear ferroelectric response characteristics for capacitors integrated directly onto silicon devices.

Acknowledgements: Collaboration with K. D. Budd,\* S. K. Dey,\* D. J. Eichorst,+ R. W. Schwartz\*.

Supported by DOE DMS\* and NSF ERC+.

18-11-02-G

## Texture and Photochromic Characteristics of ZnOx thin films.

N.Fujimura, T.Nishihara\* and T.Ito

\*Graduate school: University of Osaka Prefecture  
 Metallurgical Engineering, College of Engineering  
 University of Osaka Prefecture  
 Mozu-Umemachi, Sakai, Osaka 591 Japan

Zinc Oxide piezoelectric films have been applied to ultrasonic devices for bulk acoustic waves as well as surface acoustic waves in VHF and UHF ranges, because ZnO has a low dielectric constant and a large electromechanical coupling factor among nonferroelectric crystals. Several techniques have been developed to deposited the films since the early works in 1965(1). Especially, there are many investigations about highly (002) orientated films by RF magnetron sputtering. There is no report about highly (110) orientated films on glass.

In this conference, the influence of the deposition parameters on texture of ZnOx films(especially highly (110) orientated films) will be reported. Moreover, the photochromism by X-ray irradiation will be discussed.

ZnOx films were deposited by a rf magnetron sputtering method. A pressed disk of ZnO was used as the target. Corning 7059 was used as the substrates. The sputtering conditions were; rf power of 100W and gas pressure of 6 mTorr and the gas composition (Ar:O<sub>2</sub>) was changed extensively. The structural change of prepared ZnOx films was evaluated by X-ray Diffraction (XRD), X-ray Photoelectron Spectroscopy (XPS) and Reflection of High Energy Electron Diffraction (RHEED). The electrical resistivity and the optical transmittance spectra in visible radiation were measured by using conventional four probe system and spectra photometer, respectively.

ZnOx films deposited on Corning 7059 without heating substrates were evaluated by X-ray diffraction. The sputtering gas composition dependence on preferred orientation of films are shown in Fig.1. The (002) or (110) orientated films were obtained by controlling gas compositions.

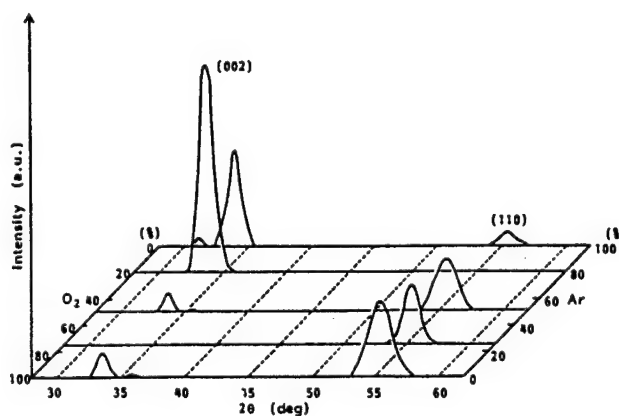


Fig.1. The gas composition dependence on preferred orientation.

Generally, the increasing of the substrate temperature( $T_s$ ) on deposition promotes the highly oriented films. In this study, however, although the highly (002) oriented films were obtained at higher  $T_s$ , the (110) oriented films could not be obtained at above 300 °C. The (110) oriented films can be formed under low  $T_s$  and the suitable  $O_2$  partial pressure. As the  $T_s$  is raised, the (110) peak disappeared and the (002) peak become strong. But, when the excellent (110) oriented films deposited without heating substrate are post-annealed, the (110) preferred orientation is kept and become stronger with increasing annealing temperature(Fig.2).

$ZnO$  has a layered structure, called Wurtzite type. Only Zn or O atoms exist in the each (002) plane, while, both Zn and O atoms exist in the (110) plane alternately, that is, there is no Zn-Zn bonding toward the <002> direction. Therefore, during deposition at high  $T_s$ , as the metallic bonding can not exist because of high vapor pressure of Zinc, the films may grow toward only the <002> direction.

By the way,  $ZnO_x$  films are darkened by X-ray irradiation. The optical transmittance at visible radiation decreases after X-ray irradiation(Fig.3), but the change of band gap was not observed. This darkened film returns by annealing, which is called photochromism. This may be caused by the F center. The degree of darkness by X-ray irradiation was not almost influenced by the difference of orientation.

XPS analysis was performed to investigate the change in composition and valence electron state during X-ray irradiation and annealing in vacuum. Those results indicate that, there is little volume change of oxygen defects introduced by X-ray irradiation. And, the increment of adsorbed surface oxygen is observed for both the X-ray irradiated sample and annealed one, that results from the diffusion of interstitial oxygen from the inside to the surface. This causes the relaxation of lattice strain.

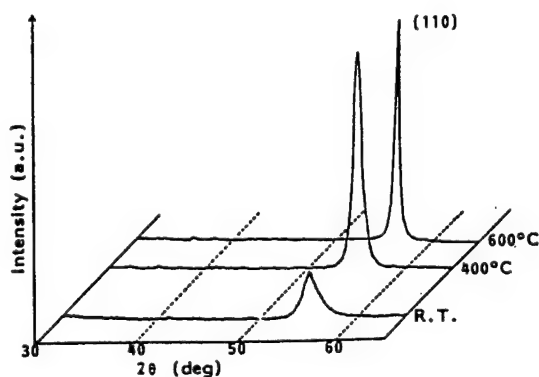


Fig.2. Effect of the annealing temperature on the texture formation.

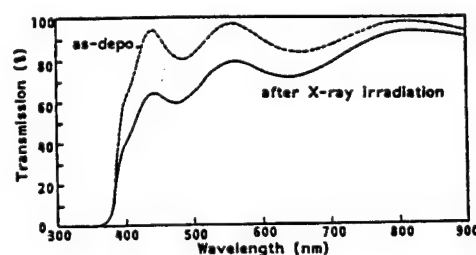


Fig.3. The optical transmittance at visible radiation.

(1) S.Wanuga, T.A.Midford and J.P.Dietsi; Ultrasonic Sympo., I-6, Dec.(1965)

18-11-03-G

## FORMATION OF YTTRIA STABILIZED ZIRCONIA FILM BY PLASMA MOCVD

Osamu Matsumoto, Nobuhiro Oka, Isao Ono, and Haruo Uyama  
 Department of Chemistry, Aoyama Gakuin University,  
 Chitosedai, Setagaya-ku, Tokyo 157, Japan

The powder of yttria stabilized zirconia (YSZ) had been prepared and sintered bulk YSZ was found to be an ionic conductor at high temperatures. However, the formation of thin film of YSZ was only prepared by sputtering [1]. We have carried out the deposition of thin film of YSZ from the mixture of tetraacetylacetonato zirconium (IV)  $((C_5H_7O_2)_4Zr)$  and trisdipivaloylmethanato yttrium (III)  $((C_{11}H_{19}O_2)_3Y)/O_2$  plasma prepared using microwave discharge.  $(C_5H_7O_2)_4Zr$  (v.p.:130Pa, at 360K) and  $(C_{11}H_{19}O_2)_3Y$  (v.p.:1300Pa at 420K) were heated to 400K and 380K, respectively, and the respective vapor was carried with oxygen into the oxygen plasma prepared using microwave discharge at a pressure of 400Pa. The fused silica substrate was placed in the discharge tube set in the cavity. The temperature of the substrate was 670K. The deposition was carried out for 1 h, after which the deposit was further heated in the atmosphere for 1 h at 1270K. The sample as deposit as well as after heating were characterized by means of X-ray diffraction, XPS, and SEM observation. The electrical conductivity of the both samples was measured by the DC four probe method. The thickness of the deposited film was estimated to be about 3  $\mu m$  using weight gain and density.

In scanning electron micrograph, plate like patterns were observed in the both samples as deposit and after heating. In the sample after heating, a grain was enlarged. The sample as deposit was identified as cubic YSZ by X-ray diffraction method as compared with bulk sample of YSZ. After heating for 1 h at 1270K, every diffraction line sharpened. In the X-ray diffraction patterns, the line due to (200) plane grew as compared with that in bulk YSZ. Thus the deposit strongly oriented along the a plane. This is supported by SEM observation.

The binding energies of electrons due to constituent elements are given in Table 1, as compared with those of bulk YSZ. The values in the both samples, as deposit as well as after heating, are approximately same. Thus the composition would not change with heating. These values are also correspond with those of  $ZrO_2$  and  $Y_2O_3$ , respectively. The concentration of  $Y_2O_3$  in the solid solution is estimated to be about 12 mol % from the relative ratio of peak areas of  $Zr3d_{3/2}$  and  $Y3d_{3/2}$  electrons.

Table 1 Binding energies of  $Zr3d$  and  $Y3d$  electrons of the samples as deposit and after heating comparing with those of bulk YSZ

Electron	Binding energy (eV)		
	As deposit	After heating	Bulk YSZ
$Zr3d_{5/2}$	184.4	184.2	184.1
$3d_{3/2}$	186.8	186.7	186.5
$Y 3d_{5/2}$	159.0	159.4	159.2
$3d_{3/2}$	161.2	161.5	161.1

The electrical conductivity of the deposit on the substrate was measured from 770K to 1270K. As the conductivity ( $\sigma$ ) increased with increasing

temperature, the dependence of the conductivity on reciprocal temperature for some samples is shown in Fig. 1. The  $\sigma$  of the sample as deposit was considerably low and the straight line was only obtained between 920K and 1120K. After the heating of the deposit at 1270K for 1 h, the straight line was obtained between 820K and 1270K and the value of  $\sigma$  was approximately same to that in the literature [2]. However, the value was slightly smaller than that of bulk YSZ measured at same time. The activation energy for the electrical conduction is estimated from the gradient of the line in Fig. 1. The activation energies for samples are given in Table 2. The activation energy of the sample as deposit was 1.45 eV and it changed to 0.85 eV after heating and the corresponds to that of bulk YSZ. In conclusion, the thin film of yttria stabilized zirconia was obtained by the MOCVD method assisted by the microwave discharge.

By the further heating of the deposit at 1270K for 1 h, the grain growth was observed and the electrical conductivity of the deposited film increased and the activation energy for electrical conduction decreased.

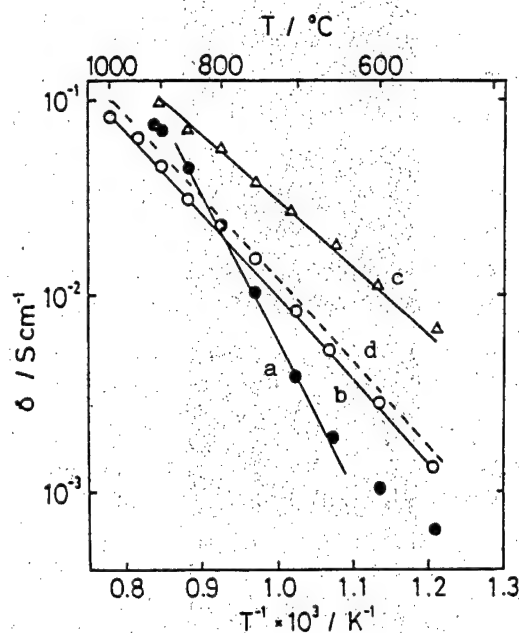


Fig. 1 Temperature dependence of electrical conductivity of some samples  
a: as deposit, b: after heating of a,  
c: bulk YSZ, d: bulk YSZ in ref. 2.

Table 2 Activation energy for electrical conduction of some samples of YSZ

Sample	Activation energy (eV)	Temperature range (K)
As deposit	1.45	920 - 1120
After heating	0.87	820 - 1270
Bulk YSZ	0.76	820 - 1170
Ref. 2	0.87	870 - 1270

- [1] N. Nakagawa, C. Kuroda, and M. Ishida, *Denki Kagaku*, **57**, 215 (1989).  
 [2] A.I. Ioffe, M.V. Inozemtsev, A.S. Lipilin, M.V. Perfilev, and S.V. Karpachov, *Phys. Stat. Sol. (a)*, **30**, 87 (1975).



18-11-04-G

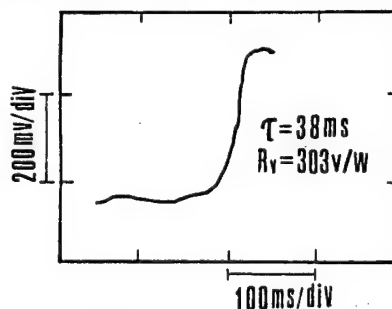
INFRARED-SENSITIVE SiC FIBER THERMISTOR

N. Muto, M. Miyayama and H. Yanagida

Research Center for Advanced Science and Technology, University of Tokyo

4-6-1 Komaba, Meguro-ku, Tokyo, Japan 153

The importance of Silicon Carbide(SiC) in electrical applications has increased due to its thermal durability and semiconducting nature. In our previous experiment [1], it was found that the SiC fiber behaves as an n-type semiconductor and shows NTC resistance-temperature characteristics with stable reproducibility. The response time is one of the important characteristics of thermistors for infrared-ray sensing. Fast response with time constant of a few tens ms is required for detection of moving heat source. Since the thermal time constant is proportional to the heat capacity of thermistor material, the fibrous thermistor with a small volume is expected to have a fast response. Commercial SiC fibers(Nicalon) manufactured by Nippon Carbon Co., Ltd. were used for SiC-fiber thermistor. The fibers are synthesized from an organo-silicon polymer, and consist of cubic  $\beta$ -SiC, and an excess carbon and oxygen of totally 10~25 at %. The diameter of SiC fiber is ranged 8~20  $\mu$ m. Thermal response against infrared ray from black body furnace(600k) was measured for SiC-fiber thermistor. Irradiation energy was 51mW/cm<sup>2</sup> at the thermistor position. A change in output voltage of the electric circuit was measured with an amplifier (x100) and an storage scope. A typical change of output voltage by infrared ray is shown in fig.1, where horizontal and vertical divisions are 100 ms and 200mV, respectively. Thermal time constant  $\tau$  and responsivity  $R_v$  of SiC single fiber(resistivity 24  $\Omega$ cm) were  $\tau$ =38 ms and  $R_v$ =303v/w, respectively. On the contrary, those for randomly arranged SiC yarn(200 fibers with resistivity 4.1k  $\Omega$ cm) were  $\tau$ =286 ms and  $R_v$ =4.7v/w, respectively. In such a yarn, fibers are partially stacked and hence effective heat (light)-receiving area is smaller than its surface area. By using single SiC fiber with adequate resistivity and diameter, faster response and larger responsivity will be expected.



[1]N. Muto, M. Miyayama and H. Yanagida, Fig.1. A change of output voltage by in-  
J. Ceramic Soc. Japan, 97, 403-05(1989). -frared ray in SiC-fiber thermistor

18-11-05-G

# CHARACTERIZATION OF TRAP CENTERS IN SEMICONDUCTING CERAMICS BY ICTS

T. Maeda and M. Takata

Department of Electrical Engineering, Nagaoka University of Technology,  
Nagaoka, Niigata 940-21

ZnO varistors have highly nonlinear current-voltage characteristics. This nonohmic behavior can be explained in terms of the double Schottky barriers formed in the vicinity of ceramic grain boundaries. The double Schottky barriers are formed by electrons trapped in the interface states which are compensated by ionized shallow donors and donorlike traps (bulk traps) within the depletion layer (Fig. 1). Therefore, the characterization of interface states and bulk traps is important in clarifying the varistor behavior. So far, various techniques were employed for that purpose, such as the measurement of thermally stimulated current (TSC method), admittance spectroscopy or deep level transient spectroscopy (DLTS) etc. However, they have not satisfactory results of interface states except for the DLTS [1]. We applied isothermal capacitance transient spectroscopy (ICTS) [2] to ZnO varistor. In this technique, the capacitance transient response is measured under isothermal conditions, which is similar to the DLTS with regard to the measurement of transient capacitance.

Samples were prepared by a conventional ceramic method. ZnO (purity 99.99%) and two additives of 0.5 mol%  $\text{Bi}_2\text{O}_3$  (purity 99.99%) and 0.5 mol%  $\text{MnO}_2$  (purity 99.9%) were mixed for 2 h using an agate mortar in ethanol. The mixture was dried and calcined at  $780^\circ\text{C}$  for 2 h. Then, calcined powder was ground for 2 h using an agate mortar in ethanol and dried. The powder was pressed into discs and sintered at  $1150^\circ\text{C}$  for 2 h

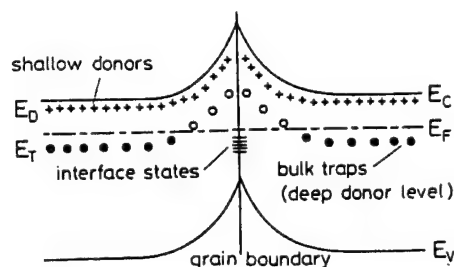
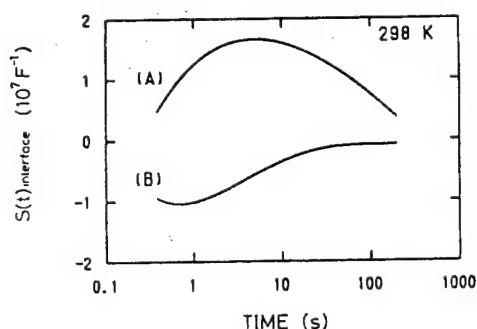
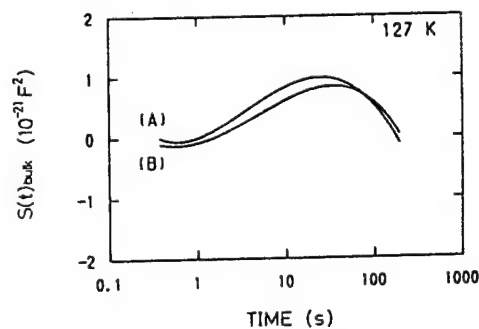


Fig. 1. Electron energy level diagram for a ZnO-ZnO grain boundary.



(a)



(b)

Fig. 2. Bias voltage dependence of ICTS signal of ZnO varistor at (a) 298 K and (b) 127 K; (A): after applying 10 V for 30 s under zero bias state and (B): after applying 0 V for 30 s under -10 V bias state.

in air. Both sides of the sintered discs were polished. The shaped samples were 0.5 mm thick and 8 mm in diameter. Aluminum electrodes of 6 mm diameter were deposited on either side of the samples by vacuum evaporation. ICTS measurement was carried out using impedance analyzer (YHP-4192A) which was connected to a calculator by a GP-IB interface. The measurement frequency was 1 MHz. ICTS signal is defined as  $S(t) = tdf/dt$ , with  $f(t) = -(1/C(t) - 1/C(\infty))$  (interface states) or  $f(t) = C_2(t) - C_2(\infty)$  (bulk traps). Here,  $f(t)$  is described by  $f(t) \propto \exp(-t/\tau)$ , where  $\tau$  is the time constant of thermal emission at deep levels.  $S(t)$  has a minimum or maximum value at  $t = \tau$ . The time constant is the exponential function of trap centers below the conduction band edge. Therefore the trap level is obtained from the slope of the Arrhenius plot. For comparison with the ICTS method, admittance spectroscopy was performed using an impedance analyzer.

ICTS signals were detected in the temperature ranges 277 to 326 K (room temperature range) and 121 to 153 K (lower temperature range). Figures 2(a) and 2(b) show the bias voltage dependences of ICTS signals in the room temperature range and in the lower temperature range, respectively. Here, (A) denotes ICTS signals after applying a voltage of 10 V for 30 s under a zero bias state and (B) the signal after applying a zero voltage for 30 s under a -10 V bias state, respectively. In Fig. 2(a), signal (A) has a positive peak and signal (B) has a negative peak, which suggests that the detected trap is an acceptor type of interface state. In Fig. 2(b), the ICTS signal is independent of bias voltage. Since the bulk traps exist in both sides of grain boundaries, the emission and capture of electrons occurred simultaneously when the applied voltage was changed. Therefore, the detected level can be attributed to bulk traps.

Figure 3 shows Arrhenius plots calculated from peaks. The depth of trap levels below the conduction band edge is estimated from the slope in Fig. 3. We calculated the trap levels of 0.60 eV from the detection peak series at around room temperature and 0.27 eV from those in the lower temperature range, respectively. Furthermore, the latter result corresponds with that from admittance spectroscopy.

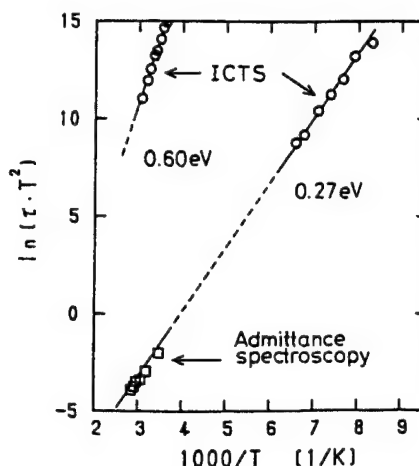


Fig. 3. Arrhenius plots of  $\ln(\tau \cdot T^2)$  vs  $1000/T$ .

- [1] K. Tsuda and K. Mukae; IECEJ Technical Report CPM86-29 (1986) 27
- [2] H. Okushi and Y. Tokumaru; Jpn. J. Appl. Phys. 19 (1980) L335

18-11-06-G

EVALUATION OF SOME AMORPHOUS METAL ELECTRODES FOR ALKALINE ELECTROLYSIS: STANDARD VERSUS NOVEL TECHNIQUES

M.I. Ismail\*, M.A. Daous\*, G. Kreysa\*\*

\* Chemical Engineering Department, King Abdulaziz University,  
P. O. Box. 9027, Jeddah 21413, Saudi Arabia.

\*\* Dechema-Institute, Theodore-Hevess-Allee 25, 600  
Frankfurt/M. 97, W.Germany.

Several amorphous alloys were previously evaluated for hydrogen and oxygen evolution in alkaline media by Kreysa et al [1,2] using standard electrochemical techniques (steady state polarization and cyclic voltametry). These alloys were used here to evaluate the suitability of using novel techniques based on the transient response to short heat and DC pulses for evaluating these electrodes. These new methods are, fast, economic and suitable for in-situ measurements.

EXPERIMENTAL: Some of the amorphous metal samples which were previously evaluated by Kreysa et al [1] were used to measure their response to short heat and DC pulses. The transient heat transfer data (response to short heat pulses) were generated using a thermistor or a thermocouple preheated electrically by a resistor while in contact with the test sample. The heat transfer area was kept constant in all the test trials and the rate of the temperature decay was recorded. The temperature after 10, 20 s from the heat pulse was used for the comparative analysis of turn off time of the various test samples. The response to positive or negative DC pulses (9V for 0.2 s) was used for evaluating these amorphous alloys. The test was performed by contacting parallel copper wire electrodes to a wet separator placed on the test sample. The wetting solution was 0.2 or 1 M KOH electrolyte at room temperature. The open cell voltage (OCV) decay after the short DC pulse was recorded after 10 and 20 s; These times were selected as response signals to compare the various test samples. More details about this novel test methods are available elsewhere [3-5].

RESULTS AND DISCUSSIONS: A) The response to heat pulse data: All experimental conditions were kept constant for all the tested specimens. The amorphous ribbon alloys were tested on their bright surface of the ribbon. The results (temperature after 10 and 20 s from the short heat pulse) showed similar behavior as the standard electrochemical evaluation test of these alloys. Most of the alloys with lower Tafel line slope [1] showed lower temperature signals after 10 or 20 s from the heat pulse. The following alloys 4040 (FeNiMoSiB), 6025(CoFeMoSiB), 0080(NiSiB) G14 and G16 (CoNiSiB) showed lower signals compared to others (G13, G15). Most of such alloys have electrocatalytic activities [1] for Oxygen and hydrogen evolution. The alloy G13 (Cu70 Ti30) which showed maximum  $i_0$  [1] showed also maximum temperature signal compared to other tested alloys.

B) The response to DC pulse data: The signals generated from the measurement of the open cell voltage decay after  $\pm 9V$  DC pulse in wire electrodes contacting separator wetted with 0.2 or 1 M KOH placed on the test specimens showed a general well agreement with the standard electrochemical evaluation of such alloys as reported recently [1]. The alloy G13 showed the minimum level of OCV under all experimental conditions tested on all test alloys. Other alloys showed graduation in rates of OCV decay in a way similar to the change in the electrochemical characteristics of such alloys. It is known that certain electrodes (such as Ni containing electrodes) act as electrocatalysts for oxygen evolution when are covered with spinel oxides [1,6,7]. The formation of mixed oxides and soluble products on DC pulse electrolysis is a possible explanation of the nature of the measured OCV in response to the short (high applied potential, 9V) DC pulse and its correlation to the nature of test samples. The test samples might act as bipolar electrodes in the conventional electrolysis cells which contribute to the measured electrode potential as confirmed experimentally here. The repetition of the DC pulses in the wire electrodes contacting the separator placed on the test samples showed reproducible curves after several cycles which indicates the formation of stable film on the test material. However, no trails were done yet for testing the formation of such a film during the repetition of the DC pulse. The measured OCV after the DC pulse depends on the type of electrode, film deposits and/or reactions during or after the DC pulse. Several possible chemical reactions are reported [1]. The alloy G13 (Cu70 Ti30) showed fast dissolutions on DC pulse application when electrolyte used was sulfuric acid [8].

**CONCLUSIONS:** The measurement of the temperature decay after heat pulse or the open cell voltage after a short DC pulse (9V for 0.2 s) in parallel wire electrodes contacting the amorphous alloys tested correlated well with the standard electrochemical characterization of such alloys using standard test methods. Ranking of electrode materials could be done using the introduced transient techniques (response to short heat and DC pulses).

#### REFERENCES

- [1] G. Kreysa, B. Hakansson, J. Electroanal chem.;
- [2] 201 (1986) 61-83 G. Kreysa, B. Hakansson. P. Ekdunge, Electrochim. Acta, 33 10, (1988)135.
- [3] M. I. Ismail, Novel systems for applied research, CRM Publ., Toronto, 1989 [ISBN 0 921478 003].
- [4] M. I. Ismail, Engineering polymers for high technology application, M. Dekker, 1989 (expected).
- [5] N.A. I. Ahmed, R.S. Al-Ameeri M.I. Ismail, Corrosion-NACE, 44, 10 750 (1988).
- [6] J. Fischer, H. Hofmann, H. Wendt, AIChE J., 26 (1980) 794.
- [7] H. Wendt, V. Plzak, Electrochim. Acta 28 (1983) 27.
- [8] M.I. Ismail, U. Dawood, to be published.

18-11-07-G

## PREPARATION OF CORDIERITE CERAMICS FROM METAL ALKOXIDES

M. Okuyama, T. Fukui, C. Sakurai  
Colloid Research Institute,  
350-1, Ogura, Yahata-Higashi-Ku, Kitakyushu 805 Japan

Cordierite( $2\text{MgO} \cdot 2\text{Al}_2\text{O}_3 \cdot 5\text{SiO}_2$ :MAS) or cordierite-based glass-ceramics are attractive materials for electroceramics, in particular the electronics packaging ceramics, because of their low dielectric constant, low thermal expansion coefficient comparable with that of silicon chips and so on. Low-temperature processing is also very attractive to multilayered substrates, which can be cofired with good conductors such as Cu, Au and Ag-Pd. Recently, sol-gel processing has been applied to prepare cordierite, taking advantage of low-temperature synthesis.

In this study, cordierite powders were prepared by hydrolyzing the modified alkoxide precursors, and the influence of the alkoxide precursors on powder characteristics was investigated. The sinterability and crystallization behavior of obtained powders were also studied, and the mechanical and electrical properties of sintered bodies were measured.

The approach used in this study was to synthesize homogeneous MAS alkoxide precursors which contained three elements by incorporating Al-O-Si ester and magnesium alkoxide.  $\text{SiO}_2$  and  $\text{Al}_2\text{O}_3$  are classified into network-former group in glass structure.

$\text{Si}(\text{OEt})_4$ ,  $\text{Al}(\text{OBu}^s)_3$  and metal magnesium were used as starting materials. As shown in Fig.1,  $\text{Si}(\text{OEt})_4$  was partially hydrolyzed with  $\text{HCl-H}_2\text{O}$  in cold ethanol, and then mixed with the dried ethanol solution of  $\text{Al}(\text{OBu}^s)_3$  for preparing Al-O-Si ester. After refluxing at  $80^\circ\text{C}$  for an hour, metal magnesium was added to the Al-O-Si ester solution and refluxed furthermore for 12 hours. MAS alkoxide precursors obtained were concentrated and diluted in various solvents,

and then hydrolyzed with  $\text{NH}_4\text{OH-H}_2\text{O}$  to make precipitation. The precipitates were filtered, rinsed in solvents, dried at  $100^\circ\text{C}$  and characterized with SEM, particle size analyzer, XRD and TG-DTA. The morphology of precipitates was strongly influenced by the experimental conditions such as added  $\text{H}_2\text{O}$  amount, PH, kinds of solvents and concentration of MAS precursors. MAS precursor solutions tended to make gelation without precipitation when the amount of added  $\text{H}_2\text{O}$  was not sufficient, or precursor concentration was low. The use of higher alcohol to dilute precursor also increased gelation tendency. The amount of  $\text{H}_2\text{O}$  used for partially hydrolyzing  $\text{Si}(\text{OEt})_4$  had remarkable influence on precipitation of cordierite powders. No powder was obtained from MAS alkoxide precursors synthesized with less than 1.5 of  $\text{H}_2\text{O}/\text{Al}(\text{OBu}^s)_3$  ratio, and gelation oc-

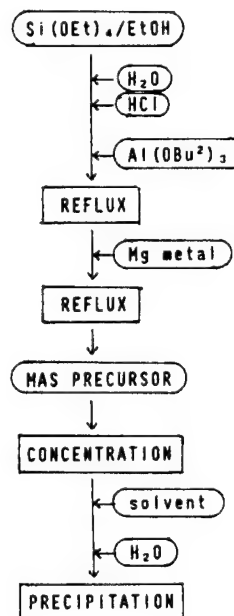


Fig.1 Flow of Precipitation

**a4**

curred. The structure of precursor seemed to be strongly effected by the amount of H<sub>2</sub>O used for synthesizing precursors, according to Ramman spectroscopy results. The obtained powders could be densified below 900°C and crystallized into  $\alpha$ -cordierite at 1050°C. The mechanical and electric properties were measured.

- (1) K.Kondo, M.Okuyama and Y.Shibata, Advances in Ceramics, vol.19, Edited by J.B.Blum and W.R.Cannon, Amer. Cer. Soc. Westerville, OH, 1986 pp.77-87
- (2) C.Gensse and U.Chowdhry, Better Ceramics Through Chemistry, Edited by C.J.Brinker, D.E.Clark and D.R.Ulrich, Mat. Re. Soc., Pittsburgh, Pa, 1986 pp693-703

18-11-08-G

Electronic Materials Using the Energy Barrier Associated with Oxygen

Satoru FUJITSU, Kunihiro KOUMOTO and Hiroaki YANAGIDA  
Department of Industrial Chemistry, Faculty of Engineering, University of  
Tokyo, 7-3-1 Hongo, Bunkyo-ku, Tokyo 113, JAPAN

It is known that ZnO-based varistor and BaTiO<sub>3</sub>-based PTCR thermistor are the electronic materials using the energy barrier along the grain boundary. The energy barrier is formed by the acceptor states at the grain boundary which trap the conduction electrons from the grain. Though the physical origin of the property of such materials is explained by this model satisfactorily, the problem why such an effective acceptor state could be formed has not been clarified yet. Since the property of these materials depends on the atmosphere, especially oxygen, during the preparation, it has been recognized that oxygen played an important role to develop the energy barrier along the grain boundary. In this study, we will discuss the role of the oxygen to develop the energy barrier from the viewpoint of the analogy between oxygen in grain boundary and on the surface.

The non-ohmic characteristics could be observed in porous ZnO whose electrical properties strongly depended on the chemisorbed oxygen and hence surface energy barrier formed. It is also well known that the large PTCR effect is observed in porous BaTiO<sub>3</sub> with chemisorbed oxygen. The chemisorption state of oxygen is attained by trapping the conduction electron on the surface of n-type semiconducting materials as ZnO and BaTiO<sub>3</sub>, that is, the chemisorbed oxygen forms the acceptor state to develop the energy barrier.

The non-ohmic property of a varistor and the large change in the resistivity of a PTCR thermistor disappear when heated in oxygen free ambient, while it is restored when heated in air. If the penetrated oxygen into such materials formed "the quasi-chemisorption state" along the grain boundary, it might be expected that the energy barrier similar to that at the surface with the chemisorbed oxygen should be formed along the grain boundary.

Based on the above assumption, it is possible to estimate the chemical role of the useful additives to modify the property as CoO into a varistor and MnO into a PTCR material. The non-ohmic property of ZnO-Bi<sub>2</sub>O<sub>3</sub> ceramics is modified by doping with CoO. Similar effect of CoO doping was observed in porous ZnO. When CoO was doped into porous ZnO, the non-ohmic coefficient and the barrier height increased. In this material, the amount of the chemisorbed oxygen increased and the high-temperature oxidized state of the chemisorbed oxygen was stabilized at low temperature. The increase in the amount of chemisorbed oxygen (quasi chemisorption state along the grain boundary) means the increase in the acceptor state and the stabilization of the oxidized state means the stabilization of the effective acceptor state.

The common phenomenon in the materials using the energy barrier associated with oxygen is the rapid diffusion of oxygen through the grain boundary. This result might suggest the facile oxidation of the grain boundary region by the penetrated oxygen as the surface by the chemisorbed oxygen.



18-11-09-G

HETERO-CONTACT EFFECTS OF ATMOSPHERE-SENSITIVE CERAMIC SEMICONDUCTOR

M. Miyayama, Y. Nakamura, H. Yanagida

Research Center for Advanced Science and Technology, University of Tokyo  
4-6-1 Komaba, Meguro-ku, Tokyo 113, Japan

Conventional ceramic sensors for combustible gases and humidity utilize a resistance change of ceramic surface, and have several disadvantages such as lacking of gas selectivity, nonlinear sensitivity and resistance shift after a long-term use. The hetero-contact type atmosphere sensors have promising sensing characteristics overcoming such disadvantages.

The hetero-contact is made of two different sintered pellets contacted by mechanical pressure. Since the surface of ceramic materials is rough, the contact area is small and there exists "a space" of 5-20  $\mu\text{m}$  between them. Gas molecules can reach the contact points through this space very easily. therefore, the electrical current flowing across the interface is affected strongly by atmospheric gases.

P-n hetero-contact made by CuO (p-type) and ZnO (n-type semiconductor) shows a I-V characteristics affected by water vapor (humidity). As humidity increases, the current in forward bias (CuO+, ZnO-) increses markedly while the reverse current decreases, as a result, a high rectifying character can be observed. The mechanism of the enhancement of forward current is considered as follows; electron holes are supplied from the p-type semiconductor into physisorbed water at the interface. The protons are transferred to surface of the n-type semiconductor, where electric charges are liberated. This is an electrolysis of adsorbed water enhanced by the p-n contact. Accordingly, a resistance shift due to an accumulation of water molecules is small even after a long-term use. This "self-recovery nature" makes a cleaning at high temperatures unnecessary.

When combustible gases ( $\text{CO}$ ,  $\text{H}_2$ ,  $\text{C}_3\text{H}_8$ ) are introduced to CuO/ZnO contact, the current in forward bias increases. At 260°C, the sensitivity (current with gas/current without gas) of CO gas is 3 or 4 times larger than that of  $\text{H}_2$  and  $\text{C}_3\text{H}_8$ . Such a high CO selectivity is difficult for conventional-type ceramic sensors. Production of  $\text{CO}_2$  by CO oxidative reaction was confirmed by gas composition analysis. An increase in capacitance by CO gas was also observed. Accordingly, charge transfer would be conducted through the following scheme; CO and  $\text{O}_2$  gas molecules adsorb at the interface and ionized.  $\text{CO}^+$  on CuO and  $\text{O}^-$  on ZnO react to produce  $\text{CO}_2$  and are released from the interface. Through these steps, electric current passes only from CuO to ZnO under forward bias.

One of the peculiar aspects of the p-n contact gas sensors is that the gas sensitivity and selectivity can be controlled by changing the applied voltage. This suggests a possibility of electric field control of gas sensing property and oxidative reaction of gas molecules.

The interesting atmosphere-sensing characteristics of hetero-contact arise from the interaction of two different materials and the space gap between them. By searching for other materials system, new atmosphere-sensing phenomena can be expected.

18-11-10-G

HUMIDITY SENSITIVITY OF CaO DOPED YTTRIA

K. Katayama, H. Ousawa, T. Akiba  
 Research & Development Div., Chichibu Cement Co., Ltd.  
 5310 Mikajiri, Kumagaya, Saitama 360  
 H. Yanagida

Research Center for Advanced Science and Technology, University of Tokyo  
 Komaba, Meguro-ku, Tokyo 153

The need for measuring the humidity at high temperatures has been growing. Norby and Kofstad[1] showed that the electrical conductivity of yttria was sensitive to water vapor pressures at 500°C or above although the conductivity was relatively low. They had to prepare yttria samples by hot-pressing because the sinterability of yttria is quite poor. In order to improve the sinterability and to increase the electrical conductivity of yttria, the doping of divalent metal oxide has been studied and CaO was found to be the most effective. Figure 1 shows that the water vapor pressure dependence on the electrical conductivity of 1 mol% CaO doped yttria. The electrical conductivity decreases with increasing the water vapor pressures. This might be attributed to the decrease of electron hole conductivity although the proton conductivity increases with water vapor pressures. The EMF of the same sample is shown in Fig. 2. The deviation from theoretical values might be attributed to both oxygen ion and electron hole conductions. It was found from these results that CaO doped  $Y_2O_3$  might possibly be used as a humidity sensor at high temperatures.

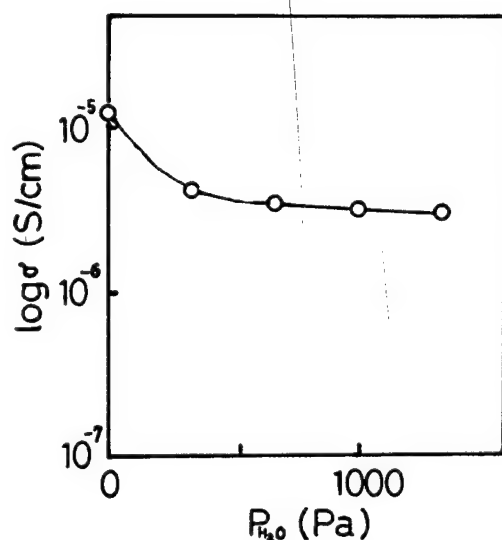


Fig. 1.  $\sigma$  vs  $P_{H_2O}$  of CaO added yttria measured at 600°C

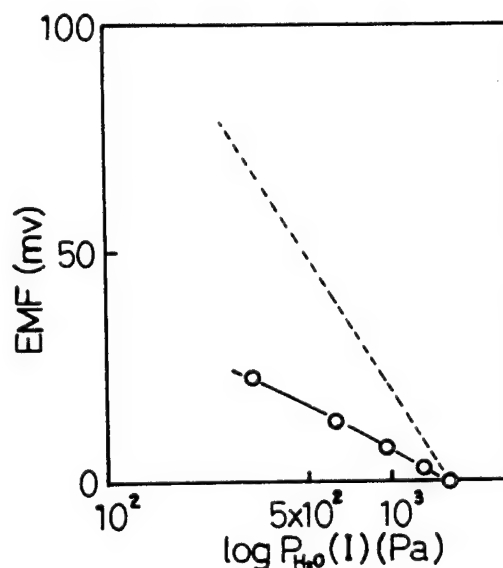


Fig. 2. EMF measured at 600°C

[1] T. Norby and P. Kofstad; Solid State Ionics, vol. 27 (1986) 169

18-11-11-G

# MICROSTRUCTURE AND THE DIELECTRIC PROPERTIES IN $\text{SrTiO}_3\text{-Pb}(\text{Fe,W})\text{O}_3$ BL-TYPE CAPACITORS

M. Kuwabara

Department of Applied Chemistry, Kyushu Institute of Technology,  
Sensui-Cho, Tobata, Kitakyushu, 804 Japan

There have been many studies on semiconducting  $\text{SrTiO}_3$  (STO) base internal barrier layer (BL) capacitors to obtain materials with high performance dielectric properties, i.e., high apparent dielectric constant, low dissipation factor and low temperature coefficient of dielectric constant. The microstructure of conventional STO base BL capacitors can substantially be described as semiconducting large STO grains separated by thin insulating layer consisting mainly of  $\text{PbO-Bi}_2\text{O}_3\text{-B}_2\text{O}_3$  glasses, and the procedure for preparing such STO base BL capacitors has entirely been established so that anyone could easily produce the materials with an apparent dielectric constant of more than 40000 and  $\tan\delta < 1\%$ . Under such situation as this in relation to the STO base BL capacitors the forthcoming of a new type of BL capacitor on the base of a new concept is strongly desired today.

To that end, a preliminary experiment has been made in the present study in an attempt to produce a new type of STO base BL capacitor with ferroelectric  $\text{Pb}(\text{Fe}_{2/3}\text{W}_{1/3})\text{O}_3$  (PFW) as the grain boundary second phase instead of  $\text{PbO-Bi}_2\text{O}_3\text{-B}_2\text{O}_3$  glassy phases in the conventional ones. The STO-PFW BL capacitors were made as follows: Semiconducting STO ceramics were prepared using commercial STO powders and almost the same procedure as described in the literature<sup>1)</sup>. PFW ferroelectric materials were prepared using  $\text{PbO}$ ,  $\text{Fe}_2\text{O}_3$  and  $\text{WO}_3$  as starting materials. Exactly required amounts of the respective materials were well mixed and then calcined at  $870^\circ\text{C}$  for 2h in air to yield PFW. The obtained PFW powders mixed with ethyl cellulose were painted on one surface of a STO sample, and the sam-

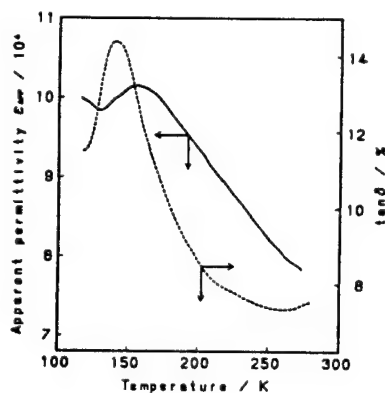


Fig. 1. Temperature dependences of dielectric constant and  $\tan\delta$  of a STO-PFW BL capacitor.



Fig. 2. An SEM photograph of a polished surface of the STO-PFW BL capacitor. Bar=10  $\mu\text{m}$ .

ple was heat-treated at 1160°C for 1h in air to let PFW diffuse into the STO ceramic along the grain boundaries. Electrical measurements were conducted on the obtained STO base BL capacitors with In-Ga alloy rubbed on their both surfaces as electrodes at room temperature down to about 120K.

Figure 1 shows typical temperature dependences of the apparent dielectric constant and  $\tan\delta$  obtained for one of the present STO base BL capacitors. An SEM photograph taken on a polished surface of the sample is given in Fig. 2. From this figure it is obvious that STO grains are covered with crystalline materials, the main phase of which may be confirmed to be PFW by comparing the dielectric constant-temperature characteristic of the present BL capacitor with that of PFW itself (not shown here). An anomalous peak in the dielectric constant-temperature characteristics of the PFW ceramics was observed around 180K, which is associated with the phase transition at the Curie point, just as seen in the characteristic of Fig. 1, though a little difference in the peak temperature of dielectric constant between the two characteristics exists.

1) M. Fujimoto and W.D. Kingery, J. Am. Ceram. Soc., 68, 169-73 (1985).

18-01-01-K

The Alkaline Fuel Cell Program for the European Space Vehicle HERMES  
 (Its possible "Spin-off" on Commercial Fuel Cell Technology)  
 K. Kordesch, Technical University Graz, A-8010, Austria

The European manned space vehicle program HERMES (1) as established by the European Space Agency (ESA), requires a fuel cell system for its electric power supply (Fig.1). It shall produce 3 times 2-6 kW at a voltage between 85 and 120 V. DORNIER System GmbH has performed a feasibility study under contract with ESA (2). Four different alkaline systems have been evaluated and two of the designs are systems with mobile electrolyte. A favorite decision in that direction will constitute the most important difference in fuel cell system concepts compared to the US-Space Shuttle System, which uses an immobile alkaline matrix electrolyte, a separate (static) water removal system and special cooling accessories (3, 4).

In a mobile electrolyte system, the water removal and heat management task can be accomplished within the electrolyte and gas circulation loops. It has not yet been decided which system of the three competing firms will actually win the contract, but the probability is high, that the HERMES Fuel Cell System will be built with a mobile electrolyte system. A big influence on the fuel cell technology on earth is to expect, if one of the three large industrial manufacturer is chosen, which then could become the leader in a commercial low-cost production of fuel cells (5, 6, 7).

The cost of catalysts has played a major role in the past. At the present time, high-performance PTFE-bonded carbon  $H_2$ -electrodes with only 0.2 mg Pt/Pd in the active layer can produce up to 400 mA/cm<sup>2</sup> at very low polarization values (50 mV). Combined with oxygen-air electrodes, carrying a very small amount of gold catalyst with platinum group doping, a cell voltage of over 0.8 V is obtained and kept for many thousands of operating hours. That at least is the state of the space technology. In order to make such cells mass-producible and construct high voltage stacks for industrial or electric vehicle use, the "bipolar" design must be adopted (Fig.2).

The bipolar design avoids current collection from the edges of the electrodes and the resulting non-uniformities of current distribution. The conductive and gas-impervious separation plate between the gas manifolds can be made from extruded or rolled carbon-plastic materials. This is also the way to avoid metal screens or porous metals as carriers in the carbon electrodes themselves, again removing a considerable cost increment. In addition, the elimination of the screens will prolong the life of the PTFE-bonded electrodes, which are easily damaged by the thermal expansion and contraction movements, which in turn introduce a gradual loss of electronic conductivity by gradually wetting the screen-carbon interfaces.

At the Technical University in Graz we study bipolar fuel cell designs and test and compare different production methods. Carbon-plastic plates serve as separation means between the gas manifolds (8). The design is similar to that of the Alstom-Oxy batteries of the early eighties (9).

Special emphasis is given to the investigation of the water- and heat management by the movements of excess gas streams behind the electrodes and removing the reaction water in traps and condensers. The circulation of the hydrogen is done by means of a "jet pump". At temperatures between 80°C and 90° C it is possible to obtain self-regulating steady state electrolyte concentrations between 7 and 14 normal KOH, at current densities between 20 and 200 mA/cm<sup>2</sup> (10). Operation at 3 to 5 bar nearly doubles the output.

b1

#### References:

1. J. Herholz & W. Peeters (ESA, Toulouse) The Hermes Development Programme ESA Bulletin, No. 57, February 1989, pp. 6-16, 1989
2. F. Baron (ESA, Noordwijk), European Activities on Fuel Cells for Space Applications, Fuel Cell Seminar, Long Beach Calif., pp. 255-258 (1988)
3. Assessment of Research Needs for Advanced Fuel Cells. S.S. Penner, Ed., US-DOE/AFCWG, Contract No. DE-AC01-84ER30060, Washington DC, Nov. 1985
4. R.A. Martin, International Fuel Cell Corp., Proceedings of the IECEC-Meeting in Denver, Col., Vol.1, pp. 301-303. Paper No. 889498 (1988)
5. H. Van den Broeck, ELENCO n.v., Belgium, Commercial Development of Alkaline Fuel Cells, CEC-Italian Fuel Cell Work Shop, Taormina, 1987, The Commission of European Communities (CEC), Brussels, 1987
6. 20 kW Fuel Cell System of Compact Design, SIEMENS AG, Report BMFT-FB-T 80-055 to 80-059, 7 parts, 940 pages, Siemens, October 1980.
7. A. Winsel, VARTA Batterie AG, The ELOFLUX Fuel Cell System, DECHEMA Monographie, 92, pp. 1885-1913 (1983)
8. K. Kordesch, Ch. Gruber, J. Gsellmann, P. Kalal, J.C.T. Oliveira, K-H. Steininger, O. Taghezout, G. Winkler and K. Tomantschger, Fuel Cell Research and Development Projects in Austria, Proceedings of the 7 th World Hydrogen Conf, Moscow 1988. Hydrogen Energy Progress-VII, T.N. Veziroglu, ed., Pergamon Press 1988
9. A.T. Emery, Occidental Petroleum Co., and B. Warszawski, Alstom-Atlantique, Fuel Cell Seminar in Tucson, Arizona, pp. P1-9A (1985)
10. K. Kordesch, J. Oliveira, Ch. Gruber and G. Winkler, High-Power Alkaline Fuel Cell System for Electric Vehicles (Hybrid System with Zinc- Bromine Battery). This Meeting, ISE 1989.

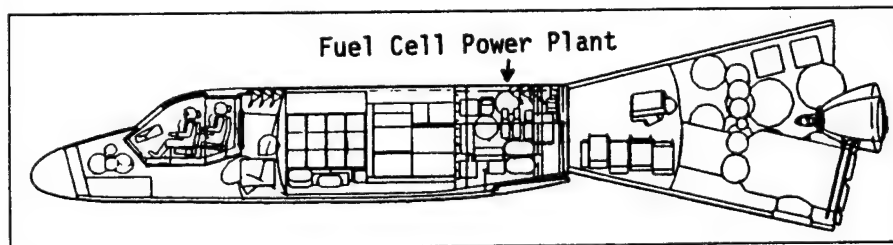


Fig. 1: Configuration of the HERMES Spaceplane, indicating the fuel cell power plant location (Courtesy of ESA/ESTEC).

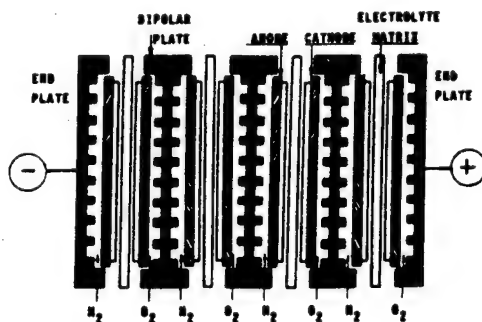


Fig. 2: A sketch of the bipolar Fuel Cell Stack construction used in design studies at the Technical University of Graz, Austria.

18-01-02-G

High-Power Alkaline Fuel Cell System for Electric Vehicles  
(Hybrid System with Zinc-Bromine Battery)

K. Kordesch, J. Oliveira, Ch. Gruber and G. Winkler  
Technical University Graz, A-8010, Austria

Several times in modern fuel cell history electric vehicles with fuel cell systems have been modeled, breadboard-designed and a few were even built and demonstrated in actual service (1, 2, 3, 4).

The General Motors "Electrovan" of the Sixties used a 450 V / 50 kW hydrogen-oxygen fuel cell system with circulating KOH electrolyte, built by Union Carbide Corp. It performed nearly like the gasoline counterpart, but was twice as heavy. Oxygen was used to obtain the needed power (5).

The Kordesch "City Car", a fuel cell hybrid vehicle of the early seventies used a 90 V / 6 kW hydrogen-air fuel cell system and a 20 kW-peak lead-acid battery. It had a range of 300 km and operated 3 years on public roads, but was under-powered (6). The same fate seems to be in store for the 20/40 kW hybrid "Elenco Van", built in Belgium in the early eighties. It is still tested, but the lead-acid battery is too heavy (7). General Electric Co. studied SPE-Fuel cells for automotive applications (8).

Since 1987, a program sponsored by the Department of Energy (DOE) and Department of Transportation (DOT) in the USA has the objective to build a fuel cell/battery powered bus for public transportation (9). The first hybrid models are designed to operate with a phosphoric acid air fuel cell (PAFC) and a nickel-cadmium battery. The fuel shall be methanol, converted on board to hydrogen. Energy Research Corp (ERC) will construct the fuel cell system and the special Ni-Cd battery (10).

However, considering the progress in alkaline fuel cell batteries for space applications (e.g. the "Shuttle") the performance and low weight of alkaline systems can not be reached by any other system (11). Therefore it should be chosen, inspite of the need for a purer hydrogen (which is now available from converters) and the requirement for a CO<sub>2</sub>-free air.

In order to make a fuel cell system mass-producible and suitable for a consumer market, its electrodes must be made without porous metals and with a minimum of noble metal catalysts. This can be done with PTFE-bonded carbon anodes, catalyzed with not more than 0.02 mg Pt/Pd per cm<sup>2</sup> and air-cathodes without Pt-metal catalysts. The construction must be "bipolar" in order to avoid expensive porous metal structures for current collection. This leaves only conductive plastic sheets as carriers for active carbon layers with catalysts. The methods for applying these layers (spraying, rolling, etc.) are common technology (12). Metal screens are expensive and should be avoided as current collectors, because they are damaging the electrodes during thermal cycling. Porous conductive plastic is suitable.

At the Technical University of Graz we are investigating bipolar structures for fuel cells (see the other paper of K. Kordesch at this ISE-meeting). Recently we have studied alkaline systems operating at higher temperatures (up to 120° C) and found excellent performance and reaction water removal properties with PTFE-bonded carbon structures (Fig. 1).

The choice of the secondary battery of the hybrid system should be a Zn-Br<sub>2</sub> battery, due to its light weight and deep discharge capability. The zinc-bromine batteries of S.E.A. in Austria is using a bipolar design and we have now applied active carbon layers, lowering the cost and improving the performance considerably (13).

b1

References:

1. K.V. Kordesch, Power Sources for Electric Vehicles, Modern Aspects of Electrochem., Vol.10, J'OM Bockris, B.E. Conway eds. Plenum Press 1975
2. K.V. Kordesch, "25 Years of Fuel Cell Development" (1951-1976), Jorنال Electrochem. Soc. 125, 77 C - 91 C (1978)
3. B. McCormic, J. Huff, S. Srinivasan, R. Bobbett, Fuel Cells in Transportation, Los Alamos Scientific Laboratory, Report LA-7634, 1979
4. K. Kordesch, "Brennstoffbatterien", Kapitel 8.: Brennstoffbatterien für den Fahrzeugbetrieb, S. 142-169, Springer Verlag, Wien, N.Y., 1984.
5. The General Motors Corp. "Electrovan", Soc. of Automotive Engineers, Papers No. 670176, 670181 and 670182, SAE-Congress Detroit, Jan. 1967
6. K.V. Kordesch, Union Carbide Corp., H<sub>2</sub>-Air/Lead Battery Hybrid System for Vehicle propulsion", J. Electrochem. Soc., 118, 815 (1971)
7. H. Van den Broeck, ELENCO, Commercial Development of alkaline Fuel Cells Fuel Cell Work Shop in Taormina, Italy, Com. Eur. Com., Brussels, 1987
8. Feasibility Study of SPE-Power Plants, Los Alamos National Laboratory, Contract PO 4-L61-38631 IV-1, US-National Research Council, March 1982.
9. S. Romano, Georgetown Univ.: Design Considerations for a F.C./Battery Powered Transit Bus, Fuel Cell Seminar 1988, Long Beach (pp. 296-299.
10. C. Chi, D. Glenn, S. Abens (ERC), PAFC- Battery Powered Bus, Fuel Cell Seminar, Long Beach 1988, Proceedings pp. 365-368, ,
11. R.A. Martin, International Fuel Cell Corp., Proceedings of the IECEC-Meeting in Denver, Col., Vol.1, pp. 301-303. Paper No. 889498 (1988)
12. P. Kalal, K. Kordesch: A new design for a bipolar Fuel Cell Construction Ext. Abstr. 38th ISE Meeting in Maastricht, Vo.2, pp. 792-794 (1987)
13. K. Kordesch, K-H. Steininger, K. Tomantschger, Electric Vehicle Hybrid Consisting of an Alkaline Hydrogen-Air Fuel Cell System and a Zn-Br-Rechargeable Battery, pp. 285-288, Fuel Cell Seminar, Long Beach 1988

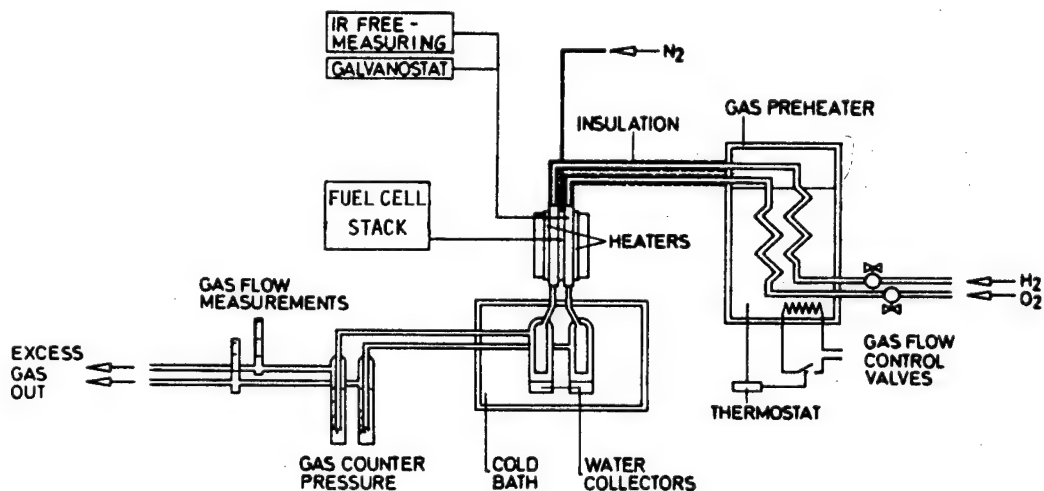


Fig.1: Schematics of the high temperature alkaline fuel cell breadboard test bench at the TU-Graz. The water- and heat management is studied with self-equilibrating KOH electrolyte and excess gas circulation.



18-01-03-K

IN-SITU INVESTIGATION OF FUEL CELL CATALYSTS  
BY SNIFTIRS AND ON-LINE MASS SPECTROSCOPY

W. Vielstich, B. Bittins-Cattaneo and T. Iwasita  
Institut für Physikalische und Theoretische Chemie an der Universität Bonn, Wegelerstr. 12, 5300 Bonn 1

The acidic methanol/air fuel cell is an ideal system for a portable or mobile unit to convert the chemical energy of the fuel methanol into electricity. Up to now many efforts have been made to develop electrocatalysts for methanol oxidation in acid solution. This is a difficult task, because the activity of methanol anodes is usually effected by the formation of poisons and intermediates such as CO or COH. The poisoning results in an increase of the anode potential and hence lowers the terminal voltage of a respective methanol/air fuel cell.

In-situ IR spectroscopy, a relatively new thin layer technique can identify submonolayers of dipoles formed an electrode during adsorption, oxidation or reduction of active species. In order to compensate for the background, a modulation of electrode potential (EMIRS /1/ or Subtractively Normalized Fourier Transform Infra Red Spectroscopy (SNIFTIRS) /2/ is suggested. In this study SNIFTIRS is used to follow the electrocatalysis of fuels like methanol, ethanol or glycol. In stepping the potential from a reference potential in anodic direction, allowing sufficient time to reach stationary conditions, it is possible to study not only the formation of adsorbates but also the occurrence of intermediates and final products of fuel reactions /3,4/. Additional experiments using on-line mass spectroscopy as an independent method support part of the IR result. It is well known that adsorption of methanol or ethanol on platinum results in a strong surface coverage with linearly bonded CO. The amount of coverage depends on electrolyte composition and time of adsorption. At molar concentrations even for potentials at +1200 mV versus RHE, signals for the C=O stretch vibration can be observed suggesting the formation of adsorbed carbon monoxide. This fact could be explained by the assumption that CO is formed also as a reaction intermediate in the course of methanol oxidation to CO<sub>2</sub>. Following SNIFTIRS spectra for different binary and ternary alloys of platinum, suitable catalysts for the oxidation of methanol, ethanol and formic acid in sulfuric acid solution have been found.

- /1/ B. Beden, C. Lamy, A. Bewick and K. Kunitatsu,  
J. Electroanal. Chem., 121 (1981) 343
- /2/ S. Pons, J. Electroanal. Chem., 150 (1983) 495
- /3/ D. Corrigan and M. Weaver, J. Electroanal. Chem.,  
241 (1988) 143
- /4/ T. Iwasita and W. Vielstich, J. Electroanal. Chem.,  
250 (1988) 451

b1

18-01-04-G

**MOLECULAR DESIGN OF A METHANOL FUEL CELL ELECTRODE BASED ON FUNDAMENTAL STUDIES OF THE DIRECT OXIDATION OF METHANOL ON POLYCRYSTALLINE AND SINGLE CRYSTAL PLATINUM ELECTRODES**

C. LAMY, B. BEDEN and J.M. LEGER

Laboratoire de Chimie I, UA au CNRS n°350, Université de Poitiers,  
40, avenue du Recteur Pineau, 86022 POITIERS (France).

The electrochemical oxidation of methanol has been the subject of numerous investigations, due to its possible use in a direct methanol fuel cell (1). However, the design of practical electrodes has failed until now, because of the difficulty to find relatively cheap electrocatalysts, which would be stable and active during long term working of the fuel cell. Indeed the only effective catalytic materials are platinum-based electrodes, which are relatively expensive, and which poison slowly during the course of methanol oxidation.

To overcome these difficulties, our Laboratory has carried out detailed fundamental studies on methanol oxidation at platinum electrodes in order to determine the reaction mechanisms. This can only be achieved through the identification of the adsorbed intermediates, and the analysis of the reaction products and by-products. Powerful surface techniques and analytical techniques were thus developed : Electro-Modulated Infrared Reflectance Spectroscopy (EMIRS), and chromatographic techniques (Gas Chromatography, GC, and High Performance Liquid Chromatography, HPLC). In order to correlate the reaction mechanisms to the electrode structure, different kinds of platinum-based electrodes were used : smooth polycrystalline Pt, platinized Pt, Pt single crystals, Pt modified by foreign metal adatoms (Pb,...) and dispersed Pt.

**RESULTS**

**1 - Identification of the adsorbed intermediates by EMIRS(2)**

The first spectroscopic investigation of the adsorbed species resulting from methanol adsorption was realized by EMIRS, in 1981, which showed unambiguously the presence of adsorbed CO, both linearly-bonded CO<sub>l</sub> (the major species at 2080 cm<sup>-1</sup>) and bridge-bonded CO<sub>b</sub> (a minor species at 1870 cm<sup>-1</sup>) (3). These preliminary results were later confirmed by other investigators (4)(5). Under usual experimental conditions (small surface areas, concentrated methanol solutions, long spectral acquisition times,...) strongly adsorbed CO accumulates at the electrode active sites, thus explaining the self-poisoning of platinum electrodes during long term methanol oxidation.

In order to favor weakly adsorbed species, particularly linearly-bonded to the surface, the amount of adsorbed CO must be decreased. This was realized using either small methanol concentrations (<10<sup>-2</sup> M) or high surface areas (roughness factor >10). The adsorption of 5x10<sup>-3</sup> M CH<sub>3</sub>OH in 0.5 M HClO<sub>4</sub> at a smooth platinum electrode leads to several EMIRS bands, particularly at small adsorption times. Apart from a very small band at 2050 cm<sup>-1</sup> assigned to CO<sub>l</sub>, there are a complex band at around 1700 cm<sup>-1</sup> resulting from a carbonyl group (-COOH, or more probably -CHO), a band at 2340 cm<sup>-1</sup> due to adsorbed CO<sub>2</sub>, bands at around 2940 cm<sup>-1</sup> resulting from C-H stretching modes, a small band at 1640 cm<sup>-1</sup> due to the pending mode δ(HOH) of adsorbed water, and a small band at around 1400 cm<sup>-1</sup> presumably due to

$\delta(\text{C-H})$  of some  $\text{CH}_x\text{O}$  groups ( $x = 1, 2$  or  $3$ ) (6). But after long accumulation times (25 averaged scans) the EMIR Spectrum changes greatly: the intensity of the  $\text{CO}_\text{L}$  band increases markedly, whereas the intensity of the other bands decreases drastically. The adsorption of CO removes the other adsorbed species from the electrode surface, explaining thus the poisoning behaviour of CO and the difficulties to observe reactive intermediates. A similar behaviour was observed with rough platinum electrodes, but for concentration of methanol below  $10^{-1}$  M, the amount of adsorbed CO is greatly reduced at any adsorption time (7).

In order to investigate the effects of the electrode structure on the relative distribution of the adsorbed species, and on the catalytic activity of the electrode surface, the adsorption and oxidation of methanol was investigated on low index platinum single crystals Pt(100), Pt(110) and Pt(111) (8). Cyclic voltammograms, recorded in the spectroelectrochemical cell, show clearly structural effects, since the peak shape and the peak current densities depend greatly on the single crystal plane. EMIR Spectra recorded under potentiostatic control of the electrode display similar structural effects. Three types of adsorbed intermediates are detected:  $\text{CO}_\text{L}$  at  $2070\text{ cm}^{-1}$ ,  $\text{CO}_\text{B}$  at  $1870\text{ cm}^{-1}$  and a formyl-like species  $-\text{CHO}$  at around  $1700\text{ cm}^{-1}$ . But conversely to polycrystalline Pt,  $\text{CO}_\text{L}$  is not the main adsorbed species, except for Pt(110), the behaviour of which is very similar to that of polycrystalline Pt. Blocking and poisoning of the Pt catalytic surface, which occurs during methanol electrooxidation, were thus interpreted in terms of attractive lateral interactions between the different adsorbed CO species. Moreover the behaviour of polycrystalline Pt was computer simulated as the weighted contribution of each single crystal electrode.

## 2 - Analysis of the reaction products by chromatography

A few methods are available for the analysis of reaction products, such as Differential Electrochemical Mass Spectroscopy (9), or Electrochemical Thermal Desorption Mass Spectroscopy (10), and Liquid Chromatography (11)(12). To perform long time electrolysis of methanol on smooth platinum electrodes, a special potential programme was computer synthesized in order to renew periodically the electrode surface by oxidation of the poisoning intermediates. This allowed us to carry out the electrolysis during several hours and days. The reaction products of  $\text{CH}_3\text{OH}$  oxidation on smooth Pt electrodes were identified by HPLC and GC, as  $\text{HCHO}$ ,  $\text{HCOOH}$  and  $\text{CO}_2$ , the latter being the main product (greater than 95 %) (13). By plotting the amount of remaining methanol as a function of the electrolysis time, a first order kinetics law was shown, and the reaction rate constant was evaluated.

Modification of the electrode surface by lead adatoms, or dispersion of the platinum catalysts, greatly improves the selectivity of the reaction towards a total oxidation to  $\text{CO}_2$ , and increases markedly the overall reaction rate constant.

These fundamental results allows us to conceive new methanol fuel cell electrodes, with a reduced amount of platinum, and with a greater resistance to self-poisoning.

## ACKNOWLEDGEMENTS

The authors are very grateful to the Commission of the European Communities for supporting this work (grant n EN3E-0071-F).

b1

#### REFERENCES

- (1) R.S. Cameron, G.A. Hards, B. Harrison and R.J. Potter, *Platinum Metals Review*, 31 (1987) 173.
- (2) B. Beden and C. Lamy, in R.J. Gale (Ed.), *Spectroelectrochemistry - Theory and Practice*, Plenum Press, New York (1988), chap.5, p.189.
- (3) B. Beden, A. Bewick, K. Kunimatsu and C. Lamy, *J. Electroanal. Chem.*, 121 (1981) 343.
- (4) K. Kunimatsu, *J. Electroanal. Chem.*, 140 (1982) 207.
- (5) B. Beden, F. Hahn, S. Juanto, C. Lamy and J-M. Léger, *J. Electroanal. Chem.*, 225 (1987) 215.
- (6) B. Beden, F. Hahn, J-M. Léger, C. Lamy and M.I. Dos Santos Lopes, *J. Electroanal. Chem.*, 258 (1989) 463.
- (7) B. Beden, F. Hahn, C. Lamy, J-M. Léger, N.R. de Tacconi, R.O. Lezna and A.J. Arvia, *J. Electroanal. Chem.*, (1989), in press.
- (8) B. Beden, S. Juanto, J-M. Léger and C. Lamy, *J. Electroanal. Chem.*, 238 (1987) 323.
- (9) J. Willsau and J. Heitbaum, *J. Electroanal. Chem.*, 161 (1984) 383.
- (10) S. Wilhelm, T. Iwasita, H.S. Bushmann and W. Vielstich, *J. Electroanal. Chem.*, 229 (1987) 377.
- (11) K.I. Ota, Y. Nakagawa and M. Takahashi, *J. Electroanal. Chem.*, 179 (1984) 179.
- (12) M. Shibata and S. Motoo, *J. Electroanal. Chem.*, 201 (1986) 151.
- (13) E.M. Belgsir, H. Huser, J-M. Léger and C. Lamy, *J. Electroanal. Chem.*, 225 (1987) 281.

18-01-05-G

## THE 40TH ISE MEETING

ELECTROCATALYTIC OXIDATION OF ALCOHOLS ON NON PRECIOUS CATALYSTS  
SUCH AS MIXED CARBIDES OF TUNGSTEN AND MOLYBDENUM

G. BRONOEL\*

G. LECLERCQ\*\*

R. ROUGET\*\*\*

E. MUSEUX\*

L. LECLERCQ\*\*

S. BESSE\*\*\*

\* LEI/CNRS, 1 place Aristide Briand, 92190 MEUDON (FRANCE)

\*\* Laboratoire de Catalyse Hétérogène et Homogène, UNIVERSITE DES  
SCIENCES ET TECHNIQUES DE LILLE-FLANDRES-ARTOIS, UA 402, Cité  
Scientifique, 59655 VILLENEUVE D'ASCQ (FRANCE)

\*\*\* SORAPEC, 192 rue Carnot, 94124 FONTENAY-SOUS-BOIS CEDEX (FRANCE)

Mixed tungsten and molybdenum carbides have been studied as catalysts for the oxidation of alcohols in sulfuric acid. These carbides were tested as received or deposited on carbon (active carbon -  $900 \text{ m}^2.\text{g}^{-1}$  - or carbon black -  $270 \text{ m}^2.\text{g}^{-1}$ ). In order to determine the relation being in their electrocatalytic activity and their composition, it was necessary to measure exactly the active surfaces of the different materials prepared. These measurements have been made for the carbon supported catalyst by CO adsorption in gaseous phase and for the non supported catalyst by electrochemical oxidation in cyclic voltametry.

Different tests have been made in N sulfuric acid with M ethylen glycol and M methanol, at temperatures between 20 °C and 90 °C. The electrodes were prepared with small amounts of catalyst, totally wetted by the electrolyte and in order to reduce the superficial oxides, were primary

b1

submitted to a cathodic polarization. The steady state polarization curves show that in these conditions the electrochemical reaction is not limited by transport of reactives.

The polarizations made without alcohol show a slight oxidation current of carbides at potential inferior to 550 mV/RHE ; so, the curves obtained for the oxidation of methanol and ethylen glycol were corrected of these values.

From the different results ( $I = f(E)$  curves), one can say that there is an interaction adsorption-transfer which limitates the kinetic of the reaction.

The curve showing the current density of alcohol oxidation (calculated from the measures of active surface) vs the  $\frac{Mo}{V+Mo}$  values of different

materials shows a maximum at 50-50 ratio for the ethylen glycol and at lower ratio for the methanol. Moreover, one can observe an increase of these current densities at + 550 mV/RHE when the temperature reaches 90 °C (by 5 for EG).

Finally, one can say that, even at 90 °C, the oxidation currents of methanol remain weak (2  $\mu A/cm^2$  at 550 mV/RHE for the most active material). These results are in agreement with the results obtained during the tests of PTFE bonded electrodes prepared from the mixed carbides  $C Mo_{0.5} W_{0.5}$  deposited on carbon (0,9  $m^2/g$  electroactive surface). The catalyst weight deposited (C + carbides) was around 50  $mg/cm^2$  and the apparent current density was 1  $mA/cm^2$  at potential + 550 mV/RHE.

So the use of these materials as substitutes of platinum commands to develop their intrinsical catalytic activity and to increase their specific surfaces by the improvement of the preparation method.

GB/MF-15 mars 1989

18-01-06-G

THE ELECTROCATALYTIC OXIDATION OF SOME ORGANIC ACIDS ON METAL/NAFION ELECTRODES

O. Enea, D. Duprez

Laboratoire de Chimie 4, UA 350 CNRS, Université de Poitiers  
40, avenue du Recteur Pineau, 86022, POITIERS, FRANCE.

Metal/Nafion electrodes have proved very efficient for the electrocatalytic oxidation of alcohol vapors [1],[2],[3],[4], but none of these metallized membranes has yet been used to study the electrooxidation of organic acids.

Formic acid, the simplest and most reactive of them, presents a considerable interest in fuel cell applications. A very large number of publications (exhaustively reviewed in ref. [5]) describes the behavior of formic acid and of formate ions on the surface of small area electrodes: pure metals (Pt, Au, Rh, Pd, Ir, Ag,...), alloys (Pt+Au, Pt+Rh, Au+Pd, Pt+Pd,...), or metals covered with adatoms like Tl, Pb, Bi, Cd, Hg, Sn, Sb, Ge,...

The electrocatalytic oxidation of oxalic acid has been described in several papers (reviewed in ref. [6]), as a function of the nature of the electrode material and of the solvent. Surprisingly, in 0.5 M H<sub>2</sub>SO<sub>4</sub>, the polarization curves were similar for platinum and for gold electrodes. It is however generally established that gold is not so efficient as platinum when the dehydrogenation occurs during the adsorption of the organic compounds and if the electrooxidation proceeds with the participation of an active form of the adsorbed oxygen, like OH<sup>ads</sup>.

Both formic and oxalic acids are hardly oxidized on Au electrodes in alkaline media, while the reverse is true for alcohols, which are not oxidized at all in acidic media. The amount of OH<sup>-</sup> (or H<sup>+</sup>) ions present in the bulk of the solution governs, through the protolytic equilibria, the superficial concentration of the electroactive species, and plays a major role in the electrooxidation of organics on small area electrodes. Consequently, when the electrode is surrounded by only one solution, it can be difficult or even impossible to optimize the concentration of the electroactive species.

In contrast, an optimum concentration of reactants can be matched more easily in the case of a metallized membrane used as working electrode at the limit between two compartments containing solutions with different compositions.

The aim of the present study is to investigate these possibilities for the electrocatalytic oxidation of formic and oxalic acids, and of their anions on a porous metallic film formed by small gold particles deposited on one side of a Nafion membrane.

In some experiments, the counter compartment, containing the counter electrode and the Luggin capillary of the reference electrode, was filled with 1M KOH. In other experiments, the supporting electrolyte was a solution of 1M H<sub>2</sub>SO<sub>4</sub>. In both cases, the metallic film was facing the working compartment in which the organic species were introduced.

b1

The influence of pH value in the working compartment on the oxidation currents greatly depends on the solution introduced in the counter compartment:

- the oxidation of formic and oxalic acids in the working compartment occurs only in acidic solutions ( $\text{pH} < 5$ ) if 1M KOH is the counter electrolyte;

- the pH range in which the electrocatalytic oxidation of the investigated acids and of their anions occurs is extended up to pH 12.5 if the counter compartment is filled with 1M  $\text{H}_2\text{SO}_4$ .

By using an appropriate concentration of each reactive species in the counter and working compartments separated by a metallized membrane it becomes possible to reach, under potentiostatic conditions, their optimal mixing and to avoid the inhibition of the oxidation process by the formation of inactive oxides on the surface.

#### REFERENCES

- [1] M. Nakajima, H. Kita; *Electrochim. Acta*, 33 (1988) 531.
- [2] J. Wang, H. Nakajima, H. Kita; *Electrochim. Acta*, in press.
- [3] O. Enea; *J. Electroanal. Chem.*, 235 (1987) 393.
- [4] O. Enea; *J. Electrochem. Soc.*, 135 (1988) 1601.
- [5] R. Parsons, T. VanderNoot; *J. Electroanal. Chem.*, 257 (1988) 9.
- [6] Yu. B. Vassiliev, S.A. Sarghisyan; *Electrochim. Acta*, 31 (1986) 645.



18-01-08-G

## Development of Air-cooled Phosphoric Acid Fuel Cell

Haruo Suzuki

Tokyo Electric Power Co., Engineering Development Center  
1-3, Uchisaiwai-cho 1-chome, Chiyoda-ku, Tokyo 100, Japan

Masahiro Ide, Nobuyoshi Nishizawa, Osamu Tajima, Akira Hamada  
Sanyo Electric Co., Ltd. Fuel Cell Project Team  
100 Dainichi Higashi-machi, Moriguchi-shi, Osaka 570, Japan

Introduction

The phosphoric acid fuel cell generation system is a candidate for a new generation system which would be made practical. One of the key points for realizing this system is to establish the stability of the cell performance over a long period. The sintering and dissolution of electrode catalyst causes the deterioration of cell performance. The wetproofing of the electrode also has an influence on cell life. The relationship between these factors and cell life was examined to improve durability of the cell performance.

Sintering and dissolution of platinum in the electrode

Sintering and dissolution of platinum in the electrode were evaluated by hot acid treatment. Three different types of carbon black were used as the catalyst support. Table 1 shows results for the sintering and dissolution test. The increase in particle size was restrained to some degree by using heat treated types as the catalyst. However, the dissolution was accelerated by using the heat treated types.

Acid volume in the electrode

The existence of excess phosphoric acid in the electrode accelerates the sintering and dissolution rate as Table 1 shows. Therefore, PTFE content of the electrode was controlled to optimize the wetproofing of the electrode. Fig.1 shows the relationship between PTFE content and amount of the acid in the electrode using type A catalyst support. An approximate estimate of the relationship is shown by the following equation:

$$V(x) = -0.44x + S \quad [V(x): \text{acid volume in the electrode}]$$

where x indicates PTFE content and S indicates the constant determined from specific surface area of catalyst support. Table 2 shows the result of the cell generation test. The decay rates of cells depend on the PTFE content and the decay rate was minimized in the case of 50wt% PTFE content. From these results, the optimized amount of the acid in the electrode was estimated at 8-11mg/cm<sup>2</sup> in the case of cells using type A. The electrode using type B and type C were optimized in the same way.

The cells generation test was conducted for 10,000H using optimized electrode. The dissolution of platinum in every electrode was restrained to a very small amount. However, the increase in the particle size still occurred.

The dissolution of the electrode catalyst can be restrained to control the wetproofing of the electrode. After this, the sintering must be improved to realize the long life fuel cell.

b1

Table.1 Pt size and Pt loading in oxygen electrode

Catalyst	initial Pt size	Hot acid treatment ( float on electrolyte )		Hot acid treatment ( electrolyte limited )	
		Pt size ( Å )	Pt loading ( mg/cm <sup>2</sup> )	Pt size ( Å )	Pt loading ( mg/cm <sup>2</sup> )
A type	30	195	0.15	103	0.20
A' type	40	123	0.05	52	0.07
B type	28	550	0.05	109	0.22
B' type	30	500	0.03	128	0.02
C type	35	---	---	250	0.16

initial Pt loading ; 0.5 mg/cm<sup>2</sup>

Hot acid treatment condition; 190°C, 1000h, Air, OCV

Table.2 decay rate of cells for A type

PTFE content wt%	Cell performance mV, IR-free	Decay rate mV/1000h
20	696	550.0
30	688	12.5
40	681	7.5
50	670	5.0

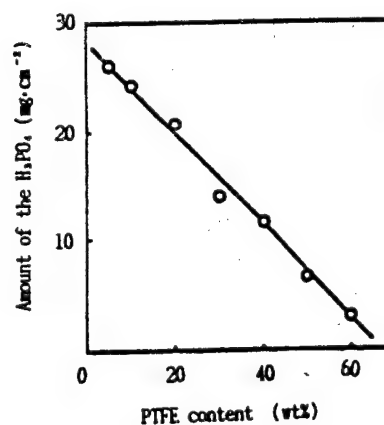


Fig.1 The relationship between PTFE content and amount of the acid in the electrode.

18-01-09-G

Improvements in Performances for Phosphoric Acid Fuel Cell  
Cathodes Using Thinner Electrode Substrates

M. Inoue, H. Fukui, K. Miwa  
Toray Industries, Inc.,  
3-3, Sonoyama 3-chome, Otsu-shi, Shiga, 520 JAPAN

M. Watanabe  
Yamanashi University,  
Takeda 4-3, Kofu-shi, Yamanashi, 400 JAPAN

P. Stonehart  
Stonehart Associates, Inc.,  
P.O.Box 1220, Madison, CT 06443 USA

Porous carbon paper is used as the electrode substrate for phosphoric acid fuel cell (PAFC) electrodes. By thinning the carbon paper, both the height and weight of the PAFC stack can be reduced. In addition, improvements in electrical and thermal conductivity are achieved.

In order to improve the performances of gas-diffusion electrodes for PAFC, we have also studied gas-diffusion in cathodes by the use of thinner carbon substrates for the electrodes.

Carbon papers in a series of thicknesses made from PAN based carbon fiber (Toray Ind., Inc.) were wet-proofed with FEP and fabricated into conventional gas-diffusion electrodes with supported platinum (Japan Engelhard, Inc.) or supported platinum alloys (TKK, Inc.) on carbon blacks. The electrocatalyst layers were loaded at  $0.5\text{mg-Pt}/\text{cm}^2$ . The cathode performances for the reduction of  $\text{O}_2$  and air were measured at  $190^\circ\text{C}$  in  $105\% \text{H}_3\text{PO}_4$  using a half cell, by attaching a ribbed graphite plate to the back of electrode in a similar way to that reported previously [1].

An example of IR free cathode performance is shown in Fig.1. A remarkable diffusion overpotential appears at high current density and the potential deviates from Tafel line at a constant current density when air is used as the reactant. This deviation from the Tafel line by the cathode performance is attributed to a gas-diffusion overpotential ( $\eta_{\text{diff}}$ ) and indicates both the influence of electrode substrate and diffusion losses in the electrocatalyst layer on the cathode performance.

Some examples of the relationship between the thickness of electrode substrate and the diffusion overpotential ( $\eta_{\text{diff}}$ ) are shown in Fig.2. The  $\eta_{\text{diff}}$  increases with increasing thickness of the electrode substrate. When the thickness is extrapolated to zero, the extrapolated value ( $\eta_0$ ) is considered to be the diffusion overpotential in the catalyst layer, independent of thickness of the electrode substrate. On

b1

the other hand, the overpotential in the substrate ( $\eta_s$ ) is evaluated by the equation,

$$\eta_s = \eta_{diff} - \eta_o.$$

This is directly proportional to the thickness of the electrode substrate. It is clear that polarizations in the substrates are strongly dependent on the thickness and are reduced by decreasing thickness, e.g. 5.4mV for every 0.1mm at 350mA/cm<sup>2</sup> and 60% air utilization.

The diffusion overpotential in the catalyst layer  $\eta_o$  is dependent on current density, e.g. 29mV at 200mA/cm<sup>2</sup> and 47mV at 350mA/cm<sup>2</sup>, so there are still significant gains to be made by reducing the the diffusion overpotential further.

[1] M. Watanabe, S. Motoo, Nippon Kagaku Kaishi, No.8(1988)1308

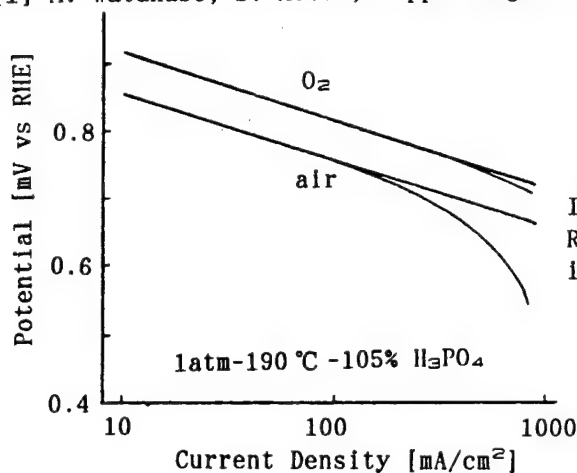
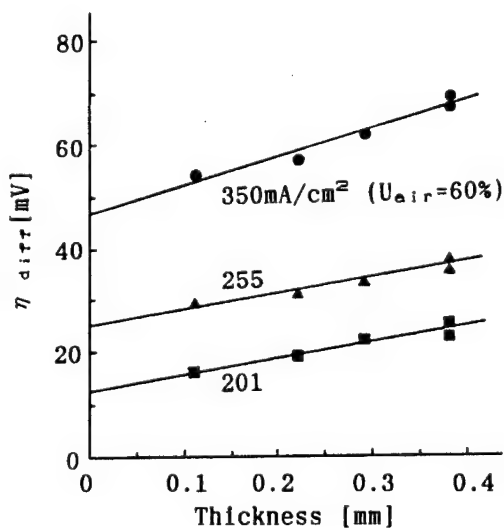


Fig.1.  
IR Free Polarization Curves for  
Reduction of O<sub>2</sub> and Air at 190°C  
in 105% H<sub>3</sub>PO<sub>4</sub>

Fig.2.  
Relationship Between the Thickness of  
Electrode Substrate and the Diffusion  
Overpotential ( $\eta_{diff}$ ) in Cathodes at  
a Series of Current Densities and Air  
Utilization



18-01-11-G

INFLUENCE OF ACID OCCUPATION ON PERFORMANCE OF PAFC GAS-DIFFUSION CATHODES

N. Giordano\*, E. Passalacqua\*, V. Recupero\*, M. Vivaldi\*, E.J. Taylor\*\* and G. Wilemski\*\*

\* Institute CNR-TAE - Via S. Lucia - MESSINA (ITALY)

\*\* PSI, Technology Co Andover

Phosphoric acid fuel cell (PAFC) technology has greatly advanced to the stage of large scale units. A critical component of this technology is the porous gas diffusion electrode typically fabricated from carbon supported Pt electrocatalysts. The performance of a porous gas diffusion electrode is determined by a number of highly interrelated factors, i.e. pore structure, electrolyte content, surface area, transport phenomena and electrode kinetics. Great interest has been paid to basic and mechanistic aspects [1-2], to the Pt crystallite size and orientation effects [3-4] but little attention to the morphological-wettability characteristics of the electrodes. In the present paper, we present the results of a study of the morphological and absorptive characteristics of a series of cathodes made with varying TEFLON contents (20-60%), sintering temperature (320°-360°C), and a constant Pt loading of 0.5 mg Pt/cm<sup>2</sup> and the correlation with electrochemical performance. The "as prepared" electrodes were characterized in terms of percentage acid occupation (PAO) and in terms of their electrochemical performance in air and oxygen in 98% phosphoric acid at 170°C. As anticipated in a previous paper [5] the electrochemical activity on both air and oxygen exhibits a broad maximum between 30-50% PAO, irrespective of the preparative conditions (i.e. Ts or % TEFLON) used to yield this range of PAO. This behaviour is generally valid at any level of current density, as shown in (Fig. 1).

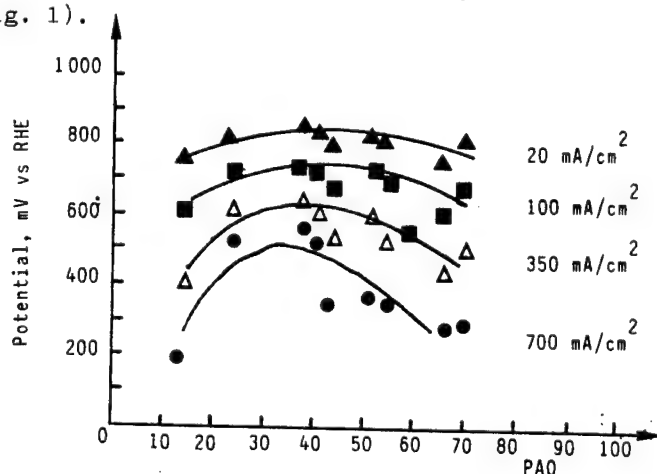


Fig. 1 - Cathode performance vs PAO

However, the effect of PAO is more pronounced at higher current densities (700mA/cm<sup>2</sup>) where a sharper maximum of the cathode performance is localized in a narrower range of acid occupation (30-40%). Due to increase wetting

b1

of the catalyst layer with time, electrodes with greater than 40% PAO tend to be flooded with performance degradation, as also confirmed by Mori [6]. Electrode operation under either activation polarization or combined activation and diffusion polarization was also screened in terms of oxygen gain (the difference in potential between oxygen and air, at constant current density). A comparison of oxygen gains as a function of current density, sintering temperature and TEFLON content showed the electrodes prepared with 40% TEFLON and sintered at 340°, 350°, 360°C and with 50% TEFLON and sintered at 340°C exhibit an oxygen gain of approximately 75 mV through the whole range of current densities investigated, a value which is approximately equal to the value expected for conditions of activation polarization. Consequently, the performance of these electrodes is dominated by activation polarization, at least up to current densities of 1 A/cm<sup>2</sup>. For the other electrode preparations, the observed oxygen gains of 120 mV or greater suggest a performance dominated by both activation and diffusion polarization. More interestingly, plots combining the variation of T<sub>S</sub> and TEFLON indicate that the oxygen gains are at their minimum at 30-40% PAO (Fig. 2), which thus defines conditions in the electrode fabrication at which the cathode performance is dominated by activation polarization only. The PAO appears to be the unifying characteristic binding differently prepared electrodes.

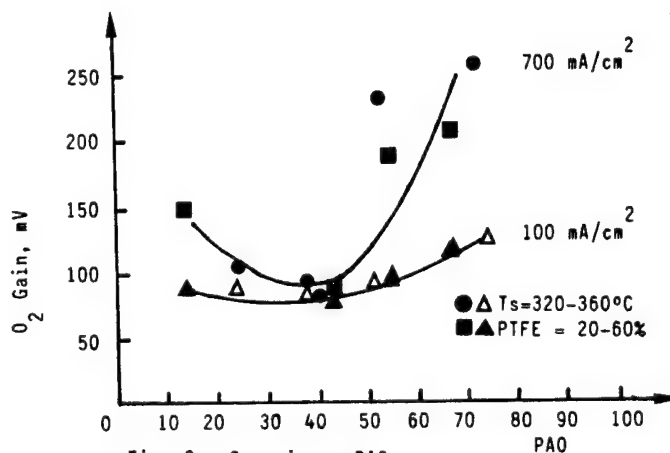


Fig. 2 - O<sub>2</sub> gain vs PAO

- [1] A.J. Appleby and A. Borucka; J. Electrochem. Soc., 116, 1212 (1969).
- [2] P. Stonehart and P.N. Ross; Electrochim. Acta, 21, 441 (1976).
- [3] H.R. Kunz and G.A. Gruver; J. Electrochem. Soc., 122, 1279 (1975).
- [4] L.J. Bregoli; Electrochim. Acta, 23, 489 (1978).
- [5] N. Giordano, E. Passalacqua, V. Recupero, M. Vivaldi, E.J. Taylor and G. Wilemski; J. Fuel Cells submitted.
- [6] T. Mori, J. Imahashi, T. Kamo, K. Tamura and Y. Hishinuma; J. Electrochem Soc., 133, 869 (1986).

18-01-12-G

# HIGH-PERFORMANCE GAS DIFFUSION POROUS ELECTRODE STARVED OF ELECTROLYTE SOLUTION

Z. W. Tian, Z. G. Lin, J. K. You  
Department of Chemistry, Xiamen University, China

Uneven Liquid Film Model for gas diffusion porous electrode has been presented previously<sup>(1,2)</sup>. According to this model, the rough envelop surface of catalyst agglomerate is covered with the electrolyte solution film of uneven thickness by capillary force, and the electrode process is controlled mainly by four processes in practical current density region, one of these processes is that dissolved reactant diffuses from gas-liquid interface across the uneven liquid film to the envelop surface of the agglomerate of catalyst particles (abbreviated to F-process). The effect of the rate of F process on the slope of the linear segment of polarization curve is significant.

In the case of gas diffusion porous electrode starved of electrolyte solution, the thickness of uneven liquid film becomes thinner; the hindrance of F process decreases and performance of electrode improved. The experimental results of oxygen electrode in neutral electrolyte solution of NaCl are shown in Fig.1.

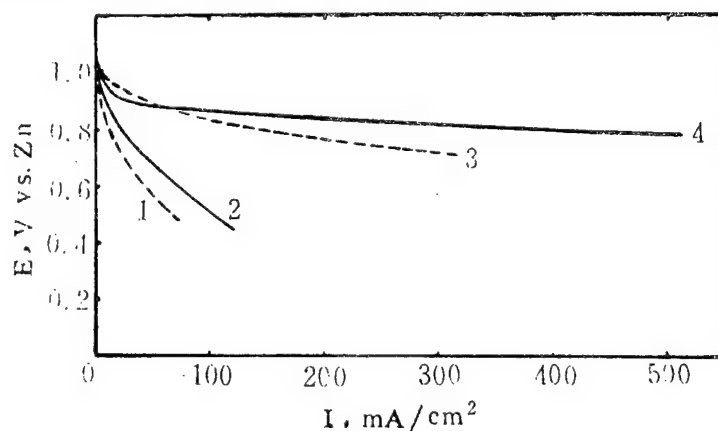


Fig.1 Performance of Teflon bonded electrode in 25% NaCl aqueous solution at room temperature, scan rate 1mV/s.  
curve 1,2: electrode supplied with sufficient electrolyte solution  
curve 3,4: electrode starved of electrolyte solution  
-----, Mn/carbon                      ———, high surface graphite

- (1) Z. W. Tian, T. K. Lin, J. K. Yu; Extended Abstract, Electrochem. Soc. Meeting, Los Angeles, (1979), Abstract No. 88.
- (2) Z. W. Tian, Z. G. Lin, and J. K. Yu, Scientia Sinica, Vol. 24 (1981), 1391.

b1

18-01-13-G

POLARIZATION STUDY OF FUEL CELL WITH MULTI-REFERENCE ELECTRODES

K.Mitsuda and T.Murhashi  
Central Research Laboratory, Mitsubishi Electric Corporation  
Tsukaguchi-honmachi 8-1-1, Amagasaki-shi, Hyogo, Japan 661

The potential changes in the anode and cathode potentials of a phosphoric acid fuel cell (PAFC) under starving conditions of fuel or air were studied using a single cell with twenty-four reference electrodes (reversible hydrogen electrode; RHE) which were located around the anode or the cathode. The gas composition of the exhaust gas of fuel and air was analyzed using a gas chromatography.

Fig.1 shows the position of the reference electrodes. They were named R1 to R12 for the cathode side and R13 to R24 for the anode side. Gas flow configuration was cross-flow type. The sizes of the cathode, the anode and the matrix were 100 cm<sup>2</sup>, 110 cm<sup>2</sup> and 225 cm<sup>2</sup>, respectively. The size of the reference electrode was 0.3 cm<sup>2</sup>. Fig.2 shows a cross-sectional view of the cell near a reference electrode.

We have reported previously [1] the inhomogeneous distribution of polarization in the plane of a cell using a single cell with four reference electrodes imbedded in a matrix layer. The cathodic shifts of the cathode and anode potentials at the fuel outlet area were found to be caused by increase of H<sub>2</sub> utilization or by CO poisoning. Those phenomena were observed also with multi-reference electrodes imbedded in the anode or the cathode separators. Fig.3 shows the change of the cathode and anode potentials at each position (against R1 to R12) with H<sub>2</sub> utilization of fuel (H<sub>2</sub> 80% + N<sub>2</sub> 20%). The cathode and anode potentials at the fuel outlet area shifted toward cathodic direction when H<sub>2</sub> utilization increased. At 92% H<sub>2</sub> utilization these potentials shifted up to about 300 mV. The potentials against R13 to R24 (which was not shown in figure) coincided with those in Fig.3 within 0.3 mV. At that time, CO and CO<sub>2</sub> were detected in the air outlet gas, which indicates the carbon corrosion of the cathode components; furthermore, H<sub>2</sub> was also detected in the air outlet gas, which means the H<sub>2</sub> generation at the cathode. The carbon corrosion and H<sub>2</sub> generation can not occur at the same time in the cathode if the potential is homogeneous in the plane of a cell. However, one can explain these phenomena clearly using Fig.3, because above 92% H<sub>2</sub> utilization, the cathode potential at the fuel outlet area is cathodic enough to generate CO or CO<sub>2</sub> (cathodic zone) and that at the fuel inlet area is anodic enough to generate H<sub>2</sub> (anodic zone). At negative cell voltage (above 95% H<sub>2</sub> utilization), CO and CO<sub>2</sub> were not detected in the air outlet gas, but those were detected remarkably in the fuel outlet gas, which means the carbon corrosion of the anode components occurred. Fig.4 shows the influence of air utilization on the cathode and anode potentials. The potentials were little changed in the plane of a cell. From 84% to 161% O<sub>2</sub> utilization, H<sub>2</sub> was detected in the air outlet gas, however CO or CO<sub>2</sub> was not detected in the exhaust gases of fuel and air.

[1] K.Mitsuda, H.Shiota, J.Aragane, and T.Murahashi, The Electrochemical Society 174th Meeting, Abstracts No.52 Chicago, Illinois (1988).

(This work was supported by The New Energy and Industrial Technology Development Organization (NEDO).)



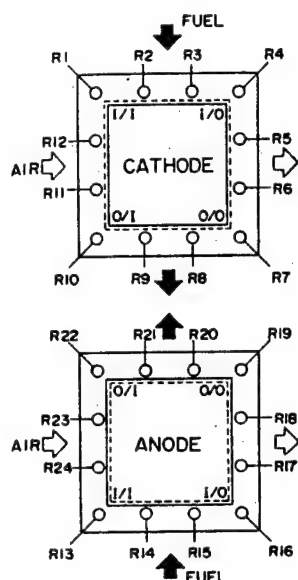


Fig.1 Schematic figure showing the location of the twenty-four reference electrodes.

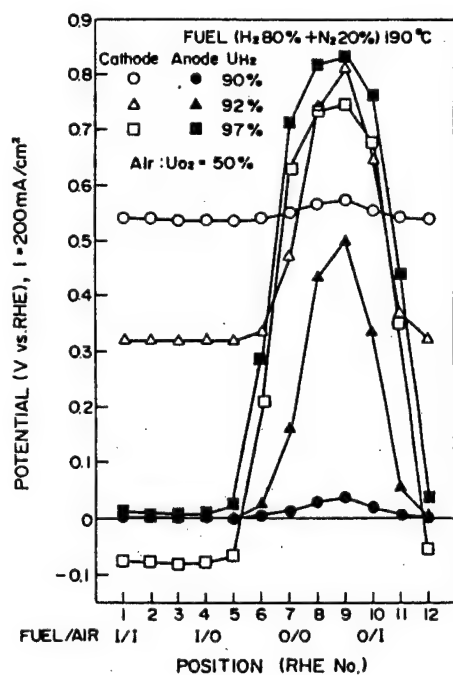


Fig.3 Influence of fuel utilization on the cathode and anode potentials.

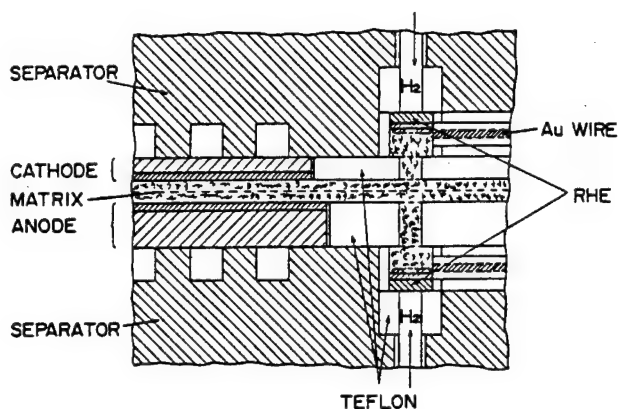


Fig.2 Cross-sectional view of the reference electrode in a cell.

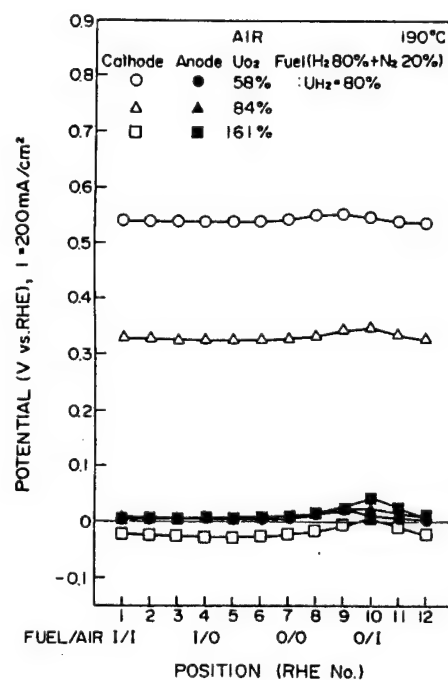


Fig.4 Influence of air utilization on the cathode and anode potentials.

b1

19-01-01-K

Status of Advanced Fuel Cell Technology in Japan

Y. Kurihara

Moonlight Project Promotion Office, AIST, MITI  
1-3-1, Kasumigaseki, Chiyoda-ku, Tokyo, 100 Japan

R&D of fuel cell power generation technologies in Japan was begun about 30 years ago at research institutes of national laboratories and by the private sector. In 1981, such R&D was chosen as one of the Large-Scale R&D Projects for Energy Conservation by the Moonlight Project Promotion Office. Since then, activities in Japan to realize commercialization at an earlier stage have been accelerated.

The Moonlight Project is now promoting R&D of fuel cells, focusing on civilian electric utilities; on Phosphoric Acid Fuel Cells (PAFC), which are expected to be commercialized at the earliest stage; and Molten Carbonate Fuel Cells (MCFC) and Solid Oxide Fuel Cells (SOFC), which are expected to have higher performance.

As for PAFC, R&D of 1000kW power generation system for dispersed power generation and substitute thermal power plants was successfully accomplished early this year. Subsequently, operating research of 200kW power generation systems for commercial buildings and isolated islands are to be initiated from this summer to autumn.

Regarding MCFC, with the aim to develop a 1000kW power generation system, R&D of two different types of 100kW cell-stack, BOP and component technology for a 1000kW plant are being promoted. The Technology Research Association for MCFC Power Generation Systems, which was established in February of last year, is now undertaking full-scale MCFC R&D.

In the area of SOFC, R&D for basic technologies is by proceeding at the Electrotechnical Laboratory and the National Chemical Laboratory for Industry. R&D on elemental fabrication technologies and so on is to be initiated by NEDO from this year.

Fuel cell R&D has also been intensively promoted by the private sector now in the form of in-house or cooperative research. Some companies are demonstrating cell-stacks developed in the U.S..

R&D of PAFC is already near the demonstration stage. In the first half of the 1990's, on-site type power plants are expected to be placed in commercial use, followed with expansion to applications in dispersed power generation systems. Although R&D of MCFC and SOFC are as yet development stage and basic research stage respectively, R&D activities are steadily proceeding in order to take full advantage of their features.

The beneficial features of full scale, such as their energy conservation ability and environmental acceptability, have great global meaning. This is the reason why the importance of fuel cell technologies is recognized by many countries, and R&D in this area is intensively being promoted. At present, international R&D cooperation is being promoted at both the governmental level and private level. Early commercialization of fuel cell technologies should be undertaken through increased international cooperation.

b1

19-01-02-G

The Development of the Large-Scale Molten Carbonate Fuel Cell

Y. Yamamasu, M. Hotta, S. Satou  
Fuel Cell Development Dept.  
Ishikawajima-Harima Heavy Industries Co., Ltd.  
1-15, Toyosu, 3-Chome, Koto-ku, Tokyo 135 Japan

IHI has been developing the large-scale Molten Carbonate Fuel Cell (MCFC) stacks since 1988, in Moonlight Project supported by the Japanese government. The type of the MCFC stack proposed by IHI consists of the concepts of the parallel gas flow type and the internal manifold.

Fabrication of cell components

Electrodes and tiles are fabricated by the tape-casting method with a doctor blade. The green tape of electrodes, Ni-8%Cr Anodes and Ni Cathodes, were cut into the size of 2500 x 1000 (mm) and sintered in an electric furnace. The furnace was specially designed and manufactured to develop the sintering technology of the large-scale rectangular electrodes. The  $\text{LiAlO}_2$  green tapes were directly installed in the cells, and dewaxed and impregnated with carbonate "in-situ". Fig-1 shows the  $\text{LiAlO}_2$  green tape. The data of the thickness distribution and the microstructure of the electrodes were obtained and were correlated with the cell performance.

The rectangular separator having 1 m<sup>2</sup> active area, 1800 x 560 (mm), was designed and fabricated. It consisted of a center plate (Ni clad), corrugated plates, punched plates and mask plates. The materials of corrugated plates and punched plates were selected Ni and 310S SS for anode side and cathode side, respectively. These plates were assembled by the automatic resistance welding. Fig-2 shows the large-scale separator.

Stack test

A 3 kW stack consisting of 3 cells with 1 m<sup>2</sup> active area were assembled and tested prior to the 10 kW stack test in order to evaluate the cell components and the test facilities. Fig-3 shows the performance of the stack under the condition of 70% fuel utilization at 615 °C. The average cell voltage is lower than the value of our standard-type cells because of the lower average cell temperature and the insufficient uniformity in the fuel flow distribution. Fig-4 shows the horizontal distribution of fuel utilization and temperature in a cell. The temperature and fuel utilization on both sides of the separator were lower than the central position. The temperature distribution of the test stand has been already improved by the efforts to decrease the heat losses, and the test of the 10 kW stack will be started soon.

Conclusion

- 1) The fabrication technology of the large-scale cell components has been established.
- 2) The feasibility of the large scale MCFC stack has been demonstrated.

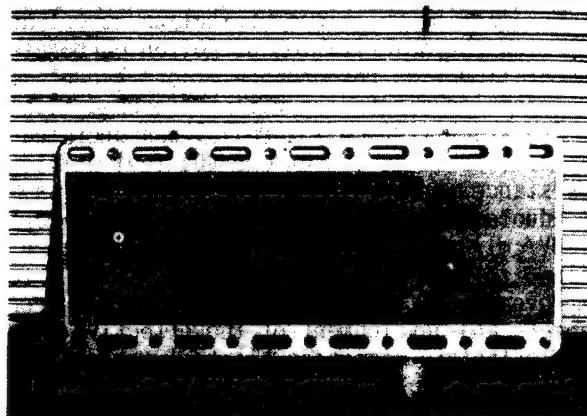
Fig.1  $\text{LiAlO}_2$  green tape

Fig.2 Large-scale separator

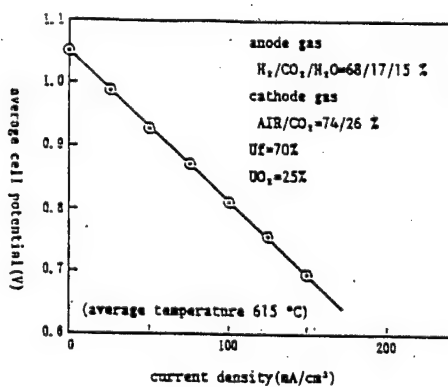


Fig.3 I-V relation of 3 kW stack

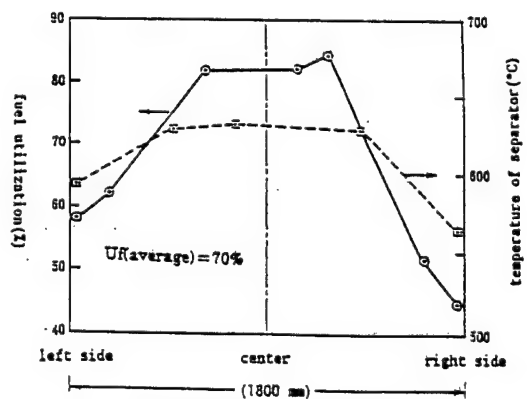


Fig.4 Distribution of fuel utilization and temperature for 3 kW stack

b1

19-01-03-G

MOLTEN CARBONATE FUEL CELL TECHNOLOGY IMPROVEMENT

T. Murahashi, T. Tanaka, E. Nishiyama  
Central Research Laboratory, Mitsubishi Electric Corporation  
Tsukaguchi-honmachi 8-1-1, Amagasaki, Hyogo, Japan 661

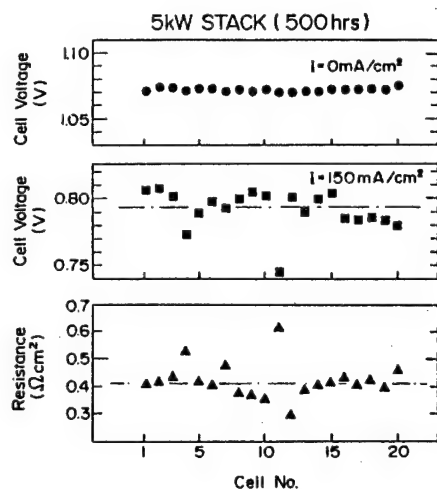
We describe in this contribution recent activities in the development, evaluation, and characterization of molten carbonate fuel cell at Mitsubishi Electric Corporation. The performance of our recent stack was satisfactory, so in this contribution discussion will be focused mainly on the cell/stack life issues.

5KW stack (2000cm<sup>2</sup>\* 20cells) was operated for 4000 hours. Stack performance was 0.79V/cell at 150 mA/cm<sup>2</sup>, 80% fuel utilization (Fig.1). Voc, V150 and internal resistance were quite stable throughout the operation (Fig.2). Thermal cycling was conducted three times. Our goal of the performance is tentatively set as 0.80V/cell at 150 mA/cm<sup>2</sup>, 80% fuel utilization, 1 ata and our result of 5KW stack was close to that goal. Therefore our recent efforts are focused primarily on the improvement of the cell/stack life, which are identification of the life limiting factors and development of the effective countermeasures to those factors.

Electrolyte migration, electrolyte loss and Ni dissolution have been recognized as the major life limiting factors. Negative end cell of 5KW stack showed a noticeable degradation with time [1], and this was ascribed to the flooding in the anode which was due to the migration of the electrolyte through the manifold gasket because open circuit voltage was still high and high H<sub>2</sub> gain indicated the deterioration of the gas diffusivity in the anode. Modeling and estimation of the rate of transfer of the electrolyte in the gasket are in progress. We have intensively accumulated large amount of experimental data concerned with the corrosion and electrolyte loss through the operation of laboratory-scale cells (25 cm<sup>2</sup>, 250cm<sup>2</sup>) and stacks (1000cm<sup>2</sup>, 2000cm<sup>2</sup>). Almost all the paths of electrolyte loss and loss-rate were identified and estimated (Fig.3). The total loss-rate of the electrolyte in a 25cm<sup>2</sup> single cell was estimated as 17t+250 mg/cell. To reduce the electrolyte loss consumed in the corrosion scales on the metal hardware intensive work has been done and two candidate materials, SS316L and SS310S, are selected. SS310S is superior to SS316L from the view point of the good resistance to the corrosion in the high temperature environment, however, since it has high chromium contents, the electrolyte loss due to the formation of K<sub>2</sub>CrO<sub>4</sub> is significant. This means SS310S still does not meet completely the requirements for the metal hardware.

One possible approach to the electrolyte loss is to increase the initial inventory of the electrolyte in the electrodes. Fig.4 shows the experimental data which describe the relation between V150, gain and the electrode thickness. In the experiment, the fill level of the electrolyte was fixed against the pore volume in the electrode and the data show that it is possible to increase the thickness of the electrode as much as to 1.0 and 1.5 mm for an anode and a cathode, respectively without sacrificing the cell performance. Thicker electrode can store more electrolyte in it and in Table 1 the predicted cell life for different size of the electrode area is shown on the assumption that the loss rate of the migration is constant and irrelevant to the size of the electrode area.

[1] H. Urushibata, K. Sato, T. Murahashi and E. Nishiyama;  
Abstracts from 1988 Fuel Cell Seminar, Long Beach, California



Fuel; 73%  $\text{H}_2$ -18%  $\text{CO}_2$ -9%  $\text{H}_2\text{O}$   $U_f = 80\%$   
 Oxidant; 70% Air-30%  $\text{CO}_2$   $U_o = 20\%$

Fig. 1. Stack Performance of MS20-4

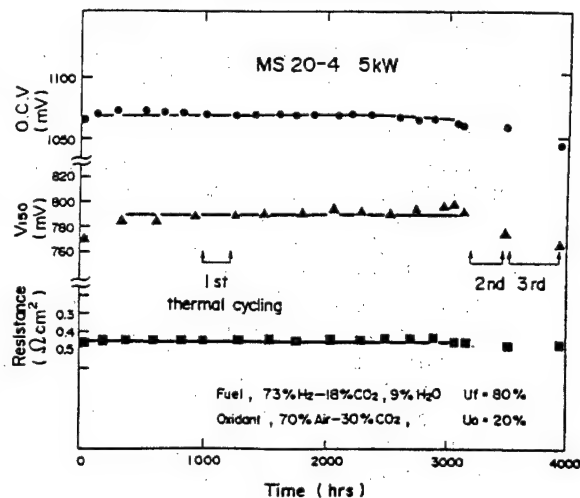
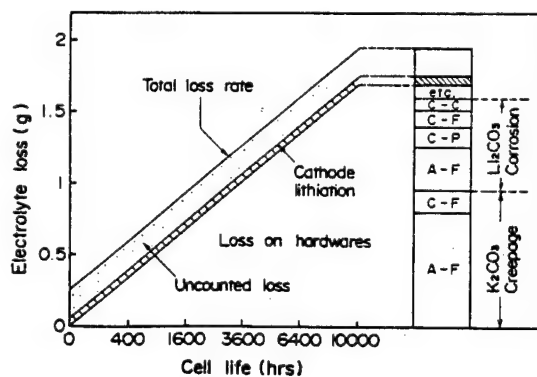


Fig. 2. Performance Stability of MS20-4



cell size (cm <sup>2</sup> )	loss rate (g)		electrolyte store (g)	predictive cell life (hrs)
	migration	hardware *		
250	0.0071	0.025 <sup>1/2</sup> + 0.55	16	2000
1000	0.0071	0.10 <sup>1/2</sup> + 2.2	50	5700
2000	0.0071	0.20 <sup>1/2</sup> + 4.4	100	10000
5000	0.0071	0.50 <sup>1/2</sup> + 1.1	270	25000

\*  $0.10^{1/2} + 2.2$  (mg/cm<sup>2</sup>)

Table 1. Prediction of cell life

Fig. 3. Electrolyte Loss in the 25cm Single Cell

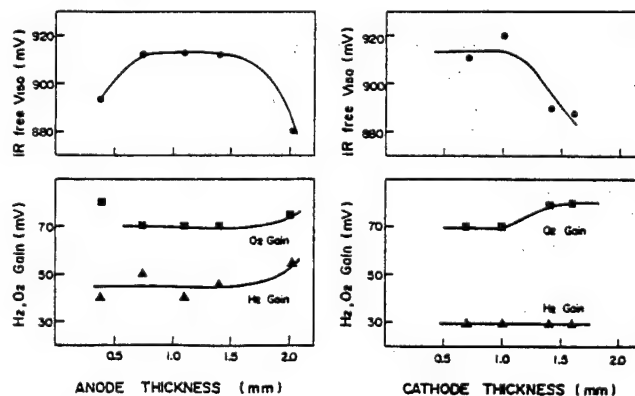


Fig. 4. Influence of the Electrode thickness on the performance

b1

19-01-06-K

Status of Advanced Fuel Cell Technology in Sweden

Lars A Sjunnesson  
Sydkraft AB  
S-217 01 MALMÖ Sweden

The decision to close down the nuclear power in Sweden has been taken. This has resulted in an increased interest in finding methods to secure the long-term energy supply

The activities in the fuel cell area in Sweden have during the last years for this reason received additional support. The future users of the technique, e.g. the power companies, as well as universities and technical institutions have increased their activities.

The present research is mainly working on basic issues within the molten carbonate area but other types of fuel cells may also be investigated. Other areas in question are; alkaline cells, catalyst research, proton conducting materials and mathematical modelling. The financial means allocated for this purpose have so far been modest.



19-01-07-K

STATUS OF ADVANCED FUEL CELL TECHNOLOGY IN ITALY

F. Di Mario, R. Vellone

ENEA, Dep.t of Renewable Energy Sources and Energy Saving (FARE)

CRE Casaccia - 00060 Roma

Italian fuel cell program, coordinated by ENEA, includes both activities on phosphoric acid and advanced fuel cells (polymer electrolyte-PEFC, Molten carbonate-MCFC, Solid Oxide-SOFC).

In the field of PEFC an R/D program, started in 1988, is carried out by S.E.R.E. (De Nora Group), with the aim of developing and testing a 10 kW stack by the end of 1990. Transportation seems to be the more promising application of this technology.

The major efforts are focused on MCFC technology. Activities on materials, components and small cells have been carried out since the late 70's by industry (Ansaldo) and research bodies (CISE, CNR, Universities). A larger program will start in 1989, in the framework of an international cooperation; its main objective will be the development of cell and stack technology, with the realization and test of a 50-100 kW stack within 1992.

R/D activities on SOFC are growing in industry (ENI) and research centers, in consideration of the recent progress in this field. The fabrication and evaluation of cells and small stack are foreseen, in order to develop systems made by processes easily amenable to mass production and that guarantee at the same time the higher efficiency and power density possible.

Results of relevant interest on the above mentioned items will be carried out in the paper.

b1

19-01-08-K

STATUS OF THE ADVANCED FUEL CELL TECHNOLOGY IN THE NETHERLANDS

K. Joon and S.B. van der Molen  
Netherlands Energy Research Foundation ECN  
P.O. Box 1, 1755 ZG PETTEN, the Netherlands

**Introduction**

The Dutch R&D programme on molten carbonate fuel cells started in 1986.

The Netherlands Energy Research Foundation ECN is the main contractor of the programme with MCFC material research and technology development as major subjects. Basic electrochemical research is carried out by the University of Delft while System and Market studies have been performed by an industrial partner. This paper describes the electrochemical research, the materials R&D, the technology development for the first Dutch 1 kW stack, the test results up to now and the most important results of the system studies.

**Electrochemical Research**

The aim of the electrochemical research is to clarify the oxygen reduction at the cathode in different molten carbonate melts and the reaction rate determining step for state-of-the-art NiO(Li)-cathodes. Furthermore, fundamental research is carried out to understand the role of water and OH<sup>-</sup> ions in the reaction mechanisms at the anode. One of the main conclusions so far is that neither from half cell experiments nor from porous electrode studies it can be concluded that the cathode reaction kinetics are much slower than anode kinetics. Therefore, adjustment of the mass flow and modification of the mean pore size and flow distributions should result in similar polarizations at both electrodes, which has been experimentally verified.

**Materials Research and Development**

After a three years programme a thorough knowledge has been built up pertaining to materials properties and fabrication techniques. Tape casting and related powder and suspension technology as well as drying and sintering have been developed to a sophisticated level for routine production of porous components on the basis of state-of-the-art (Ni- and LiAlO<sub>2</sub>- based) materials. The research includes extensive physical, chemical and morphological characterization. To reduce cathode dissolution and anode creep problems, alternative cathode (LiFeO<sub>2</sub>) and anode materials (Ni-Al, solid solution of FeO and LiFeO<sub>2</sub>) respectively have been investigated. Screening of the materials is made by 3 cm<sup>2</sup> cell tests and small scale out of cell creep tests. The materials performance tests have been carried out in bench scale cells (10x10 cm<sup>2</sup>) and a 1000 cm<sup>2</sup> single cell to investigate the influence of the characteristics of the porous components, the carbonate content and gas utilisation.

#### Technology Development

The work concentrated on the bipolar plate design, corrosion research and on stack development. Corrosion, coating and welding experiments were needed. ECN has chosen for an internal manifold system in combination with a soft rail wet seal construction. The formability of the plate material plays an important role for the realization of an uniform gas flow distribution with minimum resistance. The behaviour of the soft rail separator plate concept was tested in a 1000 cm<sup>2</sup> twin cell. The construction of the first ECN 1 kW stack is finished. Operational data of this test will be presented.

#### Test results

Materials screening tests in 3 cm<sup>2</sup> lab cells showed the influence on the performance of the type of electrode material, the porosity of the matrix and the use of a bubble barrier. For standard gas conditions, the best test results are obtained with Ni-Al anode material, LiAlO<sub>2</sub>-Al<sub>2</sub>O<sub>3</sub> matrix material with a porosity of 65-70%. Also cells without a bubble barrier showed high performance. Cell voltages between 915 and 930 mV are routinely obtained. Screening tests showed also a strong influence of the holding force and carbonate content on the cell performance. For a number of tests the anode post test characteristics and pore volume < 1.0 µm are similar which is in agreement with measured anode polarizations. The bench scale cell tests (100 cm<sup>2</sup>) and the 1000 cm<sup>2</sup> material tests showed reproducible cell voltages of 760-790 mV for standard gas conditions temperature and a fuel utilization of 75%. From the post test analysis, a NiO cathode dissolution of 3.4 µg/hr cm<sup>2</sup> could be calculated.

#### System Studies

A system study was made for a 200 KWe pilot plant which can be used as a test facility. Furthermore, the system is equipped for CO<sub>2</sub> recirculation and reforming of CH<sub>4</sub> as fuel. Low pressure operation of the system (1-3 bar) showed an electrical efficiency of 50.2%. The maximum electrical efficiency of 65.1% is obtained for a pressure of 7.5 bar. Cell models are rather optimistic. State-of-the-art cell performance showed an efficiency of 59% at 7.5 bar. However, long term high pressure operation cannot be reached with NiO(Li) cathodes. Therefore alternative cathode material development is needed.

19-01-10-G

ELECTRODE/ELECTROLYTE COMBINED TAPE FOR MOLTEN CARBONATE FUEL CELL

K.Hatoh, J.Niikura, N.Taniguchi, T.Gamo, T.Iwaki  
 Central Research Laboratory, Matsushita Electric Industrial Co., Ltd.  
 3-15, Yagumo-Nakamachi, Moriguchi, Osaka, 570 Japan

whereas the extensive works are being carried out for developing the molten carbonate fuel cell (MCFC), this paper reports on the development of MCFC where the electrode and the electrolyte composite are combined for simplifying the manufacturing process.

The developed combined tape was to make possible to carry out the initial burn-out process in the cell by heating at 650°C to turn it into the sintered electrode, eliminating the conventional firing process required before the cell assembling process.

A mixture of carbonate electrolyte and  $\text{LiAlO}_2$  was prepared at the starting for the present purpose. This composite electrolyte mixture was kneaded at 650°C, cooled, and grounded, and was milled with added organic solvents and binders. The composite electrolyte mixture slurry was first formed into a tape of 1 mm thick by means of a doctor blade method and dried, whereon the electrode slurry was casted for the thickness of 0.8 mm by the same method to form the combined tape of which structure is shown in Fig. 1. The optimum burn-out condition in the cell was experimentally determined. The performance of combined tape was evaluated by constructing single cell shown in Fig. 2, and the effectiveness of it for the cell assembly process was confirmed.

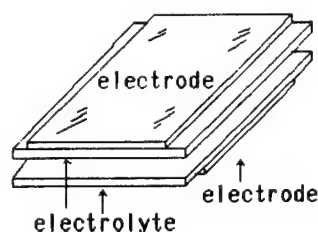


Fig.1. Structure Of  
 Combined Tape

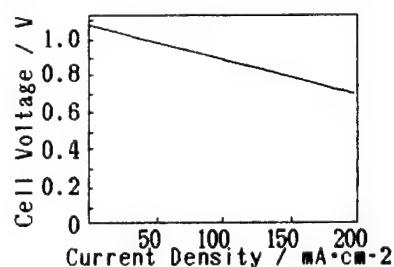


Fig.2. Cell Performance Using  
 Combined Tape

The present work was supported by New Energy Development Organization under the MCFC program.

b1

19-01-11-G

A Study on Electrolyte Management of MCFC

Y. Akiyama, Y. Tonoike, Y. Itoh, T. Nakajima, M. Nishioka, Y. Miyake,  
S. Murakami, T. Saito  
Sanyo Electric Co., Ltd. Functional Materials Research Center  
1-18-13, Hashiridani, Hirakata, Osaka 573, Japan

INTRODUCTION

The long run stability of MCFC depends on electrolyte management, especially retention of electrolyte by a matrix which supports electrolyte.

Reformed naphtha gas can be used in a MCFC system as a fuel gas. In this case, fuel gas contains more moisture than reformed natural gas.

Therefore, we investigated retention of electrolyte by a matrix under anode gas conditions with various moisture levels.

EXPERIMENTAL

Retention of electrolyte by a matrix prepared from  $\text{LiAlO}_2$  and having various surface areas was investigated under various humidified anode gas conditions. Experiments were carried out by pot-test. The BET surface areas and SEMs of samples were also examined.

RESULTS AND DISCUSSION

Retention of electrolyte by a matrix with  $\text{LiAlO}_2$ -19 (surface area :  $19\text{m}^2/\text{g}$ ) is higher than that with  $\text{LiAlO}_2$ -14 (surface area :  $14\text{m}^2/\text{g}$ ) up to 1000hrs in the low humidity region (10vol% humidity). In the middle humidity region (30vol% humidity),  $\text{LiAlO}_2$ -19 performs well up to 500hrs. However from 500hrs to 700hrs, retention suddenly drops and is surpassed by the retention levels of  $\text{LiAlO}_2$ -14. In the high humidity region (50vol% humidity),  $\text{LiAlO}_2$ -14 behaves better than  $\text{LiAlO}_2$ -19.

Fig. 1 shows the relation between retention of electrolyte after 700hrs and humidity.

SEM observation shows particle growth of  $\text{LiAlO}_2$ -19 after testing. (Fig.2(a)(b))

The BET surface area of samples drops below initial values, i.e., from  $19\text{m}^2/\text{g}$  to  $13\text{m}^2/\text{g}$  after 500hrs in 50vol% humidity condition, from  $19\text{m}^2/\text{g}$  to  $5\text{m}^2/\text{g}$  after 1350hrs in 30vol% humidity condition and so on.

CONCLUSION

In the low humidity region, retention of electrolyte by a matrix with a higher surface area ( $19\text{m}^2/\text{g}$ ) of  $\text{LiAlO}_2$  is better than that with a lower surface area ( $14\text{m}^2/\text{g}$ ) of  $\text{LiAlO}_2$ .

However, in the high humidity region, the behavior of higher surface area ( $19\text{m}^2/\text{g}$ )  $\text{LiAlO}_2$  is not as good because of particle growth of  $\text{LiAlO}_2$  due to humidity.

So, we have to choose the optimum  $\text{LiAlO}_2$  with an optimum surface area when considering the humidity conditions of fuel gas.

ACKNOWLEDGEMENT

The work upon which this abstract is being performed under Petroleum Energy Center Project which is subsidized by MITI.

b1

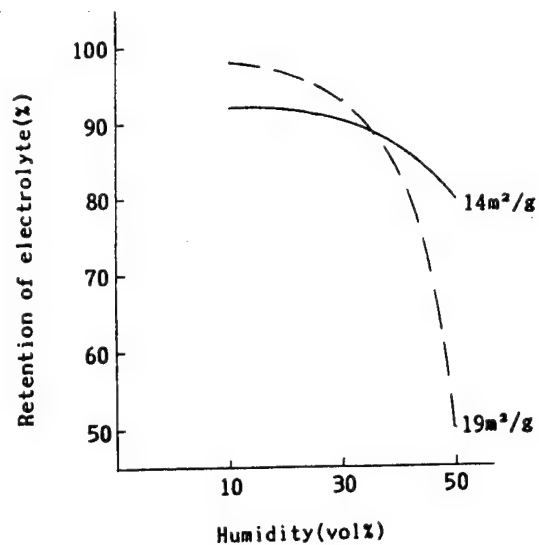


Fig.1 The relation between the retention of electrolyte and humidity



(a) Before testing



(b) After testing  
(50 vol% humidity  
500 hrs)

Fig.2 SEM photograph of Matrix

The Effect of Pore Structure on Polarization Characteristics of MCFC Cathodes.

S. Kuroe, Y. Iwase, H. Okada, K. Iwamoto, M. Takeuchi, T. Mori  
Hitachi Research Laboratory, Hitachi, Ltd.  
4026 Kuji-cho, Hitachi-shi, Ibaraki-ken, 319-12, Japan

There have been proposed some models on the electrolyte behavior in molten carbonate fuel cell (MCFC) electrode<sup>1)2)</sup>. Electrolyte is thought to distribute in pores of the electrodes. And the distribution parameters such as the areas, the thickness, etc. are substantial to determine the polarization of the electrodes. The present study focussed on clarifying how the occupation and distribution of electrolyte in a cathode of MCFC related to its polarization.

A plate of NiO with a porosity of 54% was used as a cathode. The polarization at 100mA/cm<sup>2</sup> was measured in the electrolyte occupation range from 5 to 80%. The composition of electrolyte was 62mol% Li<sub>2</sub>CO<sub>3</sub> and 38mol% K<sub>2</sub>CO<sub>3</sub>. A mixture of 15% O<sub>2</sub>, 30% CO<sub>2</sub> and 55% N<sub>2</sub> was used as a reactant gas. The electrolyte in pore was observed by SEM and EPMA. The film thickness and distribution of electrolyte were determined by processing the data of EPMA with an image analyser. It was presumed that the distribution of K corresponded to that of electrolyte.

The relationship between electrolyte occupation and polarization is shown in Fig.1. The polarization is small in the electrolyte occupation range from 20 to 40%. Fig.2 shows the distribution of electrolyte in case of the occupation of 24% at which the polarization is small. Most of NiO particles are covered with the electrolyte film and pores larger than 4μm remain empty. It was found from the data analysis of Fig.2 that the film thickness of electrolyte was approximately 1μm. On the other hand, number of pores were fully filled with the electrolyte in case of the occupation of 64% at which the polarization was increased. In this case, gas diffusion was considered to be retarded. This work was preformed under the support of MITI and NEDO.

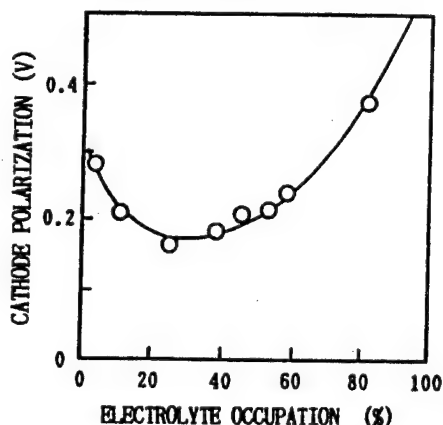


Fig.1. Relationship between electrolyte occupation and polarization at 100mA/cm<sup>2</sup>.



Fig.2. Distribution of Ni and K in cross-section.(electrolyte occupation;24%)

- 1) V. Sampath A. F. Sammells and J. R. Selman, J. Electrochem. Soc., 127, 79(1980).
- 2) G. Wilemski, J. Electrochem. Soc., 130, 117(1983).

19-01-13-G

SOLUBILITIES OF METAL OXIDES IN MOLTEN CARBONATE

K. Ota, S. Mitsushima, S. Kato and N. Kamiya  
 Department of Energy Engineering, Faculty of Engineering,  
 Yokohama National University, 156 Tokiwadai, Hodogaya-ku, Yokohama 240

NiO has been utilized for cathode of the molten carbonate fuel cells (MCFC). But NiO is reported to be unstable for the long-time operation, since it dissolves in the carbonate melt. In order to improve the stability of a cathode of MCFC, two ways could be thought. One is a selection of the salt composition that is suitable for NiO cathode, and the other is the development of a new cathode material that is more stable than NiO. The solubility of a cathode material in electrolyte is an important factor for the evaluation of the stability of the cathode. In this study, two sorts of experiments have been carried out. At first, the solubilities of NiO have been measured in the Li/K=62/38, 50/50, 42.7/57.3 and Li/Na=52/48 in order to obtain the salt composition that is suitable for NiO cathode. The solubilities of nickel ferrites and lanthanum oxides which are candidates for new cathode materials have been also measured in the Li/K=62/38 carbonate melt.

Solubility of nickel oxide in molten carbonate --- The solubilities of NiO in Li/K=62/38, 50/50, 42.7/57.3 carbonate melts at 1023K are shown as a function of  $P_{CO_2}$  in Fig.1. In these melts, the acidic dissolution occurred under high  $P_{CO_2}$ , while under low  $P_{CO_2}$  the basic dissolution occurred. In Li/K=62/38 carbonate melt, it was found that the solubilities were independent of  $P_{CO_2}$  under both high  $P_{CO_2}$  (acidic dissolution) and low  $P_{CO_2}$  (basic dissolution). The solubilities decreased with a rise in temperature at the acidic dissolution, while the solubilities increased in any melt at the basic dissolution. With increasing  $Li_2CO_3$  content in the melt, the solubilities decreased at the acidic dissolution, while the solubilities increased at the basic dissolution. The minimum solubilities were independent of the melt composition. This result suggests that the solubility is determined by the basicity  $[pO^{2-}]$  of the melt. The minimum solubility which can be attained by the selection of the melt composition was found to be  $3-4 \times 10^{-7}$  (mole fraction) at 923K.

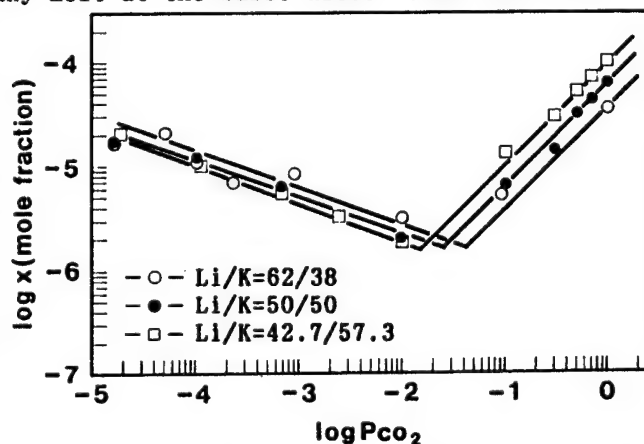


Fig.1 Solubilities of NiO in carbonate melts as a function of  $P_{CO_2}$  at 1023K.

Fig.2 shows the dependence of the solubilities on the Li content in the melts. The solubility decreased as the Li content increased. The melt that had  $Na_2CO_3$  showed the low solubility of NiO. From these results  $Li_2CO_3$  melt might be most basic and  $K_2CO_3$  melt might be most acidic among



b1

the three kinds (Li, Na and K) of alkaline metal carbonates.

Solubility of nickel ferrite in molten carbonate --- The solubilities of nickel ferrites ( $\text{Ni}_x\text{Fe}_{3-x}\text{O}_4$ ) of several compositions ( $x=0.33, 0.53, 0.75, 1.00$ ) have been measured in a Li/K=62/38 eutectic carbonate melt under a  $\text{Pco}_2$  ranging from 0.1 to 1atm in a temperature range from 873 to 1023K. The solubilities of nickel and iron in the ferrites increased as  $\text{Pco}_2$  increased. This might be explained by the acid fluxing mechanism. The dependence of the solubilities of nickel ferrites on the pressure was smaller than that of nickel oxide.

The solubilities of nickel decreased with a raise in temperature in any composition of nickel ferrite. In the ferrite of lower nickel content the solubility of iron decreased at higher temperatures. The solubilities of iron in the higher nickel ferrites increased at higher temperatures.

The dependence of the solubilities on the composition of nickel ferrite at 923K under  $\text{Pco}_2=1\text{atm}$  is shown in Fig.3. This figure suggest that the solubility of nickel can be decreased as compared with the pure substance by making a solid solution of NiO.

The solubilities of nickel ferrite were much smaller than that of nickel oxide by a factor of 1/3~1/18 under any conditions of this work. Considering the solubilities, the nickel ferrite might be a more stable cathode material of MCFC than nickel oxide. However, the ferrite reacted with the carbonate melt and the reaction products had a low electrical conductivity, although the nickel ferrites themselves have a good electrical conductivity, especially for the low nickel ferrite. These points should be improved in utilizing these materials as the cathode of MCFC.

The oxide that contains lanthanum have a good electrical conductivity and are going to be utilize as an electrode material of high temperature processes. the stability of  $\text{LaNiO}_3$  and  $\text{La}_2\text{O}_3$  have been also studied in the melt.  $\text{LaNiO}_3$  was not stable and easily decomposed in  $\text{CO}_2$  atmosphere at 923K.  $\text{La}_2\text{O}_3$  dissolved much in carbonate melt. The metal oxides that contains lanthanum might be unstable in the carbonate melt.

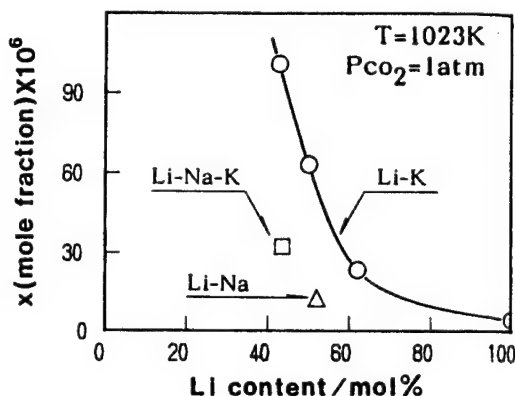


Fig.2 Solubilities of NiO in carbonate melts as a function of Li content in the melt under  $\text{Pco}_2=1\text{atm}$  at 1023K.

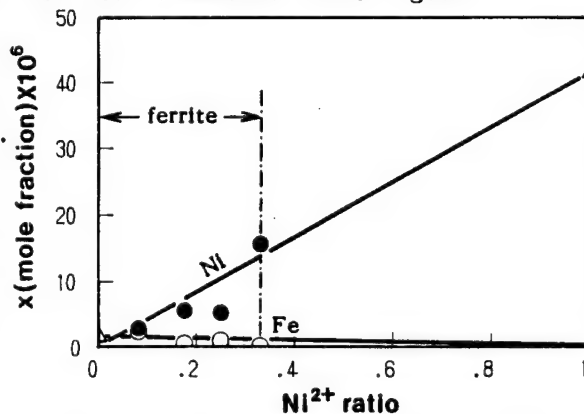


Fig.3 Solubilities of  $\text{Ni}_x\text{Fe}_{3-x}\text{O}_4$ , NiO (●) and  $\text{Fe}_2\text{O}_3$  (△) in Li/K=62/38 carbonate melt as a function of Ni content in oxides under  $\text{Pco}_2=1\text{atm}$  at 923K.

19-01-14-G

ELECTROCHEMICAL BEHAVIOR OF POROUS NiO IN MOLTEN CARBONATE FUEL CELLS  
EFFECT OF ELECTROLYTE COMPOSITION

H. Numata, \*T. Shimada, \*M. Tamura, I. Ohno, S. Haruyama  
 Tokyo Institute of Technology, Tokyo Japan  
 \*NKK Corporation, Kawasaki Japan

In Molten Carbonate Fuel Cells (MCFC), a sintered porous NiO is used as positive electrode to decrease the polarization, since the cathodic reduction of oxygen is a major factor to contribute the efficiency of the cell. The electrolyte in the cells creeps into pores of the porous electrode and a three-phase boundary, i.e. liquid, solid, gas-phase, is formed at the liquid meniscus. Although the cathodic reduction of oxygen at the three-phase boundary is a very important reaction in the electrochemical process, very few studies have been conducted hitherto [1].

In this study, electrochemical measurements of oxygen electrode for a lithiated NiO electrode have been conducted to explain the mechanism of oxygen reduction at the three-phase boundary. The electrolyte bath constitutes alkali chloride, carbonate and their mixtures to detect the influence of the electrolyte bath, especially anions. Furthermore, a lithiated NiO was equipped in a laboratory type MCFC where the electrolyte tile was prepared from the alkali carbonate and chloride mixtures.

Experimental

Electrolyte The experiments were conducted in molten chloride and carbonate respectively. An equimolar mixture of reagent grade NaCl-KCl was dried in an oven at 453K for more than 20h. The mixture (0.09 kg) was contained in an alumina cylinder (99.5%)  $3.7 \times 10^{-2}$  m in inner diameter, and deaerated and dehydrated by bubbling dry argon gas. The concentration of oxide ion was changed by the addition of reagent grade  $\text{Na}_2\text{CO}_3$  followed by argon bubbling. Temperature was kept at  $1023 \pm 3$  K except otherwise noted. A mixture of  $\text{Na}_2\text{CO}_3$  and  $\text{K}_2\text{CO}_3$  (56:44 in mol%) was dried in an oven. After melting the mixture, the melt was dehydrated by bubbling  $\text{CO}_2$  gas for 1h.

Electrodes A preparatory experiments were conducted using various types of electrode. As the result, it was found that the electrode assemblies, electrolyte tile and the counter electrode as shown in Fig. 1 shows good reproducibility.

Results and Discussion

Figure 2 shows a schematic diagram for the cathodic reduction of oxygen at the three-phase boundary. Oxygen diffuses through a thin electrolyte film to the electrode surface and cathodically reduced. The reaction products,  $\text{O}^{2-}$  or  $\text{CO}_3^{2-}$  will be transported to the bulk electrolyte by electromigration. Levich [2] discussed the kinetics on the electrode which is partially immersed in the electrolyte. In Levich's model, the electrolyte at the reaction site is a rectangular thin film where an overpotential is simply governed by the resistance of the electrolyte film. According to his model, the larger the  $i_0$  value is, the steeper the rise of the current in the vicinity of the immersion potential. The current increases in the form of an exponent function of the overpotential at low overpotentials, exhibiting a diffusion limiting current determined by  $p\text{O}_2$  at high overpotentials.

b1

Figure 3 shows the cathodic polarization curves for the lithiated NiO electrode in NaCl-KCl-LiCl melt containing  $26 \text{ mol} \cdot \text{m}^{-3} [\text{O}_2^{2-}]$  under various  $p_{\text{O}_2}$ . The cathodic polarization curves obey an exponential relation at low oxide ion concentration. The current-potential curves for the lithiated NiO at 130, 260  $\text{mol} \cdot \text{m}^{-3} [\text{O}_2^{2-}]$  exhibited the similar behavior as that at low oxide ion concentration. The cathodic current (ref. -0.6V) increases with the increase of  $p_{\text{O}_2}$  and the reaction order regarding  $p_{\text{O}_2}$  at the 26, 130 and 260  $\text{mol} \cdot \text{m}^{-3}$  are 0.39, 0.50 and 0.37. The results are well explained by Levich's model. Similar experiments were conducted in alkali carbonate melt at 1023K. Figure 4 shows the cathodic polarization curves for the lithiated NiO under various  $p_{\text{O}_2}$  and  $p_{\text{CO}_2}: 0.1 \times 10^5 \text{ Pa}$ . The current at the potentials noble to -1.5V increases in proportion to the potential and the slopes increase with the increase of  $p_{\text{O}_2}$ . This polarization behavior is quite different from those on alkali chloride melts as was mentioned above. The comparison of the polarization curves in the two melts reveals that the magnitudes of the current in the chloride melts are several times larger than those in the carbonate melts. The results suggest that the electrolyte tiles containing alkali chloride are highly attractive for oxygen gas electrode. Effect of electrolyte composition on the cell voltage of MCFC will be discussed.

- [1] H.Numata, K.Asako, T.Kawasaki, A.Momma, and S.Haruyama; Proc. Joint Int. Sympo. on Molten Salts, The Electrochem.Soc., Vol.87-7, P557, Hawaii(1987)  
 [2] V.G.Levich; DAN, 157(1964), 404

#### Acknowledgement

The authors are grateful to Mr. K.Wakasaki for technical assistance. The author (H.N.) would like to acknowledge Mr. Y.Yamamasu in I.H.I. for helpful suggestions.

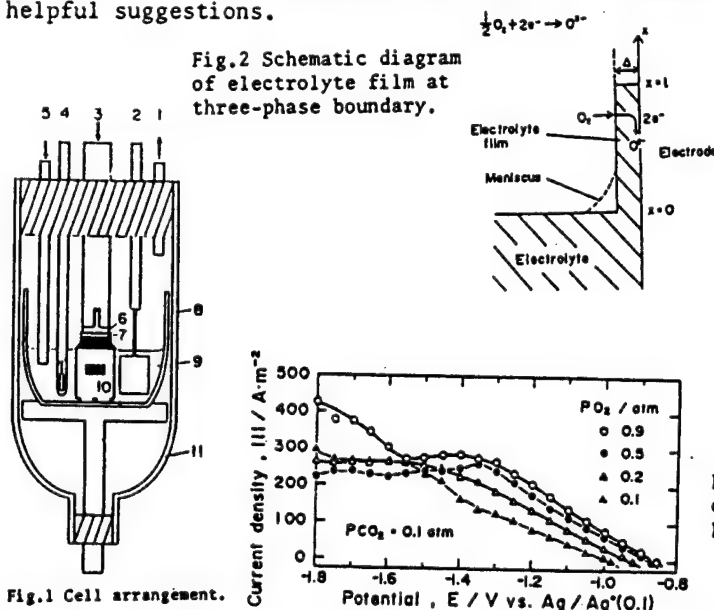


Fig.1 Cell arrangement.

Fig.2 Schematic diagram of electrolyte film at three-phase boundary.

Fig.3 Cathodic polarization curves on NiO in NaCl-KCl-LiCl melt at 1023K.

Fig.4 Cathodic polarization curves on NiO in  $\text{Na}_2\text{CO}_3\text{-K}_2\text{CO}_3\text{-Li}_2\text{CO}_3$  melt at 1023K.

19-01-15-G

THE EFFECT OF ELECTROLYTE CONTENT ON AC IMPEDANCE IN  
MOLTEN CARBONATE FUEL CELL ELECTRODES

K.Yamashita, K.Murata  
Toshiba Research and Development Center  
4-1, Ukishima-Cho, Kawasaki-Ku, Kawasaki, 210, Japan

The performance of Molten Carbonate Fuel Cell (MCFC) electrodes depends on its electrolyte fill ratio (ratio of the electrolyte volume to the total void volume of the electrode) [1]. To analyze this performance variation experimentally, an in-situ measurement technique which can detect electrolyte fill ratio variation is necessary. Here we present the effect of the electrolyte fill ratio on AC impedance and overpotential for different types of anodes.

Several types of sintered nickel porous bodies, one of which had a mean pore diameter of  $13\text{ }\mu\text{m}$  with 75% porosity, were used as working electrodes. As shown in Fig.1 the working electrode,  $3\text{ cm}^2$  frontal area and 2 mm thickness, was layed on a staggered corrugated nickel plate to minimize gas diffusion resistance. A gold reference electrode contained in an alumina holder and a nickel sintered counter electrode contained in an SUS310 holder were both placed on a tile. The working gas was 80% $\text{H}_2$ /20% $\text{CO}$ , mixed gas passed through  $50^\circ\text{C}$  water, and both the counter and reference gases were 70%air/30% $\text{CO}$ , mixed gas. AC impedance data were measured by a Solartron 1255 frequency response analyzer at open circuit voltage with 5 mV AC amplitude. The electrolyte fill ratio in the working electrode was calculated from the electrolyte content measured by the atomic absorption spectrometry and the total void volume of the washed post-test electrode measured by the mercury intrusion method.

The overpotential at  $150\text{ mA/cm}^2$  of  $13\text{ }\mu\text{m}$  mean pore diameter electrode as a function of the electrolyte fill ratio is shown in Fig.2. At very small fill ratio region, overpotential decreased as the electrolyte fill ratio increased, and on the contrary, between 48% to 76% fill, overpotential gradually increased as the electrolyte fill ratio increased.

In Fig.3 Cole-Cole plots of AC impedance data obtained at the same experiments with respect to several different fill ratios are shown. From the fact that the low frequency end of all loci bent toward real axes, finite diffusion concept was considered to be applicable to these cases. Increase of extrapolated intersect of the real ax at low frequency end as electrolyte fill ratio increses above 48% fill, which coincides the variation of the overpotential in Fig.2, seems to be explained by the increase of the thickness of diffusion layer of this concept. On the other hand, at very small fill ratio region, decrease of impedance as electrolyte fill ratio increases could be attributed to increse of reaction area, because impedance varies lineally at all frequencies.

This study was sponsored by New Energy and Industrial Technology Development Organization(NEDO) under MITI's Moon-Light project.

[1] H.R.Kunz, L.J.Bregoli, S.T.Szymanski, J.Electrochem.Soc. 131, 2815 (1984)

b1

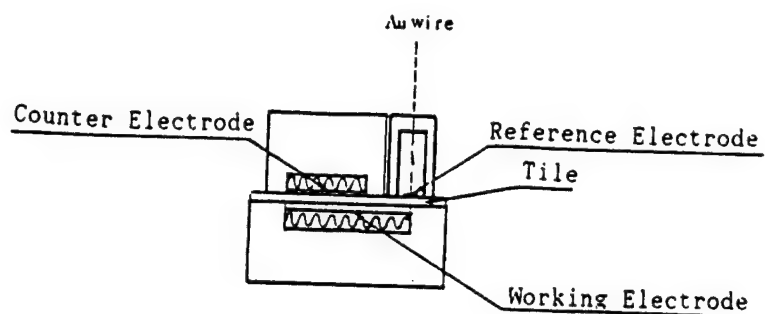


Fig.1 Cell arrangement

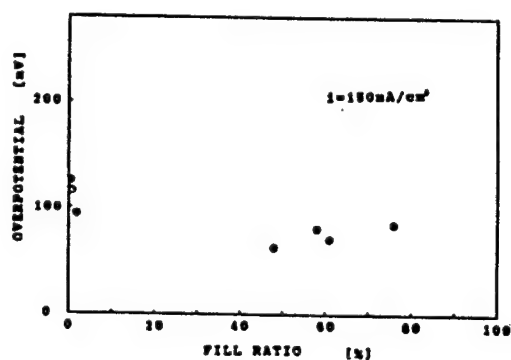


Fig.2 Overpotential as a function of fill ratio

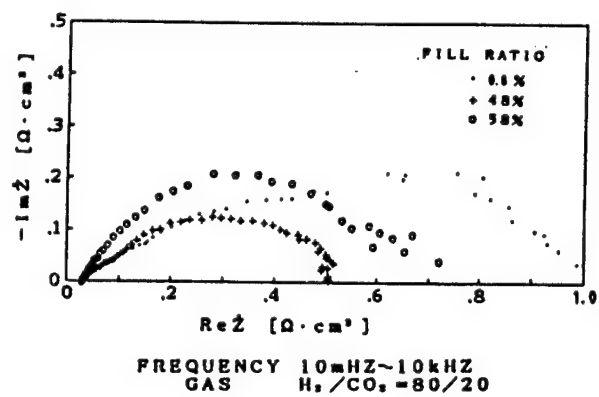


Fig.3 Cole-Cole plots for different fill ratios

19-01-16-G

CHARACTERIZATION OF POROUS ELECTRODES FOR MCFC  
BY IMPEDANCE MEASUREMENTS

J.Niikura, K.Hatoh, N.Taniguchi, T.Gamo, T.Nishina\*, I.Uchida\*  
Matsushita Electric Ind.,Co.Ltd.,Yakumonakamachi 3-15 Moriguchi Osaka  
\*Faculty of Engineering Tohoku University, Aoba Aramaki Sendai

Introduction

In development of MCFC, it is very important to clear effects of conditions of porous electrodes on their performances. The conditions investigated in this work are electrolyte contents, gas flow rate, gas compositions, temperatures and micro structure. Impedance measurements are versatile in obtaining information concerning to the correlation between them. Results of impedance measurements on cathodes under various conditions are discussed.

Experimental

Impedance measurements was conducted by using SOLARTRON model 1250 and 1286 in a half cell assembly as shown in Fig.1. The cathodes were fabricated from nickel powder(INCO 255) and subjected to in-situ oxidation. A reference electrode (Au,  $O_2/CO_2=1/2$ ) was placed near the working electrodes. Gas flow rates were changed from "natural diffusion" (zero rate) to forced "flow". The electrolyte contents of the cathodes were changed by the addition of electrolyte to the electrolyte composite.

Results

Fig.2 shows the effect of gas flow rate on impedance behavior of cathode. Without the flow (i.e. natural diffusion), the impedance plots consisted of two parts. But with the flow, the semicircle of low frequency region was no longer observed and the plot had one semicircle. The penetration depth of AC signal is a function of frequency, so the low frequency signals would penetrate into the inner phase of the micro pores of electrode. Under flow conditions, the reactant gas must be rich in the inner phase of micro pores. Therefore the semicircle of a low frequency region which reflects the gas phase mass transfer did not appear under the forced gas flow condition.

Fig.3 shows the effect of melt contents. The impedance of the over flooded electrodes became large compared with that of the normal electrolyte contents electrode. This would be explained by the increased thickness of electrolyte film and a choking effect of micro pores. Fig.4 shows the effects of temperature and polarization. The latter effect was not remarkable at low oxidant utilization.

Further, impedance analyses by parameter fitting for an assumed equivalent circuit were under investigation.

Reference

- (1)Y.Iwasa, M.Takeuchi, H.Okada and Y.Hishinuma, Ext.Abstr. 87-2, No.196, Electrochem. Soc. Meeting in Honolulu.
- (2)R.Holze and W.Vielstich, J.Electrochem.Soc.131,2298(1984).

b1

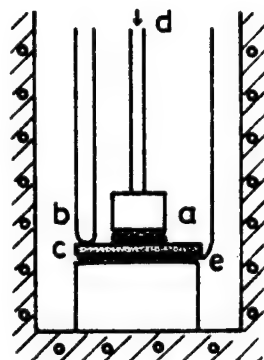


Fig.1 A half cell assembly for impedance measurements. a:cathode, b:reference electrode, c:tile, d:gas flow e:counter electrode(Au)

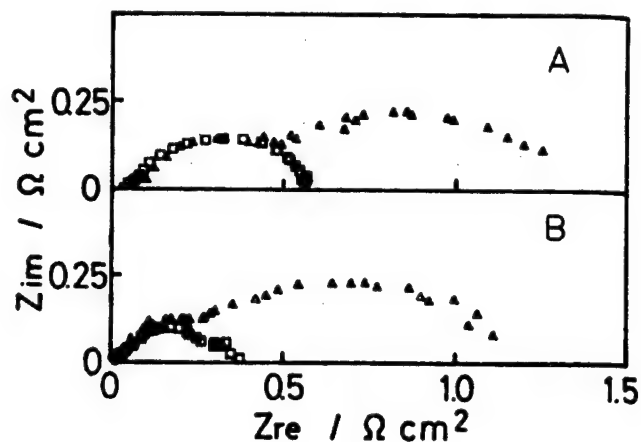


Fig.2 Effect of gas flow on impedance. (650°C)  
A:CO<sub>2</sub>/O<sub>2</sub>/N<sub>2</sub>=20/10/70  
B:CO<sub>2</sub>/O<sub>2</sub>/N<sub>2</sub>=66/34/0  
Δ:natural diffusion  
□:flow (100cm<sup>3</sup>/min)

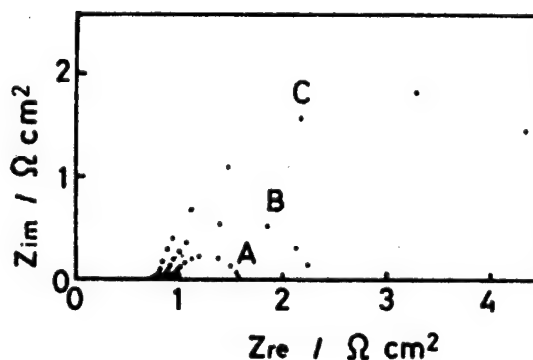


Fig.3 Effect of melt contents on impedance. (650°C)  
A:normal(24%) B:melt added  
C:flooded(58%)

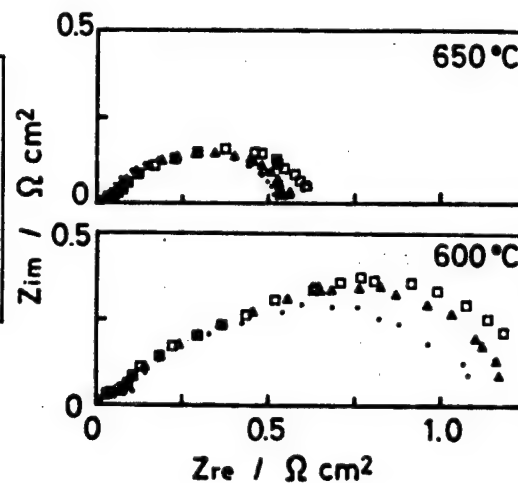


Fig.4 Effect of temperature and discharge. flow(100cm<sup>3</sup>/min)  
CO<sub>2</sub>/O<sub>2</sub>/N<sub>2</sub>=20/10/70  
●:open, Δ:η=-100mV,  
□:η=-200mV

19-01-17-G

REACTION MECHANISM AND KINETICS OF HYDROGEN OXIDATION IN MOLTEN CARBONATES

T. Nishina, I. Uchida

Department of Molecular Chemistry and Engineering, Faculty of Engineering,  
Tohoku University, Aramaki-Aoba, Aoba-Ku, Sendai 980, JAPAN

**Introduction** Nickel has been employed almost exclusively as the anode material in the recent development of the molten carbonate fuel cells (MCFC). Recently, the use of alternative electrode materials is in consideration to reduce the weight of Ni and the cost of the cell. However, electrode kinetic data for hydrogen oxidation at various materials are limited, and there are some conflicting results in previous work with respect to reaction mechanism. In this work, a new method to determine stoichiometric number  $\nu$  is presented, and the electrode kinetics and mechanism of hydrogen oxidation at pure metals and alloys are discussed.

**Experimental** The eutectic mixture of alkali carbonate, (62+38)mol% (Li+K)CO<sub>3</sub>, was used as a solvent. The working electrodes were fully immersed flag type electrodes. Ni, Pt, Ir, Au, Ag, Cu and Ni-Cu alloy were used as electrode material. Electrode kinetic data were measured using the potential step, chronocoulometry, coulstatic transient and ac impedance methods, and subsequently analyzed. Experimental techniques, melt purification, apparatus and cell assembly have been described in a previous paper[1].

**Results and Discussion** It can be shown that one of the excellent features of chronocoulometry is that it is very suitable for the investigation of electrode kinetics and mechanism of fast reactions such as hydrogen oxidation in molten carbonates, while other methods used in this study have less resolution. Therefore, results from this method are emphasized here.

Fig.1 shows typical chronocoulometric responses for hydrogen oxidation at various pure metals. According to J.H. Christie et. al.[2], chronocoulometric transients may be expressed as follows for long time region;

$$Q = \int_0^t i dt = \frac{2K\sqrt{t}}{\lambda\sqrt{\pi}} - \frac{K}{\lambda^2} \quad (1)$$

where

$$K = nFAk_a \{ C_R \exp[\frac{\alpha nF}{RT}(E - E^\circ)] - C_O \exp[-\frac{(1-\alpha)nF}{RT}(E - E^\circ)] \} \quad (2)$$

$$\lambda = k_a \left\{ \frac{\exp[\frac{\alpha nF}{RT}(E - E^\circ)]}{\sqrt{D_R}} + \frac{\exp[-\frac{(1-\alpha)nF}{RT}(E - E^\circ)]}{\sqrt{D_O}} \right\} \quad (3)$$

Therefore,  $Q$  vs  $t^{1/2}$  gives a linear plot, and the diffusion-free current  $K$  and diffusion-included term  $\lambda$  can be obtained from the slope of plot and its extrapolation to  $Q=0$ . Equation (1) was derived for simple charge transfer reactions, but is also applicable to hydrogen oxidation because the long-time data have an identical response[3]. Our data showed good linearity and clear dependence on electrode material.

An especially useful feature of chronocoulometry is the determination of stoichiometric number  $\nu$ . From Eqs.(2) and (3), we may derive the following equation which makes it possible to determine the stoichiometric number:

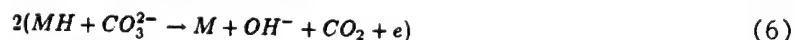
$$\ln \frac{(K/\lambda) - (K/\lambda)_{CL}}{(K/\lambda)_{AL} - (K/\lambda)} = \ln \sqrt{\frac{D_O}{D_R}} + \frac{n}{\nu} \eta \quad (4)$$

Here  $(K/\lambda)_{AL}$  and  $(K/\lambda)_{CL}$  are the saturated value of  $K/\lambda$  at large anodic and



b1

cathodic overpotential respectively. Fig.2 shows polarographic type logarithmic plots of  $K/\lambda$  according to this equation. The linearity of these plots is fairly good, and the slope is 1, which means that stoichiometric number is 2. Therefore, we concluded the reaction mechanism of hydrogen oxidation is as follows[4].



We also constructed Allen-Hickling type plots of  $K$  using  $n/v=1$ . Their linearity was good throughout the range of overpotentials used in this study. The kinetic parameters thus obtained are summarized in Table 1. Exchange current densities at various metals were very high (10 to 200  $\text{mA}/\text{cm}^2$ ), and the effect of electrode material was small compared to that in aqueous solutions. Therefore, it is concluded that Cu can be used as an alternate anode material without any kinetic penalty in MCFC performance.

#### References

- [1] I. Uchida, T. Nishina, Y. Mugikura, K. Itaya; J. Electroanal. Chem., 206(1986)229
- [2] J.H. Christie, G. Lauer, R.A. Osteryoung, F.C. Anson; Anal. Chem., 35(1963)1979.
- [3] L.K. Bieniasz; J. Electroanal. Chem., 195(1985)419, 197(1986)387
- [4] J. Jewulski, L. Suski; J. App. Electrochem., 14(1984)135

Table 1. Kinetic parameters of hydrogen oxidation in (62+38)mol% (Li+K) $\text{CO}_3$  melt at 650°C by using chronocoulometry. Gas composition same as in Fig.1.

	$n/v$	$(D_{\text{ox}}/D_R)$	$I_0 (\text{mA}/\text{cm}^2)$	$\alpha_c$	$\alpha_a$
Ni	1.08	0.11	134.9	0.56	0.44
Pt	1.27	0.33	85.5	0.42	0.58
Ir	1.26	0.38	26.5	0.83	0.17
Au	1.28	0.48	25.1	0.89	0.11
Ag	1.24	0.42	18.0	0.75	0.25

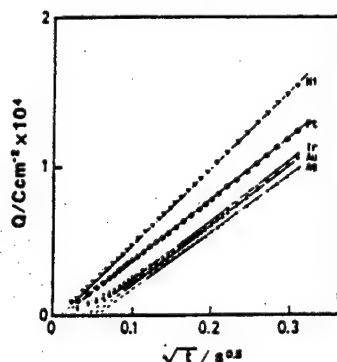


Fig.1 Chronocoulometric responses for hydrogen oxidation at various metal at 650°C.  $P(\text{H}_2):P(\text{CO}_2):P(\text{H}_2\text{O})=0.691:0.296:0.013$  atm. Over potential is 20 mV.

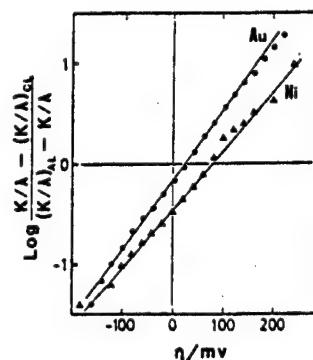


Fig.2 Polarographic type plots of  $K/\lambda$  according to Eq.(4). Notations are same as Fig.1.

19-01-18-P

ELECTRODE MODELLING OF POROUS ANODE OF SINTERED Au AND Ni SPHERES FOR MCFC

T. Nishina, T. Kudo, I. Uchida, J.R. Selman\*

Department of Molecular Chemistry and Engineering, Faculty of Engineering,  
Tohoku University, Aramaki-Aoba, Aoba-Ku, Sendai 980, JAPAN\* on leave from: Department of Chemical Engineering, Illinois  
Institute of Technology, Chicago, IL60616, U.S.A.

**Introduction** In recent research concerning the electrode kinetics of oxygen reduction and hydrogen oxidation in molten carbonates[1,2], we established that the charge transfer processes of both reactions are very rapid. Therefore an important aim of further work is to construct the gas-diffusion type porous electrodes of higher performance than obtained today. The main objective of further study should be to establish the relationship between preparation method and electrode performance. As preliminary steps, it is necessary (1) to clarify the principal factors which dominate the electrode performance; (2) to develop a modeling technique which successfully simulates the polarization behavior of porous electrodes. From this point of view, we report here some results for a newly designed MCFC anode structure using Raney nickel powder and we provide a modeling interpretation for these results.

**Experimental** The porous Raney-Ni (R-Ni) electrodes were prepared by composite coating of R-Ni powder onto reticulated Ni substrate from a nickel plating solution, followed by developing in NaOH solution. The results reported here were obtained on samples having a pore size distribution characterized by three peaks, at 90 $\mu$ m, 3 $\mu$ m, and 0.2 $\mu$ m. Typical specifications of the R-Ni porous electrode were: 54.4% porosity,  $2.8 \times 10^{-2}$  cm<sup>3</sup>/cm<sup>2</sup> total pore volume, and 2.0 m<sup>2</sup>/cm<sup>2</sup> total surface area.

Porous gold and Ni electrodes of simplified structure were prepared by sintering gold spheres(0.1 mm dia.) and nickel spheres(0.3 mm dia.) at 900°C for 15 min. These electrodes were used as model electrodes and their ac impedance behavior compared with predictions of a model.

The electrodes thus prepared were set on a tile of 62mol% Li<sub>2</sub>CO<sub>3</sub>-38mol% K<sub>2</sub>CO<sub>3</sub> with LiAlO<sub>2</sub> matrix, and electrochemical measurements were carried out using a gold counter-electrode and standard reference electrode connected to the anode/tile assembly by a thin electrolyte junction. The cell assembly, melt purification and measurement technique have been described in a earlier paper[3].

**Results and Discussion** The performance of gas-diffusion type electrodes depends strongly on the amount of melt occupying the pores. Fig.1 shows this effect for the polarization conductance of a R-Ni anode. It is obvious that the conductance increases with decreasing amount of melt in the pores. The log-log slope of this plot is almost -1.0, i.e. the conductance is inversely proportional to the amount of melt in the pores. The deviation from this relationship the range below 100 mg/cm<sup>2</sup> appears to be proportional to the amount of R-Ni powder coated on the reticulated substrate, i.e., proportional to the total surface area.

According to the pore size distribution obtained by mercury porosimetry (Fig.2), only 20 mg/cm<sup>2</sup> are needed to fill up all pores smaller than 2  $\mu$ m dia. (It is assumed that such filling starts from the smallest pores.). As

b1

indicated above, the 2  $\mu\text{m}$  pore size may be taken to correspond to the pores between the R-Ni agglomerates which form the active area of the gas-diffusion electrode. Thus, the wet and dry conditions of electrode are shown schematically in Fig.3, where the wet condition corresponds to 40  $\text{mg}/\text{cm}^2$  and the dry one to 20  $\text{mg}/\text{cm}^2$ .

It appears plausible that the smallest pores of the R-Ni function as the electrolyte network, while the agglomerate-sized pores of R-Ni form the active reaction zone and the large reticulated-nickel pores supply the reactant gas. This leads to the conclusion that in the design of high-performance porous electrodes one should seek to separate these three functions by providing appropriately-sized pores for the electrolyte network, the agglomerate spacing, and the gas-supply network. The composite Raney nickel porous electrode is an example of this and appears very suitable as anode for the MCFC.

#### References

- [1] I. Uchida, T. Nishina, Y. Mugikura, K. Itaya; J. Electroanal. Chem., 206(1986)229.
- [2] S.H. Lu, J.R. Selman; J. Electrochem. Soc., 131(1984)2827.
- [3] T. Kudo, T. Nishina, I. Uchida; 28th Battery Symposium, Extended Abstracts, (1987), p.75, Tokyo, November 1987.

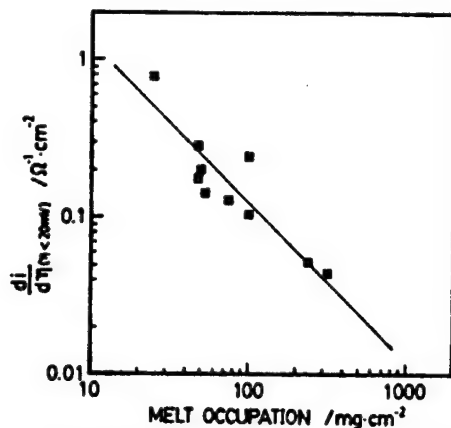


Fig.1 Relationship between the polarization conductance and the amount of melt occupied in the R-Ni porous electrode (log scale).

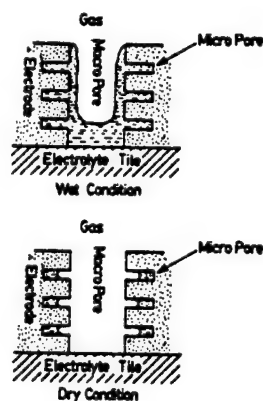


Fig.2 Schematics of a porous gas-diffusion electrode with the wet and dry conditions.

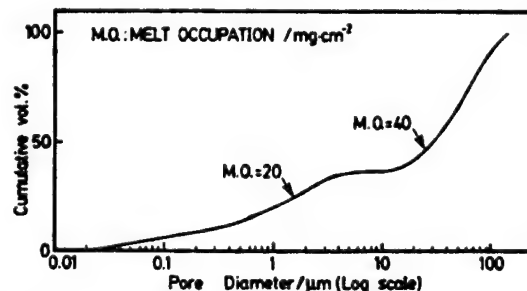


Fig.3 Cumulative pore volume percent of the R-Ni porous electrode.

19-01-19-P

CELL TESTING OF ALTERNATIVE ELECTROLYTES FOR MCFC

Y.Miyazaki, K.Tanimoto, M.Yanagida, S.Tanase, T.Kojima and T.Kodama  
 Government Industrial Research Institute, Osaka  
 1-8-31, Midorigaoka, Ikeda, Osaka, Osaka 563 Japan

Introduction

The Li-rich eutectic carbonate ( $\text{Li}_2\text{CO}_3:\text{K}_2\text{CO}_3=62:38$ ) has been used in molten carbonate fuel cell(MCFC) as electrolyte. This composition is not necessarily the optimum one from the viewpoint of cell endurance, for example, the solubility of NiO in carbonate, vaporization, and the corrosion of wet seal area. One of solutions for these problems is to replace with the alternative carbonate electrolyte. The cells with various compositions in Li/K system were tested and the availability was examined by the cell performance.

Experimental

The carbonate compositions were selected, Li/K=70/30, 62/38, 50/50, 43/57, as alternative electrolyte. The carbonate of each composition was mixed with gamma- $\text{LiAlO}_2$  and electrolyte tile was fabricated by hot-pressing. The small size cell( $10\text{cm}^2$ ) with reference electrode( $\text{Au}:\text{O}_2/\text{CO}_2=1/2$ ) was operated for four days until the cell performance became steady state. After that, the polarizations of anode and cathode were measured and iR drops was determined by the current interrupter technique.

Result

The result is shown in Fig. 1. The anode polarization (iR-free) is slightly varied in the tested composition range, but the cathode polarization is decreased with increasing lithium content. The tendency is similar to IGT's data(1). We will try to discuss this behavior from the viewpoint of the wettability of the electrode interface.

Reference

(1).Project 9150, Final Technical Report, Oct. 1, 1977-Sep. 30, 1978, SAN-1735-4, IGT. Chicago.

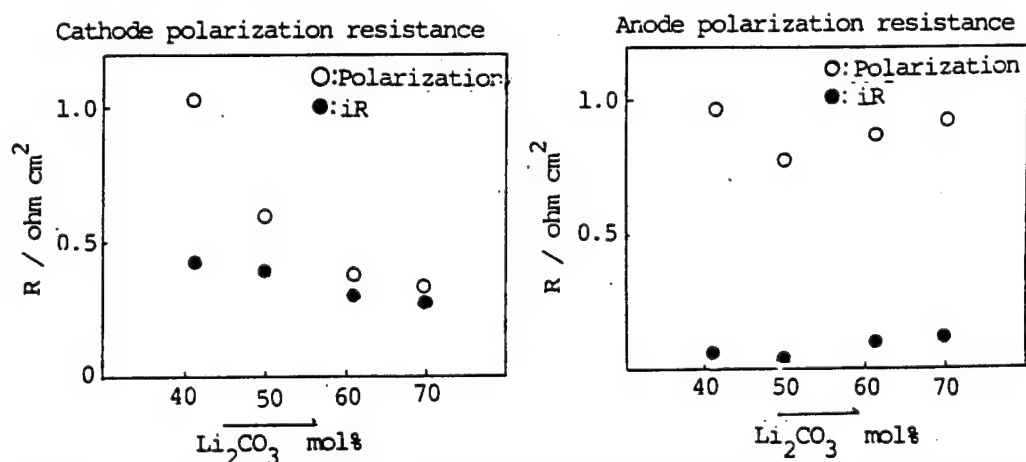


Figure 1. Anode and cathode polarization in various carbonate electrolyte.

b1

21-01-01-K

R&D ON SOFC IN JAPAN AND RELATED PROBLEMS

Masayuki Dokiya

National Chemical Laboratory for Industry

1-1 Higashi, Tsukuba, Ibaraki 305 Japan

1. Introduction

This paper summarizes R&D on solid oxide fuel cell (SOFC) in Japan. Recently, a number of research groups are engaged in research on SOFC in Japan. There are three objectives in these research works;

- (1) to have better understandings on SOFC as future users,
- (2) to fabricate small scale SOFC for co-generation, etc.,
- (3) to fabricate large scale SOFC for on-site or stationary power generation plant (power plant cell).

There is a strong desire to develop SOFC for power plants among Japanese research groups.

SOFC can have various shapes. This is one of the characteristics of SOFC. The fabrication process relates not only with raw materials but also with these cell shapes. Related problems will be discussed in relation with the shapes and the fabrication processes of cells.

2. Financial support for R&D on SOFC in Japan

The R&D in Japan can be grouped as follows according to the financial supports.

- (1) Basic research at universities supported by Ministry of Education.
- (2) Fundamental research at The National Chemical Laboratory for Industry (NCLI) and at Electrotechnical Laboratory (ETL) supported by AIST (Moon-Light Project)
- (3) Development research at private industries supported by MITI; New Energy Development Organization (NEDO, Moon-Light Project) and Petroleum Activation Center (PEC).
- (4) Development research at private industries supported by Tokyo Electric Power Company (TEPCO) or without any support.

3. Cells investigated in Japan

The type of SOFC can be classified as follows:

- (A) Supported tubular single or multi-cell
- (B) Non-supported tubular cell
- (C) Supported planar cell on insulating plate
- (D) Supported planar cell on conducting plate
- (E) Composite membrane cell
- (F) Non-supported planar cell
- (G) Monolithic cell or honeycomb cell

- (1) There are no research groups on the cells of Type (B) and (G) at present; some groups have intention to develop Type (G) in future.
- (2) Many research groups started investigation on single cells of Type (F). It was pointed out that the very thin sintered zirconia film is very fragile to handle by hands. Therefore, some research groups shifted their research to the other type of cell. A few groups, however, remain in this Type (F), when their target is not large scale power plant cells. Partially stabilized zirconia, which is very tough, is being investigated to make the handling of non-supported zirconia films possible.
- (3) Tokyo Gas and Osaka Gas finished a field test of 3 kW module of Westinghouse Cell (Type A) in 1989. Gas companies and Kansai Electric Power Corporation will start another field test of Westinghouse cell (25 kW) next year. ETL

have carried out a feasibility test with a multi-cell stack (1 kW) after their 16 years investigation. TEPCO and Mitsubishi Heavy Industry have been finished a test of a multi-cell module (2 kW) of this Type (A). Several private companies are also performing R&D on this Type (A) multi-cell.

- (4) Type (C) has essentially the same electrical connecting character of tubular cell. It is a planar cell which has an unfolded structure of single or multi tubular cells. In this Type (C) cells, single or multi sets of an electrolyte, electrodes, and an interconnector are mounted on a support plate of zirconia or alumina by dry or wet processes. Z-tek is also developing a planar cell of this type.
- (5) Type (D) is a planar cell fabricated by dry processes. Type (E) is constructed by piling composite plates which are prepared by co-firing the green films of an electrolyte, electrodes, and distributors. Several groups are developing planar cells of Type (C) and (D) aiming large scale power plant cells. NCLI is investigating on Type (E) cell and materials which can make the co-firing process possible.

#### 4. Problems to be solved

The merits of tubular cell are

- (1) strength against thermal stress, and
- (2) easy fabrication technique.

The main demerits of tubular cells are as follows.

- (1) Large internal resistance.
- (2) Necessity of too many cell tubes to construct a power plant.
- (3) Much cost of fabrication.

Increase of current density and elongation of unit tube will contribute to cover these demerits of tubular cells. It will be, however, still difficult to utilize the tubular cells for on-site or stationary power plants, even if improvement could be achieved. The large internal resistance will not restrict the use of tubular cells for the co-generation system, since heat loss can be recovered by a bottoming cycle.

Planar cells attracted much attention, because they are considered to be suitable for power plant cells. Type (C), (D), and (E) are the candidates for this purpose. These planar cells should solve the following problems.

- (1) How to fabricate cells.
- (2) How to design stable cells against thermal stress.

Type (C) and (D) will be fabricated more easily than Type (E), although the production cost will be apparently cheaper for the latter. Type (C) has a kind of dilemma. If this Type (C) can be fabricated by either wet or dry processes, Type (D) and (E) can also be fabricated by the same methods and the latter have smaller internal resistance than the former. The possibility of large scale cell is suspected with Type (E) and (F), because of the difficulty of sintering process. Type (F), which is fabricated by sintering as one piece, will be fairly difficult in enlarging its scale compared to Type (C) or (D). We think, however, that Type (E) is more suitable for a power plant cell than the other type, because it can be fabricated by cheap tape casting process and the composite plates can be enlarged more easily than the case of Type (F).

Increase of current density will be an effective means to reduce the scale of unit cell. Thermal stress is predicted to be the most serious problem for planar cells. It will be the most important factor to reduce the temperature gradient within a cell to release thermal stress. Design of cell configuration will be the key technology to solve this problem. For this purpose, the setting of cooling plates will be an effective means as well as the arrangement of gas inlet and outlet.

b1

21-01-02-G

# Planar Solid Oxide Fuel Cell: Nickel Cermet Anode

T.Kawada, N.Sakai, H.Yokokawa and M.Dokiya,  
National Chemical Laboratory for Industry,  
1-1 Higashi, Tsukuba, Ibaraki, 305 Japan  
and M.Mori  
Central Research Institute for Electric Power Industry,  
2-11-1 Iwato-kita, Komae, Tokyo, 201 Japan

Cermet of nickel and yttria stabilized zirconia (Ni-YSZ) is widely used as a solid oxide fuel cell (SOFC) anode because of its high catalytic activity for oxidation of hydrogen or hydrocarbons and of its thermal expansion coefficient which is relatively compatible with a YSZ electrolyte. In planar SOFC, over-voltage of Ni-YSZ anode appears to contribute dominantly to the total cell voltage drop. Polarization characteristics of Ni-YSZ anodes are highly dependent on their preparation method. During our study to fabricate a planar SOFC, it became necessary to know the relation between anode characteristics and its preparation method in order to search for a better way of stacking cells.

We measured DC and AC polarization behaviors of several Ni-YSZ anodes prepared by different ways. Since we are going to construct a planar cell by a tape casting method, there are two different ways of adhering anode materials on electrolyte substrates, i.e. co-firing of electrodes with electrolytes and slurry coating or screen printing of electrode materials on sintered electrolytes. The latter is easily applied for a small cell, so we studied a typical anodic polarization behavior using the electrodes prepared by this method. Powders of NiO and YSZ were mixed by dry or wet procedure and calcined at 1473-1773 K (pre-calcination temperature,  $T_{pc}$ ). They were crushed again and dispersed in isopropyl alcohol, and the slurry was painted on a YSZ pellet, and then they were baked at 1473-1773 K (baking temperature,  $T_b$ ) for several hours. Polarization characteristics were measured for these electrodes at  $H_2$ - $H_2O$  mixed gas atmospheres using a reference Pt electrode in air. Ohmic drops in the electrolyte and the electrode were subtracted from the measured values by current interruption method.

Polarization behavior of Ni-YSZ cermet electrodes changed drastically with Ni content around 30 vol%, where a drastic change was observed in conductivity of porous Ni-YSZ cermet by Dees et.al.<sup>1)</sup> In this study, Ni content was mainly fixed at 40 vol% to investigate effects of preparation methods.

It was found that the typical polarization curve with a Ni-YSZ cermet anode has a linear region in a  $\log(i)$  vs.  $\eta$  plot (Tafel plot), represented by following equation;  $i = k \exp(2Fn/RT)$ , where  $k$  is a constant (fig.1). Some electrodes showed larger over voltage when preparation conditions were not adequate. AC impedance measurements revealed that these electrodes had a wider frequency dispersion of capacitive impedance compared to such an electrode shown in fig.1. These 'additional' impedance seems to arise from poor

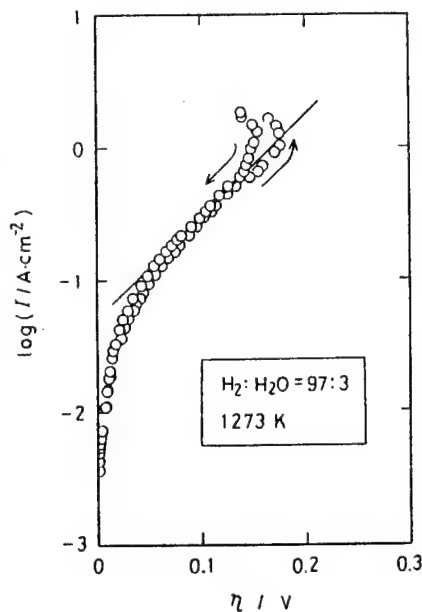


Fig.1 Polarization behavior of a Ni(40V%)YSZ cermet anode. Solid line has a slope of  $2F/RT$ .

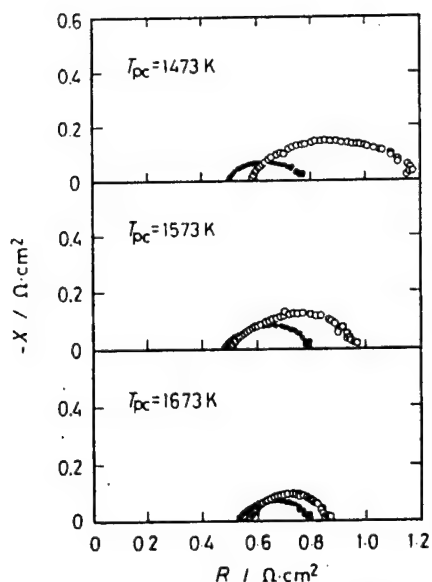


Fig.2 Effect of pre-calcination temperature ( $T_{pc}$ ) on complex impedance of a Ni(40V%)-YSZ cermet anode at 1273K,  $H_2/H_2O=97/3$ , immediately after the fuel gas was introduced; ● and after the initial drift of electrode resistance ceased; ○

precipitated around dispersed YSZ powder, and co-precipitated Ni and Y and Zr oxalates, etc. Drastic improvement, however, has not been achieved up to now.

Another interesting electrode processing method will be to modify the electrode/electrolyte interface by doping cerium oxide. Takahashi et al.<sup>2)</sup> reported that  $Y_2O_3$  doped  $CeO_2$  electrode showed much smaller anodic over voltage than that of Pt on YSZ, and recently, Schouler and Kleitz<sup>3)</sup> reported that  $CeO_2$  doped YSZ surface plays a catalytic role for electrode reaction at  $H_2-H_2O$  atmosphere. In our laboratory, a  $CeO_2$  doped Ni-YSZ cermet anode was prepared by the same method as the Ni-YSZ cermet electrode and its polarization behavior was investigated. It showed, however, rather high anodic over voltage. It is probably because the grain growth was promoted excessively by doped  $CeO_2$ . The optimum preparation condition is thought to be different from that for undoped Ni-YSZ electrodes.

In fabrication of a large scale cell, above mentioned electrode preparation methods or slurry coating may not be used because wide and thin YSZ electrolyte plates are very difficult to be stacked. In our recent studies, it was found that co-firing of relatively large cell stacks may be possible using ceramic foam gas-distributors. To simulate the behavior of such a co-sintered anode, NiO and YSZ mixed powder was painted on a green YSZ pellet and sintered together. Some of them showed a small 'additional' impedance and relatively low over voltages. Further investigations should be carried out to get the optimum co-firing conditions.

[1] D.W.Dees, T.D.Claar, T.E.Easler, D.C.Fee and F.C.Mrazek; J.Electrochem.Soc., **134**, 2141 (1987)

[2] T.Takahashi, H.Iwahara, I.Ito, DENKI KAGAKU, **38**, 509 (1970)

[3] E.J.L.Schouler and M.Kleitz; J.Electrochem.Soc., **134**, 1045 (1987)



b1

21-01-03-G

## A PLANAR TYPE SOLID OXIDE FUEL CELL TECHNOLOGY

Shin-ichi Maruyama, Kazuo Koseki, Tsuneo Nakanishi  
Fuji Electric Corporate Research and Development, Ltd.  
2-2-1 Nagasaka, Yokosuka City, 240-1 JAPAN

### Introduction

Solid Oxide Fuel Cell is considered to be a promising electricity generating facility with high energy conversion efficiency. But the development is behind the other fuel cells because the ceramic components are very fragile. Since the electrolyte is solid and therefore easy to be managed, the various configurations such as a tubular type, a planar type and a honeycomb type have been proposed so far.

Fuji Electric Corporation investigated the technical and economical possibility of solid oxide fuel cell and as a result decided to develop the planar type fuel cell as a trial because a high power density and economical cell stack is expected. To begin with, we have tested a single cell with 10cm<sup>2</sup> electrode to know the preliminary performance, we will herewith report the result of planar type single cell testings.

### Experimental

An electrolyte plate of 50mm diameter and 0.3mm thickness was made of ZrO<sub>2</sub> stabilized with 8 mole% Y<sub>2</sub>O<sub>3</sub>. Ni-ZrO<sub>2</sub> cermet powder as anode and LaMnO<sub>3</sub> powder as cathode were coated on each side of the electrolyte plate with binders and sintered at elevated temperature. The electrolyte plate with both electrodes was assembled in a cell housing made of a heat resistant alloy. 10cm<sup>2</sup> single cell testings were carried out at 1000°C by supplying air and humidified hydrogen.

### Test results and discussion

Figure 1 shows a typical I-V characteristic of the single cell. The cell voltages are 0.72V and 0.47V at 0.5A/cm<sup>2</sup> and 1.0A/cm<sup>2</sup> respectively. From this result, the power density is expected to be more than 0.3W/cm<sup>2</sup> at least. Figure 2 shows the effect of gas utilization on cell voltage. The solid line presents the effect of fuel gas utilization and the dashed line is that of oxydant gas utilization. In both cases the cell voltage decreases as the utilization increases. And the decreasing rate of cell voltage for fuel gas is larger than that for oxydant gas. According to the following Nernst's equation,

$$E = E_0 + \frac{RT}{2F} \ln \frac{P_{H_2}}{P_{H_2O}} + \frac{RT}{4F} \ln P_{O_2}$$

the high concentration of H<sub>2</sub>O lowers the cell voltage. The high polarization at fuel electrode compared to the polarization at air electrode can be explained considering H<sub>2</sub>O generation at fuel side.

Figure 3 shows the effect of temperature on cell voltage and on internal resistance. At above 950°C, the increase of cell voltage with temperature increase nearly corresponds to the decrease of the internal resistance. However at under 950°C the decrease of the cell voltage is larger than the voltage calculated from the internal resistance increase. Also cell voltage decrease with temperature decrease at high current density is much larger than that at lower current density.

This result suggests that cell voltage is much affected by electrode polarization at low temperature and at high current density. Unfortunately we could not make clear which electrode, anode or cathode, is more sensitive to temperature because of the lack of a reference electrode.

Figure 4 is the result of a continuous ten days' operation. The cell voltage was kept stable even at high current density of 0.5 and 1.0A/cm<sup>2</sup>.

### Conclusion

Above mentioned preliminary test results reveal that a planar type solid oxide fuel cell has high power density and stable performance. Hereafter we will proceed the development of stack configuration which withstands various operation conditions and will develop the economical manufacturing process.

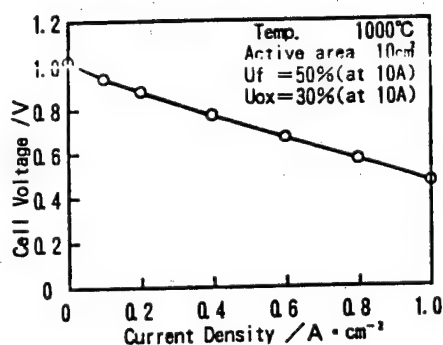


Fig-1 I - V Characteristics

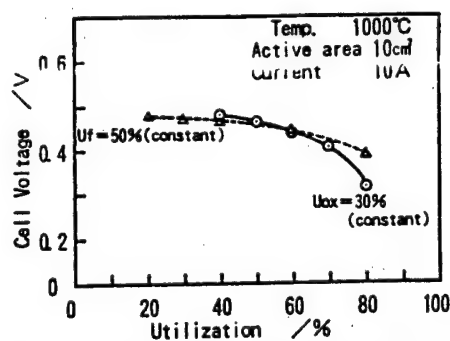


Fig-2 Effect of Gas Utilization on Cell Performance

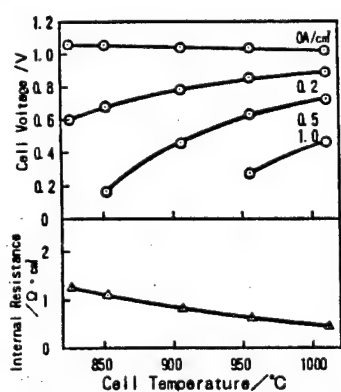


Fig-3 Effect of Temperature on Cell Performance and Resistance

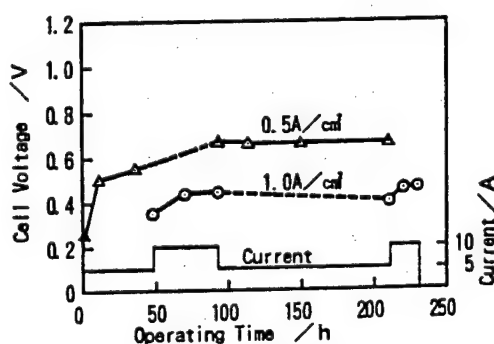


Fig-4 Cell Performance Stability

b1

## 21-01-04-G

### PREPARATION OF PLANER THIN FILM SOLID ELECTROLYTE FUEL CELLS

H. Michibata, H. Tenmei, T. Namikawa, Y. Yamazaki

Tokyo Institute of Technology at Nagatsuta,

4259 Nagatsuta, Midori-ku, Yokohama, 227, Japan

#### 1. INTRODUCTION

It is a fundamental requirement to reduce the electric resistances of high temperature materials used in the solid oxide fuel cells. In particular, the positive electrode materials have been investigated from this point. It was reported that some oxides having perovskite structure showed the suitable characteristics for the positive electrode<sup>1)</sup>. We have been developed the design and the fabrication process of a thin film SOFC<sup>2)</sup>. The proposed thin film cells have a planer structure. The zirconia ( $\text{ZrO}_2\text{-8mol\%Y}_2\text{O}_3$ ) thin film electrolyte was prepared by vacuum evaporation. In this paper, we present a preparation process of  $\text{LaMnO}_3$  thin film cathode for planer thin film solid electrolyte fuel cells by using vacuum evaporation.

#### 2. CATHODE PREPARATION

$\text{LaMnO}_3$  thin film was prepared as follows. First  $\text{La}_2\text{O}_3$  (99.9% purity) and  $\text{MnO}_2$  (99.9%) powders were mechanically mixed and calcined at  $1100^\circ\text{C}$  for 24h. The product was pressed to be pellets with a pressure of  $5000\text{kg/cm}^2$ , then it was sintered at  $1100^\circ\text{C}$  for 24h. The molar ratio of La to Mn of the evaporation source was adjusted to 2 because of the reduction in La content during the evaporation. The evaporation condition is shown in Table 1. The films were deposited on PSZ films, and they were oxidized at  $800^\circ\text{C}$  for 1h. The phases of the prepared films were examined by X-ray diffraction analysis. The PSZ electrolyte thin films were fabricated in the same manner shown in the previous report<sup>3)</sup>. The thickness and the diameter of the prepared cathode of the test cell are  $0.4\mu\text{m}$  and  $3\text{mm}$ , respectively.

#### 3. RESULTS and DISCUSSION

Composition deviation during the evaporation process was carefully examined by EDAX and X-ray diffraction analysis. The diffraction pattern of as-deposited film showed an amorphous structure. The X-ray diffraction patterns of oxidized films are shown in Figure 1. When the film was evaporated with a source material having the composition of  $\text{La/Mn}=1$ , the content of La in the deposited film largely lowered from the stoichiometric value of  $\text{LaMnO}_3$ , and the most part of the annealed film was a  $\text{MnO}_2$  phase containing a small amount of  $\text{LaMnO}_3$ . When the film was deposited with a source material of  $\text{La/Mn}=4$ , the most part of the film was  $\text{La}_2\text{O}_3$  and the other was  $\text{LaMnO}_3$ . These results can be summarized that homogeneous  $\text{LaMnO}_3$  films are prepared by evaporating sintered source materials, and the optimum composition of the source material is  $\text{La/Mn}=2$ .

The thin film cells were tested with hydrogen as fuel gas and air as oxidizing gas. The flow rate of the fuel gas was  $50\text{ml/min}$ . Leaks of the fuel gas were carefully checked throughout the experiment. When the cell test assembly was heated, the cell voltage was detected from  $300^\circ\text{C}$ . The maximum open circuit voltage was  $0.8\text{V}$  at  $700^\circ\text{C}$ . A linear relationship between cell voltage and current was observed for various temperatures as

shown in Figure 2. The maximum current and the maximum output power were 0.7mA and 0.14mW, respectively (Figure 3). By comparing the maximum current and the maximum output power measured with  $\text{LaCoO}_3$  thin film cathode<sup>4)</sup>, these values clearly demonstrated that the thin film cathode of  $\text{LaMnO}_3$  is superior to that of  $\text{LaCoO}_3$ .

#### REFERENCE

- 1) C.S. Tedmon, Jr., H.S. Spacil, S.P. Mitoff, J. Electrochem. Soc., 116, 117 (1969).
- 2) Y. Yamazaki and T. Namikawa, Abstract 340, p514, The Electrochemical Society Extend Abstracts, Vol. 85-2, Las Vegas, Nevada, Oct. 13-18, 1985
- 3) H. Michibata, T. Namikawa, and Y. Yamazaki, Extended Abstract, 172th Fall Meeting Electrochem. Soc., 87-2, 268 (1987)
- 4) H. Michibata, T. Namikawa, and Y. Yamazaki, DENKI KAGAKU, Vol. 57, No. 3, 255 (1989)

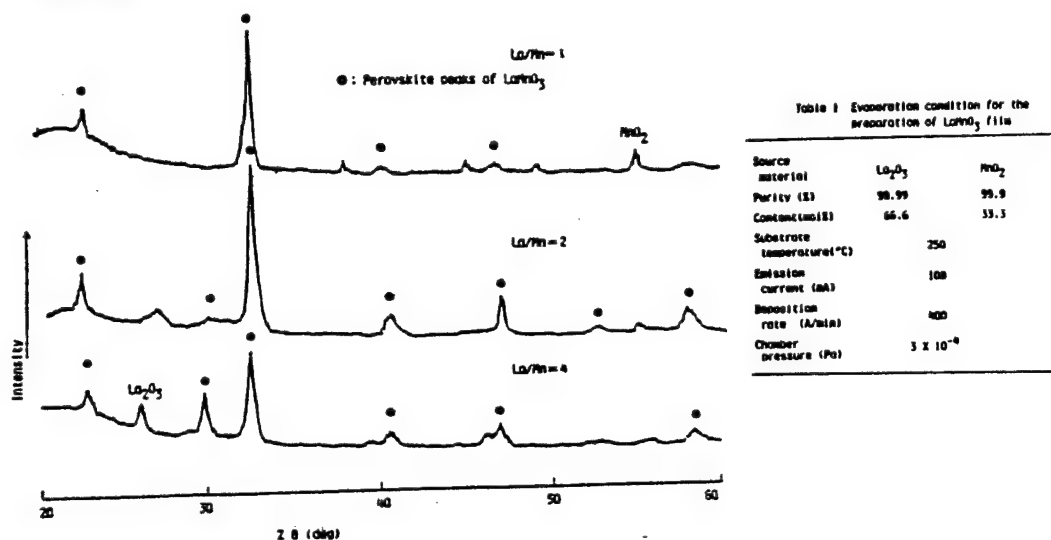


Fig. 1 X-ray diffraction patterns of the evaporated and oxidized films for various source compositions

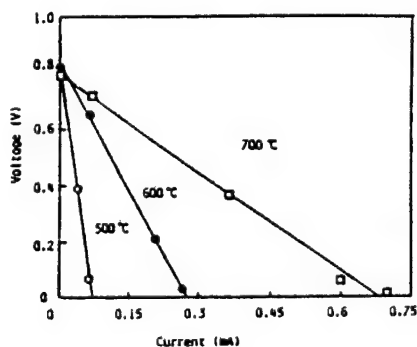


Fig. 2 Voltage vs. current for various temperature

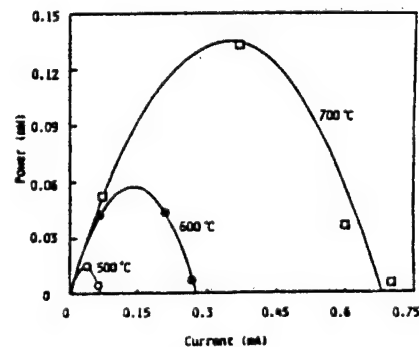


Fig. 3 Power vs. current for various temperature

b1

## 21-01-05-G

### Solid Oxide Fuel Cell with Stabilized Zirconia and Doped Ceria Thin Film

K. Eguchi, T. Setoguchi, H. Itoh, H. Arai

Department of Materials Science and Technology, Graduate School of Engineering Sciences, Kyusyu University 39, 6-1 Kasugakoen, Kasuga-shi, Fukuoka 816, Japan

Solid oxide fuel cells (SOFC) have been actively investigated as a highly efficient power generation system. In this type of fuel cells, stabilized zirconia has been generally used as an electrolyte. It is important to establish thin or thick film fabrication technique of the electrolyte such as yttria stabilized zirconia (YSZ), because of its low conductivity. In the present study, we adopted plasma spraying, slip casting, slurry coating, and RF-ion plating methods as the film fabrication techniques. The films were evaluated from the fuel cell performance. Thick films of a electrolyte and electrodes were prepared by plasma spraying method using Onoda Cement Co., Ltd. APS7000 and by RF-ion plating method using Showa Shinku SGC-8M. Current-voltage (I-V) or current-power (I-P) characteristics of the hydrogen-oxygen fuel cell was measured in a flow system. The overpotential of electrodes was evaluated by the current interruption method.

The stabilized zirconia electrolyte was first prepared by the slip casting method. The I-V characteristics of the fuel cell with this electrolyte, NiO-YSZ cermet anode and  $\text{La}_{0.6}\text{Sr}_{0.4}\text{MnO}_3$  cathode was measured at 1000 °C as shown in Fig. 1. Open circuit voltage (OCV) of the cell was close to the theoretical value which is estimated from the partial pressures of  $\text{H}_2$ ,  $\text{H}_2\text{O}$ , and  $\text{O}_2$ . High OCV results from high relative density (more than 95%) of the film. Pores were hardly observed by SEM observation of the fracture surface. The cell resistance estimated from the slope of I-V curve is plotted as a function of the electrolyte thickness in Fig. 2. The electrolyte resistance calculated from the conductivity of YSZ and the electrolyte thickness, and electrode resistance, are also shown in Fig. 2. The contribution of the electrode resistance in overall resistance increased with decreasing electrolyte thickness. Although the slip casting technique has an advantage in obtaining dense film, the flat cell still maintains many problems including the cell design.

Porous electrode substrates were prepared by sintering of NiO-YSZ or  $\text{La}_{0.6}\text{Sr}_{0.4}\text{MnO}_3$  powder. Yttria stabilized zirconia film was fabricated by slurry coating on the NiO-YSZ cermet porous substrate, whose porosity and permeation coefficient are about 34% and  $28.7\text{mm}^4\text{g}^{-1}\text{sec}^{-1}$ , respectively. After aqueous suspension of YSZ was coated on the porous cermet, the sample was heated at 1400°C. The YSZ film contained a large number of cracks after heating, because of the difference in shrinkage between the substrate and film. The cracks of YSZ could be eliminated by repeating the film coating and heating process. The electrolyte is about 100  $\mu\text{m}$  in thickness after five times of coating process. The OCV of fuel cell thus fabricated by the slurry coating procedure was 0.67V.

Yttria stabilized zirconia film was deposited on the porous  $\text{La}_{0.6}\text{Sr}_{0.4}\text{MnO}_3$  substrate by the RF-ion plating method. The substrate

porosity is about 35% and permeation coefficient is about  $6.6\text{mm}^4\text{g}^{-1}\text{sec}^{-1}$ . The I-V characteristic attained so far is not satisfactory as shown in Fig. 1. The OCV was smaller than the theoretical value. This method is suitable to prepare thin film on flat substrate, but is not on porous substrate. However, leakage through the YSZ film may be suppressed by depositing under the appropriate condition.

The tubular type fuel cell was fabricated by plasma spraying method. Nickel oxide, yttria stabilized zirconia, and  $\text{La}_{0.6}\text{Ca}_{0.4}\text{MnO}_3$  were plasma sprayed in sequence on a porous alumina tube. The OCV of the single cell (0.9V) was lower than the theoretical one. The micropores remaining in the electrolyte are the reason for low OCV. On the other hand, the Ni and  $\text{La}_{0.6}\text{Ca}_{0.4}\text{MnO}_3$  films fabricated by this method were too dense to be used as electrode. The porosity of the electrodes could be changed with spraying angle to the substrate (alumina porous tube). The permeation coefficient of  $\text{N}_2$  became large with setting the plasma spraying gun at a smaller angle to the substrate surface. And the permeation coefficient of the electrode film sprayed at  $45^\circ$  was  $4.5 \times 10^{-1}\text{mm}^4\text{g}^{-1}\text{sec}^{-1}$ , whereas that sprayed at  $90^\circ$  was  $0.78 \times 10^{-1}\text{mm}^4\text{g}^{-1}\text{sec}^{-1}$ . The short circuit current density (SCC) of the plasma sprayed single cell was  $0.98\text{A}\cdot\text{cm}^{-2}$ . But the resistance of the single cell (ca.  $9.56\ \Omega$ ) was still larger than the electrolyte resistance estimated from the conductivity of YSZ ( $3.09\ \Omega$ ). Four cells stacking fabricated by the same procedure exhibited OCV of 3.5V, SCC of  $1.04\text{A}\cdot\text{cm}^{-2}$ , and max power of  $0.82\text{W}\cdot\text{cm}^{-2}$ . The whole cell resistance of this stack was  $30.86\ \Omega$ , which is closed to quadruple of the resistance of the single cell. Preparation of the ceria-based solid oxide electrolyte was also investigated using plasma spraying method.

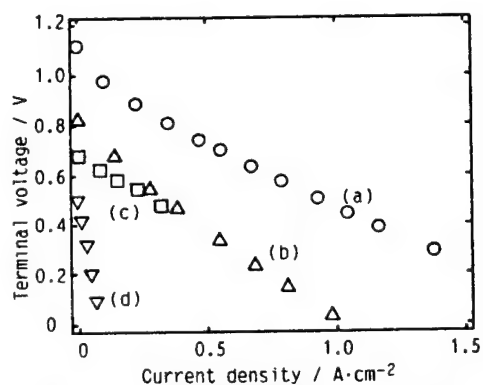


Fig. 1 I-V characteristics of fuel cell fabricated by various method at  $1000^\circ\text{C}$ .  
 $\text{H}_2$ , NiO 15at%YSZ  $\text{La}_{0.6}\text{Sr}_{0.4}\text{MnO}_3$ ,  $\text{O}_2$   
 (a) slip casting method,  $t=150\mu\text{m}$   
 (b) plasma spraying method,  $t=200\mu\text{m}$   
 (c) slurry coating method,  $t=100\mu\text{m}$   
 (d) RF-ion plating method,  $t=42\mu\text{m}$   
 $t$ : electrolyte thickness  
 1) Cathode material is Pt.

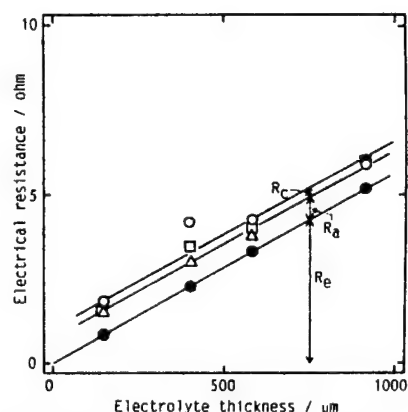


Fig. 2 Cell resistance as a function of electrolyte thickness at  $1000^\circ\text{C}$ .  
 ○: overall cell resistance,  $R_{\text{cell}}$  estimated from I-V curve  
 ●: electrolyte resistance,  $R_e$  expected from the conductivity  
 △:  $R_e$  + anodic resistance,  $R_a$   
 □:  $R_e$  +  $R_a$  + cathodic resistance,  $R_c$   
 $R_a$  and  $R_c$  were measured by current interruption method

b1

21-01-06-G

THE ELECTRICAL PROPERTY AND THE MICROSTRUCTURE OF  $ZrO_2$  BASED SOLID ELECTROLYTES

A. Yamashita\*, A. Nohtomi\*, H. Ohno\*\*, T. Nagasaki\*\*, N. Igawa\*\*

\* Nagasaki Technical Institute, Mitsubishi Heavy Industries, Ltd.

\*\*Material Innovation Laboratory, Japan Atomic Energy Research Institute

Introduction; Zirconia doped with trivalent cation have been of special interest in a variety of applications as steam electrolysis, oxygen pumps and sensors. In these applications the phase stability of  $ZrO_2$  and the relationship between the phase of  $ZrO_2$  and its conductivity both play an important role. Nevertheless, only a few researches have been done in this area.

This paper aims at evaluating the phase stability of the  $ZrO_2$ -12wt% $Y_2O_3$  (12YSZ) by using laser raman spectroscopy. It also aims at establishing the relationship between the phase of  $ZrO_2$  and its conductivity.

Experimental; Raman spectra of the 12YSZ powder, sintered disk and after plasma spraying were measured. The starting material for the 12YSZ was prepared by calcining the mixture of the zirconium and yttrium oxides. The powder of the 12YSZ was compressed into disc, 20mm in diameter and ca. 4mm thick, under hydrostatic pressure of 150MPa and sintered at 1773K in air for 10 hours. Thin (~100 $\mu$ m) layers of 12YSZ were prepared by plasma spraying directly onto porous CaO stabilized ZrO tube. Chips of these coatings were aged in air in an electric furnace at 1273K for 10 hours and preliminary treated with a D.C. current density of 200mA/cm<sup>2</sup> at 1173K for 600 hours. For measuring conductivity, two samples of Zirconia with monoclinic (2mol%  $Y_2O_3$ ) and cubic (8mol%  $Y_2O_3$ ) were prepared by calcining the mixture of the zirconium and yttrium oxides. Electrical conductivity of the  $ZrO_2$  were carried out by means of a complex impedance method over the frequency range from 5Hz ~ 13MHz. Platinum electrodes were applied to the sintered disks by coating the surface with Pt paste.

Results; Figure 1 shows the Raman spectra of 12YSZ. It is seen that the starting powder and the sintered sample was primarily a cubic phase and small amount of tetragonal phase also existed. In plasma spraying samples, while the as sprayed sample was primarily a cubic phase, after aging sample shows the tetragonal and the cubic phase. The tetragonal and the monoclinic phase was observed in the preliminary treatment with D.C. current. Figure 2 shows the electrical conductivities of the  $ZrO_2$ -8mol%  $Y_2O_3$  (cubic),  $ZrO_2$ -1.4mol%  $Y_2O_3$  (tetragonal) and  $ZrO_2$  (monoclinic) as function of temperature, respectively.

The conductivity of monoclinic phase of  $ZrO_2$  was one or two order of magnitude lower than those of cubic or tetragonal phase of  $ZrO_2$ . Accordingly the results obtained here suggest that in case of applying the  $ZrO_2$  based solid electrolytes to steam electrolysis, oxygen pumps and the other electrochemical devices, it is necessary to inhibit the appearance of the monoclinic phase of  $ZrO_2$  as much as possible.

T.K. Gupta et al.: J. Electrochem. Soc., 128(1981) 929.

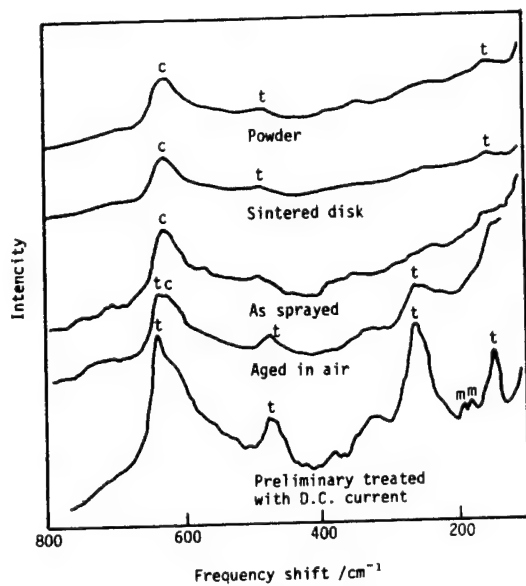


Figure 1 Raman spectra of  $\text{ZrO}_2\text{-12wt\%Y}_2\text{O}_3$ . m, t and c are monoclinic, tetragonal and cubic phase, respectively

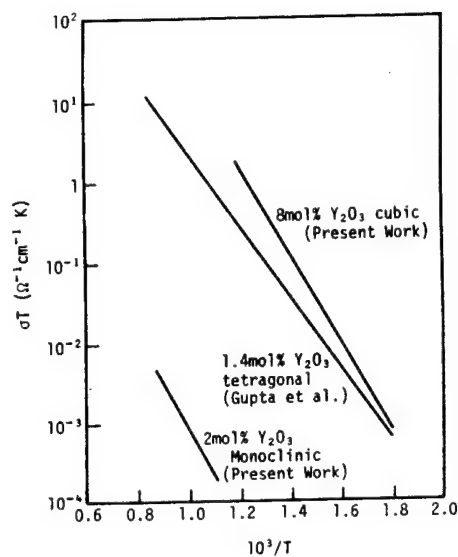


Figure 2 Temperature dependence of electric conductivity for  $\text{ZrO}_2$



b1

21-01-07-G

**A PROTON CONDUCTOR SYNTHESIZED BY THE THERMAL REACTION OF ISOPOLYTUNGSTATE.**

K. Nagata, Y. Taninaka, S. Deki, Y. Kanaji  
Faculty of Engineering, Kobe University, Rokkodai-cho, Nada-ku, Kobe 657  
Japan

**Introduction:** Solid ionic conductive materials have been extensively investigated for basic and technological aspects. Particularly, much attention has been paid to protonic conductor for useful applications such as fuel cells, electrochromic displays or sensors. We have reported that the isopolytungstates with various  $M^+/WO_3$  ratios ( $M^+$ :  $Li^+$ ,  $Na^+$  or  $K^+$ ) could be prepared by cation exchanging of tungstate solution with ion-exchange resin and they showed good ionic conductivity<sup>1)</sup>. In this paper, the isopolytungstates were prepared by the cation exchanging method, pyrolyzed at various temperatures up to 580°C, and their structure and electrical properties were investigated and discussed.

**Experimentals:**  $WO_3$  was dissolved into 1M NaOH aqueous solution for preparing the mother liquor. After pH was controlled with ion-exchange resin, the mother liquor was evaporated and gave hydrate sodium isopolytungstates with various  $Na^+/WO_3$  ratios as a powder. These sodium isopolytungstates were calcined at various temperatures up to 580°C under  $N_2$  gas flow. Samples were characterized by chemical analysis, X-ray diffraction, TG-DTA and IR spectroscopy.

Conductivity was measured by AC four probe method with impedance analyzer. The transport number of proton was measured by the mean of emf measurement of a galvanic cell<sup>2)</sup>.

**Results & Discussion:**  $Na^+/WO_3$  ratio,  $r$ , of sodium isopolytungstates was 0.38 - 1.13. Samples, calcined at temperatures up to 340°C, were all amorphous by X-ray diffraction analysis. Those calcined at 480°C were crystalline and assigned to the mixtures of  $WO_3$ ,  $Na_2W_6O_{19}$ ,  $Na_2W_4O_{13}$ ,  $Na_2W_2O_7$  and  $Na_2WO_4$  and their composition varied with  $Na^+/WO_3$  ratio of raw sodium isopolytungstates. Sodium isopolytungstate had a good protonic conductivity. Their electrical conductivity,  $\sigma$ , was  $10^{-2}$  -  $10^{-4}$  S · cm<sup>-1</sup> at 50 °C and depended on  $r$ . That of crystalline samples, calcined at 480 °C, was  $10^{-4}$  -  $10^{-9}$  S · cm<sup>-1</sup> at 50 °C and remarkably depended on  $r$ . The transport number of proton in sodium isopolytungstates was  $t_H = 1$  for  $r > 0.7$  and  $t_H < 1$  for  $r < 0.7$ . It was clear that the carrier of the electric conduction was not only protons but also electrons or sodium ions for  $r < 0.7$ , and electrons for the samples calcined at 480°C.

1) S. Deki et al., 57th National Meeting of the Chemical Society of Japan(1988).

2) Y. Ozawa et al., Denki Kagaku, 51, 350(1983).

21-01-08-P

Planar Solid Oxide Fuel Cell: Chemical Thermodynamic Considerations on Materials

H. Yokokawa, N. Sakai, T. Kawada and M. Dokiya  
National Chemical Laboratory for Industry,  
Tsukuba Research Center, Ibaraki-305, Japan

The chemical thermodynamic considerations have been made to clarify the thermodynamic features of the compatibility among various materials associated with a planar solid oxide fuel cell; special emphases are placed upon correlation between the volatility and the sinterability of  $\text{LaCrO}_3$ -based separator and upon effects of metal nonstoichiometry of lanthanum-strontium manganate perovskites on their reactivity with yttria doped zirconia (YSZ).

The lanthanum chromite based perovskites exhibit a high electrical conductivity at a hydrogen atmosphere as well as in air; this makes it attractive to use it as a separator for a planar SOFC. Even so, this materials show ill-sinterability in air; the establishment of an appropriate method of making a dense film of lanthanum chromite is therefore a crucial point in developing a solid oxide fuel cell. Thus, Isenberg et al. developed an electrochemical vapor deposition (EVD) process for a tubular cell[1]; to construct a monolithic cell, Flandermeyer et al. found sintering aids of fluoride mixtures to make dense plates by firing in air green films made with doctor blade method[2].

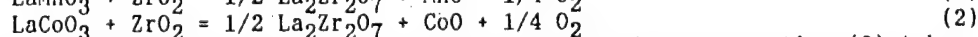
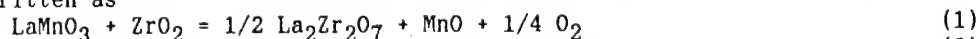
In our investigation on the sinterability of Ca doped lanthanum chromites, we found that perovskites of a slightly chromium deficient composition show a remarkably high densification in air. To clarify thermodynamically the nature of these facts, the chemical equilibria calculation has been made using CTC/SOLGASMIX system[3]. In the absence of experimental thermodynamic properties of lanthanum chromite and alkaline earth chromites, estimation has been made using the correlation between tolerance factor and the enthalpy of formation[4]. Analyses on the  $\text{MgO-Cr}_2\text{O}_3\text{-La}_2\text{O}_3$ ,  $\text{CaO-Cr}_2\text{O}_3\text{-La}_2\text{O}_3$ , and  $\text{SrO-Cr}_2\text{O}_3\text{-La}_2\text{O}_3$  systems have revealed the following interesting features between the sinterability and the phase relations including equilibrium vapor pressures:

- (1) The correlation with the tolerance factor suggests that there can be a narrow but non-zero width of chromium content as shown in Fig. 1;
- (2) The equilibrium vapor pressure shows a drastic change from  $\text{Cr}_2\text{O}_3$ -rich side to  $\text{Cr}_2\text{O}_3$  poor side of perovskites; this feature can explain why  $\text{La}(\text{Sr})\text{CrO}_3$  and  $\text{La}(\text{Ca})\text{CrO}_3$  can be well sintered in the presence of  $\text{SrCO}_3$  and  $\text{CaO}$ , respectively.
- (3) In the  $\text{SrO-Cr}_2\text{O}_3\text{-La}_2\text{O}_3$  and  $\text{MgO-Cr}_2\text{O}_3\text{-La}_2\text{O}_3$  systems, perovskite phase is in equilibrium with  $\text{La}_2\text{O}_3$ ; from the technological point of view, this equilibration with  $\text{La}_2\text{O}_3$  is unfavored.
- (4) In the  $\text{CaO-Cr}_2\text{O}_3\text{-La}_2\text{O}_3$  system, perovskite phase can be in equilibrium with  $\text{CaO}$  when  $\text{CaO}$  content is greater than about 0.1 as shown in Fig. 1.

In view of these phase relations, we can conclude that the lanthanum calcium chromite,  $(\text{La}_{1-x}\text{Ca}_x)(\text{Cr}_y\text{Ca}_{1-y})\text{O}_3$ , is quite suitable for a separator.

Recent investigations have revealed that the air electrode/electrolyte interaction may take place above 1473 K. In order to clarify the thermodynamic nature of these reactions, the chemical equilibria calculation has been also made using CTC/SOLGASMIX. The main conclusions can be summarized as follows:

- (1)  $\text{LaMO}_3$  ( $\text{M}=\text{transition metal}$ ) perovskites can react with  $\text{ZrO}_2$  to form  $\text{La}_2\text{Zr}_2\text{O}_7$  and transition metal oxide with lower valence; typical reactions can be written as



Reaction (1) proceeds in air only above 2000 K, whereas reaction (2) takes

b1

- place even at 1273 K. This reaction can be regarded as a combination of formation of  $\text{La}_2\text{Zr}_2\text{O}_7$  and the reductive decomposition of  $\text{LaMO}_3$ .
- (2) Many investigators on the other hand revealed that the  $\text{LaMnO}_3$  based perovskites actually reacted with  $\text{ZrO}_2$  at 1673 K. This contradiction to the above results can be resolved by taking into consideration the metal nonstoichiometry of  $\text{LaMnO}_3$  perovskites. Typical results of the chemical equilibria calculation (Fig. 2) show that the composition region of perovskite phase is located at Mn oxide rich side. Note that the stable region can be divided into two regions in terms of reactivity with  $\text{ZrO}_2$ ; that is, perovskites in the Mn-oxide poorer region can react with  $\text{ZrO}_2$  to form  $\text{La}_2\text{Zr}_2\text{O}_7$  or  $\text{SrZrO}_3$ .
- (3) A large number of A-site vacancies can be formed in the nonstoichiometric perovskites. This strongly suggests that sintering of manganese perovskites may occur even at 1273 K during a long period of time.

#### REFERENCES

- [1] A. O. Isenberg Solid State Ionics **3/4**, 431(1981).
- [2] B. K. Flandermeyer et al. National Fuel Cell Seminar 1986, p68.
- [3] H. Yokokawa et al. J. Natl. Chem. Lab. **83** special issue (1988).
- [4] H. Yokokawa et al. J. Am. Ceram. Soc. **72**, 152(1989).

Fig.1 calculated phase relations in  $\text{CaO}-\text{Cr}_2\text{O}_3-\text{La}_2\text{O}_3$  system at 1873 K in air: calculated vapor pressure of  $\text{CrO}_3(\text{g})$  is given.

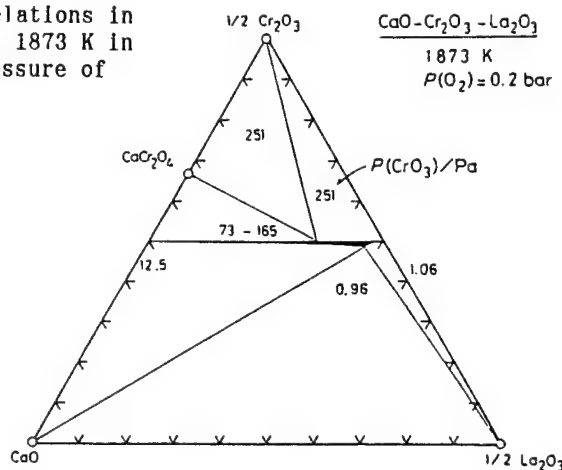
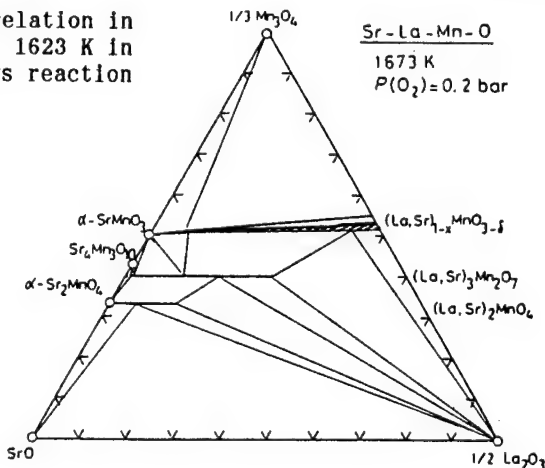


Fig. 2 calculated phase relation in  $\text{SrO}-\text{Mn}_2\text{O}_4-\text{La}_2\text{O}_3$  system at 1673 K in air: the shaded area shows reaction zone with  $\text{ZrO}_2$ .



21-01-09-P

Planar Solid Oxide Fuel Cell: Ca Doped Lanthanum Chromite Separator

N.Sakai, T.Kawada, H.Yokokawa and M.Dokiya  
 National Chemical Laboratory for Industry,  
 1-1 Higashi, Tsukuba, Ibaraki, 305 Japan  
 and T.Iwata  
 Fuji Electric Corporate Research and Development, Ltd.,  
 2-2-1 Nagasaka, Yokosuka, Kanagawa, 240-01 Japan

The alkali-earths doped lanthanum chromites such as  $\text{La}_{1-x}\text{Sr}_x\text{CrO}_3$ ,  $\text{La}_{1-x}\text{Ca}_x\text{CrO}_3$  or  $\text{LaCr}_{1-y}\text{Mg}_y\text{O}_3$  have high melting point (above 2600 K) and sufficient electrical conductivity, and can be the most hopeful materials for separators of SOFC. In a planar SOFC, it is necessary to obtain a dense plate of lanthanum chromite by tape casting method. However, it is difficult to densify these materials in air because of volatilization of chromium components.<sup>[1]</sup> We have studied composition dependence on sinterability of calcium doped lanthanum chromite, and we found that (1) sinterability of this material depended on calcium content in the samples of  $\text{La}_{1-x}\text{Ca}_x\text{CrO}_3$ , and that (2) the samples of chromium poor composition  $(\text{La}_{1-x}\text{Ca}_x)(\text{Cr}_{1-y}\text{Ca}_y)\text{O}_3$  showed high densification enough to fabricate gas-tight dense plates of lanthanum chromite.

These chromium poor lanthanum chromites were prepared by wet procedure: Nitrates of La, Ca and Cr and an excess amount of citric acid were dissolved in water and heated. After the evaporation of water, glassy products of metal citrates were obtained. These products were dried and calcined in air at 1273 K-1473 K to obtain perovskite compounds. These calcined powders were then crushed and shaped into pellets and sintered in air at 1873 K. The X-ray diffractometric results (XRD) revealed that precipitation of second phases such as  $\text{La}_2\text{O}_3$  or  $\text{CaO}$  was not observed when chromium deficit was within 4 %, and near this bound, significant improvement of sinterability occurred. The densities of these samples approached 95 % of theoretical density, and these chromium poor perovskite samples showed also weak volatility of chromium components. The images of scanning electron microscopy revealed that drastic changes of particle size and of sintering features also occurred near this bound. In the non-chromium deficient samples, particle size varied in the region from  $3 \times 10^{-6}\text{m}$  to  $5 \times 10^{-6}\text{m}$ , and no indication of sintering was recognized. Slight deficiency of chromium (about 3-4 %) brought remarkable growth and sintering of particles, which indicated the change of sintering mechanism.

These chromium poor lanthanum chromite powders were used to make films by doctor blade, and sintered at 1650 K-1850 K to measure the change of shrinkage. The relative shrinkage of samples varied 10-25 %, and depended on their composition and sintering temperatures. In our study to fabricate a planar SOFC, we think tape casting and co-firing methods are the simplest and the most hopeful. To do so, it is necessary to fit the shrinkage of separator to that of other cell components such as anodes (nickel-zirconia cermet), cathodes (strontium doped lanthanum manganate) and electrolytes (YSZ: yttria-stabilized zirconia). We can control the shrinking behavior of lanthanum chromite by changing its composition, and succeeded in fitting the shrinkage of lanthanum chromites to that of YSZ (Fig.1). This makes it more feasible to construct a planar cell by co-firing method.

Electrical conductivities of these chromium poor calcium doped lanthanum chromites were measured by four probe method. The magnitude of electrical conductivity depended linearly on total calcium content, and was essentially the same as that of non chromium deficient samples. However, the samples which had precipitation of  $\text{CaO}$  or  $\text{La}_2\text{O}_3$  showed relatively low conductivities. Oxygen partial pressure dependence of electrical conductivity was also measured in

flowing gaseous mixtures of  $O_2/Ar$ ,  $H_2/CO_2$ , and  $H_2/H_2O$ . Three samples, which had no second phase in XRD results, were selected and measured. These chromium poor samples kept sufficiently high electrical conductivity at  $p(O_2)$  from 0.2 bar (in air) to  $10^{-8}$  bar at 1416 K (Fig.2).

The separator of SOFC is exposed to both oxidative and reductive atmospheres at high temperatures (above 1200 K), and chemical stability of chromium poor lanthanum chromites is an important point. In the samples which had no second phase, the chemical stability was confirmed by the results of electrical conductivity measurement in a reductive atmosphere (Fig.2). When the total calcium content was under 10 %, chromium deficiency (more than 4 %) brought precipitation of  $La_2O_3$ , and these samples were disintegrated because of hygroscopic nature of  $La_2O_3$ . When the total calcium content was above 10 %, chromium deficiency brought precipitation of  $CaO$ . We could not observe any bad effects of  $CaO$  on chemical stability of samples in this study.

We can conclude that chromium poor lanthanum chromites have a great feasibility as suitable materials for planar SOFC separators.

[1] L.GROUPP and H.U.ANDERSON, J.Am.Ceram.Soc., 59(1976)449

[2] B.F.FLANDERMEYER, M.M.NASREALLAH, D.M.SPRLIN and H.U.ANDERSON, High.Temp.Sci., 20(1985)259

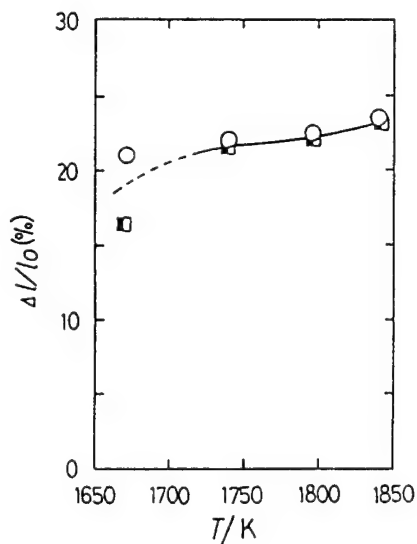


Fig.1 Shrinkage of YSZ (○) and  $(La_{1-x}Ca_x)(Cr_{1-y}Ca_y)O_3$  (■) as a function of sintering temperature.

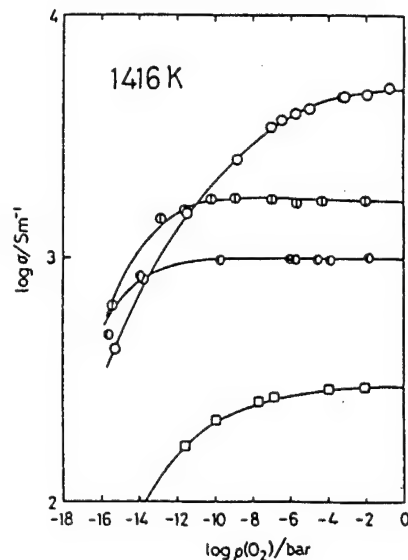


Fig.2 Oxygen pressure dependence of electrical conductivities of  $(La_{0.7}Ca_{0.3})(Cr_{0.95}Ca_{0.05})O_3$  (○),  $(La_{0.82}Ca_{0.18})(Cr_{0.97}Ca_{0.03})O_3$  (⊙),  $(La_{0.97}Ca_{0.03})(Cr_{0.97}Ca_{0.03})O_3$  (●) and  $LaCr_{0.9}Mg_{0.1}O_3$  (□) (Flandermeier, et al. [2])

21-01-10-P

Planar Solid Oxide Fuel Cell: Lanthanum Manganate Based Cathode

M. Mori and R. Ishikawa,  
 Central Research Institute for Electric Power Industry,  
 2-11-1 Iwato-kita, Komae, 201 Japan  
 and  
 N. Sakai, T. Kawada, H. Yokokawa, and M. Dokiya,  
 National Chemical Laboratory for Industry,  
 1-1 Higashi, Tsukuba, Ibaraki, 305 Japan

In order to co-fire green components of solid oxide fuel cell (SOFC), it is required to develop a stable and ill-sinterable cathode material. Although  $\text{La}(\text{Sr})\text{MnO}_3$  has been widely used as a cathode, this material will degrade during a co-firing process at temperatures above 1700 K. This is because of (1) the formation of low conductive compounds,  $\text{La}_2\text{Zr}_2\text{O}_7$  or  $\text{SrZrO}_3$ , by reaction with zirconia and of (2) decrease of porosity by sintering. These phenomena were caused by A-site metal ion deficiency of lanthanum manganate perovskites<sup>1)</sup>. To avoid the reaction with zirconia, addition of an excess amount of Mn is effective, but it in turn promotes the sintering of this material. In contrast,  $\text{LaCrO}_3$  is known as an ill-sinterable material which does not react with zirconia. We made thus an investigation on the sinterability of chromium doped lanthanum manganate ( $\text{La}_{1-x}\text{Sr}_x\text{Mn}_{1-y}\text{Cr}_y\text{O}_3$ ) with an aim at finding ill-sinterable cathode materials.

The composition investigated was in the region of  $0 < x < 0.2$  and  $0 < y < 0.2$ . Samples were prepared by usual powder mixing method, precipitation/dry up method with oxalic acid, and liquid mixing method with citric acid; note that manganese compounds volatilized in a small amount with citric acid. Powders were grounded and then baked at 1523 K for 5 hours. Powders were pressed into pellets (40 mm in diameter) at 85 MPa. The sinterability was evaluated from shrinkage of the pellets after baked at 1773 K for 2 hours.

Fig. 1 shows the shrinkage of  $\text{La}(\text{Mn}_{1-y}\text{Cr}_y)\text{O}_3$  perovskites. Chromium composition dependence of shrinkage can be apparently divided into three regions. In region I, remarkable decrease of shrinkage was observed. Region II shows a constant shrinkage. Phase transformation from hexagonal to orthorhombic was observed near the border of this region ( $0.3 < y < 0.4$ ). In region III, shrinkage decreased linearly with Cr content and fell to almost zero at  $y=1$  ( $\text{LaCrO}_3$ ). The electrode activity of  $\text{La}(\text{Sr})\text{CrO}_3$  is, however, reported to be much lower than that of  $\text{La}(\text{Sr})\text{MnO}_3$ <sup>2)</sup>. This implies that a large amount of Cr doping will not be favorable. In view of this, the drastic change of shrinkage caused by addition of only a small amount of Cr (region I) is quite attractive to obtain an ill-sinterable electrode without sacrifice of electrode activity.

Practically, doping of alkaline earth metals such as Sr is effective for improving electrical conductivity. Accordingly, effects of Sr doping on sintering have been investigated in region I. Results are summarized in Fig. 2 as a function of Cr content with a parameter of Sr content. In the region of  $x < 0.08$ , sinterability became worse by addition of a slight amount of Cr. This is common feature among the powders prepared by different methods in spite of difference in their particle sizes; submicron and micron order for citric acid and oxalic acid method, respectively. At  $x = 0.12$ , shrinkage was independent of Cr content. In the region of  $x \geq 0.16$ , shrinkage of the present samples did not show clear dependence on Cr content.

During this study, the pellets without Cr doping were disintegrated after several days because of the precipitation of  $\text{La}(\text{OH})_3$ . On the other hand, the slightly chromium doped samples of stoichiometric composition were stable. This stabilizing effect by Cr doping is quite interesting and important from the

b1

point of view of fabricating an ill-sinterable and stable cathode. This phenomena suggest that the presence of Cr ion in the perovskite structure may affect the feature of formation of A-site vacancies in  $\text{LaMnO}_3$  based perovskite. It is hoped to investigate experimentally in detail.

- 1) J. Simoyama et al., Proceedings of 53th annual meeting of Nippon Kagakukai.
- 2) O. Yamamoto et al., Solid State Ionics, 22, 313 (1987)

Fig. 1 Chromium composition dependence on shrinkage of  $\text{LaMn}_{1-y}\text{Cr}_y\text{O}_3$ .

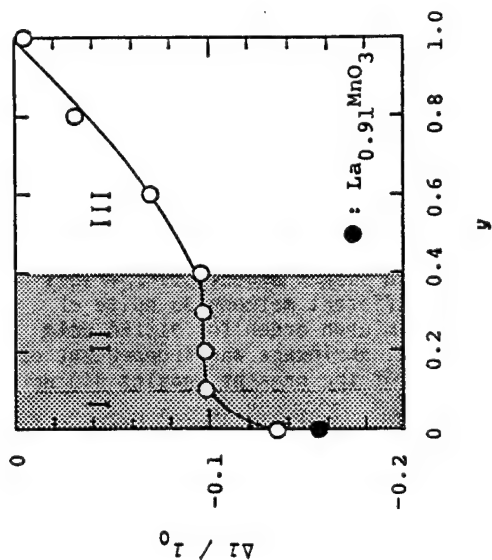
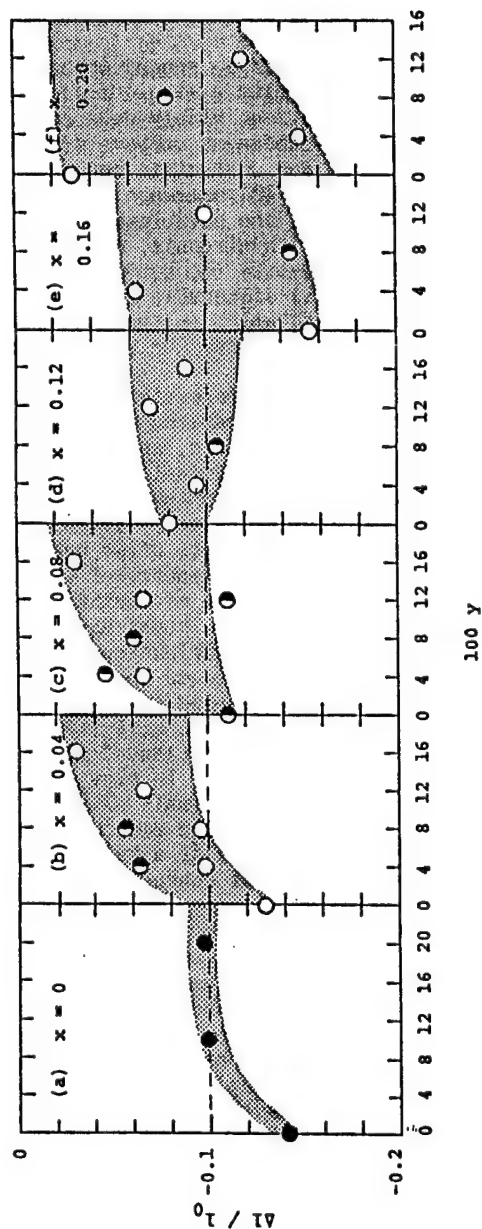


Fig. 2 The shrinkage of  $\text{La}_{1-x}\text{Sr}_x\text{Mn}_{1-y}\text{Cr}_y\text{O}_3$  prepared by powder mixing method (●), by precipitation/dry up method with oxalic acid (○), and by liquid mixing method with citric acid (◐); as a function of Cr content (y) with a parameter of Sr content (x).



## 21-01-11-P

Planar Solid Oxide Fuel Cell: Cell Performance

T. Iwata

Fuji Electric Corporate Research and Development, Ltd.,

2-2-1 Nagasaka, Yokosuka, Kanagawa, 240-01 Japan

and

T. Kawada, N. Sakai, H. Yokokawa and M. Dokiya,

National Chemical Laboratory for Industry,

1-1 Higashi, Tsukuba, Ibaraki, 305 Japan

We are interested in a planar solid oxide fuel cell (SOFC) for relatively large power plants with high efficiency and high power density. Planar cell is considered to be more suitable for large scale plants than tubular cell. We have constructed single test cells and stacks by cheap tape casting method. This paper summarizes results of single cell performance.

A single cell was composed of an anode, a cathode, and a solid electrolyte plate. A solid electrolyte plate (46 mm in diameter and 500  $\mu\text{m}$  thick) was fabricated from fully yttria stabilized zirconia (YSZ) by a doctor blade method. The electrolyte plate was coated with slurry of Ni-YSZ cermet as anode, and then was baked at 1470-1770 K. After baking of anode, the opposite surface of the electrolyte was also coated with Ca or Sr doped lanthanum manganate slurry as cathode, and then was baked at 1370-1470 K. The effective electrode area was ca. 7  $\text{cm}^2$  (i.e. 30 mm in diameter). The reference electrode of platinum paste was placed on the same side of the air electrode and platinum nets were used as electrical contacts.

A typical single cell performance is shown in Fig. 1 for a case of dry hydrogen and air at 1300 K. On the cell polarization curve, deviation from the measured straight line was observed at low current density ( $< 200 \text{ mA/cm}^2$ ). This "apparent" overvoltage seems to arise from partial pressure of steam, since hydrogen was not pre-humidified: In Nernst's equation, equilibrium voltage increases with decrease of partial pressure of steam. The fairly high latent potentiality of planar SOFC was confirmed, as shown in Fig. 1 (i.e. 1072, 769 and 437 mV at 0, 200 and 500  $\text{mA/cm}^2$ , respectively, and short circuit current was about 1  $\text{A/cm}^2$ ).

Fig. 2 shows the effect of hydrogen and air flow rates on anode and cathode voltages. The anodic polarization decreased with increasing hydrogen flow rate over the whole range of the measured current density, whereas the cathodic polarization decreased significantly with increasing air flow rate in the higher region of the measured current density. This result seems to be concerned with air leak from cathode to anode.

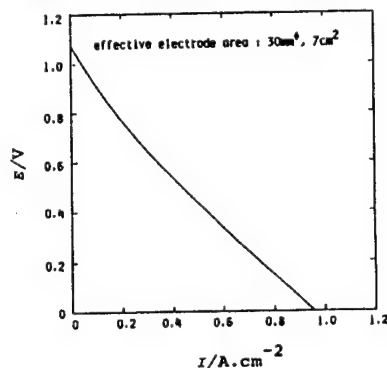


Fig. 1 Single cell performance.

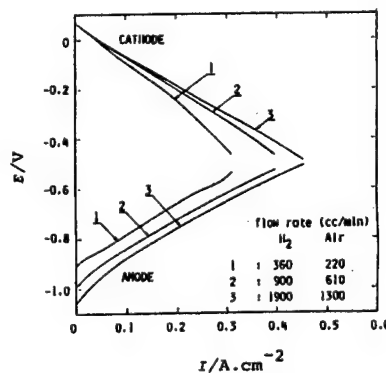


Fig. 2 The effect of flow rates on electrode voltage.



b1

Influence of temperature on the cell voltage at 0, 100, 200 and 500 mA/cm<sup>2</sup> is shown in Fig. 3. The cell voltage decreased with decreasing temperature and also decreased with the loading current density. This results were related to inner resistance arising mainly from that of the electrolyte plate and partly from lowering of anode and cathode activities, since Arrhenius' plot of current density at each cell voltage showed a similar tendency of electrolyte conductance.

Fig. 4 shows the variation of anode and cathode polarization at 100, 200 and 500 mA/cm<sup>2</sup> during experimental operation period (120 h). The anodic polarization increased slightly within about one day and then it didn't vary for the subsequent 120 h. Their tendency didn't depend on the loading current. On the other hand, the cathodic polarization decreased gradually at low current density and decreased remarkably at high current density (i.e. from 530 to 80 mV at 500 mA/cm<sup>2</sup>). This result shows that further improvement of anode is required to obtain better cell performance. The stacked cells are now being fabricated.

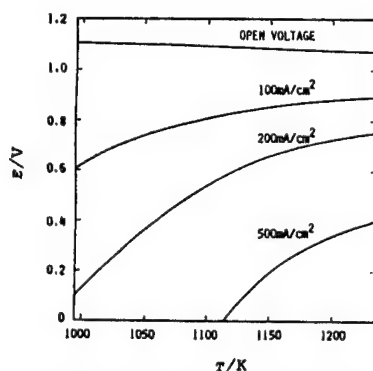


Fig.3 Influence of temperature on the cell voltage.

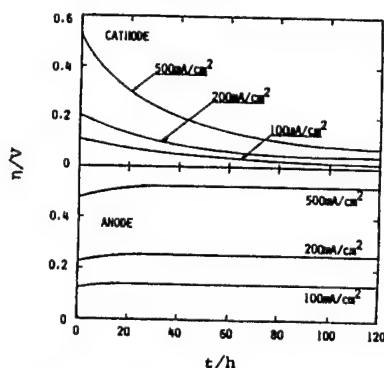


Fig. 4 The variation of electrode polarization with time.

18-02-01-K

Anodic and Cathodic Reactions on Lithium Electrodes  
in Aprotic Electrolytes

K. Wiesener\*, U. Eckoldt\*, D. Rahner\*, E. Brackmann\*\*

\* Dresden University of Technology, Department of Chemistry  
G.D.R., Mommsenstrasse 13, 8027 Dresden

\*\* VEB Fahrzeugelektrik Pirna, G.D.R., Birkwitzer Str. 79,  
8300 Pirna

The cycleability of the lithium electrode is influenced by electrochemical and chemical processes during the cathodic deposition and anodic dissolution of lithium. These are the reduction and formation of surface layers, the reduction of the electrolyte solution and chemical side reactions.

As one main possibility to improve the cycleability of the lithium electrode can be outlined the use of lithium alloys [1]. Cycling on inert and alloy forming substrates shows noticeable differences in the cycling efficiency due to the decreased side reactions when using an alloying support.

In this paper, we have examined the electrochemical behaviour of lithium on inert and alloy forming supports for improving the cycleability of the lithium electrode in secondary lithium cells based on propylencarbonate (PC)/1 M LiClO<sub>4</sub> solution.

It is evident, that in the system PC/1M LiClO<sub>4</sub> an electrolyte decomposition takes place below a voltage of 400...500 mV vs the Li/Li<sup>+</sup> couple [2]. Therefore cycling of the lithium electrode occurs always in this critical potential region. Using substrates possessing alloying properties diminishes the danger of electrolyte decomposition, because the cycling process takes place in a less critical potential region.

The occurring potentialshift normally leads to an improvement of the cycling efficiency but causes a loss of useably voltage.

In our experiments we used Al as alloying support. Besides the problems of mechanical stability Al is more or less a good example of a lithium alloying electrode.

The aluminium electrode was cathodically charged with lithium varying the current density and the intercalated amount of charge. In accordance to published data [3] it could be observed, that the composition and the cycleability of the formed intermetallic compound AlLi<sub>x</sub> depends on the electrochemical preparation procedure. The nearly optimal ratio Al:Li=1:1 seems to be formed when intercalating 5 C Li into the Al substrate at a current density of 0.5 mA/cm<sup>2</sup>. In this case more than 200 cycles can be performed at a charge depth of 20%.

The investigations by impedance spectroscopy as well as current potential plots (fig.1) give evidence, that aluminium

b4

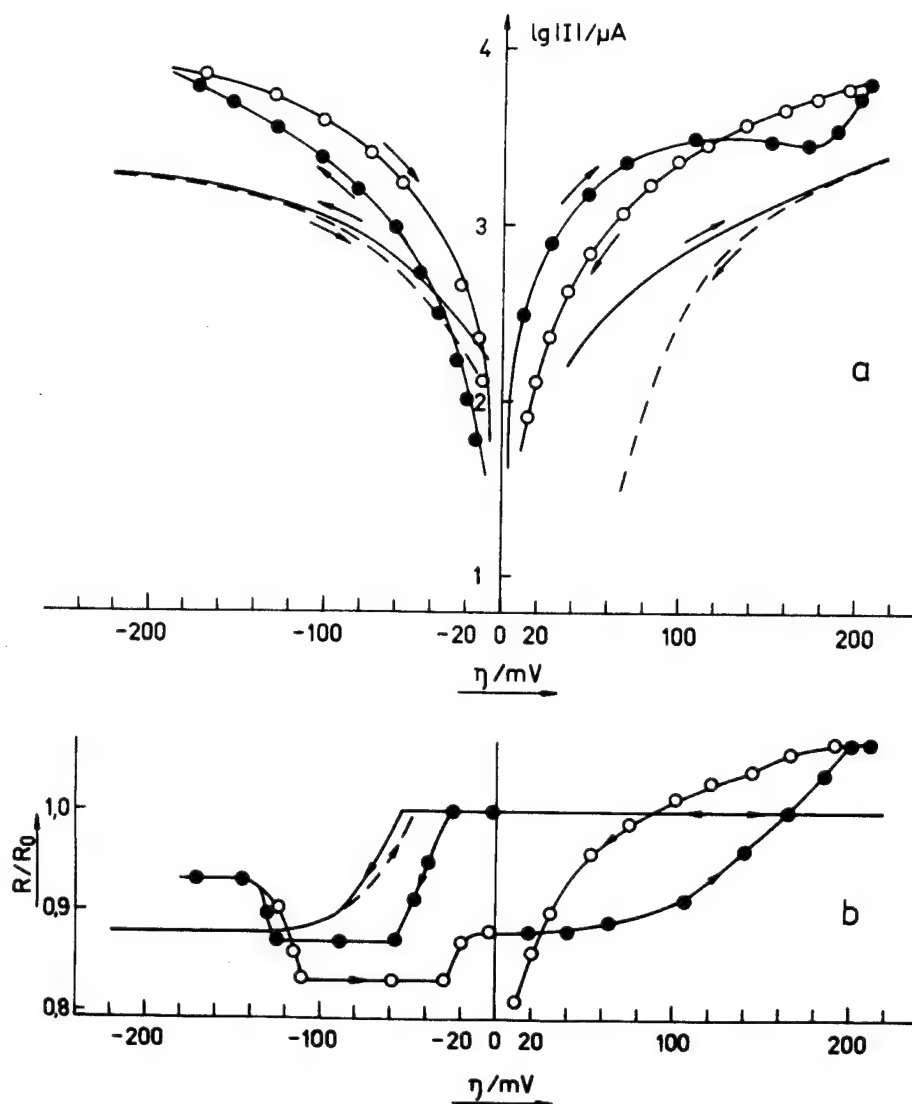


Fig. 1: a) Polarization plots and  
b) Normalized ohmic resistance  $R/R_0$   
of the lithium deposition and dissolution in PC/  
LiClO<sub>4</sub> (1M) using different working electrodes

—●—○ (forward, backward) - lithium electrode  
---○--- (forward, backward) - lithium alloy (LiAlx)

does not show a pronounced surface layer formation like it can be observed on pure lithium. The simultaneously measured resistance (fig.1b) consists of at least two components - the electrolyte resistance and a layer resistance, the latter one representing the thickness and the conductivity of formed surface films with protective properties. A significant decrease of the measured resistance (normalized to the resistance  $R_0$  measured at the rest potential) occurs during cathodic polarization in both electrode systems investigated nearly at the same overpotential (20...30 mV). Under these conditions, the surface film seems to be destroyed or reduced. At high cathodic overvoltages (>100mV) the resistance at the lithium electrode increases again, obviously due to an enhanced electrolyte reduction and to a new layer formation. In the aluminium system no further change in the resistance could be observed during cathodic polarization due to the more positive value of the absolute potential (rest potential  $U_{Al} = 330$  mV). At the lithium electrode a significant increase of the layer resistance during the anodic dissolution process is observed. Up to 100 mV the resistance is nearly constant. From this fact it could be assumed that newly deposited lithium is dissolved. In the potential region of 100...200 mV, lithium islands should be dissolved which are separated from the base material by a layer of more and more decreasing electronic conductivity. This becomes evident by the increasing resistance. Only after all newly deposited lithium ( $U > 200$  mV) is dissolved, the anodic current arises while the resistance remains constant. An anodic polarization of aluminium intercalated with lithium causes obviously no significant change of the layer properties - the resistance remains constant. The intercalated lithium dissolves uniform. The shape of the current potential plot depends not only on the amount of intercalated lithium but also on the number of the cycle after which the current potential plot is measured. Subsequent cycling diminishes the current at a given potential. From this fact one can assume that the mobility of the lithium inside the host lattice causes a change of the concentration profile of lithium and leads to an decreased inter- and deintercalation process.

Summarizing it can be stated, that for lithium alloying electrodes detailed informations on the structure and the transport processes are the prerequisite for the application of optimized alloying materials.

- [1] I. Epelboin, N. Froment, M. Garreau, J. Thevenin and D. Warin, J. Electrochem. Soc., 127(1980)2100
- [2] G. Eggert and J. Heitbaum, Electrochim. Acta, 31(1986)1443
- [3] B. M. L. Rao, R. W. Francis and H. W. Christopher, J. Electrochem. Soc., 124(1977)1490

b4

18-02-03-K

#### Several Considerations of Lithium Anode Rechargeability

J.YAMAKI

NTT Applied Electronics Laboratories, Tokai-Mura Ibaraki-Ken, 319-11, Japan.

Cycling life of lithium secondary batteries is often limited by Li cycling efficiency ( $E_a$ ). In understanding  $E_a$ , studies on so-called dead Li is very important, because the dead Li is not used during discharge. The dead Li can be explained by reactivity of electrolytes and morphology of deposited Li.

Reaction between solvent and Li metal is explained by an electrochemical reaction. When electrolyte reduction potential ( $E_{red}$ ) is high, electrolytes react very actively with the Li metal. However, measurement of  $E_{red}$  is difficult. An alternative method uses oxidation potential ( $E_{ox}$ ) instead of  $E_{red}$ . A very simple assumption (1) is made: solvents with base  $E_{red}$  show base  $E_{ox}$ . Experimental results showed that Li cycling efficiency increased with decreasing  $E_{ox}$  (2).

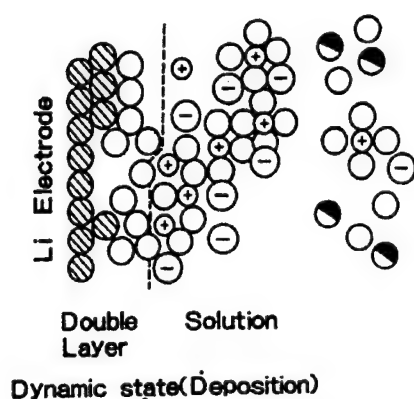
It may be thought that Li cycling efficiency is decreased by mixing high reactivity solvents. However, there is another concept (2) of interface between deposited Li and electrolyte solution in mixed solvents, illustrated in Fig. 1. Most  $Li^+$  ions are selectively solvated with the higher solvation solvent, therefore, concentration of the stronger solvation solvent becomes higher around deposited Li than in the bulk. As a result, in mixed solvents, reactivity of higher solvation solvent mainly affects the Li cycling efficiency rather than the reactivity of the higher reactive solvent.  $E_{ox}$  values shown in Fig. 2 are for a low viscosity solvent (LVS), because in many cases, LVS has higher solvation power than high dielectric solvent (HDS). Li cycling efficiency increased with decreases in the  $E_{ox}$  of the LVS.

Let us consider how "Dead Li" is created, and what "Dead Li" is. One is an isolated Li metal in a solid electrolyte interface (SEI). This mechanism is closely related to solvent reactivity. However, a very high rate of "dead Li" creation occurs even with a moderate reactivity. This suggests another reason which is "Dropping off from or accumulation on Li electrodes without electrical connections" (3). This is closely related to morphology of the deposited Li. Morphology change during cycling was examined using SEM, and results are schematically shown in Fig. 3. Cycling efficiency increases with increasing cycling capacity. This is because, at small cycling capacity, needle-like Li is deposited, while at large cycling capacity, particle-like Li is deposited.

The conclusion is that needle-like Li gives bad cycling

efficiency, and particle-like Li gives good cycling efficiency.

- (1) V.R.Koch, J.L.Goldman, C.J.Mottos and M.Mulvaney, J.Electrochem.Soc., 129, 186(1982).
- (2) S. Tobishima and T. Okada, Electrochimica Acta, 30 1715(1985)
- (3) I.Yoshimatsu, T.Hirai and J.Yamaki, J. Electrochem. Soc., 135, 2422(1988)



- ⊕ Li<sup>+</sup> ion
- ⊖ Anion
- ⊙ Li
- Stronger solvation solvent
- ◐ Weaker solvation solvent

Fig.1 Illustrated model of the interface between deposited Li and electrolyte solution.

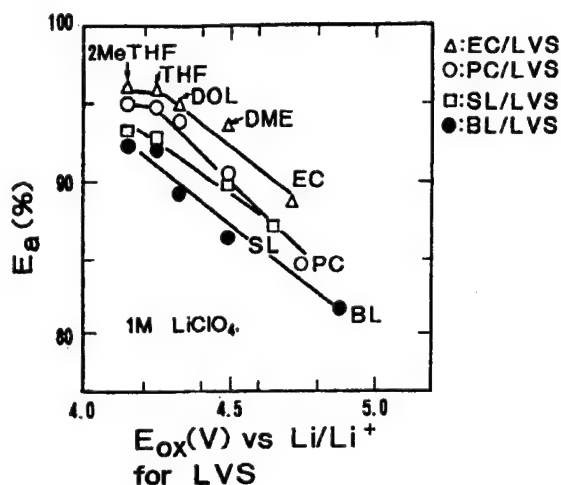


Fig.2 Relationship between Li cycling efficiency (Ea) and low LVS oxidation potential (Eox).  
 (LVS: low viscosity solvent  
 HDS: high dielectric solvent)

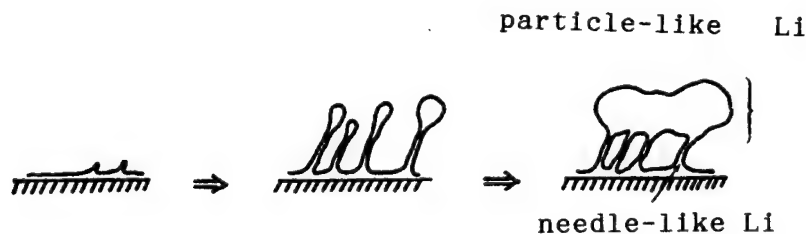


Fig.3 Illustrated model of the change in deposited Li morphology

18-02-04-G

THE COMPARISON OF THE DIFFUSION OF THE DOPANTS IN VARIOUS CATHODES,  
TiO<sub>2</sub>, MoS<sub>2</sub>, POLYACETYLENE, POLYANILINE, FOR LITHIUM BATTERIES

Z. Takehara, K. Kanamura, N. Imanishi, S. Yonezawa  
 Department of Industrial Chemistry, Faculty of Engineering,  
 Kyoto University, Yoshida, Sakyo-ku, Kyoto 606, Japan

The diffusion behavior of some chemical species in various cathodes for lithium batteries influences on their discharge and charge characteristics. In this study, lithium diffusion in MoS<sub>2</sub> and TiO<sub>2</sub> were investigated. And BF<sub>4</sub><sup>-</sup>, ClO<sub>4</sub><sup>-</sup>, and PF<sub>6</sub><sup>-</sup> in polyacetylene and polyaniline were also investigated. MoS<sub>2</sub> has an interlayer gap which is suitable for the lithium intercalation. TiO<sub>2</sub> has a channel in which lithium can intercalate. Various anions can be doped and undoped into polyacetylene and polyaniline. Therefore these materials have been utilized as a cathode material of lithium secondary battery.

In this study the diffusion coefficients have been measured by using potential step method. In this measurement, it is very important for the definition of the diffusion path length to estimate the diffusion coefficients. MoS<sub>2</sub> and TiO<sub>2</sub> electrodes were prepared by chemical vapor deposition and sputtering method, respectively. The diffusion behavior of lithium in MoS<sub>2</sub> and TiO<sub>2</sub> was approximated by the linear one dimensional diffusion. On the other hand, the diffusion behavior of various anions in polyacetylene and polyaniline was approximated by cylindrical diffusion. In using these diffusion models, the Fick's law could be applied in each case. By comparison between the theoretical and experimental values, the diffusion coefficients were estimated. In all experimental procedures, propylene carbonate containing 1.0 M LiBF<sub>4</sub> was used as an electrolyte and Li metal was used as the reference and counter electrodes.

The experimental results are shown in the Table 1. TiO<sub>2</sub> and MoS<sub>2</sub> had larger diffusion coefficients(D) than polyaniline and polyacetylene. However, these polymers had the same charge-discharge characteristics as those of TiO<sub>2</sub> and MoS<sub>2</sub>. This result would come from the smaller diffusion length(l) in these polymers. For example, in polyaniline, the diameter of the fibrils was about 0.1 μm, while the thickness of the MoS<sub>2</sub> film was 2.0 μm. This fact indicates that it is necessary to take into account the length of the diffusion paths in discussing the relation between the diffusion of lithium or anion and charge-discharge characteristics. Then the value of Dxl<sup>-2</sup> were calculated in order to estimate the actual diffusion rate in these materials. In MoS<sub>2</sub>, Dxl<sup>-2</sup> = 2.4 × 10<sup>-13</sup> cm<sup>2</sup>s<sup>-1</sup> in higher potential region (3.6 → 1.5 V vs. Li/Li<sup>+</sup>). In polyaniline, Dxl<sup>-2</sup> = 2.4 × 10<sup>-12</sup> cm<sup>2</sup>s<sup>-1</sup> in higher potential region (3.9 → 3.6 V).

In addition to the effect of the value of l, the physical properties of host matrix affected much significantly to the value of D. In the case of polyaniline, the diffusion coefficients changed drastically in different potential region. In higher potential region (3.9 → 3.6 V), D = 2.4 × 10<sup>-14</sup> cm<sup>2</sup>s<sup>-1</sup> and in lower potential region (3.2 → 2.7 V), D = 2.3 × 10<sup>-16</sup> cm<sup>2</sup>s<sup>-1</sup> at 30 °C as in Table 1. In order to investigate these differences, the activation energies of diffusion(E<sub>a</sub>) were measured. As in Fig. 1, the values of E<sub>a</sub> were measured from the temperature dependence of the

diffusion coefficients. From these result,  $E_a=35.5 \text{ kJ mol}^{-1}$  ( $3.9 \rightarrow 3.6 \text{ V}$ ) and  $E_a=55.2 \text{ kJ mol}^{-1}$  ( $3.2 \rightarrow 2.7 \text{ V}$ ). In polyaniline, the conductivity of fibrils changes very much between these two regions. The change of the value of  $E_a$  would be related with these properties.

Whereas in  $\text{MoS}_2$ , the diffusion coefficients also changed in different potential region as shown in Table 1. The activation energy was measured in the same way as the polyaniline. As shown in Fig. 2,  $E_a=36.0 \text{ kJ mol}^{-1}$  ( $3.6 \rightarrow 1.5 \text{ V}$ ) and  $E_a=62.7 \text{ kJ mol}^{-1}$  ( $1.2 \rightarrow 1.0 \text{ V}$ ). These results seem not to be consistent with the results of diffusion coefficients. Because in lower potential region, the value of  $E_a$  was larger and in higher one, the value of  $E_a$  was smaller. These phenomena would be explained by the large change of the value of  $D_0$  as shown in Table 1. This results indicate that the value of  $D_0$  in lower potential region became  $10^5$  times larger than that in higher one. Such a large change may be coming from the structural change of host matrix.

From these discussions, it is concluded that in order to improve the active materials, it is necessary to produce the structure having a large diffusion coefficients and a small diffusion path length.

Table 1 The diffusion coefficients and other experimental values related to the diffusion in  $\text{MoS}_2$  and polyaniline. ( $D=D_0\text{EXP}(-E_a/RT)$ )

	$D$ ( $\text{cm}^2\text{s}^{-1}$ )	$D \times 10^{-2}$ ( $\text{s}^{-1}$ )	$D_0$	$E_a$ ( $\text{kJ mol}^{-1}$ )
$\text{MoS}_2$	$9.5 \times 10^{-13}$ (3.6 1.5 V)	$2.4 \times 10^{-13}$	$1 \times 10^{-6}$	36.0
	$6.1 \times 10^{-12}$ (1.2 1.0 V)	$1.5 \times 10^{-12}$	$2 \times 10^{-1}$	62.7
polyaniline	$2.4 \times 10^{-14}$ (3.9 3.6 V)	$2.4 \times 10^{-12}$	$2 \times 10^{-8}$	35.5
	$2.3 \times 10^{-16}$ (3.2 2.7 V)	$2.3 \times 10^{-14}$	$8 \times 10^{-7}$	55.2

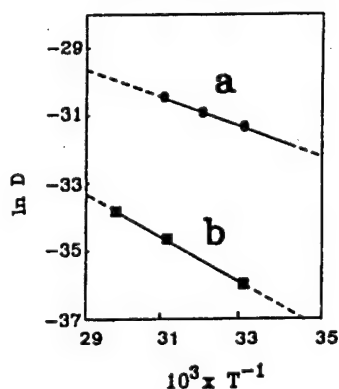


Fig. 1 The Arrhenius plot of the diffusion coefficients of  $\text{BF}_4^-$  in polyaniline. a:  $3.9 \rightarrow 3.6 \text{ V}$  b:  $3.2 \rightarrow 2.7 \text{ V}$

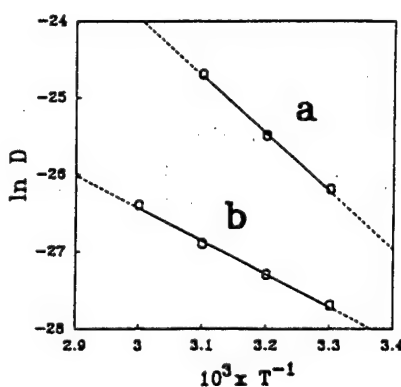


Fig. 2 The Arrhenius plot of the diffusion coefficients of lithium in  $\text{MoS}_2$ . a:  $1.2 \rightarrow 1.0 \text{ V}$  b:  $3.6 \rightarrow 1.5 \text{ V}$



b4

18-02-07-G

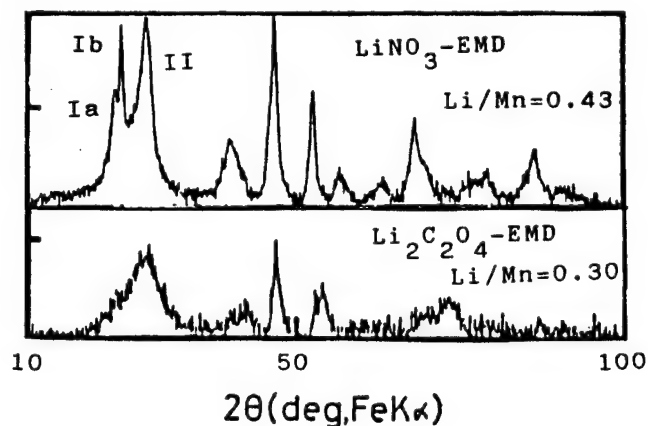
Lithium-manganese composite oxides for lithium secondary  
batteries

M.Yoshio, H.Nakamura and H.Kurimoto  
Saga University, Saga 840, Japan

The utilization of manganese compounds as the positive electrode in lithium secondary batteries brings about several advantages. Furukawa (1) proposed to use LiOH-CMD compound as the cathode material. However, detailed study on the reaction of lithium compounds with  $MnO_2$  would be needed to understand this complicate composite oxide.

In the course of our study on the heat treatment between  $MnO_2$  and Li salts, we have found that these composite oxides could be divided into two groups by the charge/discharge behavior, namely, 1) products between  $MnO_2$  and  $LiNO_3$  or LiOH, 2) products between  $MnO_2$  and organic Li compounds such as  $Li_2C_2O_4$ . Excellent rechargeability is obtained when high heat treatment of 330-400°C is done in the former case, and when low temperature of 200-300°C in the latter. Discharge capacities of each cycle in the former case are nearly the same. Discharge behavior of the latter resemble that of EMD (2), therefore 1st cycle discharge capacity is much higher than others. The values of (Mn(IV)/total Mn) of 70-80 % show good rechargeability in the both cases, although XRD patterns are quite different, as shown in Fig.1. It is noteworthy that peak I would be divided into two of  $2\theta=22.9$  (Ia) and  $23.9$  (Ib). With the increasing heat treatment temperature and the initial Li/Mn molar ratio, the peak strength of Ib is increasing. Effect of preparation method of composite oxides on rechargeability will be discussed.

Fig.1



- (1) N.Furukawa et.al., 3rd Int.Meet. Li Batt. Extended Abstract, (1986)
- (2) M.Yoshio et.al., Asahi Glass Found. Ind. Tech., 53 261 ('88)

18-02-08-K

Electrochemistry of Manganese Dioxide in Lithium Nonaqueous Cell  
: Jahn-Teller Deformation of  $\text{Li}_x\text{MnO}_{2-\delta}$

Tsutomu Ohzuku, Keijiro Sawai, and Taketsugu Hirai  
Department of Applied Chemistry, Faculty of Engineering,  
Osaka City University, Sugimoto 3-3-138, Sumiyoshi,  
Osaka 558, Japan

X-Ray diffractational and electrochemical studies of  $\text{Li}_x\text{MnO}_{2-\delta}$  were carried out in lithium nonaqueous cells. Two types of  $\text{Li}_x\text{MnO}_{2-\delta}$  were examined. One was  $\text{Li}_x\text{MnO}_{2-\delta}$  ( $\delta \approx 0$ ) of spinel-related manganese dioxide which was prepared by the electrochemical oxidation of  $\text{LiMn}_2\text{O}_4$  (cubic,  $a = 8.239(3) \text{ \AA}$ ) and the other was  $\text{Li}_x\text{MnO}_{2-\delta}$  (orthorhombic,  $a = \text{ca.} 10 \text{ \AA}$ ,  $b = \text{ca.} 5 \text{ \AA}$ , and  $c = \text{ca.} 2.85 \text{ \AA}$ ) which was prepared electrochemically from a heat-treated electrolytic manganese dioxide. Both samples exhibited rechargeability in lithium nonaqueous cells.

Reaction mechanism of spinel-related manganese dioxide was examined. The electrochemical reduction of a spinel-related manganese dioxide proceeded topotactically in the three steps, i.e., the reduction in two phases (cubic;  $a = 8.045(6) \text{ \AA}$  and  $a = 8.142(2) \text{ \AA}$ ) which was characterized by a constant open-circuit voltage (OCV) of  $4.110(5) \text{ V}$  for  $0.27(2) < y < 0.60(3)$  in  $\text{Li}_x\text{Mn}_2\text{O}_4$ , the reduction in one phase (cubic;  $a = 8.142(2) - 8.239(3) \text{ \AA}$ ) which was characterized by an S-shaped OCV curve (mid-point;  $3.94(1) \text{ V}$ ) for  $0.60(3) < y < 1.0$ , and the reduction in two phases of cubic ( $a = 8.239(3) \text{ \AA}$ ) and tetragonal ( $a = 5.649(2) \text{ \AA}$  and  $c = 9.253(5) \text{ \AA}$ ) characterized by an L-shaped OCV curve at  $2.957(5) \text{ V}$  for  $1.0 < y < 2.0$ .

Reaction mechanism of  $\text{Li}_x\text{MnO}_{2-\delta}$  (orthorhombic) in the rechargeable region was also examined and proved to be a homogeneous phase reaction in  $\text{Li}_x\text{MnO}_{2-\delta}$  matrix, i.e., orthorhombic unit cell having  $a = 9.7 - 10.3 \text{ \AA}$ ,  $b = 4.7 - 5.0 \text{ \AA}$ , and  $c = 2.82 - 2.85 \text{ \AA}$ , which shrunk and expanded anisotropically during charge and discharge, respectively, within 10 % in unit cell volume in the voltage range between 2.0 and 3.8 V.

Relation between the voltage shape and the change in unit cell dimension for both samples is discussed in terms of a solid state redox reaction of  $\text{MnO}_6^{8-} / \text{MnO}_6^{9-}$  in relation to Jahn-Teller deformation of  $\text{MnO}_6$ -octahedron from the experimental and analytical results. Rechargeable lithium manganese (di)oxide cell will be demonstrated therefrom.

b4

18-02-09-G

#### RECHARGEABILITY OF MANGANESE OXIDES IN LiPF<sub>6</sub> ELECTROLYTE

K.Yokoyama, Y.Uetani

Osaka Works, Hitachi Maxell Ltd., Ibaraki-shi, Osaka, Japan

Manganese oxide compounds (MnO<sub>x</sub>) including manganese dioxide are being studied as promising candidate for positive material of lithium secondary battery. Those investigations have mainly been made in LiClO<sub>4</sub>/PC+DME electrolyte system. We have revealed that LiPF<sub>6</sub> electrolyte system is excellent for TiS<sub>2</sub>/Li secondary battery. Although, LiPF<sub>6</sub> tends to decompose to LiF and PF<sub>5</sub>, and PF<sub>5</sub> polymerize DOL which is one of the solvent of electrolyte. Addition of HEMPA (hexa methyl phosphoric triamide) in the electrolyte, is useful to prevent the phenomenon. LiPF<sub>6</sub> electrolyte has higher conductivity than LiClO<sub>4</sub> electrolyte. Therefore, Application of LiPF<sub>6</sub> electrolyte instead of LiClO<sub>4</sub> electrolyte to MnO<sub>x</sub>/Li secondary battery is recommended. Difference of LiPF<sub>6</sub> and LiClO<sub>4</sub> solute is studied in the MnO<sub>x</sub>/Li coin type cell. Heat treated MnO<sub>x</sub> with LiOH is used as a positive material. LiAl alloy is used as an anode material. These cells are discharged to 2.0V (100% discharge depth) and charged to 3.2V. Both LiPF<sub>6</sub> cell and LiClO<sub>4</sub> cell show same initial characteristics, that is, open circuit voltage, closed circuit voltage, and internal resistance. However, LiPF<sub>6</sub> cell has a larger capacity of 12mAh/cycle comparing with LiClO<sub>4</sub> cell of 10mAh/cycle. Furthermore, LiPF<sub>6</sub> cell operates higher voltage during charge/discharge cycles than LiClO<sub>4</sub> cell dose. Several characteristics of LiPF<sub>6</sub> cells will be shown.

Summarizing, LiPF<sub>6</sub> solute is proposed for the electrolyte of manganese oxide compound/lithium secondary battery. LiPF<sub>6</sub> electrolyte cell shows better characteristics, that is, higher operating voltage and longer charge/discharge cycle life, compared to LiClO<sub>4</sub> electrolyte cell.

19-02-01-K

LITHIUM BATTERY TECHNOLOGIES IN JAPAN

Y. Matsuda

Department of Industrial Chemistry, Faculty of Engineering,  
Yamaguchi University, Tokiwadai, Ube 755, Japan

The research on batteries containing organic electrolytes started at the second half of the 1960's in Japan. The first commercial primary lithium battery was an  $\text{Li}/(\text{CF})_n$  system, which was produced by Matsushita Battery in 1973. After this, an  $\text{Li}/\text{MnO}_2$  system by Sanyo Electric was appeared in the commercial market. Then the output of primary lithium batteries in Japan has considerably increased and it is over 230 millions in 1988, as shown in Table 1.

Table 1. The output of lithium batteries in Japan (unit: million)

Year	1983	1984	1985	1986	1987	1988
Cylindrical	15	13	13	21	38	65
Coin & Others	49	72	81	95	147	169
Total	64	85	94	116	185	234

Although many kinds of primary batteries are on the Japanese market, the principal ones are  $\text{Li}/\text{MnO}_2$ ,  $\text{Li}/(\text{CF})_n$ ,  $\text{Li}/\text{SOCl}_2$  and  $\text{Li}/\text{CuO}(1.5\text{V})$ . Recently, the primary lithium batteries with higher powers [eg.:  $34(\text{L}) \times 17(\text{W}) \times 45(\text{H})$  mm, 6 V (2 unit cells), 1300 mAh] have been produced. They are mainly used in automatic cameras. In these batteries, various organic electrolyte solutions have been employed. The  $\text{Li}/\text{SOCl}_2$  system has been developed for only memory back-up use, not for military use, in Japan.

In order to realize a rechargeable battery with a high power density and a long cycle life, many excellent results on the basic researches have been reported. With respect to the field of the organic electrolyte solutions, the addition of some organic compounds to the electrolytic solution have been examined. The major additives proposed up to the present are heterocyclic compounds (2-methyl-furan, thiophenes, thiazoles, etc.) and aromatic compounds (benzene, etc.). The solvation of  $\text{Li}^+$  in organic media has also been investigated. Of course, the search of new solvents and the elucidation and application of solvent mixing effects have been still a very important subject. Most of Japanese battery makers have not used  $\text{LiAsF}_6$  as an electrolytic salt in their prototype rechargeable lithium batteries. The use of  $\text{LiAsF}_6$  has been one of the serious problems to be solved in Japan. Some researchers investigated the Li deposition process by using SEM and other spectroscopic methods. The ac impedance of the interphase between Li and the electrolyte has been

b4

measured in various electrolyte systems, and the chemical structure and the electrical properties of the surphase are now under investigation.

Many Li-alloys and carbon substrates have been tested for the negative electrodes of the rechargeable batteries. A number of positive materials have been investigated, that is,  $\text{MnO}_2$  with various structures, titanium dichalcogenides, Chevrel phase compounds, vanadium oxides, molybdenum oxides, etc.

Solid electrolytes consisting of polymer compounds (polymeric solid electrolytes) and conductive polymer electrodes have also been investigated for the development of rechargeable lithium batteries. Especially, polymers containing ethylene oxide units are the most prospective materials as the solid electrolyte. Polyaniline, polypyrrole, polythiophene, etc. are found to be promising as the positive material.

At the present, several kinds of prototype rechargeable Li batteries have been appeared in Japan. Some batteries use Li-alloys such as Li-Al or carbon-based materials like Linear-Graphite-Hybrid (LGH; Toshiba Battery) for the negative electrode. The positive electrode materials used in these batteries are manganese oxides, vanadium oxides, titanium disulphide and polyaniline. The Li-Al/ $\text{MnO}_2$  battery of Sanyo Electric uses the thermally treated  $\text{LiOH} \cdot \text{MnO}_2$  (Composite Dimensional Manganese Oxide; CDMO), whose structure consists of  $\text{Li}_2\text{MnO}_3$  and  $\beta\text{-}\gamma\text{-MnO}_2$  (composite dimension). Hitachi Maxell has presented the Li-Al/ $\text{TiS}_2$  battery. Vanadium oxides are used for the positive electrodes of the rechargeable batteries from Matsushita Battery and Toshiba Battery. The Li/polyaniline battery of Bridgestone - Seiko Electronic Components is now on the market. In the present paper, an overview of the Li battery technology in Japan is introduced and major problems concerning the battery developments will be discussed.

19-02-02-G

# A Lithium Secondary Battery Using Lithium Containing Manganese Dioxide (CDMO) as the Cathode

T.Nohma, K.Teraji, I.Nakane, Y.Fujita, H.Watanabe, Y.Yamamoto and N.Furukawa

Functional Materials Research Center, Sanyo Electric Co., Ltd.  
1-18-13 Hashiridani, Hirakata-shi, Osaka 573, Japan

## INTRODUCTION

We adopted  $\text{MnO}_2$  as a positive material for a lithium secondary battery which is inexpensive, and has a high discharge voltage and high energy density. We have already reported that lithium containing manganese dioxide (heat-treated  $\text{LiOH} \cdot \text{MnO}_2$ ) showed much better rechargeability than  $\gamma$ - $\beta$ - $\text{MnO}_2$  or spinel  $\text{LiMn}_2\text{O}_4$ (1,2). The crystal structure of lithium containing manganese dioxide consists of  $\text{Li}_2\text{MnO}_3$  and  $\gamma$ - $\beta$ - $\text{MnO}_2$  (composite dimension). So we named lithium containing manganese dioxide, composite dimensional manganese oxide (CDMO).

In this report, we examined the relation between the condition to prepare CDMO and its rechargeability.

## EXPERIMENTAL

The rechargeability of CDMOs prepared from  $\text{MnO}_2$  and several lithium salts was investigated by cycle tests on flat cells and X-ray diffractometry (XRD). Furthermore the optimum heat-treatment temperature to prepare CDMO was examined.

## RESULTS AND DISCUSSION

Fig. 1 shows the XRD patterns of CDMOs prepared from  $\text{MnO}_2$  and several lithium salts with 30 atomic percent lithium. The heat-treatment temperature was 375°C.  $\gamma$ - $\beta$ - $\text{MnO}_2$  and  $\text{Li}_2\text{MnO}_3$  peaks were observed in all

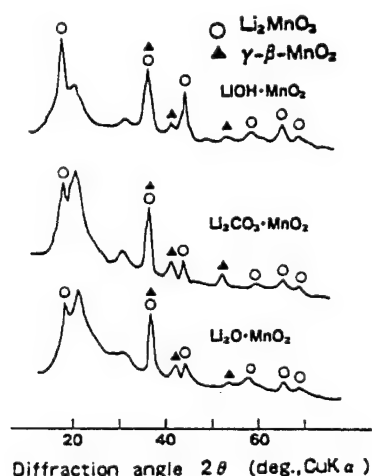


Fig. 1 X-ray diffractograms of CDMOs prepared from manganese dioxide and several lithium salts.

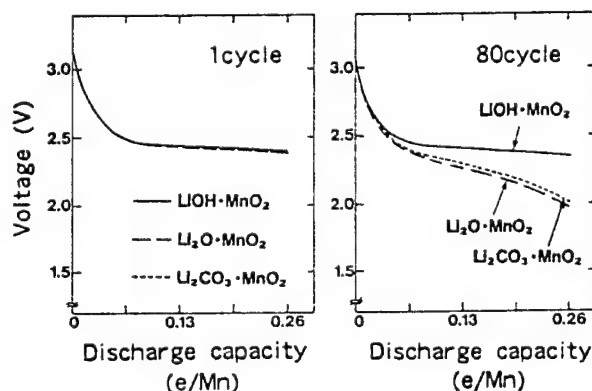


Fig. 2 Cycle performances of flat cells using CDMOs prepared from manganese dioxide and several lithium salts.

patterns. The  $\text{Li}_2\text{MnO}_3$  peaks in CDMO prepared from  $\text{LiOH}$  and  $\text{MnO}_2$  were the highest among them, which showed that  $\text{LiOH}$  had more reactivity with  $\text{MnO}_2$  to produce  $\text{Li}_2\text{MnO}_3$  than the others. Fig. 2 shows the results of cycle tests on flat cells at a depth of 0.26 e/Mn. It was found that heat-treated  $\text{LiOH}\cdot\text{MnO}_2$  had better rechargeability than the others.

From the above results, we chose  $\text{LiOH}$  to prepare CDMO. We also investigated the optimum heat-treatment temperature to prepare it. Fig. 3 shows XRD patterns of heat-treated  $\text{LiOH}\cdot\text{MnO}_2$  prepared at several heat-treatment temperatures. In the heat-treatment  $\text{LiOH}\cdot\text{MnO}_2$  prepared at 500°C and 600°C,  $\text{Mn}_2\text{O}_3$  peaks appeared and the  $\gamma$ - $\beta$ - $\text{MnO}_2$  and  $\text{Li}_2\text{MnO}_3$  peaks shifted to spinel  $\text{LiMn}_2\text{O}_4$ . These were confirmed by chemical analysis of X values in the  $\text{MnO}_x$  (Table 1). The X value of CDMO prepared at 375°C was 1.90. This indicates that the valence of Mn was nearly 4.0. An X value of 1.65 at 500°C and 600°C indicates the existence of  $\text{LiMn}_2\text{O}_4$  (X=1.75) and  $\text{Mn}_2\text{O}_3$  (X=1.5). Fig. 4 shows the results of cycle tests on flat cells at a depth of 0.14 e/Mn. It was found that CDMO prepared at 375°C showed better discharge performance and rechargeability than the others.

#### CONCLUSION

The crystal structure and rechargeability of CDMOs prepared on several conditions were examined. In result, it was found that the optimum condition for preparing CDMO was to heat-treat  $\text{MnO}_2$  with  $\text{LiOH}$  at about 375°C.

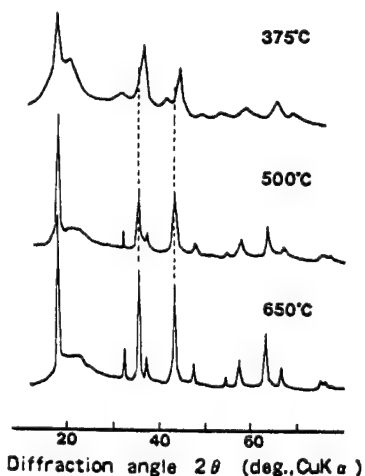


Fig. 3 X-ray diffractograms of heat-treated  $\text{LiOH}\cdot\text{MnO}_2$  prepared at several heat-treatment temperatures.

Table 1 X values of heat-treated  $\text{LiOH}\cdot\text{MnO}_2$  prepared at several heat-treatment temperatures

Temperature	375°C	500°C	650°C
X in $\text{MnO}_x$	1.90	1.65	1.65

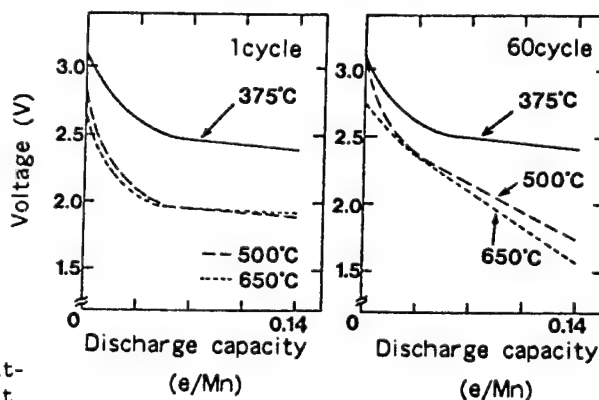


Fig. 4 Cycle performances of flat cells using heat-treated  $\text{LiOH}\cdot\text{MnO}_2$  prepared at several heat-treatment temperatures.

#### REFERENCES

- 1) N.Furukawa, et al., 172nd Electrochemical Society Meeting Extended Abstracts (1987).
- 2) H.Ikeda, et al., 4th International Meeting on Lithium Batteries (1988).

19-02-03-G

EFFECT OF ALKALI METAL CATIONS ON THE ELECTRODE BEHAVIOR OF LITHIUM BATTERIES

K.Tanaka, S.Suzuki, N.Chiba, N.Ishihara, K.Yoda  
4-10, Minamishinagawa 3-chome, Shinagawa-ku, Tokyo 140, Japan

Introduction

Lithium batteries, which employ lithium metal as a negative electrode, have high energy density and good storage characteristics. Therefore, they have been widely applied as power sources of electronic apparatuses, in particular being a small and/or a thin-type, and having long reliability. Many of these types of batteries use organic solvent as electrolyte solution because of the reactivity of the lithium anode with water, and electrolytic manganese dioxide (EMD) as a positive electrode mainly. Nevertheless, the performance of EMD in organic solutions has been insufficiently known to date. Only Miyanaga et al. <sup>(1)</sup> reported some observations on the ionic adsorption characteristics.

On the other hand, in aqueous solutions, many studies have been done to elucidate the ionic adsorption characteristics and the ionic exchange capability of EMD. In these cases, it is shown that the ionic exchange between protons in EMD and cations in solution is dependent on the acid-base properties of EMD and it is influenced by the kind and the concentration of the cations, <sup>(2),(3)</sup> and that the exchange between adsorbed cations and the different kind of cations in solution may also happen. <sup>(4)</sup> Moreover, the ionic exchange mechanism has been proposed. <sup>(5)</sup>

As we investigated the behavior of EMD in organic electrolyte solutions on the ionic adsorption and desorption, we shall report the main results of this work.

Experimental

## 1. Samples and electrolyte solutions

The samples were prepared by heat treating EMD neutralized with  $\text{Na}_2\text{CO}_3$  at  $350^\circ\text{C}$ ,  $400^\circ\text{C}$  and  $450^\circ\text{C}$  respectively. The used electrolyte solutions were propylene carbonate (PC) and 1,2-dimethoxyethane (DME) as a solvent, and lithium perchlorate ( $\text{LiClO}_4$ ), sodium perchlorate ( $\text{NaClO}_4$ ), potassium perchlorate ( $\text{KClO}_4$ ), calcium perchlorate ( $\text{Ca}(\text{ClO}_4)_2$ ), lithium chloride ( $\text{LiCl}$ ) and lithium tetrafluoroborate ( $\text{LiBF}_4$ ) as solute respectively. The water contents of the solutions prepared for various concentrations were controlled to be less than 20 ppm.

## 2. Determination

A EMD sample dried at  $250^\circ\text{C}$  just before the examination was put into the glass flask in which was the solution of the prescribed concentration, and was sealed. After the immersion at  $20^\circ\text{C}$  for 24hrs, the sample was filtered through a glass micro fiber filter to separate the solution phase and the EMD phase. The solution phase, whose organic compositions were resolved by  $\text{HNO}_3$  in order to avoid being disturbed at successive determination, was diluted by distilled water. Thereafter, the amounts of the ions in the phase, which included the extracted ones from EMD were determined by atomic adsorption spectrometry, and the ionic adsorption and desorption characteristics of EMD were investigated.



b4

### Results

When EMD samples of various sodium contents were immersed in PC containing  $\text{LiClO}_4$  within the range of  $0\text{M} \sim 0.01\text{M}$ , the ionic adsorption and desorption characteristics between  $\text{Li}^+$  in solution and  $\text{Na}^+$  in EMD were investigated. The result was shown in Fig.1.

The amounts of these ions in the solution phase changed more, the more the sodium content in EMD was and the higher the concentration of  $\text{LiClO}_4$  was. The quantitative ratio between the adsorbed  $\text{Li}^+$  and the desorbed  $\text{Na}^+$  was nearly 1:1 in all cases.

On the other hand, the concentration of  $\text{Li}^+$  little decreased in the case of using EMD neutralized with  $\text{NH}_4\text{OH}$  as no sodium contained sample. Accordingly, it is presumed that the adsorption of  $\text{Li}^+$  takes place at the site where there is the desorbable sodium, precisely this behavior is the ionic exchange between  $\text{Li}^+$  and  $\text{Na}^+$ .

In addition, we investigated the effect of the heat treating temperature of EMD, the mixed solvent composition of electrolyte solution and the others on this behavior. The above will be reported in detail.

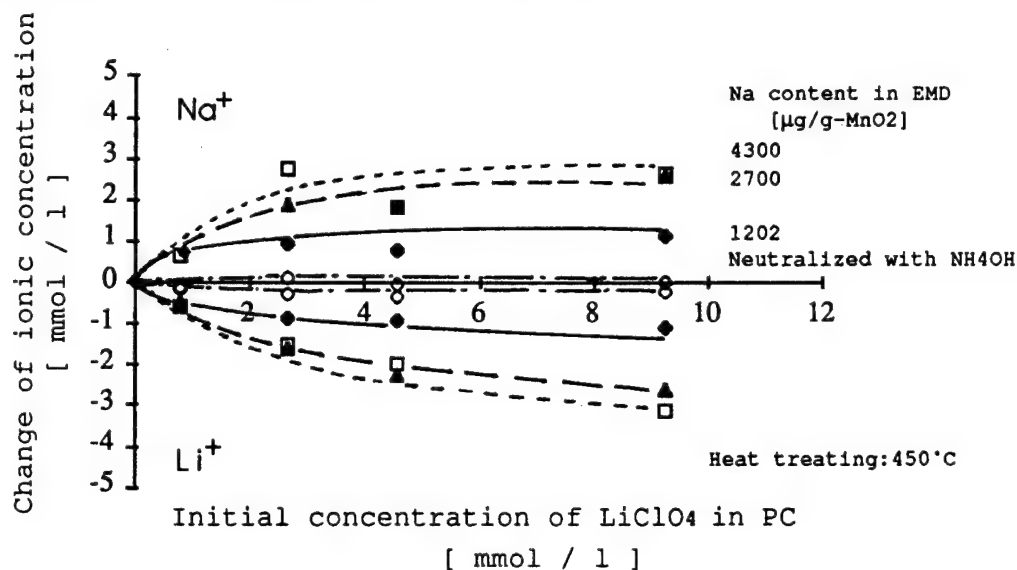


Fig.1 The effect of the Na content in EMD and the  $\text{LiClO}_4$  concentration in PC

### References

- (1) E.Miyanaga and M.Yoshio, the 52th meeting of Electrochemical Society of Japan, P.74 (1985)
- (2) I.Tari, S. Suzuki and T.Hirai, *Denki Kagaku*, 56, 124(1988)
- (3) I.Tari, T.Nakanishi and T.Hirai, *ibid.*, 56, 886(1988)
- (4) N. Chiba, K.Miyasaka, K.Yoshida and A.Matsunuma, *Progress in Batteries & Solar Cells (JEC Press Inc.)*, 5, 156(1984)
- (5) H.Tamura, M.Mitsuta and M.Nagayama, *Denki Kagaku*, 54, 250(1986)

19-02-04-K

## RECENT DEVELOPMENTS IN RECHARGEABLE LITHIUM BATTERIES

M. BROUSSELY - J. LABAT

SAFT/DGTA - Rue G. Leclanché BP 1039

86060 POITIERS FRANCE

The rechargeable lithium battery is presently one of the most exciting and promising challenge in the field of new power sources. Started in mid seventies by few laboratories, this research led to a first generation of practical products in the last few years. Progress in lithium reversibility, cathodic materials, as well as improved technologies were the key points which allowed this development, but are still the main issues in order to reach the required performances for a widely used industrial product.

After brief review of the different systems which have been studied, and comparison of their main features, the new developments will be emphasized. The remaining problems to solve will be discussed, leading to directions for future research in this field.

Electrochemical systems.

The main electrochemical systems will be described. Some of these were used to build practical high capacity cells, the performance of which are reported on Figure 1.

Different technologies are being developed in button, cylindrical and prismatic cells, corresponding to different applications.

Recent developments

During the last year, new high capacity rechargeable lithium button cells for memory back up were introduced on the market in Japan, based on several electrochemical systems :  $\text{Li-MoO}_3$ ,  $\text{LiV}_2\text{O}_5$ ,  $\text{LiMnO}_2$

The latter is probably the most studied at that time over the world, following the announcement that practical cylindrical AA cells could achieve 200 cycles or more, with an energy density of about 230 Wh/l. Only few informations are given on the crystalline structure of the  $\text{MnO}_2$ . Some patents (1, 2, 3) describe spinel  $\text{Li}_x\text{Mn}_2\text{O}_4$  or special mixture of amorphous  $\text{MnO}_2$  and  $\text{Li}_2\text{MnO}_3$ . According to the published results, the maximum degree of reversible Li insertion appears to be about 0.5 Li/Mole. Low cost, absence of toxicity, and a voltage range of 3 V make this material quite attractive. The main improvements to achieve for the system are : reversibility of the cathode over a large number of cycles without structure degradation, and efficiency of lithium cycling.

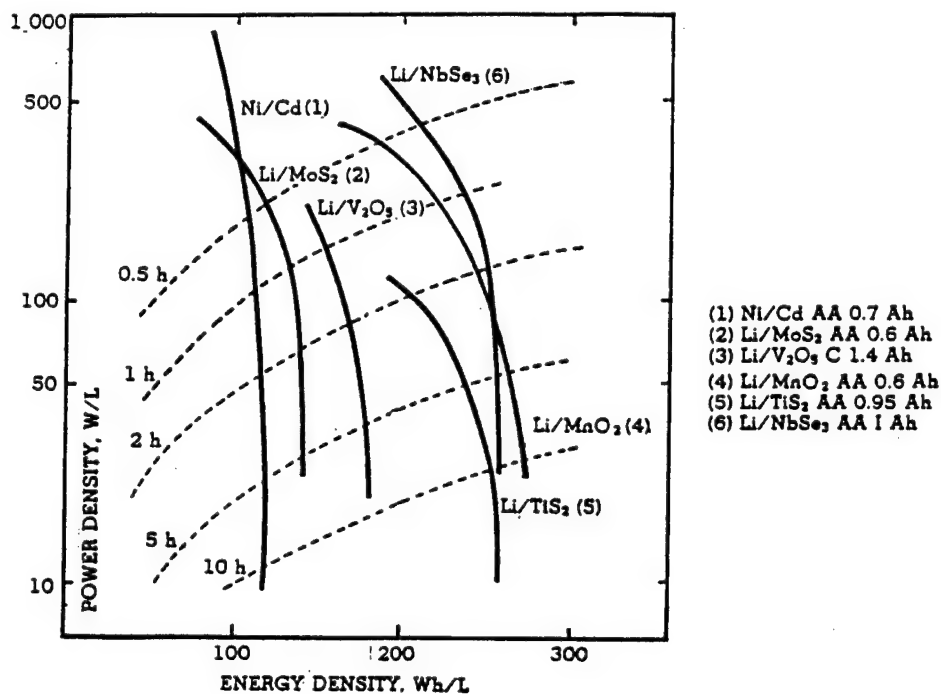
b4

Extensive research with a very high energy density material,  $\text{LiCoO}_2$ , is being carried on in U.S.A (4), for military applications. The feature of this system is a high working voltage of 4 V. This higher potential requires a very stable electrolyte. 350 Wh/l is potentially achievable for complete cells.

#### Lithium reversibility.

Besides the search of the ideal cathode well adapted to the applications, the lithium anode reversibility improvement remains the key point to reach the cycle life performance required for a widely used product. The use of alloys allows to solve the problem for the miniature cells, where energy density is not an issue, current density is low and depth of discharge quite limited. It is not suitable for larger standard size cells, where energy density is a major feature. The chance of success is to found the best electrolyte composition, possibly using additives. Lot of work is done in this way, and improvements are progressively obtained.

- 1) M. THACKERAY, U.S. Pat. 4 507 371 (3.26.85).
- 2) SONY Corp., J.P. 257479/86 (10.29.86); French Pat. 2 606 219 (10-29-87).
- 3) SANYO J.P., 258940/86 (10.30.86); Eur. Pat. 0 265 950 (10.29.87).
- 4) E. PLITCHA, M. SALOMON, S. SLUNE and M. UCHIYAMA, J. of Power Sources, 21,25,31 (1987).



RAGONE PLOTS FOR SOME SECONDARY LITHIUM SYSTEMS  
COMPARISON WITH Ni/Cd

19-02-05-G

## Amorphous $\text{FeVO}_4$ as a Cathode Active Material in Secondary Lithium Batteries

Michio SUGAWARA, Yukiteru KANEKO and Kenzo MATSUKI  
*Department of Applied Chemistry, Faculty of Engineering  
Yamagata University, Yonezawa, Yamagata 992 Japan*

Amorphous cathode active materials have been studied by several workers in secondary lithium batteries with nonaqueous electrolyte for the improvement of rechargeability and cycling behavior. In these studies some materials with good characteristics in the cycling behavior have been recommended for practical uses. The crystalline iron orthovanadate( $\text{FeVO}_4$ ) is an interesting cathode active material because of its higher discharge capacity, but its rechargeability becomes poor with the repetition of charge-discharge cycling. Accordingly, we attempted the preparation of amorphous  $\text{FeVO}_4$  and applied it for the cathode of nonaqueous electrolyte lithium batteries.

The amorphous  $\text{FeVO}_4$  was easily prepared as follows.<sup>1)</sup> An aqueous solution of  $\text{Fe}(\text{NO}_3)_3$  was added to a solution of  $\text{NH}_4\text{VO}_3$  to result in the precipitation of amorphous  $\text{FeVO}_4 \cdot 3\text{H}_2\text{O}$ , which was dehydrated by thermal treatment at a temperature below crystallization one ( $470^\circ\text{C}$ ) determined by thermal analysis (DTA). The  $\text{FeVO}_4$  obtained by such a procedure was stable and subjected to the measurements of charge-discharge curves and cycling characteristics in 1 M  $\text{LiClO}_4$  solution of propylene carbonate as an electrolyte.<sup>2)</sup> The cathode was first discharged to 2 V followed by the charge for the same time as that of discharge after a given rest time. Such a procedure was repeated for the measurement of cycling behavior.

The charge-discharge curve (Fig.1) of amorphous  $\text{FeVO}_4$  (heat treated at  $300^\circ\text{C}$  for 10 h) showed the good rechargeable property and the cycling behavior (Fig.2) was considerably improved compared with the crystalline one. The reversibility of charge and discharge was also confirmed by cyclic voltammetry. When the heat treating temperature in the preparation of amorphous  $\text{FeVO}_4$  was below  $250^\circ\text{C}$ , the potential in charging process became higher to result in the decomposition of electrolyte. However, the increase in charging potential was suppressed by the use of  $\text{FeVO}_4$  prepared by heating at  $300 \sim 400^\circ\text{C}$ . Since the heat treatment at about  $400^\circ\text{C}$  gave a slightly crystallized oxide, the required condition was the prolonged heating at  $300^\circ\text{C}$  over 10h. From these results the increase in the charging potential may be considered to be due to the remained OH group in  $\text{FeVO}_4$ . This was also confirmed by the results of IR and thermal analysis.

1) M.Touboul and A.Popot, J. Therm. Anal., 31,117(1986).

2) Y.Kitada, S.Iura, M.Sugawara and K.Matsuki, *Denki Kagaku*, 56,874 (1988).

b4

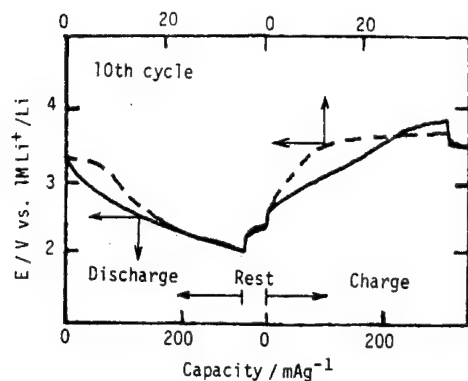


Fig. 1 Charge-discharge curves of amorphous (—) and crystalline  $\text{FeVO}_4$  (---)

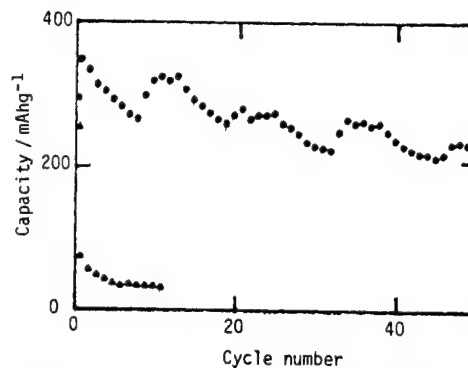


Fig. 2 Charge-discharge cycling behavior of amorphous (●) and crystalline  $\text{FeVO}_4$  (▲)

b4

19-02-06-G

Li/LiCr<sub>x</sub>V<sub>y</sub>S<sub>2</sub> SECONDARY BATTERIES

V. MANEV, A. NASSALEVSKA and A. MOMCHILOV  
Central Lab. of Electrochemical, Power Sources,  
Bulgarian Academy of Sciences  
1040 Sofia, BULGARIA

(no abstract received)

b4

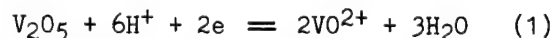
19-02-07-G

ELECTROLYTIC PREPARATION OF  $V_2O_5$  AND ITS CHARGE-DISCHARGE CHARACTERISTIC  
AS A CATHODE ACTIVE MATERIAL OF LITHIUM SECONDARY BATTERY

Y. Sato, T. Nomura, H. Tanaka, K. Kobayakawa

Department of Applied Chemistry, Faculty of Engineering, Kanagawa  
University, Rokkakubashi, Kanagawa-ku, Yokohama 221

As for the cathode active material in rechargeable lithium batteries, various kinds of inorganic materials such as metal oxides or sulfides have been studied. Vanadium pentoxide ( $V_2O_5$ ), especially,  $a\text{-}V_2O_5\text{-}P_2O_5$ <sup>1)</sup> seemed to be the most promised material among the candidates. By using  $a\text{-}V_2O_5\text{-}P_2O_5$ , a coin type lithium secondary battery has been developed.<sup>2)</sup> It is well known that electrolytic  $MnO_2$  shows different properties as cathode active materials compared to chemically prepared  $MnO_2$  or natural  $MnO_2$ . So, in the case of  $V_2O_5$ , some different properties may be expected, if the preparation method of  $V_2O_5$  is different. We tried to prepare  $V_2O_5$  from aqueous  $VOSO_4$  solution by controlled potential electrolysis and obtained amorphous  $V_2O_5(a\text{-}V_2O_5)$ . Its charge-discharge characteristics in PC containing  $1 \text{ mol} \cdot \text{dm}^{-3}$   $LiClO_4$  showed more favorable behavior as cathodic active material than crystalline  $V_2O_5(c\text{-}V_2O_5)$ . The solution containing  $VOSO_4$  showed a typical oxidation-reduction curve at pH 1.5 using Au working electrode. Anodic and cathodic peak currents were proportional to the square root of the scanning speed of applied potential around the room temperature, indicating the electrode process was diffusion controlled. The electrode process was assumed to be expressed as next equation,



According to the Nernst equation, the electrode potential is given by

$$E = E^0 - \frac{RT}{2F} \ln \frac{a_{VO^{2+}}^2 \cdot a_{H_2O}^3}{a_{V_2O_5} \cdot a_{H^+}^6} \quad (2)$$

If the activity of water and the activity ratio of vanadium compounds do not change as the pH is changed, then at  $24^\circ\text{C}$ ,

$$E = E^0' + 6/2(0.0589) \log a_{H^+} = E^0' - 0.178\text{pH} \quad (3)$$

A plot of the cathodic peak potential obtained at various pH values between 1.3 and 2.3 against pH was linear with the slope of  $-0.171\text{V/pH}$ . The fact that the obtained slope is nearly equal to the theoretical value suggests the electrode reaction proceeds reversibly according to the

equation (1). By using Au, stainless steel(SUS 304), Ti or ITO, as a working electrode, the controlled potential electrolysis in the solution containing  $0.2-0.5 \text{ mol}\cdot\text{dm}^{-3} \text{ VOSO}_4$  at  $0.5 \text{ V vs. Hg}_2\text{SO}_4$  was carried out at  $60^\circ\text{C}$ . The deposit was greenish black powder and easily peeled off from the electrode irrespective of the electrode materials. Vanadium content of the deposit coincided with the calculated value as  $\text{V}_2\text{O}_5$ . An X-ray diffraction pattern showed a weak peak at  $25.8^\circ$ , suggesting the deposit was amorphous(Fig.1). By heating the substance over  $400^\circ\text{C}$  in air, sharp peaks appeared at  $2\theta = 20.6^\circ, 22.0^\circ, 26.5^\circ, 31.3^\circ, 32.7^\circ$  and  $34.0^\circ$  corresponding to  $\text{V}_2\text{O}_5$  crystal. By using these materials, i.e. electrolytic  $\text{V}_2\text{O}_5(\text{a-V}_2\text{O}_5)$ ,  $400^\circ\text{C}$  heated  $\text{V}_2\text{O}_5(400\text{-V}_2\text{O}_5)$ , and commercialized crystalline  $\text{V}_2\text{O}_5(\text{c-V}_2\text{O}_5)$ , charge-discharge characteristics are tested in PC containing  $1\text{mol}\cdot\text{dm}^{-3} \text{ LiClO}_4$ . Figure 2 is the discharge profiles of these materials, where a- $\text{V}_2\text{O}_5$  showed the best result. When c- $\text{V}_2\text{O}_5$  is discharged till about  $2\text{V}$ , it cannot be charged while a- $\text{V}_2\text{O}_5$  can be charged, and its capacity does not decrease so much compared to the initial value(Fig.3). In the case of  $400\text{-V}_2\text{O}_5$ , charging is possible, but the capacity of the second cycle becomes about  $1/2$  of the first one and this value is maintained at the further charge-discharge cycle test. After 10 cycles of charge-discharge cycling test, a- $\text{V}_2\text{O}_5$  did not change its X-ray diffraction patterns.

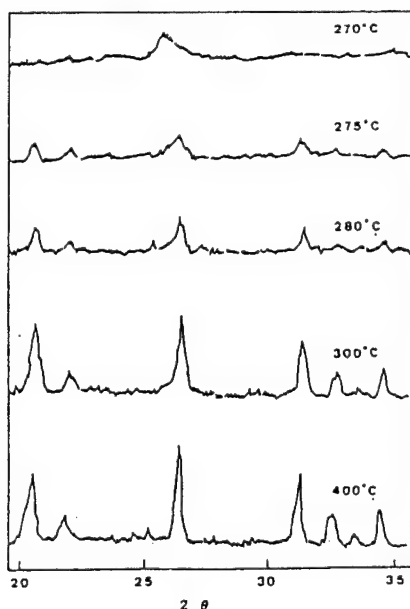


Fig.1 X-ray diffraction patterns of electrolytic oxidation product of  $\text{VOSO}_4$  heated for two hours at various temperature in air.

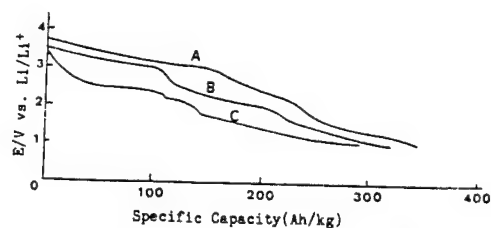


Fig.2 Discharge profile of (A) a- $\text{V}_2\text{O}_5$  (B)  $400^\circ\text{C-V}_2\text{O}_5$  and (C) c- $\text{V}_2\text{O}_5$  at room temperature. Discharge current is  $0.5\text{mA}/\text{cm}^2$ .

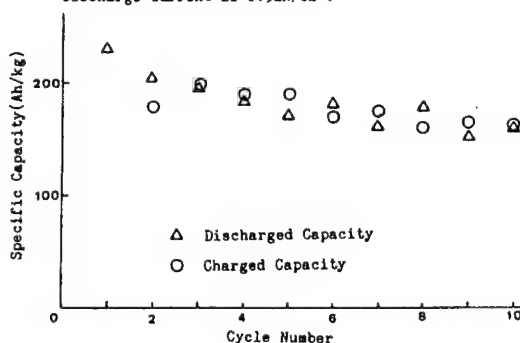


Fig.3 Cycle life performance of a- $\text{V}_2\text{O}_5$  at  $0.5\text{mA}/\text{cm}^2$ ,  $2.0-4.0\text{V}$  voltage limited cycling

- 1) Y. Sakurai and J. Yamaki, J. Electrochem. Soc., 132, 1512(1985).
- 2) K. Inada, K. Ikeda, Y. Sato, A. Itsubo, M. Miyabayashi and H. Yui, Proc. of Sym. of Electrochem. Soc., 88-6, 530(1988).



b4

19-02-08-G

STRUCTURAL AND KINETIC CHARACTERISTICS OF NIOBIUM SULFIDE ELECTRODE FOR  
A SECONDARY LITHIUM BATTERY

Naoaki Kumagai and Kazuo Tanno  
Department of Applied Chemistry, Faculty of Engineering,  
Iwate University, Morioka 020 Japan

In recent years great interest has been centered on the development of secondary lithium batteries with high energy densities. We have reported the charge-discharge cycling behavior of various Nb chalcogenides such as  $\text{NbX}_2$  ( $\text{X} = \text{S}$  or  $\text{Se}$ ) and  $\text{NbX}_3$  ( $\text{X} = \text{S}$  or  $\text{Se}$ ), as well as X-ray diffraction studies of structural changes of the chalcogenides [1~3]. In previous report, the solvent effect on the electrochemical characteristics of various Nb chalcogenides having different crystal structures was investigated [4]. In this work, the structural and kinetic characteristics of  $\text{NbS}_2$  with modifications of 3R- and 2H- types are investigated.

Experimental

Preparation of electrode materials, electrodes and electrolytes, the design of the cell and the method of conducting electrochemical measurements were as described previously [1~3]. The prepared sulfide was combined with graphite at a weight ratio of 1:1 and then the mixture was compression-moulded on a Ni mesh. The weight of the cathode was  $\sim 20 \text{ mg cm}^{-2}$ . Lithium pellets were used for both the negative and the reference electrodes. Discharge characteristics of the sulfide electrodes were measured at  $0.2 \text{ mA cm}^{-2}$  and at  $25^\circ\text{C}$  in the solution of  $1\text{M LiClO}_4$  in propylene carbonate (PC). Open circuit potentials of the sulfides were measured when they had stood for 20h after discharge.

Results and discussion

The Nb disulfide is a layered compound having a hexagonal symmetry. Layers of Nb and S are arranged in the sequence of  $-\text{S}-\text{Nb}-\text{S}-\text{S}-\text{Nb}-\text{S}$  perpendicular to the c-axis of the lattice. Lithium can be intercalated into the weak van der Waals gaps between the consecutive sulfur layers, to form  $\text{Li}_x\text{NbS}_2$  where  $x$  varies between 0 and 1. The c-axis lattice parameter of 3R- $\text{NbS}_2$  increases linearly as the  $x$ -value in  $\text{Li}_x\text{NbS}_2$  is increased. 3R- $\text{NbS}_2$  showed the reversible structural change along c-axis with cycling, while keeping the original crystal lattice, which caused excellent charge-discharge cycling behavior. The open circuit potential decreases linearly with increasing  $x$ -value and the relationship between the potential  $E$  (V) and the  $x$ -value in  $\text{Li}_x\text{NbS}_2$  is represented by  $E = 2.89 - 1.25 x$ . The standard free energy of intercalation in 3R- $\text{NbS}_2$ , calculated from the equation  $\Delta G^\circ_I = -F \int_0^1 E dx$ , is  $-52.2 \text{ kcal/mole}$  at  $x = 1$ . A thermodynamic model of Nagelberg and Worrell [5] was applicated to the sulfide system to obtain the interaction energy between intercalated lithiums in the van der Waals gaps. A low value of  $2.0 \text{ kcal/mole}$  was obtained for  $Z$  (the coordination number in the gaps) = 6.

The layered Nb sulfide contains one octahedral and two tetrahedral sites in the van der Waals gaps per molecule of  $\text{NbS}_2$  and lithium is intercalated normally to occupy the octahedral sites in the gaps. The chemical diffusion

coefficient of lithium in the gaps of  $3R-NbS_2$ , obtained from the current pulse relaxation method [6], is shown by the following form as a function of  $x$  in  $Li_xNbS_2$ .

$$\log_{10} \tilde{D} = -10.15 + 14.52x - 27.54x^2 + 13.75x^3$$

A maximum value of the  $\tilde{D}$  was observed between  $x = 0.3$  and  $0.4$ . According to the total probability of a jump to and from the octahedral sites from the neighboring tetrahedral sites during the course of self-diffusion of the lithium [6], the  $x$ -value giving the maximum  $\tilde{D}$  value corresponds to a low lithium-lithium interaction energy ( $0 \sim 5$  kcal/mole). This is coincident with the value from a thermodynamic model.

As discussed by Weppner and Huggins [7], the chemical diffusion coefficient  $\tilde{D}$  is related to the lithium component diffusion coefficient  $D_{Li}$  by

$$\tilde{D} = K_t D_{Li} \quad \text{.....(1)}$$

for the case where the electronic transference number is close to unity and the  $K_t$  in the equation is the Darken coefficient. Applying (1) eqn. to the data from the current pulse relaxation method gave the  $D_{Li}$  of  $2.2 \times 10^{-10}$  cm<sup>2</sup>/s at  $x = 0.53$  and  $5.4 \times 10^{-12}$  cm<sup>2</sup>/s at  $x = 1.00$  (25°C) (Table 1).

Table 1 Diffusion properties of lithium in  $3R-NbS_2$  as a function of  $x$ -value in  $Li_xNbS_2$

$x$	$dE/dx$	$\tilde{D}$ (cm <sup>2</sup> /s)	$K_t$	$D_{Li}$ (cm <sup>2</sup> /s)
0.293	1.25	$1.7 \times 10^{-8}$	14.3	$1.2 \times 10^{-9}$
0.526	1.25	$5.6 \times 10^{-9}$	25.7	$2.2 \times 10^{-10}$
0.762	1.25	$1.2 \times 10^{-9}$	37.1	$3.2 \times 10^{-11}$
1.00	1.25	$3.3 \times 10^{-10}$	60.9	$5.4 \times 10^{-12}$

#### Acknowledgments

The authors want to express their thanks to Mrs. Nobuko Kumagai for her helpful assistance in the experimental work.

#### References

- [1] N. Kumagai, et al., *Denki Kagaku*, **49**, 567 (1981).
- [2] N. Kumagai, et al., *Electrochim. Acta*, **27**, 1087 (1982).
- [3] N. Kumagai, et al., *J. Electroanal. Chem.*, **184**, 87 (1985).
- [4] N. Kumagai, et al., "Extended abstract of the 38th ISE Meeting", vol. 2, 1987, p.775.
- [5] A. S. Nagelbelg and W.L. Worrell, *J. Solid State Chem.*, **38**, 321 (1981).
- [6] S. Basu and W.L. Worrell in J. N. Mundy et al. (Eds.), *Fast Ion Transport in Solids*, North-Holland, Amsterdam, 1979, p.149.
- [7] W. Weppner and R.A. Huggins, *J. Electrochem. Soc.*, **124**, 1569 (1977).

b4

19-02-09-K

LITHIUM-CARBON ANODE AS LITHIUM SECONDARY BATTERIES

O. YAMAMOTO, Y. TAKEDA, R. KANNO, S. OHASHI, T. ICHIKAWA  
Department of Chemistry, Faculty of Engineering,  
Mie University, Tsu, 514 Japan

During the past decade, substantial research effort has been directed to the development of rechargeable lithium batteries. The reversibility of the lithium electrodes, however, remains as a significant problem in aprotic solvent based electrolyte: one of the major problems limiting cycle life is short circuit by the growth of lithium dendrites. We recently reported that thermal decomposition products of polymers have a capability as negative electrodes[1]. We found here that the carbon fiber showed a high efficiency in rechargeability.

Carbon fiber (M46 Toray Industries, Inc.) was used for the electrode materials. The working electrodes were consisted of a mixture of 50mg carbon and 5mg Teflon powder. The electrolyte was 1M  $\text{LiClO}_4$  in propylene carbonate - 1,2, dimethoxyethane by weight. The charge-discharge properties of carbon fiber was examined by the test cell with Li-metal/carbon fiber.

Figure 1 shows the open circuit voltage (OCV) of the cell Li/M46 at room temperature. The OCV of 3.3 V at 0.0 Li/C was due to Li/Teflon couple. After a rapid decrease in voltage from 3.3V near 0.0 Li/C, the OCV decreases slowly from 0.8 V (0.009 Li/C) to 0.0 V (0.09 Li/C).

To understand the detail of the lithium storage process, we examined cycling behavior of the Li/M46 cell at a different lithium storage level with a charge and discharge depth of  $\pm 0.005$  Li/C. The current density was  $0.5 \text{ mA/cm}^2$ . The high efficiency in rechargeability was obtained within a lithium storage level between 0.045 and 0.135 Li/C: number of charge-discharge cycles exceeded 1000 cycles at 0.1125 Li/C.

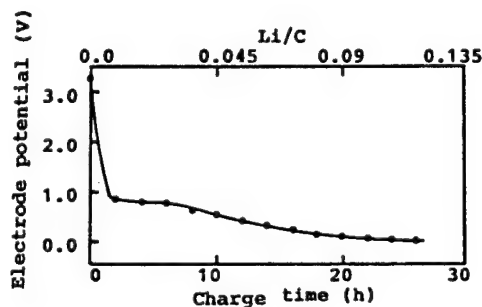


Fig. 1 Open circuit voltage (OCV) curve of the carbon fiber M46 electrode at room temperature.

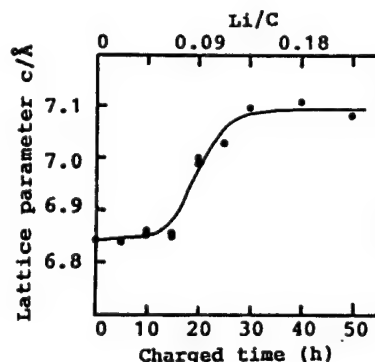


Fig. 2 C-axis parameter of the carbon fiber M46 electrode as a function of lithium storage level.

Figure 2 shows the c-axis parameter of the carbon fiber M46 electrode as a function of lithium storage level. The c-axis parameter changes from 6.85 to 7.08 Å within a lithiation range between 0.045 and 0.135 Li/C, where the best reversibility in cell reaction was obtained. The lithiation proceeded by an intercalation of lithium ions or solvated lithium ions.

Figure 3 shows the XPS spectra of lithium 1s 1/2 state and the carbon 1s 1/2 state examined at various lithium storage levels. The Li 1s 1/2 peak shifts to higher energy with lithiation: the highest energy of 55.12 eV was obtained at 0.09 Li/C, where the Li/M46 couple showed the highest efficiency in rechargeability with intercalation cell reaction. In deeper lithiation range of 0.22 Li/C, the peak Li 1s shift again to lower energy, suggesting a lithium metal deposition on the surface of carbon fiber.

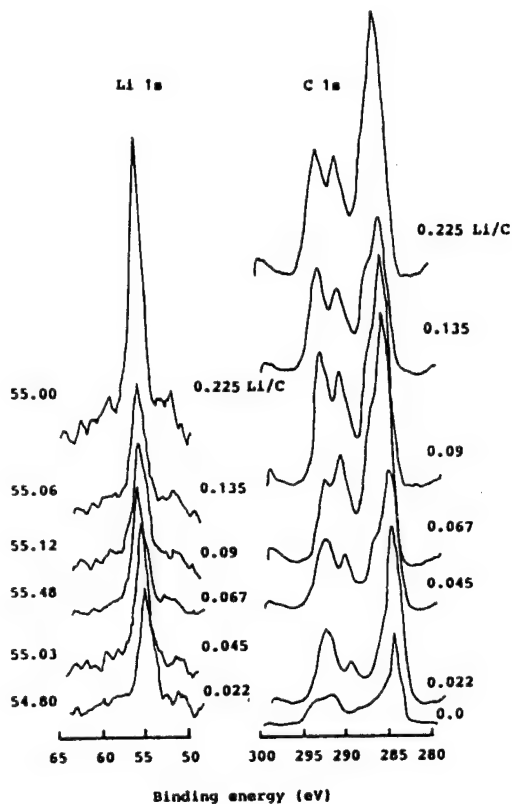


Fig. 3 XPS spectra of the carbon fiber M46 electrode as a function of lithium storage level.

[1] O. Yamamoto, Y. Takeda, R. Kanno, K. Nakanishi and T. Ichikawa, Proc. J. Electrochem. Soc., 88(6), 754 (1988).

b4

19-02-11-G

ELECTROCHEMICAL INTERCALATION OR ALKALI METALS INTO GRAPHITE  
AND GIC'S. AN APPLICATION TO LITHIUM BATTERIES, PART I.

R. Yazami

Laboratoire d'Ionique et d'Electrochimie du Solide (UA-CNRS 1213). Ecole Nationale Supérieure d'Electrochimie et d'Electrometallurgie de Grenoble. BP 75, 38402 St. Martin d'Heres, France.

One of the important features of graphite as host structure for intercalation is the possibility to accommodate both cation or anion whereas in most other bidimensional hosts such as metal dichalcogenides only cation can be intercalated. This particularity is due to the electronic structure of the semi metal like graphite in which the carbon band can accept or donate electron depending on the counter ion sign. When electron is accepted, a macroanion  $C_m^-$  is formed then the carbon atoms should be considered as reduced, the total charge being balanced by the intercalated cation. Symmetrically, when an anion is intercalated, a macrocation  $C_m^+$  is formed and the carbon is oxidized.

When an electrochemical method is used for cation or anion intercalation into graphite the first step of the reaction consists in the formation of  $C_m^-$  or  $C_m^+$  respectively through an electron exchange with an external circuit. Under this point of view, the electrochemical intercalation should be considered as an assisted reaction requiring an energy supply to be achieved. The second step of the intercalation process consists in the diffusion within the graphene layer of ion, generally solvated by neutral molecules from the electrolyte. In this case, ternary GIC's are formed as the most known examples  $C_{24}^+HSO_4^-(H_2SO_4)_n$ ,  $n=2-2.5$  or  $C_{24}^-K^+(DMSO)_6$  corresponding both to stage-1 GIC [1].

Since high voltage (4.5 to 5.2 V vs  $Li^+/Li$ ) or low voltage (1.2 to .3V vs  $Li^+/Li$ ) have to be imposed to the graphite electrode to form  $C_m^+$  or  $C_m^-$  respectively, only a limited number of electrolytes can be used due to the possibility of their oxidation or reduction prior to the intercalation. Highly oxidized and stable anion such as  $HSO_4^-$ ,  $ClO_4^-$  [1],  $C_nF_{2n+1}SO_3^-$  [2],...etc are intercalated in concentrated acid or in propylene carbonate (PC), or nitromethane solutions which have a "kinetical" stability under high voltage. On the other hand, only cation showing good stability towards reduction such as alkali or some alkali earth metals and tetraalkylammonium have been successfully intercalated in liquid (PC, DMSO, DME ...) or more recently in solid state electrolytes as polyethylene oxide (PEO)[3].

b4

One of the advantages of using PEO based electrolyte lies in the fact that the cation moves free of any solvent molecule and thus its intercalation leads to binary compounds rather than ternary ones. Under this assumption, sodium electrochemical intercalation has been attempted using (-) Na/PEO<sub>12</sub>NaCF<sub>3</sub>SO<sub>3</sub>/C (+) as chain at 80°C [4]. Intermittent galvanostatic titration technique has been used to study the reaction kinetics. The most striking result concerns the comparison between the diffusion coefficients of K and Na into graphite. Whereas at 58°C  $D(K^+)$  is in the order of  $10^{-7}$  cm<sup>2</sup>/s [5],  $D(Na^+)$  is around  $10^{-4}$  time lower even at 80°C. This difference in behavior should explain the difficulty found in the synthesis of lower stage Na-GIC's, when stage-1 compounds are easily prepared with other alkali metals. Some domain formation (clusters) during the early step of sodium intercalation can not be excluded. The evidence of sodium intercalation was given from X-ray diffraction which shows the complete disappearance of the 002 graphite strongest line and the appearance of a line at 4.6 Å. This later was ascribed to 001 line from stage-1 Na-GIC, however this line interferes with that of the crystalline part of PEO. So the sodium intercalation remains an open question.

An other use of PEO electrolyte concerned all solid state lithium batteries in which the positive electrode consisted in a new graphite fluoride synthesized at room temperature [6]. The discharge curves obtained at 80°C showed high voltage (2.9 V) and coulomb yield approaching 90 %. The energy density as high as 1300 Wh.kg<sup>-1</sup> was reached in this system which therefore should be considered as the highest using PEO as electrolyte solvent.

#### References:

- [1] J.O. Besenhard and H. P. Fritz, *Angew. Chem.*, 22(1983)952 and references therein.
- [2] B. Ruisinger and H. P. Boehm, *Angew. Chem.* 99 (1987)266.
- [3] R. Yazami and Ph. Touzain, *J. Power Sources* 9(1983)365.
- [4] R. Yazami in *Chemical Physics of Intercalation*, A. P. Legrand and S. Flandrois eds. *Nato Asi Series B172*, Plenum Press, New York (1987) p.457.
- [5] R. Yazami and Ph. Touzain, *Solid State Ionics*, 9-10(1983)489.
- [6] R. Yazami and A. Hamwi, *Solid State Ionics* 28-30(1988)1756.

b4

19-02-12-G

LITHIUM BATTERIES BASED ON GIC's WITH METAL FLUORIDES (part II)

R. Yazami and T. Nakajima.

Division of Molecular Engineering, Graduate School of Engineering, Kyoto University, Sakyo-ku, Kyoto, 606, Japan.

Graphite intercalation compounds (GIC's) have been widely studied for the potential application as positive electrode material in lithium batteries. Covalent compounds such as graphite fluoride  $(CF)_x$  or graphite oxide  $(C_8O_2(OH)_2)$  have high specific capacities (800 to 990 mAh.g<sup>-1</sup>) and good discharge potential (2.3 to 2.5 V). GIC's with metal halides generally lead to higher discharge potential (2.5 to 2.9 V), but in spite of their lower capacities (300 to 400 mAh.g<sup>-1</sup>), the possibility of their use in secondary batteries is increased.

In this part, the electrode properties of two metal fluorides-GIC's VF<sub>6</sub> and TiF<sub>6</sub>, as positives in lithium/PC-LiClO<sub>4</sub> batteries will be discussed, in relation with their structures. Although these two fluorides are intercalated into graphite under similar conditions i.e. vapor phase transport technique in high purity fluorine atmosphere, they differ in the in-plane and out of plane crystal organization. The MF<sub>6</sub> octahedra are isolated in the VF<sub>6</sub>-GIC and arrange in a superlattice, whereas the TiF<sub>6</sub> ones, form polymer chains having fluorine bridges. In addition the stage number which designs the number of graphite planes separating two intercalated layers is two in the VF<sub>6</sub>-GIC and one in the TiF<sub>6</sub> one.

The electrochemical process at the positive electrode implies the lithium diffusion within the GIC following the schema:

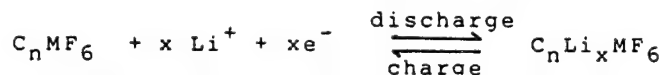


Figure-1 displays the voltammograms obtained with VF<sub>6</sub> (a) and TiF<sub>6</sub> (b) GIC's under 1mV.mn<sup>-1</sup>. Two oxidation peaks are observed in both of these diagrams and could be ascribed to the lithium de-intercalation for the lower potential ones (around 3 and 3.5 V) and perchlorate anion intercalation for the highest ones (>4.2 V). These voltammograms are reproducible over several cycles without important loss in the batteries capacities. It is worth noticing that the current intensity is almost 5 times higher for the VF<sub>6</sub>-GIC than for the TiF<sub>6</sub> one, even when the theoretical capacities were in the same order of magnitude (2 and 1.7 mAh resp.). This suggests that the lithium diffusivity is enhanced by the in-plane organization of the VF<sub>6</sub> isolated octahedrons rather than the TiF<sub>6</sub> polymerized ones.

The galvanostatic discharge curves of the VF<sub>6</sub>-GIC based battery under 100 and 10 µA are plotted in figure-2a and b respectively and show only a slight difference in the discharge average potential (2.96 V (a) and 3.02 V (b) for x=2.5) which indicates a very low electrode polarization. However the amount x of intercalated lithium is noticeably higher for the slower discharge (5.37 in (b) and 4.4 in (a)). The calculated energy density deduced from curve (b) is 1180 Wh.kg<sup>-1</sup> (2650 Wh.l<sup>-1</sup>), which is much more higher than that obtained with metal chlorides GIC's. The good electrode capacity associated with the high discharge voltage and the possible cyclability place the VF<sub>6</sub>-GIC among the very promising positive electrode materials for secondary lithium batteries.

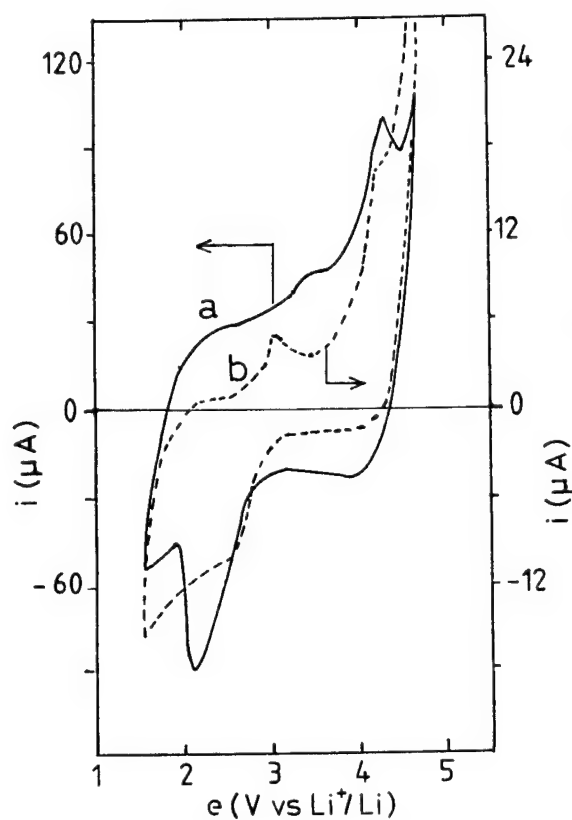


fig.1: Slow scan voltammograms ( $1\text{mV.mn}^{-1}$ ) of Li/GIC batteries (a)  $\text{VF}_6$ -GIC and (b)  $\text{TiF}_6$ -GIC having 2 and 1.7 mAh capacities, (2<sup>nd</sup> cycles)

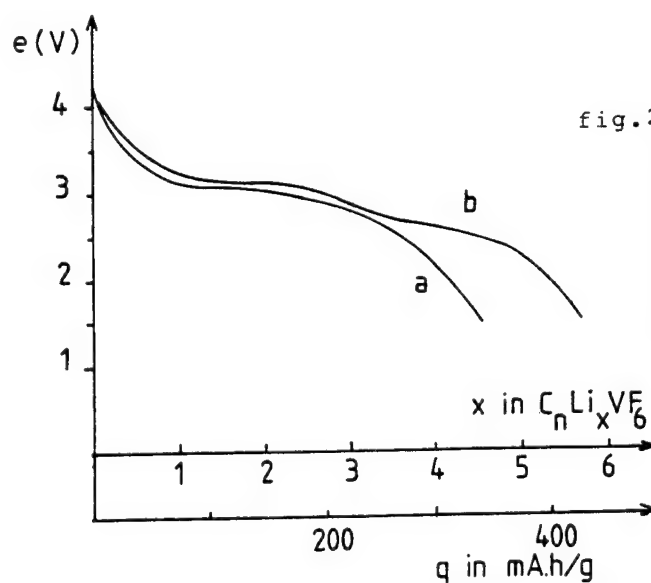


fig.2: Galvanostatic discharge curves of Li/  $\text{VF}_6$ -GIC batteries (a)  $i=100\text{ }\mu\text{A}$  and (b)  $i=10\text{ }\mu\text{A}$ . The corresponding electrode specific capacity is indicated.



b4

19-02-13-G

#### LITHIUM SURFACE ANALYSES BY FAB MASS SPECTROMETRY

M. Arakawa, S. Tobishima and J. Yamaki  
Nippon Telegraph and Telephone corporation,  
NTT Applied Electronics Laboratories,  
Tokai, Ibaraki-ken, 319-11, Japan.

##### Introduction

It has been widely accepted that cycling features in lithium secondary batteries are affected by features of passivating films which are formed on the lithium surface. Hence, some analyses of surface film with XPS or FTIR have recently been reported [1-3]. Mass spectrometry is a useful method in surface analysis. However, there have been few reports analyzing lithium surface by mass spectrometry because fragmentation of lithium compounds in the ionization process makes identification of compounds very difficult.

Fast Atom Bombardment Mass Spectrometry (FAB-MS) is a useful method for surface analysis because a more stable mass spectrum can be obtained than that in Secondary Ion Mass Spectrometry (SIMS). In this work, FAB-MS are adopted to analyze surface film.

##### Experimental

All experiments were carried out with a double focusing mass spectrometer (JEOL) using an FAB ion source. Ar and Xe were the accelerated atoms.

##### Result and Discussion

Molecular ion peak is very useful for identifying of compounds. However, molecular ion peak intensity depends on bond dissociation energy as shown in Fig. 1. Lithium halides were used in this experiment. Molecular ion peaks were observed as a form of  $\text{Li}(\text{LiX})_n^+$ , where X is a halogen atom and  $n = 1, 2, \dots$ . Relative intensities of the molecular peak were estimated by dividing molecular ion peak intensity by the intensity of  $\text{Li}_2^+$ . The relative intensity of the molecular ion peak decreased with the decrease of bond dissociation energy and the lithium iodide molecular ion peak was not observed any more. Consequently, the stability of lithium compounds must be considered in identification.

In order to apply FAB-MS to lithium surface analysis, mass spectra of some inorganic and organic lithium compounds were investigated. Lithium organic compounds were prepared by reacting lithium metal with organic solvents. Molecular ion peaks and some characteristic peaks of lithium compounds are summarized in Table I.  $\text{LiOH}^+$  ( $m/e=24$ ) and  $\text{Li}(\text{LiOH})^+$  ( $m/e=31$ ) were observed in  $\text{LiOH}$ .  $\text{Li}_2\text{O}^+$  ( $m/e=30$ ) and  $\text{Li}(\text{Li}_2\text{O})^+$  ( $m/e=37$ ) were observed in  $\text{Li}_2\text{O}$ . However, no

characteristic peak was observed in  $\text{LiCO}_3$  and  $\text{Li}_3\text{N}$ . Some characteristic peaks were also observed in lithium salts used as electrolytes except in the case of  $\text{LiClO}_4$  and  $\text{LiSbF}_6$ .

Figure 2 shows the mass spectrum of lithium surface reacted with 1M solution of  $\text{LiClO}_4$  using Propylene Carbonate (PC) as a solvent. Several kinds of lithium compounds were suggested as shown in Fig. 2 by comparing with characteristic mass peaks summarized in Table I. This data shows FAB-MS is adoptable to lithium surface analysis.

[1] S.P.S. Yen, D.H. Shen, B.J. Carter and R.B. Somoano, 31st International Power Source Symposium, p-114 (1984)

[2] D. Aurbach, M.L. Daroux, P.W. Faguy and E. Yeager, J. Electrochem. Soc., 134, 1611 (1987)

[3] id., ibid., 135, 1863 (1988)

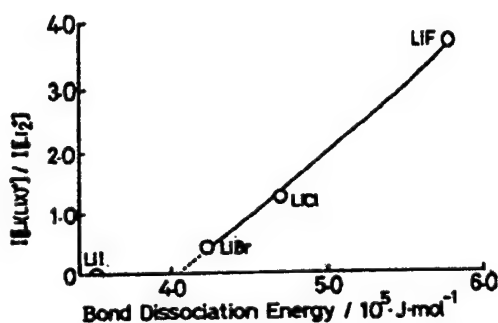


Fig. 1. Dependence of relative molecular ion peak intensities on bond dissociation energies.

Table I. Characteristic Mass Peaks

Lithium Compounds	Characteristic Mass Peaks
$\text{LiClO}_4$	-
$\text{LiBF}_4$	$\text{LiBF}_4^+$ , $\text{LiBF}_3^+$ , $\text{LiBF}_2^+$
$\text{LiPF}_6$	$\text{PF}_6^+$
$\text{LiAsF}_6$	$\text{As}^+$
$\text{LiSbF}_6$	-
$\text{Li}_2\text{O}$	$\text{Li}_2\text{O}^+$ , $\text{Li}(\text{Li}_2\text{O})^+$
$\text{LiOH}$	$\text{LiOH}^+$ , $\text{Li}(\text{LiOH})^+$
$\text{Li}_2\text{CO}_3$	-
$\text{Li}_3\text{N}$	-
$\text{C}_2\text{H}_5\text{OLi}$	-
$(\text{CH}_3\text{OLi})_2$	$\text{CH}_2\text{Li}^+$
$\text{CH}_3\text{CH}(\text{OLi})\text{CH}_2\text{OLi}$	$\text{CH}_3\text{C}(\text{OLi})\text{COLi}^+$

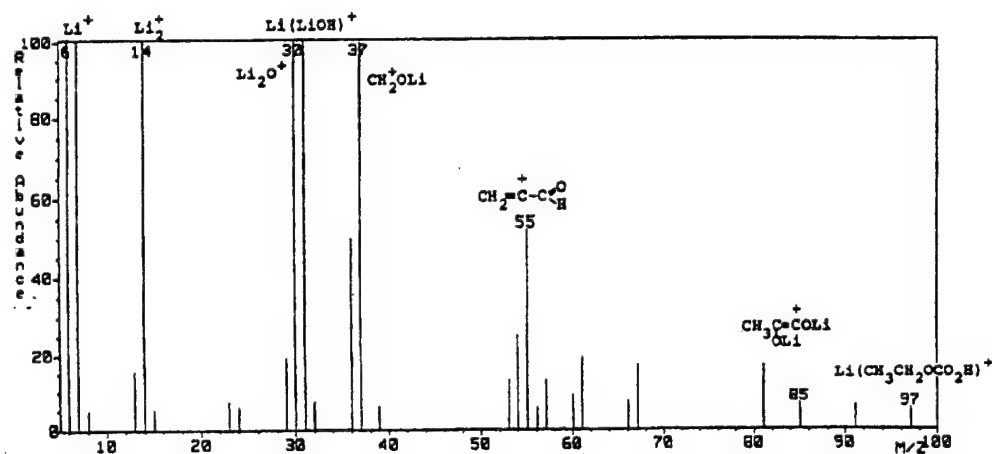


Fig. 2. Mass spectrum of lithium surface reacted with 1M  $\text{LiClO}_4/\text{PC}$ .

b4

19-02-14-G

Effects of electrolytes on electrodeposition of lithium  
H.KOSHINA, N.EDA and A.MORITA

Technology Laboratory, Matsushita Battery Ind. Co., Ltd.  
Moriguchi, Osaka 570, JAPAN

#### Introduction

Secondary lithium batteries have been studied actively in expectation of high voltage and high energy density. Our main study is the development of suitable electrolyte having electrochemical stability at high voltage and high cycling efficiency of the negative electrode.

This paper refers to the relation between morphologies of electrodeposited lithium and cycling efficiencies, with special emphasis on carbonic esters used as solvents.

#### Experimental

The potentials of anodic and cathodic decomposition of solvents were measured by the linear sweep method. Carbonic esters e.g. ethylene carbonate (EC), propylene carbonate (PC), butylene carbonate (BC) and dimethyl carbonate (DMC), tetrahydrofuran (THF) and 2-methyltetrahydrofuran (MTHF) etc. as the solvents were tested.  $\text{LiAsF}_6$ ,  $\text{LiPF}_6$ ,  $\text{LiClO}_4$ ,  $\text{LiCF}_3\text{SO}_3$  etc. as solutes were examined. The morphologies of electrodeposited lithium were observed by SEM method after constant current charge and discharge cycles in specific deposition rate using coin type cells.

#### Results and Discussion

The measuring results of potentials of anodic and cathodic decomposition of the solvents are shown in Fig.1. The results show that THF, MTHF and carbonic esters such as EC, PC, BC and DMC are stable against cathodic decomposition, whereas lactones e.g.  $\gamma$ -butyrolactone (GBL) and  $\gamma$ -valerolactone (GVL) are easily reduced. In addition, it was found that carbonic esters were electrochemically stable against anodic decomposition.

Specific conductivities of various solutes in PC are shown in Fig.2. Almost all solutes have the highest specific conductivities at the concentration of around 1 mol/l. It is supposed that these are caused by the limitation of dissociation of solutes in PC and the change of viscosity of solutions. Among the solutes,  $\text{LiPF}_6$  shows the highest specific conductivity. This might be attributable to the size of anion and transference number.

The relation between electrodeposited morphologies and cycling efficiencies in the  $\text{LiAsF}_6/\text{EC}+\text{MTHF}$  has been reported(1). In this paper, the relationship was examined for  $\text{LiPF}_6$  under various electrodeposited conditions. For electrodeposited conditions, charging current densities and concentrations of solute were varied, and the electrodeposited morphologies were observed. As shown in Fig.3, dendritic lithium was formed under the condition of low-concentration and high-current density, and mossy lithium was formed under the condition of high-concentration and low-current density. Under the moderate conditions, granular lithium might be formed. The dendritic lithium has low cycling efficiency because of its morphology sustaining low current collecting efficiency, and the cycling

efficiency increases mossy, granular and dendritic lithium in that order. Therefore it is supposed that the morphology of electrodeposition depended on the diffusion rate and bulk concentration of lithium ion.

#### Conclusion

Improvement of cycling efficiency may be achieved under the condition of making mossy lithium electrodeposited i.e. suitable combination of solutes, solvents and charging current densities.

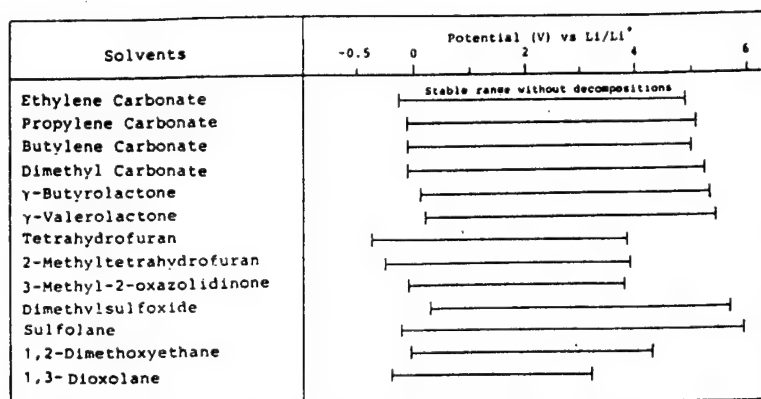


Fig.1 Electrochemical window of solvents using Pt electrode

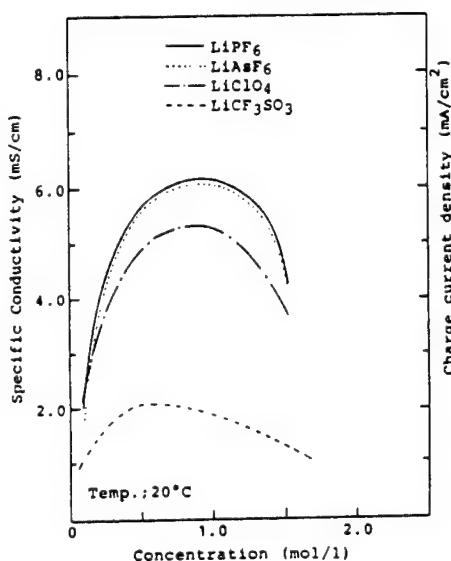


Fig.2 Relationships between specific conductivity and concentration of some solutes in PC

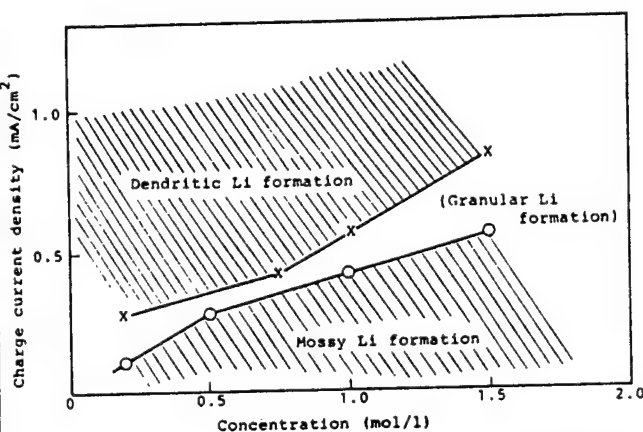


Fig.3 Influence of concentrations of LiPF<sub>6</sub> in PC+EC and charging current densities on morphology of Li

(1) I.Yoshimatsu, T.Hirai and J.Yamaki  
J. Electrochem. Soc., Vol.135, 2422 (1988)

b4

19-02-16-G

#### THE AC IMPEDANCE BEHAVIOR AT LITHIUM/ORGANIC ELECTROLYTE INTERFACE

M. Morita and Y. Matsuda

Department of Industrial Chemistry, Faculty of Engineering,  
Yamaguchi University, Tokiwadai, Ube 755, Japan

A major problem in the development of ambient temperature rechargeable lithium (Li) batteries is low cycling efficiency at Li negative electrode. Recently it has been demonstrated that the Li rechargeability can be improved by adding small amounts of some organic compounds to the electrolytic solution [1-3]. However, the details of those addition effects have not been clarified yet. In this paper we have examined some heterocyclic compounds which are expected to influence the structure of the Li/organic electrolyte interface. The relation between the coulombic efficiency in the cycle and the AC impedance behavior at the interface is discussed.

A "Battery Grade" propylene carbonate (PC) was used as the solvent. The electrolytic salt was dehydrated  $\text{LiClO}_4$  or  $\text{LiPF}_6$ . The concentration of the electrolyte was  $1.0 \text{ mol dm}^{-3}$ . 2-Methylfuran (2MeF), 2-methylthiophene (2MeTp), 4-methylthiazole (4MeTz) and benzene were used as the additives. The Li coulombic efficiency in the charge-discharge cycle was evaluated by a galvanostatic deposition-dissolution technique using an Ni substrate [4]. The AC impedance at the electrode/electrolyte interface was measured under the OCV condition by a Frequency Response Analyzer. These electrochemical measurements were carried out in a dry Ar atmosphere at room temperature (20 - 25 °C).

The Li coulombic efficiency in pure PC/ $\text{LiClO}_4$  decreased with the repeated charge-discharge cycle. The degradation of the rechargeability relates to the formation of a resistive film on the surface of deposited Li. The addition of 2MeF or 2MeTp to the electrolyte (0.5 vol.%) brought the increase in the efficiency and kept it high even after prolonged cycles. The AC impedance measured on the Li electrode in the PC-based electrolytes gave a single semicircle on a complex plane. This showed the equivalent circuit composing of a parallel combination of a interface resistance and a capacitance [5]. The resistive component,  $R_t$ , was based on the resistance of the surface film whose growing reaction involves a diffusion process. Figure 1 shows the variations of  $R_t$  in the AC impedance with the number of charge-discharge cycle. The increase of  $R_t$  in PC/ $\text{LiClO}_4$  with the cycle was owing to an increase in the thickness of the resistive film formed on the Li surface. The addition of 2MeF or 2MeTp decreased  $R_t$  and its variation with the cycle. These additives seems to inhibit the film formation reaction. The addition of 4MeTz also improved the cycling efficiency but its influence on the AC impedance was rather small. The time constant,  $\tau$  ( $= R_t \cdot C_d$ ;  $C_d$  denotes the capacitive component in the AC impedance), was also measured as a functions of the immersion time or the charge-discharge cycle. In PC/ $\text{LiClO}_4$ ,  $\tau$  kept almost constant with the immersion time, while it changed in the solution containing 2MeF or 2MeTp. These suggest that the electrical properties of the film formed in PC/ $\text{LiClO}_4$  did not vary with the immersion time but those in the solutions containing additives changed with the time. That is, the additives influenced the film composition formed on the Li surface in contact with the PC-based electrolyte. Figure 2 shows the variation of the time constants with the charge-discharge cycle. The differences between  $\tau$  in PC/ $\text{LiClO}_4$  and  $\tau$  in 2MeF- or 2MeTp-containing PC/ $\text{LiClO}_4$  are probably based on the differences of the film composition. Thus the added

2MeF and 2MeTp react with Li to form rather conductive films whose chemical compositions are probably different from that formed from the neat PC solution. The action of 4MeTz may be somewhat different from those of 2MeF and 2MeTp. Similar results were obtained in the PC/LiPF<sub>6</sub> solution.

The addition of benzene to PC/LiClO<sub>4</sub> (ca. 5 vol.%) was also effective on the cycling efficiency of Li, as already reported by Yoshio et al. [6]. The resistance at the Li/electrolyte interface was lowered by the addition of benzene. However, the time constant in the benzene-containing PC/LiClO<sub>4</sub> was almost the same as that in PC/LiClO<sub>4</sub>. That is, the composition of the film was scarcely changed by the addition of benzene. The added benzene adsorbed on the Li surface to inhibit the film formation reaction of Li with solvent PC.

Summarizing, the effects of the additives to the PC-based electrolytes are based on either a chemical reaction to form a conductive film on the Li surface or an adsorption to inhibit the growth of the less conductive film formed by the reaction of Li with solvent PC.

- [1] K.M. Abraham; J. Power Sources, 14, 178(1985).
- [2] S. Tobishima, T. Okada; Denki Kagaku, 53, 742(1985).
- [3] Y. Matsuda, M. Morita; Progress in Batteries & Solar Cells, 7, 266 (1988).
- [4] M. Morita, H. Miyazaki, Y. Matsuda; Electrochim. Acta, 31, 573(1986).
- [5] Y. Matsuda, M. Morita; J. Power Sources, in press.
- [6] H. Nakamura, S. Ito, K. Isono, M. Yoshio; Extended Abstracts of the 28th Battery Symposium in Japan (1987), p.191 (No. 3B03).

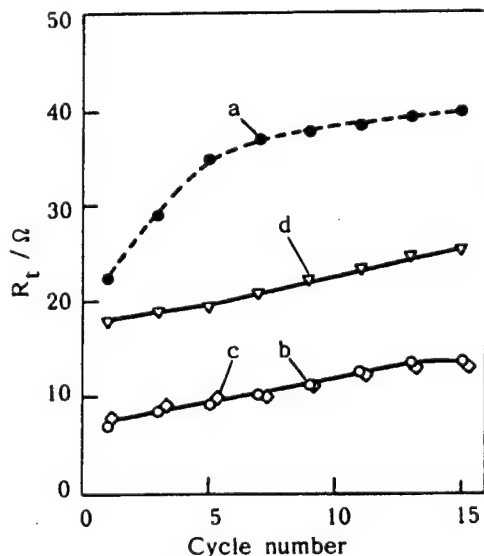


Fig. 1 Variation of the resistance ( $R_t$ ) with the cycle number, a: PC/LiClO<sub>4</sub>, b: (a) + 2MeF, c: (a) + 2MeTp, d: (a) + 4MeTz, Conc. of the additives: 0.5 vol.%.

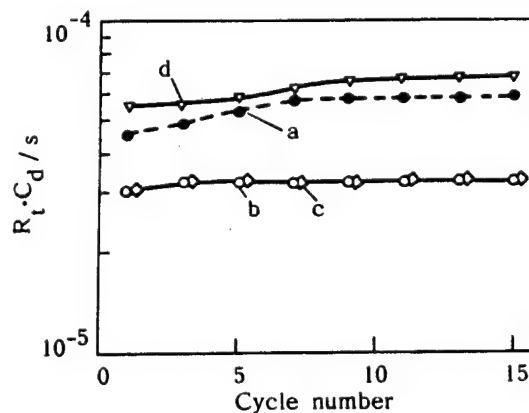


Fig. 2 Variation of the time constant ( $R_t \cdot C_d$ ) with the cycle number, a: PC/LiClO<sub>4</sub>, b: (a) + 2MeF, c: (a) + 2MeTp, d: (a) + 4MeTz, Conc. of the additives: 0.5 vol.%.

b4

19-02-17-G

IONIC TRANSPORT IN PASSIVATING LAYERS ON LITHIUM ELECTRODE

A.L. L'vov, E.S. Nimon, A.V. Churikov, A.A. Senotov,  
A.N. Chuvashkin, I.A. Pridatko  
Department of Chemistry, Saratov State University,  
410601 Saratov, U.S.S.R.

In the present work ionic transport in passivating layers on lithium in thionylchloride (TC) and propylenecarbonate (PC) solutions has been studied using the single current impulse technique.

For the studied systems square-law  $j, E$  relationships were found under sufficiently large polarizations (Fig. 1). In the low polarization region the  $j, E$  relationships gave straight lines extrapolated to the origin of coordinates. Both the square law found (Fig. 1) and the fact that anodic lithium dissolution rate was inversely proportional to the cubed value of the passivating layer thickness show the existence of space-charge-limited currents. The basis of the proposed model is the idea of a lithium electrode as an infinite reservoir of ions which can be injected into the passivating layer and create space charge limiting the ionic carrier current, with the polarization uprise leading to the increase of the injected ions concentration.

Lithium electrode polarization curves in a wide range of current densities and polarizations were stated to be described with high accuracy by an equation which takes into account the transport of both the intrinsic mobile passivating layer ions and ions injected from the electrode. Using this equation the concentration and mobility values for mobile lithium ions in passivating layers were calculated from experimental data. Fig. 2 shows that the concentration of mobile ions averaged by the passivating layer thickness decreases appreciably with time which is obviously

bound up with the perfection process of the passivating layer. The dependence of the mobility value on storage time was much weaker.

Temperature dependences of transport characteristics of passivating layers on lithium in PC, 1 M  $\text{LiClO}_4$  solutions have been studied. It has been stated that temperature dependences of mobile lithium ions concentration and specific ionic conductivity are described by the equations of the Arrhenius and Frenkel types with activation energy values of 0.40 and 0.60 eV, respectively.

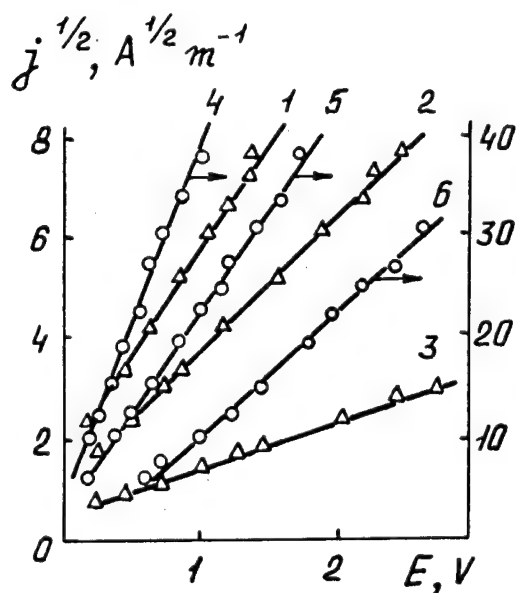


Fig. 1

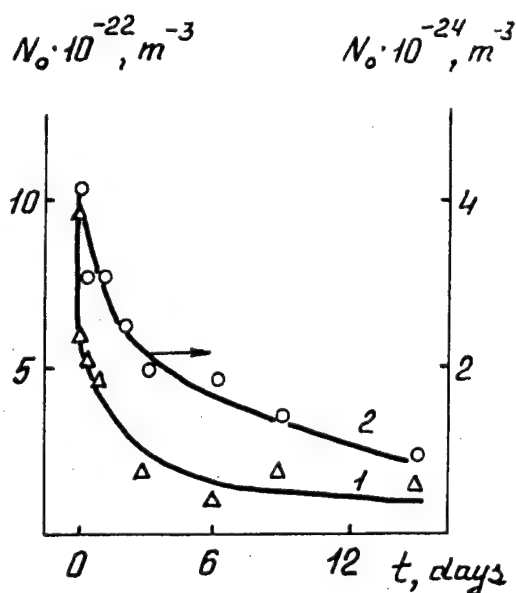


Fig. 2

Fig. 1. Anodic polarization curves of lithium electrode in TC, 1 M  $\text{LiAlCl}_4$  (1, 2, 3) and PC, 1 M  $\text{LiClO}_4$  (4, 5, 6) solutions for various storage time values (hrs): 1 - 5, 2 - 10, 3 - 216, 4 - 0.5, 5 - 216, 6 - 2160.

Fig. 2. Time dependences of the mobile ions concentration in passivating layers on lithium electrode in the TC, 1 M  $\text{LiAlCl}_4$  (1) and PC, 1 M  $\text{LiClO}_4$  solutions (2).



b4

21-02-01-G

ELECTROCHEMICAL BEHAVIOUR OF GRAPHITE FLUORIDES IN PROPYLENE CARBONATE

D. Devilliers, T. Nakajima<sup>(1)</sup>, B. Teisseyre and M. Chemla,  
Université Pierre & Marie Curie ; Laboratoire d'Electrochimie  
4, Place Jussieu ; 75252 PARIS Cedex 05 France

<sup>(1)</sup>Department of Industrial Chemistry, Faculty of Engineering,  
Kyoto University, Yoshida Honmachi, Sakyo-ku, Kyoto 606 Japan

The application of graphite fluorides ( $CF_x$ ) as active species in primary lithium batteries has been extensively reported in the literature. Non-aqueous solvents such as propylene carbonate or  $\gamma$ -butyrolactone are required in these batteries. In several recent papers, it has been found that the discharge performances of  $(CF)_n$  and  $(C_2F)_n / Li$  batteries depend on the crystallinity and composition of the graphite fluoride [1].

The aim of this work was to study the electrochemical reduction of  $CF_x$  in propylene carbonate with different supporting electrolytes (molar solutions of  $LiClO_4$  or  $nBu_4NClO_4$ ) in order to confirm the hypothesis of the insertion of  $Li^+$  cations during the reduction process. The reduction of several  $CF_x$  compounds was compared, in relation to their stoichiometry  $x$ , structure and method of preparation (laboratory-scale samples or commercial compounds).

As graphite fluorides are very insulating compounds, the electrochemical properties of  $CF_x$  were determined, using the carbon paste electrode technique [2].

The reduction of the electroactive species occurs, according to the overall reaction :



However, a two-step reduction mechanism has been proposed, including the formation and decomposition of an intermediate compound  $Li_xCF_x$  ; solvent molecules actually participate in the cell reaction [3] and the intermediate phase is composed of carbon, lithium fluoride and solvent molecules.

Our results are in agreement with this mechanism ; the reduction of  $CF_x$  in the presence of  $Li^+$  cations is easier (it occurs at higher potentials) because the bulky  $nBu_4N^+$  cations can barely form intercalation compounds ; thus the reduction peak is shifted towards a more negative potential. This shift is not due to a higher ohmic drop because the two electrolytes  $LiClO_4$  and  $nBu_4NClO_4$  have the same conductivity.

Well-defined crystalline compounds are more difficult to reduce in both supporting electrolytes ; they are less reactive than commercial compounds, in agreement with their higher decomposition temperature.

- [1] N. Watanabe, T. Nakajima and H. Touhara, "Graphite Fluorides", Elsevier, Amsterdam (1988) Chapter 5.
- [2] D. Devilliers, B. Teisseyre, M. Chemla, T. Nakajima and N. Watanabe, *J. Fluorine Chem.*, 40 (1988) 1.
- [3] N. Watanabe, R. Hagiwara and T. Nakajima, *J. Electrochem. Soc.*, 131 (1984) 1980.

21-02-02-G

DISCHARGE CHARACTERISTICS OF THE Li/LiBF<sub>4</sub>-QUINOLINE/CARBON SYSTEMS AS A PRIMARY CELL

M. Dohzono, T. Yamada, Y. Shimizu\*, M. Egashira\*

Fuji Research Laboratory, Tokai Carbon Co., Ltd., 394-1 Oyama-cho, Sunto-gun, Shizuoka 410-14, Japan

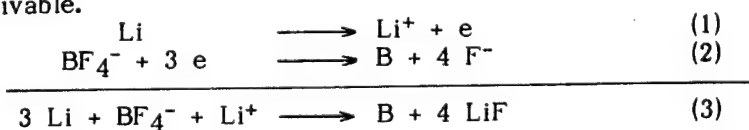
\* Department of Materials Science and Engineering, Faculty of Engineering, Nagasaki University, 1-14 Bunkyo-machi, Nagasaki 852, Japan

Lithium salts such as LiClO<sub>4</sub>, LiBF<sub>4</sub> and LiPF<sub>6</sub> have been used as the electrolyte in lithium cells. These salts have some advantages including high solubility and stability in non-aqueous solvents. In the case of LiPF<sub>6</sub>, however, it has been suggested [1] that the salt not only acts as the electrolyte in the primary Li/graphite fluoride cell, but also is electrochemically active. Namely, the discharge capacity was almost doubled by employing LiPF<sub>6</sub> instead of LiBF<sub>4</sub> as the electrolyte, though the details of electrochemical reduction of LiPF<sub>6</sub> was unknown. The present paper reports that LiBF<sub>4</sub> is also electrochemically active when a small amount of quinoline is mixed in the electrolyte solution.

The cells examined were the Li/LiBF<sub>4</sub>-quinoline/carbon systems. Quinoline was added into purified propylene carbonate (PC) at 17 vol%. LiBF<sub>4</sub> was dissolved into the mixed solvent at 1 mol l<sup>-1</sup>. The anode was a Li disk of 10 mmφ × 0.5 mm pressed on a Ni net. The cathode was made of acetylene black (AB), artificial graphite (AG), and downy carbon microfiber graphitized at 3000°C (GDCF<sub>30</sub>) [2]. Surface areas of the three carbons were 80, 15 and 10 m<sup>2</sup>/g, respectively. The carbons were wrapped with a Ti net (15 × 20 mm). In the case of AB and AG, a small amount of polytetrafluoroethylene (PTFE) was mixed as a binder. Both the anode and the cathode were inserted into an evacuable glass cell [3], and then the electrolyte solution of 25 ml was introduced into the cell. The cells thus prepared were subjected to measurement of discharge characteristics. During the measurement, the electrolyte solution was continuously stirred.

Figure 1 shows the 1 mA discharge characteristics of the Li/LiBF<sub>4</sub>-quinoline/carbon cells. It is noted that the three cells exhibited considerably large discharge electricity with the discharge voltage of 2.0-1.8 V; 305, 151 and 730 coulombs for AB, AG and GDCF<sub>30</sub>, respectively. In contrast, when quinoline was not mixed, the discharge electricity was only 1.8 coulombs in the case of the AB cathode, and the discharge plateau at 2.0-1.8 V was not observed. The reason for the variation in discharge electricity with the carbon species is not clear at present.

Figure 2 shows the X-ray diffraction pattern of the AB cathode mixture after discharge. Diffraction lines attributable to LiF were observed in addition to those from AB and PTFE. Similar results were obtained for the AG and GDCF<sub>30</sub> electrodes. It is of no doubt that fluorine atoms in the observed LiF came from LiBF<sub>4</sub>, not from PTFE, because PTFE was not used in the case of GDCF<sub>30</sub>. Therefore, the following anode and cathode reactions are conceivable.



Standard electrode potentials for eqs. (1) and (2) are -3.03 V and -1.04 V vs. SHE in aqueous solution, respectively. Thus, the electromotive force should be 1.99 V, which well agrees with the observed cell voltage.

Quinoline tends to donate an electron pair on its nitrogen atom to Lewis acid. On the other hand,  $\text{BF}_3$  having a vacant orbital tends to accept an electron pair. Thus, it is very likely that a certain complex, for example ( $\text{quinoline} \rightarrow \text{BF}_3$ ), is formed in the solution to leave  $\text{LiF}$ , and that chemical bonds between boron and fluorine atoms in the complex are weakened by such an interaction. As the result, it is considered that fluorine atoms in the  $\text{BF}_4^-$  ion are reduced at the cathode. Boron was not detected by X-ray diffraction but by ion microanalysis of the cathode after discharge. In addition,  $\text{H}_3\text{BO}_3$  was clearly identified by X-ray diffraction when the used carbon electrode was exposed to air for a few days.

Based on eq. (3), theoretical discharge electricity is calculated 7240 coulombs for the present cells using 25 mmol  $\text{LiBF}_4$ , if assumed that all the  $\text{LiBF}_4$  is reduced. It is apparent that all the  $\text{LiBF}_4$  cannot be reduced, because it must act also as the electrolyte. Even so, the observed electricity in Fig. 1 seems too small compared with the theoretical value. The small electricity may have arisen from the following two factors. One is the self-discharge problem. Some  $\text{BF}_4^-$  ions may have been reduced at the anode Li electrode. Another factor is the deposition of insulating  $\text{LiF}$  on the carbon cathode. This would decrease the effective surface area of the cathode. Differences in discharge electricity among the carbons may be related to this  $\text{LiF}$  deposition, because the macrostructure of the electrodes considerably differs from each other.

The detailed mechanism of  $\text{BF}_4^-$  reduction is not clear at present, but the  $\text{Li/LiBF}_4$ -quinoline/carbon system is very interesting as a primary cell.

- [1] T. Koyama, T. Maeda, K. Okamura, Jap. Pat. Kokai, 61-39368 (1986)
- [2] H. Katsuki, Y. Uchida, M. Egashira, S. Kawasumi, Tanso, 118, 117 (1984)
- [3] M. Dohzono, H. Katsuki, M. Egashira, J. Electrochem. Soc., in press

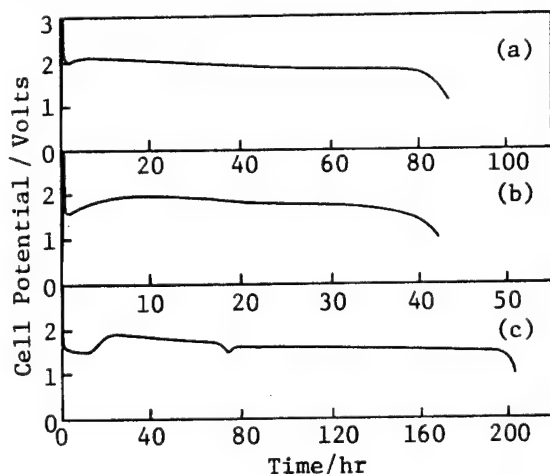


Fig. 1 Discharge curves of the cells  $\text{Li/LiBF}_4$ -quinoline/carbon. Cathode was (a) AB, (b) AG, and (c) GDCF30.

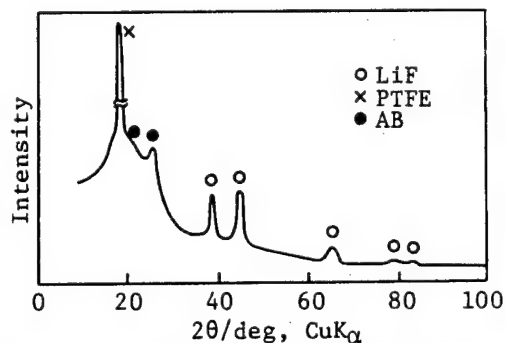


Fig. 2 X-ray diffraction pattern of the AB cathode after discharge.

b4

21-02-05-G

Effects of Electrolyte Compositions on the Discharge Characteristics  
of the Positive Electrode of Li-Al/FeS<sub>2</sub> Thermal Batteries

H. Tsukamoto, M. Terasaki, S. Kashihara  
Japan Storage Battery Co., Ltd.  
Nishinosho, Kisshoin, Minami-ku, Kyoto, Japan

1. Introduction

The capacity of Li-Al/FeS<sub>2</sub> thermal batteries is known<sup>1,2)</sup> to decrease with decreasing temperature and increasing current density. In this report we show that the utilization of FeS<sub>2</sub> active mass at low temperatures and high current densities is much improved by the change of electrolyte composition.

2. Experimental

Positive-limited single cell held between copper heating blocks was discharged at 1 A/cm<sup>2</sup> in an argon atmosphere at several constant temperatures from 450 to 550°C. The composition, weight and theoretical capacity of test cell are summarized in Table 1. The theoretical capacity of the positive electrode refers to the 4-electron reaction from FeS<sub>2</sub> to Li<sub>2</sub>S and Fe. The cut-off voltage was fixed at 1.2 V which corresponds to 70 % of the initial voltage.

3. Results

Electrolyte usually used in Li-Al/FeS<sub>2</sub> thermal batteries is the eutectic mixture of LiCl and KCl. Fig. 1 shows the discharge characteristics of the test cells with different compositions of LiCl-KCl binary electrolyte at 450°C. The utilization of the positive active mass increased in the order of KCl-rich, eutectic and LiCl-rich electrolyte.

Next, we tried LiF-LiCl-LiBr eutectic electrolyte. As seen in Fig. 2, this ternary system showed higher utilization as compared with the LiCl-KCl binary eutectic over the entire temperature range tested, in spite of its nearly 100°C higher melting-point. Large improvement in performance at a low temperature of 450°C deserves special note.

4. Discussions

In the case of LiCl-KCl eutectic mixture, lithium ion within the positive electrode is consumed by the positive electrode reaction and supplied from the bulk of the electrolyte solution by electrophoresis and diffusion. At low temperatures and high current densities the rate of consumption exceeds the rate of supply, and the resultant enrichment of potassium ion relative to lithium ion causes the melting-point to rise, leading to precipitation of KCl. KCl precipitation within the electrode reduces the electric conductivity of the electrode and interferes electrolyte penetration into the electrode, so that both the discharge voltage and utilization of the positive active mass are reduced<sup>3,4)</sup>.

The different characteristics of Fig. 1 can be explained by the retardation of KCl precipitation with increased starting lithium content in the electrolyte.

In the case of LiF-LiCl-LiBr electrolyte large composition change during discharge could not be considered, because this electrolyte is

composed of a single cationic species. This characteristic is the origin of the advantage of this electrolyte over the ordinary LiCl-KCl eutectic electrolyte (Fig. 2).

#### References

- 1) H. Tsukamoto, M. Terasaki, GS News Technical Report, 47 (1), 37 (1988)
- 2) H. Tsukamoto, M. Terasaki, S. Kashihara, Prog. Batteries Sol. Cells, 8 in printing (1989)
- 3) R. Pollard, J. Newman, J. Electrochem. Soc., 128, 491 (1981)
- 4) L. Redey, J. A. Smag, J. E. Battles, and R. Guidotti, ANL-87-6, Argonne National Laboratory, April (1987)

Table 1. Composition, weight and theoretical capacity of single cell

	Composition (wt%)	Dimensions	Theoretical Capacity
Positive electrode	FeS <sub>2</sub> (70), Electrolyte (30)	19x0.6 mm	950 As
Electrolyte layer	Electrolyte (60), MgO(40)	24x1.2 mm	
Negative electrode	Li-Al(70), KCl(30)	24x1.4 mm	2600 As

#### \* Electrolyte Compositions [mol%]:

LiCl[50]-KCl[50]	(m. p. 450°C, KCl-rich electrolyte)
LiCl[58]-KCl[42]	(m. p. 352°C, eutectic electrolyte)
LiCl[70]-KCl[30]	(m. p. 450°C, LiCl-rich electrolyte)
LiF[22]-LiCl[31]-LiBr[47]	(m. p. 445°C, eutectic electrolyte)

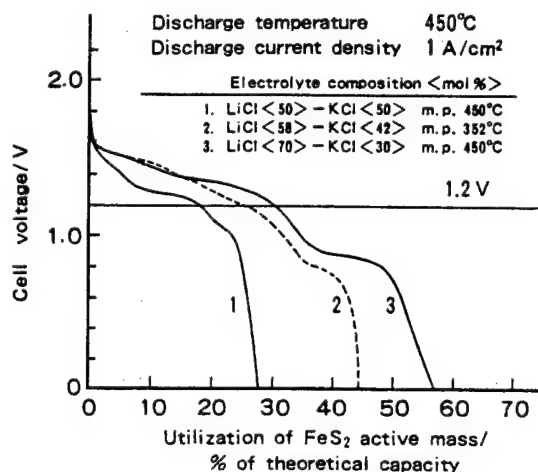


Fig. 1 Discharge characteristics of FeS<sub>2</sub>/LiCl-KCl/Li-Al cells with various electrolyte compositions.

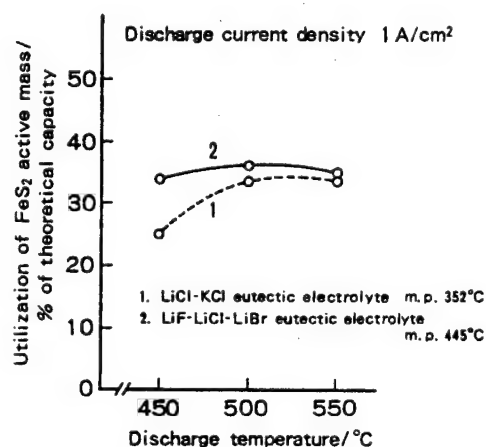


Fig. 2 Improvement of performance by using LiF-LiCl-LiBr electrolyte.

b4

21-02-06-G

ELECTROCHEMICAL STUDIES OF LiAl IN 1-METHYL-3-ETHYLIMIDAZOLIUM CHLORIDE-  
AlCl<sub>3</sub>-MELT

Y.S. Fung and S.M. Chau,  
Department of Chemistry,  
University of Hong Kong, Hong Kong.

One of the major problems facing the development of secondary lithium battery is the reactivity of the solvent system towards the lithium anode [1]. The use of the molten salt medium offers an inert solvent system but it suffers the disadvantage of the necessity of heating and cooling to maintain a constant high temperature, leading to the weight and volume penalty due to the addition of heat insulating material. Thus, one major direction of research in this field is to find an inert, preferably inorganic solvent system to be used as medium for the lithium battery. The recent development of the room temperature molten salt (RTMS) based on the 1-methyl-3-ethylimidazolium chloride-AlCl<sub>3</sub> system provides a promising solvent medium for application in the secondary lithium battery system [2,3].

The alloying of lithium with aluminium provides a suitable LiAl anode for use in the lithium battery; as it is less corrosive, give a stable voltage and is a solid at ambient temperature. Thus, the present work reports the investigation of the kinetics of the LiAl anode in the 1-methyl-3-ethylimidazolium room temperature molten salt system.

The synthesis of the 1-methyl-3-ethylimidazolium melt had been described elsewhere [4] and the working electrode was made up of an aluminium wire 7 mm long and 0.7 mm diameter. The reference electrode was aluminium wire in acidic melt and the counter electrode was an aluminium foil, 2 cm<sup>2</sup> area. The waveform was generated by a Chemical Electronic Waveform Generator model 01 which was imposed on the electrochemical cell via the PAR/363 Potentiostat/Galvanostat. The signal was recorded either by the Esterline Angus Model 575 X-Y recorder or the Linesis chart recorder model L6510. Two electrochemical techniques were used for the present investigation - cyclic voltammetry and chronoamperometry.

From the results on the solubility of LiCl in the RTMS, up to 0.17 mole/Kg of LiCl was found soluble in the melt (LiAlCl<sub>4</sub>/RAlCl<sub>4</sub> = 1:21) with density 1.286 g/cm<sup>3</sup> and specific conductivity 5.66 mS/cm. The cyclic voltammogram for the deposition of lithium on aluminium in RTMS was shown in fig. 1. No stripping of lithium was observed before -1.95V switching potential. However, the surface of the electrode was activated once lithium was deposited, leading to large current in the reverse sweep. The lithium stripping peak was observed to shift anodically with more negative switching potential and in general less lithium was stripped as compared to the lithium deposited on the electrode. However, no apparent interaction between the melt and the LiAl anode was observed up to -2.51V in the switching potential. The nucleation of lithium on LiAl anode was shown in fig. 2. Nucleation of lithium was started to occur at the aluminium electrode surface from a stepping potential more negative than 2.2 volts.

In general, more negative the stepping potential, less time was needed for nucleation. At present, the nucleation kinetics was studied using a transient recorder to obtain more accurate current/time data at the milli-second time interval and cycling test was performed on the LiAl anode formed in-situ in the melt. The above results will be discussed in the meeting.

We acknowledge the support of the Hong Kong University Research Grant Committee for the above work.

- [1] Y.S. Fung and H.C. Lai, *J. Appl. Electrochem.*, 1989, in press.
- [2] J.S. Wilkes, J.A. Levisky, R.A. Wilson and C.L. Hussey, *Inorg. Chem.* 1982, 21, 1263.
- [3] G. Cheek and R.A. Osteryoung, Report-NR-051-715, 1982, 9, 37pp.
- [4] B.J. Piersma and J.S. Wilkes, Report-FJSRL-TR-82-004, 1982, 64pp.

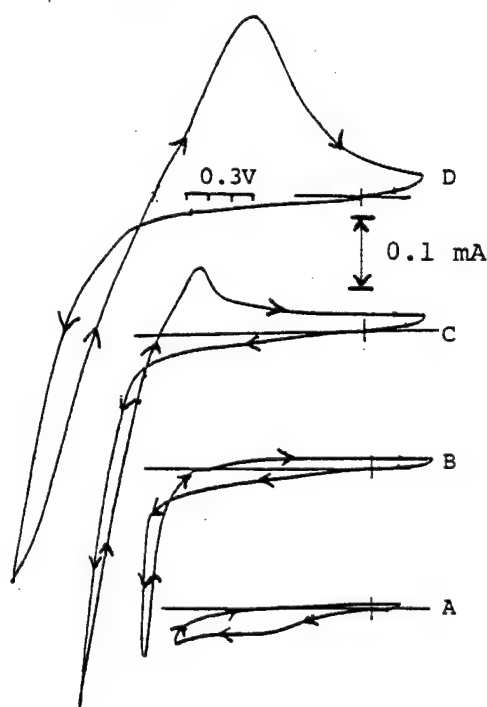


Fig. 1 Cyclic voltammogram of RTMS with 0.24 mole/Kg of Li<sup>+</sup> in melt  
[A = -1.8 V, B = -1.95 V  
C = -2.33 V, D = -2.51 V  
switching potential]

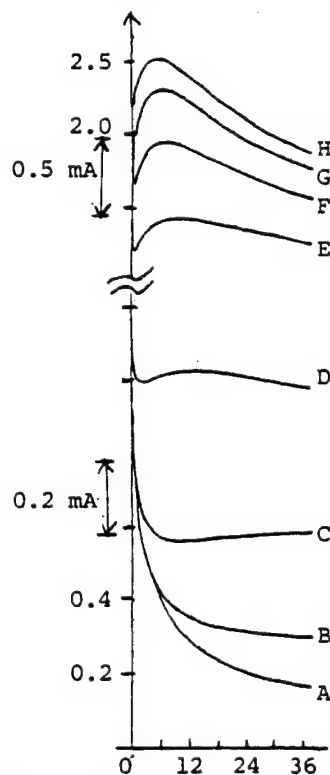


Fig. 2 Chronopotentiogram of RTMS with 0.17 mole Li<sup>+</sup>/Ag melt [stepping potential  
A = -2.085, B = -2.178  
C = -2.202, D = -2.238  
E = -2.266, F = -2.303  
G = -2.330, H = -2.355 V]

b4

21-02-08-K

IONICALLY CONDUCTIVE PLASMA POLYMER AS AN ELECTROLYTE FOR LITHIUM BATTERIES

Z. Takehara, Z. Ogumi, Y. Uchimoto  
Department of Industrial Chemistry, Faculty of Engineering,  
Kyoto University, Yoshida, Sakyo-ku, Kyoto 606, Japan

On account of their ionic conductivities and flexibilities, the polymer complexes formed by polyethers and alkali metal salts recently have received considerable attention as the electrolyte materials for use in solid-state lithium batteries. Since such polymer complexes generally have lower ionic conductivity than liquid electrolytes, thin film are required to decrease actual film resistance of the solid polymer electrolyte. However, it is not easy to prepare a thin film of solid polymer electrolyte by conventional techniques, because the thinner the film becomes the easier the generation of pin-holes. Polymeric solid electrolyte thin membranes can be prepared from a host polymer for the formation of network structure, hybridized with polyethers, such as poly(ethylene oxide) (PEO) and poly(propylene oxide) (PPO). Glow discharge (plasma) polymerization is a useful method to provide an ultrathin uniform polymer layer strongly adherent on various substrates from different kinds of monomers. Therefore, a plasma polymerization technique can be utilized to prepare a host polymer film for pinhole-free thin solid polymer layer.

1. Ionically conductive hybrid polymers formed from network polymer, polyethers, and alkali metal salts

It is well known that a low glass transition temperature favors the enhancement of the ionic conductivity of a solid polymer electrolyte. Accordingly, siloxanes-containing polyethers hybridized with alkali metal salts are attractive, because the incorporation of a siloxane unit into a polymer generally lowers the glass transition temperature. Ultra-thin solid polymer electrolyte film by hybridization of plasma polymerized octamethylcyclotetrasiloxane (OMCTS) with PPO (average molecular weight 4000) and  $\text{LiClO}_4$  was prepared. The apparatus used for the plasma polymerization was consisted of a glass reactor equipped with capacitively coupled inner electrodes connected with an RF power supply (13.56 MHz). An actual conductivity of the hybrid film ( $\sim 1 \mu\text{m}$  thick), plasma polymer/PPO/ $\text{LiClO}_4$  (78/20/2 wt%), was  $2.6 \times 10^{-6} \text{ S cm}^{-1}$  ( $40 \text{ ohm cm}^2$ ) at  $60^\circ\text{C}$ . The hybrid polymer electrolyte was considered to have a micro-heterogeneous structure and PPO segment mainly contributes to the ionic dissociation of  $\text{LiClO}_4$ .

2. Ionically conductive polymer films, without oligomer of polyethers

The polarity of polysiloxane is so low that the interaction between ions and lone pairs of electrons from oxygen atoms of siloxane group does not generate a significant number of mobile ionic carriers. Polyethers are highly polar and often are used as a solvent for ionic compounds. Thus, the substance with both the ether and the siloxane group can be selected as a monomer for the plasma-polymerized film. Tris (2-methoxyethoxy) vinylsilane (TMVS) was selected as a monomer and ultra-thin solid polymer electrolyte films were prepared by the hybridization of plasma-polymerized TMVS with  $\text{LiClO}_4$ . The three-layer composite, with a thin



layer of  $\text{LiClO}_4$  between two layers of plasma-polymerized TMVS, was maintained at  $80^\circ\text{C}$  for 24 hours under  $10^{-3}$  torr to enable the  $\text{LiClO}_4$  to distribute uniformly throughout the plasma polymer, and an ultra thin film ( $\sim 1 \mu\text{m}$  thick) without a pinholes was produced. The ionic conductivities of such hybrid electrolytes were about  $1.0 \times 10^{-5} \text{ S cm}^{-1}$  ( $10 \text{ ohm cm}^2$ ) for formulation containing  $3 \sim 7 \text{ wt\% LiClO}_4$  at  $60^\circ\text{C}$ . The optimum contents of  $\text{LiClO}_4$  at various temperature were existed, because the increasing the  $\text{LiClO}_4$  content increased the carrier ion concentration but decreased the carrier ion mobility.

### 3. Ionically conductive polymer film with one mobile species

In the solid film, described in above sections, both anion and cation are mobile. When such a electrolyte is used in batteries, charge separation by unbalanced distribution of anion and cation takes place, which results in the remarkable increase of electric resistance. Thus, the use of the solid films with only one mobile species has been desired. A solid film with lithium sulfonate group can be used as a lithium ion conducting electrolyte. Thus, a ultra-thin film of a lithium conducting electrolyte of about  $1 \mu\text{m}$  thickness was prepared by the plasma polymerization of OMCTS and methylbensulfonate, followed by the transformation of the resulting sulfinic ester by lithium iodide into lithium sulfonate. Such a plasma polymer having lithium sulfonate was hybridized with PEO (average molecular weight, 300) by soaking in butanol and PEO solution and dried under vacuum to evaporate butanol. The conductivity of hybrid plasma polymer containing  $\text{Li}^+$  (0.3 wt%) and PEO (10 wt%) reached  $1.3 \times 10^{-6} \text{ S cm}^{-1}$  ( $80 \text{ ohm cm}^2$ ) at  $60^\circ\text{C}$ . This film was pinhole-free and uniformity in film thickness.

### 4. Construction of all solid-state lithium battery

All solid-state lithium batteries were constructed with such these ionically conductive electrolytes ( $2 \sim 3 \mu\text{m}$ ) deposited on a  $\text{TiS}_2$  cathode ( $10 \sim 15 \mu\text{m}$ ) and a lithium foil anode. Thin film of  $\text{TiS}_2$  for the cathode active material was prepared by a low pressure chemical deposition technique from a mixture of  $\text{TiCl}_4$  and  $\text{H}_2\text{S}$  diluted with argon as the surface gas. A film prepared by this method was nearly stoichiometric  $\text{TiS}_2$  film which had predominant (110) orientation. The electrolytes were pin-hole free, and covered with  $\text{TiS}_2$  film completely.

For example, when the hybrid polymer in section 1 was used, the fairly good rechargeability of the battery was confirmed, while internal resistance of this battery was fairly large. The first discharge performances at room temperature are given in Fig.1. At a low current density of  $8 \mu\text{A cm}^{-2}$ , the discharge curve plateau extended to 85% of utilization of  $\text{TiS}_2$ . The utilization was highly enough for practical batteries at low discharge current densities.

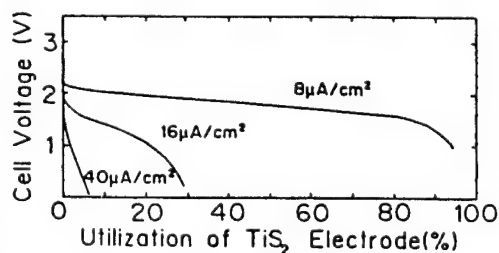


Fig.1. The effect of current densities on discharge curves at room temperature

b4

21-02-09-G

IONIC CONDUCTIVITY OF POLY(ETHYLENE OXIDE) (PEO)-BASED SOLID ELECTROLYTES  
FOR RECHARGEABLE LITHIUM BATTERIES

Y. Matsuda, M. Morita, M. Motoda, H. Tsutsumi, T. Takahashi\*,  
and H. Ashitaka\*

Department of Industrial Chemistry, Faculty of Engineering,  
Yamaguchi University, Tokiwadai, Ube 755, Japan

\*Chiba Laboratory, Ube Industries, Ltd., Goi-Minamikaigan 8-1,  
Ichihara 290, Japan

Solid polymer complexes such as poly(ethylene oxide) (PEO) with some lithium (Li) salts, which are generally called polymeric solid electrolytes, have been widely investigated as the electrolyte of Li batteries [1,2]. From the viewpoints of the practical use, it is desirable to obtain as high conductivity as possible. Thus the main subjects have been concentrated on the relation between the ionic conductivity and the polymer composition. The polymeric solid electrolytes that have most widely been studied up to the present are PEO-based complexes. In this paper we have synthesized PEO-grafted poly(methyl methacrylate) (PEO-PMMA) by photo-polymerization, and measured the ionic conductivities of the polymer/lithium salt complexes.

The solid polymer was a copolymer of acryloil-modified PEO's, methoxy poly(ethylene glycol) monomethacrylate (PEM: 1,  $n = 9$ ) and poly(ethylene glycol) dimethacrylate (PED: 2, normally  $m = 9$ ) whose structural formulas are shown in Fig. 1. The polymer was synthesized by photo-polymerization of the mixed monomers (generally 3:1 by mole ratio) with 2,2-dimethoxy-2-phenylacetophenon as an initiator (sensitizer) under UV irradiation (1 J). The electrolytic salts,  $\text{LiClO}_4$ ,  $\text{LiBF}_4$  and  $\text{LiCF}_3\text{SO}_3$ , were dissolved in the mixture before polymerization. In most cases poly(ethylene glycol) dimethylether (PEG: average MW = 400) was blended in the monomer mixture to improve the flexibility and then the ionic conductivity of the resulting complex. The thickness of the polymeric electrolyte film was 0.3 - 0.8 mm. The conductivity of the electrolyte was measured by an AC impedance meter (10 kHz) in the temperature range of  $-20 - +60^\circ\text{C}$ . The transport number of  $\text{Li}^+$  in the electrolyte was determined by a potentiometric method [3] at room temperature (ca.  $20^\circ\text{C}$ ).

Figure 2 shows the temperature dependence of ionic conductivity for the  $\text{LiClO}_4$ /(PEO-PMMA) complex, compared with that of a usual  $\text{LiClO}_4$ /PEO complex. Conductivity of about  $10^{-5} \text{ S cm}^{-1}$  was obtained for the complex containing 7 wt%  $\text{LiClO}_4$  at room temperature. Similar conductances have been reported for the complexes with analogous polymer matrixes such as poly(PEM) containing  $\text{LiCF}_3\text{SO}_3$  [4] and poly(PED) (or PEO-crosslinked polyacrylate) containing  $\text{KCF}_3\text{SO}_3$  [5]. The apparent activation energy for the ionic conduction was  $51 \text{ kJ mol}^{-1}$ , which was calculated from the slope of the plot. The conductance behavior of  $\text{LiClO}_4$ /(PEO-PMMA) containing PEG is shown in Fig. 3. In this case the concentration of PEG is indicated by wt% in the complex, and the concentration of  $\text{LiClO}_4$  was kept constant ( $0.75 \text{ mol dm}^{-3}$  [M]) with respect to PEG. The ionic conductivity was improved by the addition of PEG to the polymer electrolyte. The conductivity of  $[\text{PEG-LiClO}_4 (0.75 \text{ M}, 50 \text{ wt\%})]/(\text{PEO-PMMA})$  was about  $10^{-4} \text{ S cm}^{-1}$  at  $30^\circ\text{C}$ . The added PEG would support the increase in the ionic mobility of  $\text{Li}^+$  through "ion solvation". The excessive addition of PEG decreased the solidity of the polymeric electrolyte film. The bending of the  $\log \sigma - (1/T)$  curves relate to the solidification of added PEG in the polymer

electrolytes. The addition of other organic solvents such as propylene carbonate and 1,2-dimethoxyethane also improved the conductivity.

The polymer complex containing  $\text{LiBF}_4$  as the electrolytic salt showed a similar conductance to that containing  $\text{LiClO}_4$ , but the salt of  $\text{LiCF}_3\text{SO}_3$  with the same polymer matrix lead to somewhat low conductivity. This was owing to the lower ionic mobility of  $\text{CF}_3\text{SO}_3^-$  compared with those of  $\text{ClO}_4^-$  and  $\text{BF}_4^-$ , which was supported by the transport numbers of the ions determined experimentally. The ionic conductivity was also dependent on the polymer matrix composition. Polymers synthesized from PED with lower  $m$  (eg.  $m = 4$ ) gave lower conductivities. Polymers containing low PEM/PED ratio also decreased the conductivity. These are probably caused by a limited thermal motion of ethylene oxide segments in the polymer matrix.

- [1] P.V. Wright; Br. Polym. J., 7, 319(1975).
- [2] M. Watanabe, K. Sanui, N. Ogata; Solid State Ionics, 18 & 19, 338 (1986).
- [3] A Bouridah, F. Dalard, D. Deroo, M.B. Armand; J. Appl. Electrochem., 17, 625(1987).
- [4] D.J. Bannister, G.R. Davies, I.M. Ward, J.E. McIntyre; Polymer, 25, 1600(1984).
- [5] H. Tada, H. Kawahara; J. Electrochem. Soc., 135, 1728(1988).

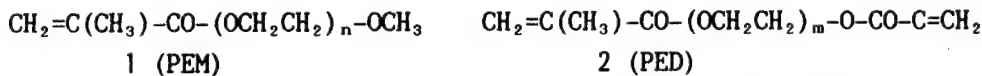


Fig. 1 Structural formulas of monomers for PEO-PMMA.

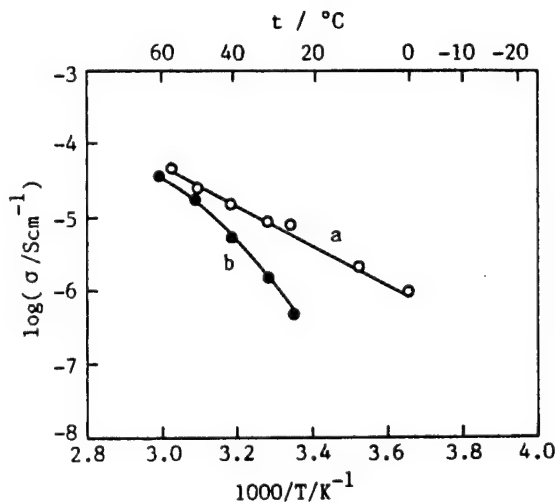


Fig. 2 Temperature dependence of ionic conductivity for  $\text{LiClO}_4/\text{PEO}$  ( $[\text{LiClO}_4]/[\text{EO unit}]=0.03$ ) and  $\text{LiClO}_4/(\text{PEO-PMMA})$  ( $\text{LiClO}_4$  content in the complex: 7 wt%).

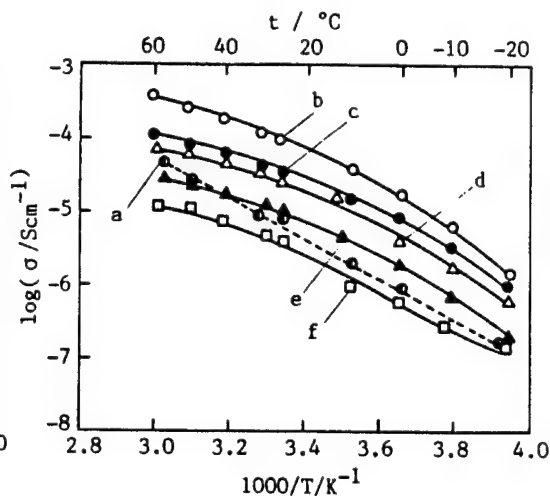


Fig. 3 Temperature dependence of ionic conductivity for  $\text{LiClO}_4/\text{PEO}$  (a:  $\text{LiClO}_4$  content; 7 wt%) and  $[\text{PEG-LiClO}_4(0.75 \text{ M})]/(\text{PEO-PMMA})$  (b-f), (PEG- $\text{LiClO}_4$ ) content: b; 50 wt%, c; 40 wt%, d; 30 wt%, e; 20 wt%, f; 10 wt%.

b4

21-02-10-K

### POLYMER ELECTROLYTE LITHIUM BATTERIES

G. Vassort, M. Gauthier.  
Institut de recherche de l'Hydro-Québec  
1800 Montée Ste Julie, Varennes, Canada J0L 2P0

Lithium rechargeable systems, which hold particular interest from the energy standpoint, have marked noteworthy progress of late, owing especially to the work of Moli Energy and Sanyo. The factors behind this success, which have generated renewed interest in Li-rechargeable systems, and more particularly in liquid electrolytes, include the following:

- the large developed surfaces associated with low current densities;
- thin, homogeneous separators;
- the elastomer binder (at the cathode).

A series of all-solid-state systems using similar electrode materials and having the advantage of being easily amenable to the application of these parameters has recently emerged.

Despite their apparent similarity, they have some basic differences arising from the potential impact of solid-state polymeric electrolytes (SPE) on battery chemistry, performance characteristics, technology, cost and safety.

#### SPE lithium battery concept

Figure 1 presents this battery concept, which employs a lithium metal foil anode and a composite cathode as its electrodes. Figure 2 illustrates the wide range of performance characteristics offered by some electrochemical couples.

The polymeric electrolyte plays a vital part in the cross-compatibility of cell components owing to its inherent properties:

- adhesiveness and elastomericity in order to maintain physical contact and ion exchange with solid phases;
- aptitude to form a useful passivating film on the surface of lithium anodes;
- electrochemical stability to oxidation.

#### Components

Considerable efforts have been made in recent years to improve ionic conductivity and broaden the range of application of SPE batteries for operation at room temperature. This has brought about a generation of high-amorphicity electrolytes obtained mostly by modifying the solvating polymer chain (essentially EO chains). Many of them, however must be tested in complete battery set-ups and prolonged cycling.

Furthermore, whereas  $\text{LiClO}_4$  and  $\text{LiCF}_3\text{SO}_3$  were the main lithium salts used thus far, a new proprietary nonexplosive salt, free of toxic elements, identified in the course of the ACEP research program has been successfully tested in SPE batteries operating at moderate temperature and has contributed to improving performances at ambient temperature.

### Technology

Concurrently with development of the materials, the success of SPE batteries requires the adaptation of proven technologies or the development of innovative processes for large-scale production at competitive prices.

By their very nature, polymer-based materials lend themselves extremely well to highly automated production and packaging processes. In this respect, the absence of gases and potent corrosive solvents is a particular advantage.

Solvent-casting (i.e. doctor blade) or extrusion are existing processing techniques readily adaptable to the fabrication and assembly of electrolytes and composite cathodes.

One interesting example of the innovative approaches to producing ultra-thin SPE is based on plasma polymerization.

Lithium metal foils suited for anode fabrication are available commercially in thicknesses down to 50  $\mu\text{m}$ . Thinner films can be obtained by lamination or by processes from the molten state, while plastic metallization (chemical vaporization or sputtering) appears to be a good means of reducing the cost and weight associated with current collectors.

### Room-temperature performances

Following the development of SPE of higher conductivity for operation at room temperature, a few results have been published (1) or are now being published (2), and a state-of-the-art report on characteristic performances, such as power, cyclability and self-discharge, will be drawn up.

### Electric propulsion

Electric propulsion has been the main objective behind the SPE lithium rechargeable battery programs of Harwell and Hydro-Québec. A design analysis was conducted at Hydro-Québec to evaluate the performances of a battery intended for an urban-van (3) and (4 in abridged version) in compliance with the standards of the US Department of Energy (DOE).

The conclusions of that evaluation tend to show that SPE lithium rechargeable batteries can be contemplated for large systems, even with existing technologies, while meeting admissible power density and cost requirements for electric propulsion.

### Power roll concept

Results on SPE so far reflect the trend towards a unification of cell formulations and configurations and towards room-temperature operation for most applications.

This trend combined with the surface-additive properties of the SPE lithium battery, has led to the so-called "power-roll concept", which involves manufacturing and storing large rolls of multi-films materials and using them as needed to produce an almost infinite variety of customized cell designs, shapes and sizes.

This concept represents an interest to producers and users alike, since the technology is, theoretically, less expensive and more adaptable than current technologies.

### References

- (1) G.Vassort, M.Gauthier, P.E. Harvey, F.Brochu et M.B. Armand, *Proceedings of the Symposium on Lithium Batteries (Honolulu 1987)*, Vol. 88-1, Ed. A.N Dey, The Electrochemical Soc., Pennington, New Jersey, 1988.

b4

- (2) Papers to be presented at the *Second International Symposium on Polymers Electrolytes, Sienna (Italy)*, June 14th-16th 1989.
- (3) M. Gauthier, A. Bélanger, B. Kapfer, Design Concept for the Use of Polymer battery Technology in the DOE-EHP IDSEP Van, *IREQ Report # 4304-C*, 1988
- (4) M. Gauthier, A. Bélanger, B. Kapfer, G. Vassort, M. Armand, *Polymer Electrolyte Review, Vol. 2*, Eds. J.R. MacCallum and C.A. Vincent, Elsevier Applied Science, London, 1989.

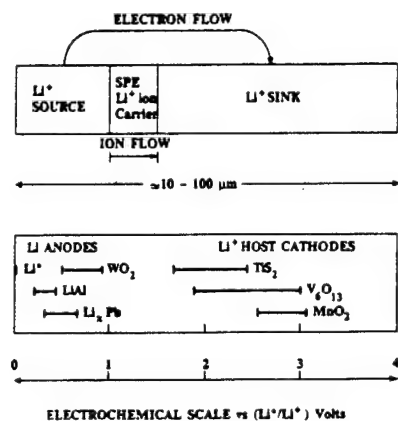


Figure 1

Spe Li-battery concept

Figure 2

Typical discharge plateaus

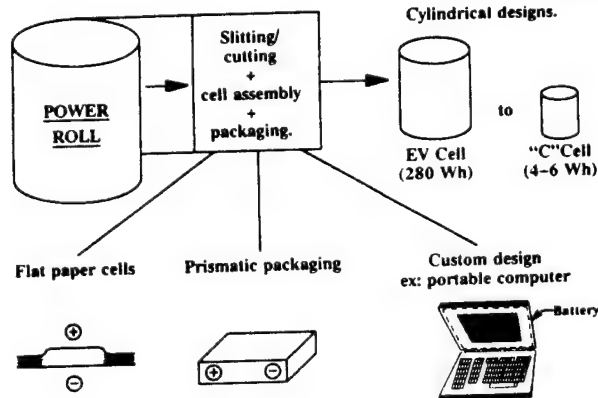
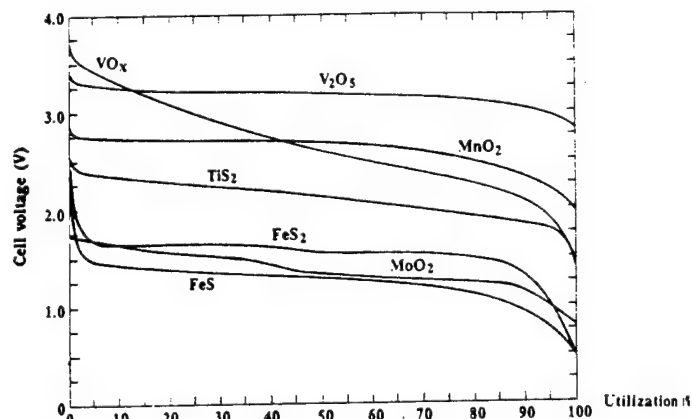


Figure 3

The "Power roll" concept  
From reference (4).

21-02-11-G

## CONDUCTIVE THIN FILMS AND MEMBRANES: THEIR SCIENTIFIC FOUNDATIONS AND INDUSTRIAL APPLICATIONS ( part 9 ).

*Sardar K. Bahador*

Dept Indus Chem Fac Eng and BAHADOR Research Room at Kumanoryo, Rm # B-311, Kyoto University, P.O. Box 51, Sakyo-ku Kyoto 606 JAPAN.

Ionically and electronically conducting polymers are crucial for basic research and ample technological instances such as advanced electrochemical energy conversion and storage devices, corrosion suppression and industrial electrolysis, sensors, optoelectronics, solar cells and the like. From a practical point of view, the main advantage of conducting polymers seems to lie in their film fabrication with relative ease. Of several synthetic methods employed so far, recent advances in the production of polymer films having varied monomer composition and structure, through electrosynthetic and plasma polymerization techniques have provided a particular impetus for an acute interest in their utilization in the afore-mentioned processes in general and as the electrode material in particular. In an attempt to verify the application feasibilities of conducting polymers as electrocatalyst material in solid state and electrochemical solar energy conversion devices, fuel cells, ion selective electrodes, industrial electrolytic processes, etc, and as either positive or negative (or both) electrode active mass in lithium batteries and the like, extensive studies have been conducted with respect to the preparation and characterization, and application feasibilities of some model conducting materials.

In connection with the photoelectrochemical, PEC, devices, narrow band gap semiconductors are required to achieve high conversion efficiencies. The oxidative degradation of these materials, and in particular of the n-type semiconductor photoanodes, through corrosion or the formation of an insulating oxide barrier layer has become an important problem in quest for producing useful fuels by the photoelectrolysis of water or other materials. Several strategies have emerged to alleviate the photodegradation problem. One approach is regarding utilization of conducting polymer films to stabilize semiconductor surfaces, kinetically by greatly enhancing the rate of charge transfer between the semiconductor and redox ions in the electrolyte. A second approach concerns the application of solvent free ion conducting polymers as electrolytes. Such electrolytes are solid state ionic conductors, where the absence of solvents ensures the absence of semiconductor surface degradation.

New plasma polymerization techniques have provided means for the deposition of adherent protective, metallized, electrically conductive polymer films on to a variety of photoactive semiconducting catalysts which have already been proved effective, however unstable, in production of hydrogen from water. The application of r.f. plasma sputtering and r.f. plasma polymerization processes are the adequate means for producing plasma polymer coatings on the photoanode surface, while carefully selecting the materials and composition, assists in obtaining hydrophobic, electrically conductive and reasonably transparent coatings. One of the promising approach to the stability problem of semiconductor electrodes is the introduction of thin film polymeric solid electrolytes, PSE, based on solvent free high molecular weight PEO complexed with some alkali metal salts. These materials are crucial for both PEC devices and all solid state batteries. The major limitations of PEC and photovoltaic energy conversion devices using conducting polymers as photoactive

elements is the low quantum efficiency of charge carriers generation.

The use of conducting polymer materials as the photoactive element, that is, the material within which light absorption & carrier generation occur, has so far mainly been limited to  $(CH)_x$ . It is the simplest linear conjugated polymer, i.e. a low dimensional conductor, with a simple chain structure and has attracted considerable attention because of its unique electrical properties. The electrical conductivity of conjugated polymers changes widely upon doping and strongly depends on the concentration of dopants. Chemical doping is known to introduce new

internal vibrational modes to the IR absorption spectra of charged defects in  $(CH)_x$ , is the appearance of strong localized vibrations. Such strong absorption lines have never been observed in conventional semiconductors. These vibrations appear whenever charges are added to the polymer chains either by doping or by photoexcitations.  $(CH)_x$  and other conjugated polymers are mainly unsaturated polymers with electrons that can easily be removed or added to the polymer chains. By exposing these intrinsically non-conductors to an oxidizing agent X (or reducing agent M), one obtains a positively (or negatively) charged high conductive polymeric complex and a counter ion which is the reduced  $X^-$  (or  $M^+$ ) form of the Ox (or Red). The products of the doping can be formulated as  $(CHX_n)_x$  or  $(MnCH)_x$ , where  $n$ =mole number of dopants per repeated unit. In this paper, characterization, several physico-chemical properties and some application examples of polyacetylene and polyaniline film and powders will be taken into account. A particular emphasis will be put on the structural and conductivity features of these polymers.

#### POST-WORDS:

On account of becoming a well documented victim of the extremely deplorable circumstances in the near-most environment since 1980, the entire expenses of the work in this series, conducted in several research laboratories and institutions, has been covered from the authors' private fund. However, my hearty thanks are due to all those who honestly and impartially coordinated the corresponding affairs from the very beginning.

#### REFERENCES:

- 1) IUPAC, Chem.Intl., 10 (3,5), 85, 170 (1988).
- 2) S.K. Bahador, "Conductive thin films and membranes: their scientific foundations and industrial applications, parts I-III", to be published.
- 3) S.K. Bahador, In: (i) Ext.Abst. 40th Symp.Coll.Surf.Chem., Chem.Soc. JPN, Kyoto 1987, P. 176; (ii) Ext.Abst. 56th Ann. Meet.Electrochem.Soc.JPN, P. 362, Tokyo 1988; (iii) Book Abst. Vol. I, Chem.Soc.JPN, Spring Meet., 1989, Kyoto JPN; (iv) Ext.Abst. Electrochem.Soc. JPN, Spring meet., Tokyo, 1989, (v) Book Abst., Surf.&Coll. Sci.Symp. ACS, Washington, 1989.

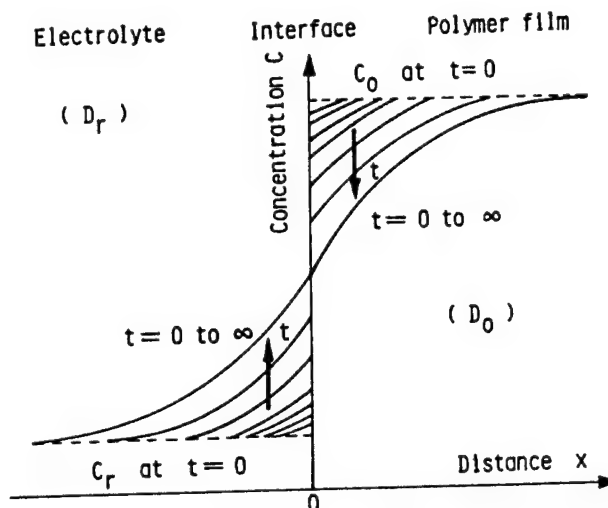


FIG. , Dopant concentration profiles in polyacetylene electrodes at variable times during charge - discharge processes.



21-02-13-G

ELECTROPOLYMERIZED POLYANILINE AS A POSITIVE ELECTRODE IN A LITHIUM SECONDARY CELL  
-MORPHOLOGY CHANGES AND THEIR EFFECT IN CHARGE-DISCHARGE CHARACTERISTICS-

K.Takei, K.Ishihara, T.Iwahori, T.Tanaka

Load Conditioner Task Team, Central Research Institute of Electric Power Industry(CRIEPI)

1.Introduction

Polyaniline(PAN) has a potential of high energy density and efficiency as cathode material of a lithium secondary battery. PAN is polymerized from aniline in acidic aqueous solution by the electrochemical oxidation. It was found that morphologies of PAN changed with polymerizing current densities in the galvanostatic method. Then the effect of morphology on cell performance and characteristics was investigated.

2.Experimental

PAN was prepared by the galvanostatic method, current density ranged from  $0.2 \text{ mA/cm}^2$  to  $10 \text{ mA/cm}^2$ , using the solution of  $2\text{M HClO}_4 + 1\text{M aniline}$ . Electricity utilized for polymerization was  $30 \text{ coulomb/cm}^2$ . After the polymerization it was rinsed with water for 1 h. Cell tests were carried out at  $25^\circ\text{C}$  mainly by the galvanostatic charge-discharge method at voltage between  $4.0 \text{ V}$  and  $2.5 \text{ V}$  (vs.  $\text{Li/Li}^+$ ).

3.Results

SEM observation showed that PAN grew fibrous with the increase of electricity and the diameters of its fibrils decreased with the increase of polymerizing current densities. On the other hand BET absorption results showed that its specific surface areas increased.(Fig.1)

Anion undoping percentages, which were calculated from discharge capacities, were found to be dependent on fibril diameters of PAN.(Fig.2)

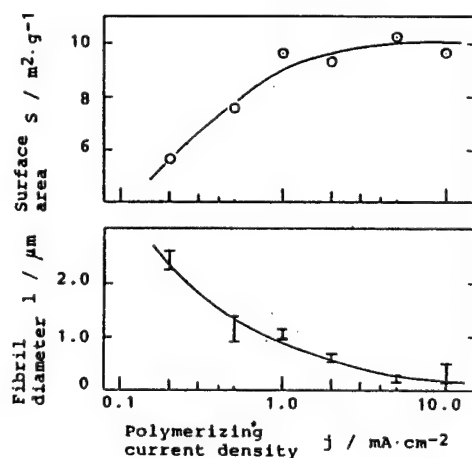


Fig.1 Morphology changes by polymerizing current densities

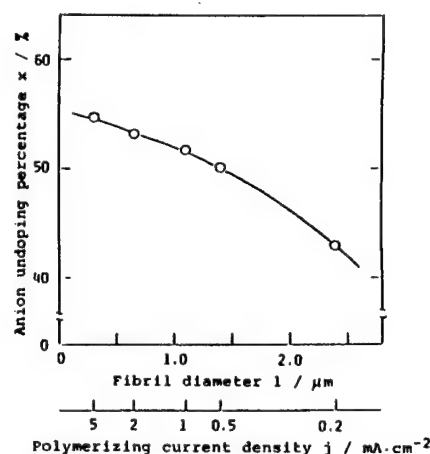


Fig.2 Dependence of anion undoping percentage on fibril diameter  
 test condition ; charge  $0.2 \text{ mA} \cdot \text{cm}^{-2} (1/10\text{C})$   
 discharge  $0.5 \text{ mA} \cdot \text{cm}^{-2} (1/3\text{C})$

b4

21-02-14-K

## ADVANCES IN POLYMER ELECTRODES FOR RECHARGEABLE LITHIUM BATTERIES

Bruno Scrosati  
Dipartimento di Chimica, Università di Roma  
'La Sapienza', Rome, Italy

Large technological interest is presently devoted to polymers which, following reversible doping reactions, are capable to acquire high electronic conductivity. This interest mainly resides in the fact that these new materials combine properties which are typical of metals with those which are typical of plastics and in the fact that the doping processes may be run and controlled electrochemically.

This allows the use of the polymers as advanced, highly-conductive electrodes, both in the positive (p-doping) and in the negative (n-doping) side of rechargeable batteries. Such an application has been particularly successful in lithium batteries where some prototypes have already reached an advanced stage of development.

However, the behaviour of these batteries is somewhat limited by still unsolved specific problems of the polymer electrodes, namely the relatively slow kinetics of the electrochemical doping process and the poor capabilities of charge retention.

The first problem is mainly associated to the diffusion of the counterion within the polymer matrix, whose mechanism is not yet fully understood. The second problem is related to self-undoping processes whose nature is still a matter of discussion.

These critical aspects seem to be particularly influenced by the conditions of the electrosynthesis and by the type of the doping counterion. These conditions will be here examined and discussed with the attention mainly focused on polypyrrole as standard polymer electrode in lithium cells.

21-02-15-G

CHARGE-DISCHARGE CHARACTERISTICS OF POLYANILINE ELECTRODES IN VARIOUS NONAQUEOUS SOLUTIONS

K.Nishio, M.Fujimoto, N.Yoshinaga, N.Furukawa, O.Ando\*, H.Ono\*, T.Suzuki\*  
 Functional Materials Research Center, Sanyo Electric Co.,Ltd.  
 1-18-13, Hashiridani, Hirakata, Osaka, 573 Japan  
 \*Research Center, Mitsubishi Kasei Limited.  
 1000, Kamoshida-cho, Midori-ku, Yokohama, Kanagawa, 227 Japan

INTRODUCTION

We have been investigating the chemical synthesis of conductive polymers and have already reported on the charge and discharge characteristics of polyaniline and polypyrrole synthesized with various oxidizing agents (1, 2).

In this study, chemically synthesized polyaniline was employed as a positive electrode material of a lithium secondary battery and the influence of physical properties of the electrolyte solution on the electrochemical behavior of the polyaniline electrode was investigated in various nonaqueous solutions.

EXPERIMENTAL

Polyaniline was prepared by chemical polymerization of aniline using  $\text{Cu}(\text{BF}_4)_2$  as an oxidizing agent and used as the positive electrode. The scheme of chemical polymerization is shown in Fig. 1. Li or Li-Al alloy was used as the negative electrode. A mixture of cyclic alkylene carbonate (ethylene carbonate, propylene carbonate, butylene carbonate) and dialkoxyethane or lactone ( $\gamma$ -butyrolactone) and dialkoxyethane was employed as a solvent.

Charging and discharging of experimental cells were carried out under constant current. Charging was cut off at 3.2V and discharging was cut off at 2.0V.

Potential step measurements were carried out in the range of 3.1V to 3.6V (vs  $\text{Li}/\text{Li}^+$ ) to determine the diffusion coefficient of the dopant.

RESULTS and DISCUSSION

The chemically synthesized polyaniline used in this study had a fibril structure as shown in Fig.2.

Table 1 shows the discharge capacity ( $\text{mAh/g-PANI}$ ) and coulombic efficiency of test cells using a mixture of PC and several dialkoxyethane as solvents of the electrolyte solution. A test cell with PC-DME as a solvent showed the highest discharge capacity.

Two ingredient electrolyte solutions consisting of dimethoxyethane and ethylene carbonate, butylene carbonate or  $\gamma$ -butyrolactone were also examined. As shown in Fig. 3, these

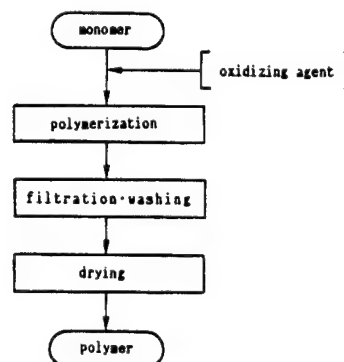


Fig. 1. Scheme of chemical polymerization

test cells exhibited good discharge characteristics.

Thus, the charge-discharge characteristics of a polyaniline cell were strongly influenced by the electrolyte solution. Table 2 and 3 show the conductivity of the solvents and the diffusion coefficient of the dopant in the positive electrode, respectively.

It is believed that high conductivity and high diffusion coefficient contributed to the good charge-discharge characteristics.

#### SUMMARY

A polyaniline/Li-Al cell using PC-DME or  $\gamma$ BL-DME showed a high discharge capacity and 100% coulombic efficiency.

It is believed that the high conductivity and the diffusion rate of the dopant contributed to the charge-discharge characteristics of the polyaniline/Li-Al cell.

Table 2. Diffusion coefficient of dopant in the positive electrode

solvent	diffusion coefficient
PC	$1.9 \times 10^{-14} \text{ cm}^2/\text{s}$
PC-DME	$4.7 \times 10^{-14} \text{ cm}^2/\text{s}$
$\gamma$ BL-DME	$5.1 \times 10^{-14} \text{ cm}^2/\text{s}$

Table 3. Conductivity of electrolyte solution

Electrolyte solution	conductivity (r.t.)
PC	$3.7 \times 10^{-3} \text{ S/cm}$
PC-DME	$9.5 \times 10^{-3} \text{ S/cm}$
$\gamma$ BL-DME	$9.4 \times 10^{-3} \text{ S/cm}$

#### REFERENCES

1. T.Sakai, et al., 3rd International Meeting on Lithium Batteries, Kyoto, 27-30 May 1988.
2. K.Nishio, et al., The 29th Battery Symposium in Japan, Ube, 19-21 October 1988.



Fig. 2. SEM photograph of chemically synthesized polyaniline

Table 1. Discharge capacities of polyaniline/Li-Al cells

Electrolyte solution	Discharge capacity (mAh/g)	Coulombic efficiency (%)
PC-DME	115	100
PC-DDE	103	100
PC-DBE	29	100
PC-TMP	78	100
PC-DOXL	81	100
PC	71	100

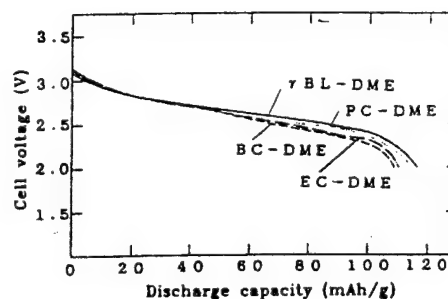


Fig. 3. Discharge characteristics of polyaniline/Li-Al cells

18-12-01-K

ELECTROCHEMICAL ANALYSIS OF PLATINUM-DNA INTERACTIONS:  
RELATIONS TO ANTI-CANCER ACTIVITY OF PLATINUM COMPLEXES

V. Brabec

Institute of Biophysics, Czechoslovak Academy of Sciences,  
Královopolská 135, 612 65 Brno, Czechoslovakia

Platinum coordination complexes belong to a group of potential antitumour agents. Cis-diamminedichloroplatinum(II) (cis-DDP) is the first inorganic antitumour drug introduced for clinical use. Although cis-DDP exhibits a wide spectrum of anti-tumour activity, it also exhibits severe side effects. Many laboratories have been searching for an analogue of cis-DDP yielding reduced adverse reactions. Among approaches in this kind of research those based on the knowledge of the mechanism of anti-cancer action of platinum drugs appear to be most effective. Considerable evidence suggests that the antitumour activity of platinum complexes is related to their covalent binding to DNA. Modifications of DNA induced by platinum complexes are therefore of interest. Moreover, investigations of the reactions of platinum compounds with DNA, studies of pharmacokinetics and the distribution of platinum in the body require sensitive analytical methods for trace platinum determination in biological fluids and tissues. Thus the objective of our work was to exploit voltammetric methods in connection with mercury electrodes for the characterization of distortions in the DNA molecule induced by platinum compounds and also for the determination of platinum in biological samples.

It has been shown that polarographic techniques are suitable for the detection of trace amounts of platinum in biological samples. A particular sensitivity is reached with techniques based on the electrode reactions in which catalytic hydrogen evolution is involved. The disturbing influence of a biological matrix on the electrode reaction can be suppressed by a suitable mineralization step or, in the case of DNA samples, by a precipitation of the biomacromolecule. For instance, if the mixture of DNA and a platinum compound is added to formazone (formed from formaldehyde and hydrazine) in 0.75 M sulphuric acid, DNA and its complexes with platinum precipitate. A free (unreacted) platinum compound reacts with formazone to give the  $\text{Pt}(\text{CH}_2=\text{NNH}_2)_2^{2+}$  complex. This complex yields a catalytic hydrogen evolution current at the mercury electrode at around -1.04 V (vs. SCE). The lower limit of detection of this method is about  $10^{-10}$  M, which is much lower than that attained by atomic absorption spectroscopy mostly used until recently in these determinations.

Differential pulse polarographic (dpp) analysis has been successfully exploited to study the alterations in DNA

conformation induced by the binding of various platinum compounds which differ in antitumour activity. This method is particularly suitable for the characterization of small, local single-stranded or distorted double-stranded regions in the DNA molecule: non-denaturation changes in the DNA conformation resulting in the appearance of double-stranded distorted regions can be monitored via the more positive dpp peak II at  $-1.38$  V (Fig. 1a). On the other hand, more severe conformational alterations in DNA having the character of denaturation give rise to a more negative dpp

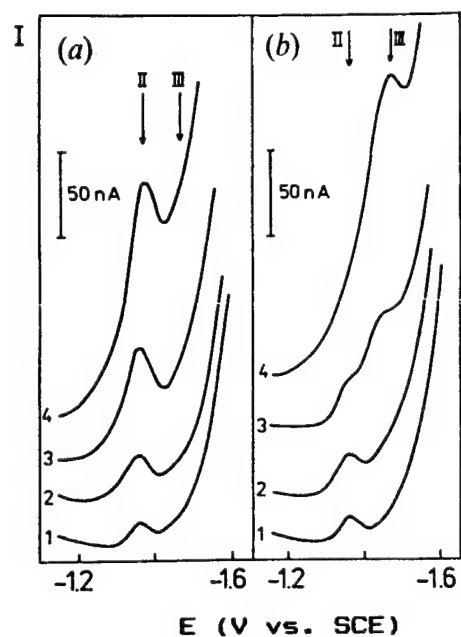


Fig. 1. Differential pulse polarograms of Pt-DNA complexes in  $0.3$  M ammonium chloride with  $0.01$  M tris.HCl buffer, pH  $7.0$ . DNA concentration was  $0.21$  mg/ml. (a) Cis-DDP - DNA complexes: curve 1,  $r_b = 0$ ; curve 2,  $r_b = 0.001$ ; curve 3,  $r_b = 0.005$ ; curve 4,  $r_b = 0.02$ . (b) Trans-DDP - DNA complexes (trans-DDP is a trans isomer of cis-DDP having no antitumour activity): curve 1,  $r_b = 0$ ; curve 2,  $r_b = 0.001$ ; curve 3,  $r_b = 0.01$ ; curve 4,  $r_b = 0.02$ .  $r_b$  is defined as the number of platinum atoms fixed per one nucleotide. Pt-DNA complexes were formed in the medium of  $0.01$  M  $\text{NaClO}_4$ .

peak III at  $-1.43$  V (Fig. 1b). The dpp analysis of complexes of DNA with various platinum compounds has revealed that there is a correlation between the antitumour activity of platinum compounds and the type of conformational alterations induced by the platinum complex in DNA. The differences in these two types of conformational changes can be monitored with exceptional sensitivity by means of dpp so that this technique serves as a suitable method for screening new platinum complexes for their antitumour activity.

#### References

- O. Vrána, V. Brabec; Bioelectrochem. Bioenerg. 19 (1988) 145
- O. Vrána, V. Brabec, V. Kleinwachter; Anti-Cancer Drug Design 1 (1986) 95

18-12-02-G

ELECTROCHEMICAL BEHAVIOR OF BLUE COPPER PROTEINS FROM *Alcaligenes faecalis* S-6

Yuzuru IWASAKI, Eiichi Tamiya, Teruhiko Beppu\* and Isao Karube.  
Research Center for Advanced Science and Technology, University of Tokyo,  
4-6-1 Komaba, Meguro-ku, Tokyo 153 (Japan)

\*Department of Agricultural Chemistry, Faculty of Agriculture,  
The University of Tokyo, Yayoi, Bunkyo-ku, Tokyo 113

Some of electron transfer proteins have been known to show direct electron transfer reaction at solid electrode. The detailed mechanism for electron transfer reaction is not clear yet. Both the net charge of the protein and the local charge of electron transfer site were considered to be important for cytochrome C, plastocyanin and azurin. But the structure of these proteins differ each other, make it very difficult to study the reaction mechanism in terms of the charge distribution. Blue Copper Protein from *Alcaligenes faecalis* strain S-6 (BCPAf) is an electron transfer protein in the anaerobic aspiration chain. BCPAf contains one  $\text{Cu}^{2+}$  as a redox center. The amino acid sequence, 3-D structure and some physical properties of BCPAf are known ( $M_w=12,000$ ,  $A_{\parallel}=55G$ ,  $pI=7.65$ )[1]. 3-D structure of BCPAf resembles that of plastocyanin but the charge distributions are differ each other. In this work, BCPAf was isolated and their electrochemical behavior on several electrodes were studied.

On bear gold electrode, BCPAf showed slow, irreversible electron transfer reaction in cyclic voltammetry (CV). At high pH (ca. 10), stable peak current in CV was observed at least for 30 min (Fig-1). The peak separation was 220mV and the intermediate potential was 75mV vs. Ag/AgCl. As pH becomes lower, BCPAf adsorbed presumably by electrostatic interaction between gold surface and protein, and was interfered redox activity.

On Tin doped Indium Oxide (ITO) electrode, BCPAf showed better CV behavior, i.e. more reversible electron reaction was observed. In the best case, peak separation was 86.5mV, closer to the expected value (57mV) for diffusion control one electron reaction. This finding may be useful for further investigation because ITO electrode can be combined with optical instrument.

BCPAf showed well defined reversible electron transfer reaction on the edge oriented pyrolytic graphite (PGE) electrode. On the contrary to PGE electrode, faradaic current was not obtained (Fig-2) on the basal plane. This indicates that electrostatic interaction and surface orientation of protein is a key to the electron transfer reaction of the protein. The same pH dependence as gold electrode of electrochemical behavior was observed on the PGE electrode. BCPAf has negative charge in basic buffer solution. This charge is opposite to that of plastocyanin, and BCPAf dose not have an acidic patch, which has an important role for electron transfer reaction from cytochrome f to plastocyanin. These differences and structural similarity indicate that the overall electron transfer path way are same but the electron transfer rates depends on their structure.

Electron transfer to nitrite reductase (NIR) via blue copper protein was also studied in term of *in vitro* driving of biological electron transfer chain. When PGE electrode was used, the inhibition from electron transfer between PGE electrode and BCPAf was found. NIR adsorbed onto the PGE electrode and blocked the access of BCPAf onto the electrode.

Reduction of NIR via mediator, which reacts with electrode and transfer electron to protein on ITO electrode was also studied. The

evidence that NIR was reduced by indirect electron transfer from electrode was observed.

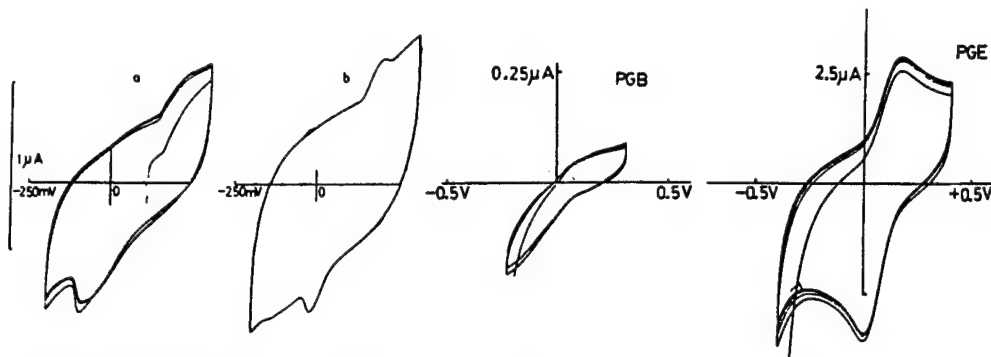


Fig-1 Cyclic Voltammogram of  $140\mu\text{mol/l}$  blue protein in  $2.8\text{mM}$  potassium phosphate buffer pH10.4 at gold electrode; scan rate  $100\text{mV/sec}$ . a) the first scan followed by two scans, b) 30 minutes after continuous scans.

Fig-2 Cyclic voltammogram of  $570\mu\text{mol/l}$  of blue protein at PGB and PGE electrodes; scan rate  $100\text{mV/sec}$ .

- [1] T.Kakutani, H.Watanabe, K.Arima and T.Beppu, J.Biochem. 89 (1981)
- [2] T. Takabe, H. Ishikawa, H.Kawamura, DENKI KAGAKU 56 (1988)



18-12-03-G

VOLTAMMETRIC RESPONSES OF CYTOCHROMES  $c_3$  FROM VARIOUS SULFATE REDUCING BACTERIA

Y. Shigematsu, T. Sagara, H. Akutsu and K. Niki  
Department of Physical Chemistry, Yokohama National University,  
156 Tokiwadai, Hodogaya-ku, Yokohama 240.

Cytochromes  $c_3$  isolated from sulfate reducing bacteria, a unique class of heme proteins, contain four hemes per molecule. They are involved in electron transfer and storage functions in the respiratory chain. The four hemes are covalently attached to the polypeptide chain through thioether linkages provided by cysteinyl residues, and the iron axial ligands are two imidazoles of histidiny residues. The primary structures of cytochrome  $c_3$  from six strains have been reported and the three dimensional structures of cytochromes  $c_3$  from D. desulfuricans Norway strain and D. vulgaris Miyazaki strain have been elucidated. The voltammetric response indicates that the four hemes in the molecule are characterized by four separate but closely spaced standard potentials, with each site exhibiting a nernstian electron transfer at mercury electrode[1,2]. The non-linear parameters, the diffusion coefficient and four macroscopic formal potentials, of the differential pulse polarogram for cytochrome  $c_3$  at a dropping mercury electrode have been evaluated by non-linear regression analysis[2].

This paper is devoted to an extensive investigation of the voltammetric responses of cytochromes  $c_3$  from D. vulgaris, Miyazaki strains F and K, and Hildenborough strain, and D. gigas. The accuracy of the subtracting method, which was applied to the determination of the macroscopic formal potentials of D. desulfuricans Norway cytochrome  $c_3$  by Bianco and Haladjian[3], was discussed by comparing with the analytical equation developed by our group[2]. The correlation between the voltammetric responses and the structures of cytochromes are discussed.

Cytochromes  $c_3$  from Miyazaki strains and Hildenborough strain were extracted and purified as described previously. The periplasmic cytochrome  $c_3$  from D. gigas was extracted by a newly developed procedure. The purities of cytochromes  $c_3$  were checked by a purity index and SDS-polyacrylamide gel electrophoresis. The macroscopic formal potentials of cytochromes  $c_3$  were evaluated by using non-linear regression analysis for 60 sets of the measured values in the differential pulse polarograms at a dropping mercury electrode.

The molecular weight (about 14,000) and isoelectric point (5.2) of cytochrome  $c_3$  from D. gigas agree well with the values reported previously. On the other hand, the amino acid composition differs significantly from the reported one. This is probably due to the difference in the isolation procedure. The differential pulse polarograms

of five types of cytochromes  $c_3$  are shown in Fig. 1. Cytochrome  $c_3$  from Miyazaki K strain shows similar voltammetric response to that from Hildenborough strain, and cytochrome  $c_3$  from *D. gigas* exhibits similar voltammetric behavior to that from Norway strain. Cytochromes  $c_3$  from both Norway strain and *D. gigas* are found to exhibit two well-separated reduction peaks corresponding to well-separated reduction steps, although their isoelectric points are markedly different. The macroscopic formal potentials are shown in Table 1.

The applicability of the subtraction method to the analysis of  $n$ -consecutive one electron process was examined by using a model system with two active centers per molecule. When the separation of two macroscopic formal potentials is greater than 80 mV, one can use the subtraction method. When the separation becomes smaller and smaller, the deviation from the theoretical polarogram grows larger and larger. If two active sites exhibit attractive interaction, it appears impossible to deconvolute the polarogram to evaluate two macroscopic formal potentials by using the subtraction method.

#### References:

- (1) K. Niki, T. Yagi, H. Inokuchi, K. Kimura; J. Electrochem. Soc., **124** (1977), 1889. (2) K. Niki, Y. Kobayashi, H. Matsuda; J. Electroanal. Chem., **178** (1984), 333. (3) P. Bianco, J. Haladjian; Electrochim. Acta, **26** (1981) 1001. (4) V. Niviere, E.C. Hachikian, P. Bianco, J. Haladjian, Biochim. Biophys. Acta, **935** (1988) 34.

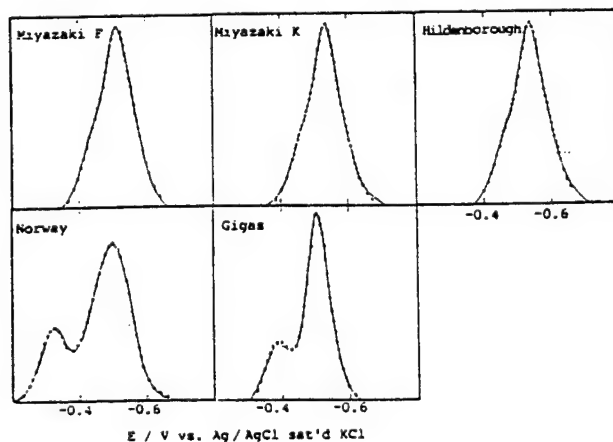


Figure 1 Differential Pulse Polarograms for Cytochromes  $c_3$  in Phosphate Buffer, pH 7.0, at 25°C; • : measured, — : simulated.

Table 1 Macroscopic Formal Potentials of Cytochromes  $c_3$

	$E_1^{\circ'}$	$E_2^{\circ'}$	$E_3^{\circ'}$	$E_4^{\circ'}$	$E^{\circ'}$
DvMF	-439	-496	-514	-556	-501
DvMK	-463	-521	-531	-577	-523
DvH	-460	-520	-533	-584	-524
Dg	-386	-485	-504	-523	-475
DdN	-325	-445	-489	-538	-449

Electrode potentials vs. Ag/AgCl sat'd KCl (mV)

$$E^{\circ'} = (E_1^{\circ'} + E_2^{\circ'} + E_3^{\circ'} + E_4^{\circ'}) / 4$$

18-12-04-G

## DETERMINATION OF BIOLOGICAL SPECIES BY MICROELECTRODE ARRAYS

T. Matsue, A. Aoki, E. Ando, M. Narumi, I. Uchida  
Department of Molecular Chemistry and Engineering, Faculty of  
Engineering, Tohoku University, Sendai 980, Japan

We report here the amperometric detection of biologically important substances in flow systems by using microelectrode arrays which consist of an assembly of microband electrodes. The microelectrode arrays were prepared by conventional photolithography from a glass plate deposited with an Au thin film. Three types of microelectrode arrays (Fig. 1) were prepared. The array A was used for the trace determination of catecholamines in HPLC. The microelectrode arrays were placed in a flow-through cell with a Teflon spacer. The array detector showed an amplification of peak currents for catecholamines by redox cycling when the up-flow electrode was set at an oxidation potential and the down-flow electrode at rereduction potential. The cathodic chromatograms on the array detector has a reduced, undesired influence [1] of ascorbic acid, usually present in a sample. Figure 2 shows the chromatograms for the brain sample on the array detector. The sample contains various electroactive materials. Thus, it is difficult to determine the catecholamines from the anodic chromatogram. On the other hand, the cathodic chromatogram clearly shows the peaks for catecholamines. From the peak heights, the concentrations of catecholamines in the sample can be determined.

The array electrode B was used for multi-channel detection in flow systems. This array consisted of 16 independent microband electrodes. The potential control and current monitoring of the individual band electrode were carried out with a multi-potentiostat made in this laboratory. To obtain a higher resolution in terms of potential, the potentials applied to 16 microband electrodes were stepped several times. Figure 3 illustrates a typical 80-channel three-dimensional FIA result for a mixture of ferrocenylmethanol and ferrocenylmethyltrimethylammonium. The hydrodynamic voltammogram of the mixture can be easily obtained by the cross-sectional view at the peak time. The voltammogram shows two plateaus corresponding to the two ferrocene derivatives. The half-wave potentials determined from the voltammogram were identical to those observed in cyclic voltammetry. The concentration of ferrocenes can be determined from the plateau heights. The present detection system was used for the determination of uric acid in human sera both in FIA and HPLC. The uric acid in the biological samples can be readily determined by the present multi-channel detection system.

The array electrode C was used for construction of an enzyme switch, sensitive to a specific chemical in a solution. The switch was prepared by electropolymerization of pyrrole in the presence of diaphorase. The oxidized polypyrrole was conductive and thus a steady-state current was observed between the adjacent band electrodes when small voltage was applied to the electrodes. The addition of NADH to the solution resulted in the decrease in the current due to the reduction of polymer by the enzyme reaction.

[1] T.Matsue, A.Aoki, T.Abe, I.Uchida; Chem.Lett., 133(1989).

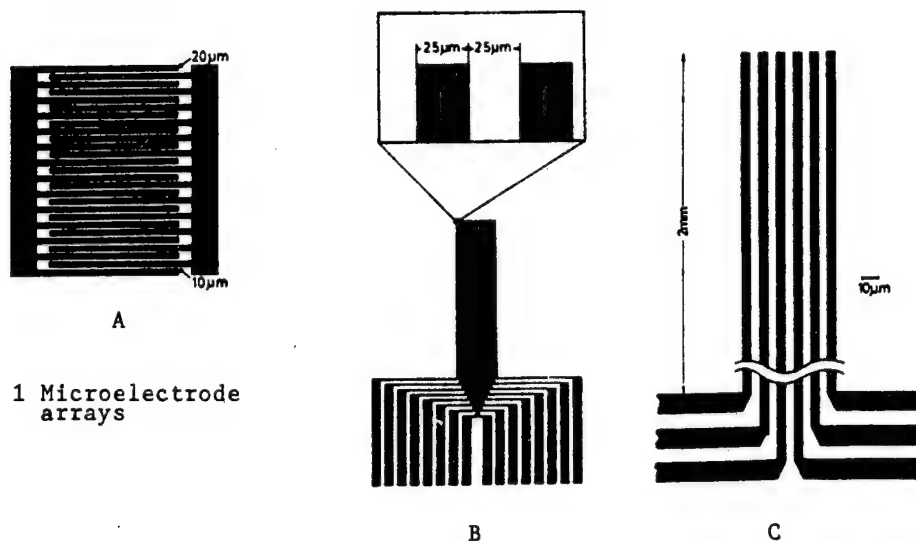


Fig. 1 Microelectrode arrays

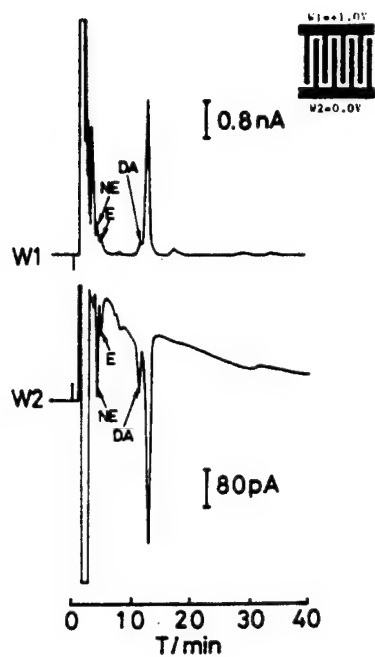


Fig. 2. Chromatograms for rat brain homogenate at Au interdigitated microelectrode arrays.

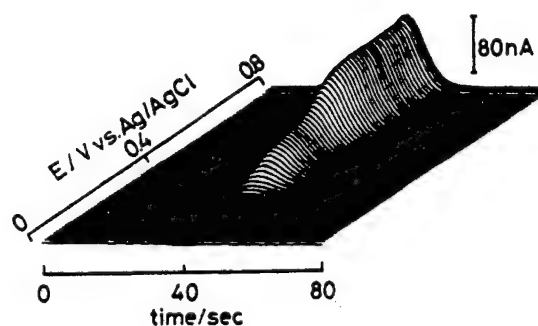


Fig. 3 A chromatovoltammogram of a mixture of 0.1 mM ferrocenylmethanol and 0.1 mM ferrocenylmethyltrimethylammonium.

18-12-06-G

ELECTROCHEMISTRY OF MODIFIED CYTOCHROME C

I. Taniguchi, M. Tominaga, K. Yoshida, K. Yasukouchi  
Department of Applied Chemistry, Kumamoto University  
Kurokami, Kumamoto 860 (Japan)

Using promoter modified electrodes, the electrode reaction of cytochrome c and the electron transfer between cytochrome c and cytochrome c oxidase in the solution have been examined electrochemically [1,2]. In the physiological electron transfer reactions, amino acid residues of the protein surface have been known to play an important role. In the present study, electrochemical techniques have, thus, been applied to estimate how the chemical modification of amino acid residues of cytochrome c affects reactions of cytochrome c at an electrode and with cytochrome c oxidase in the solution.

Cyclic voltammetry was mainly used to examine electrochemical behavior of cytochrome c. The electron transfer reaction between cytochrome c and cytochrome c oxidase was estimated from the cathodic catalytic current ( $I_c$ ) using the electrochemical model of the terminal of the respiratory chain: promoter modified electrode/ cyt.c/ cyt.c ox./  $O_2$ . Bis(4-pyridyl)disulfide and 6-mercaptopurine were used as promoters to prepare effective modified electrodes. Native cytochrome c (Sigma, Type VI) was reacted with 2,4-dinitrofluorobenzene (DNFB) in a phosphate buffer (pH=7.8) solution at room temperature to obtain modified cytochrome c. After DNFB remained unreacted was removed by the gel filtration using a Sephadex G-25 column, the modified cytochrome c was separated into several fractions by cation exchange chromatography using a Whatman CM-32 column [3]. The numbers of DNFB immobilized per a molecule of cytochrome c were calculated to be one to four per a cytochrome c molecule from the difference in absorbance at 360 nm between the modified cytochrome c and native one (Fig. 1).

As the number of modified DNFB increased, the formal redox potential,  $E^{\circ'}$ , of the modified cytochrome c shifted negatively, indicating that the modified ferricytochrome c was stabilized relatively to the corresponding ferrocyanochrome c. This is probably because modification of cytochrome c with DNFB caused somewhat changed in the cytochrome c structure; actually, the modified cytochrome c showed a change in its CD spectra. However, cathodic current of modified cytochrome c scarcely changed until at least one molecule of DNFB was modified on cytochrome c (Fig. 2), meaning no significant decreases in the diffusion coefficient and also in the apparent activity occurred. More modification of DNFB began to cause a decrease in the observed current (Fig. 2). This may be because some cytochrome c molecules became inactive and/or the effective area of the electrode surface decreased; adsorption of modified cytochrome c onto the electrode may change an effective surface structure for the rapid electron transfer of cytochrome c. Also, the peak separation of the redox wave changed in a

similar manner as cathodic current: the peak separation increased rapidly after more than one DNFB molecules were modified on cytochrome c, indicating that also the rate of electron transfer became small by the modification of cytochrome c. Although the interfacial structure of the electrode surface and the mechanism of electron-transfer of modified cytochrome c have not yet been clear at present, but from these results an important point can be drawn: the electron transfer reaction of modified cytochrome c at the promoter modified electrode surfaces begins to be affected when at least more than one molecules of DNFB are modified.

On the other hand, using the electrochemical model of the terminal of the respiratory chain, the electron transfer reaction between modified cytochrome c and native cytochrome c oxidase in the solution was demonstrated to be inhibited significantly even at the beginning of the modification of amino acid residues (mainly lysine) of cytochrome c (Fig. 2); the catalytic current reduced significantly when modified cytochrome c was used.

In summary, these results indicate that the molecular recognition of cytochrome c is more rigorous for the protein-protein reaction (with cytochrome c oxidase) than for the electrode reaction.

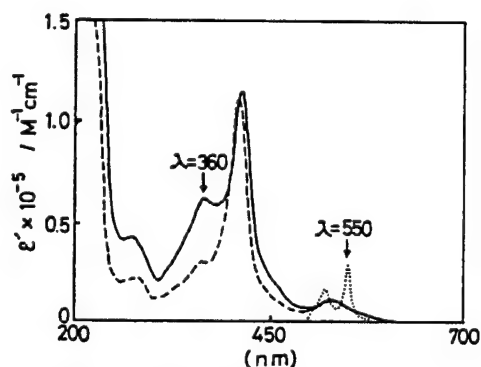


Fig. 1. UV-Vis spectra of  
—: DNP-Cyt.c,  
----: native Cyt.c in oxidized form  
.....: native Cyt.c in reduced form.

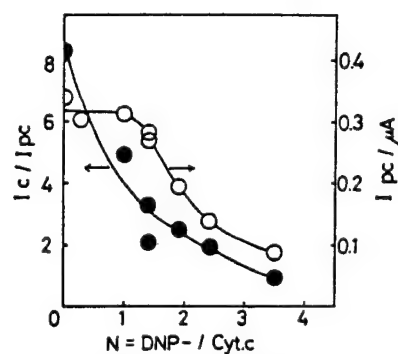


Fig. 2. Effect of Cyt.c modification on  
(○) the electrode reaction of Cyt.c and  
(●) the reaction between Cyt.c and Cyt.c ox.

- [1] I. Taniguchi et al.; J. Electroanal. Chem., 140 (1982) 187; 164 (1984) 385; 206 (1986) 341.
- [2] I. Taniguchi; Proc. 2nd Japan-Korea Joint Symp. on Anal. Chem., 2 (1987) 55.
- [3] H.A.O. Hill and D. Whitford; J. Electroanal. Chem., 235 (1987) 153.

18-12-09-G

SPECTROELECTROCHEMICAL STUDY ON ADSORPTION OF AMP AT A GOLD ELECTRODE  
— USES OF SPECULAR REFLECTION, LOPTLC, AND MAGNETIC OPTICAL ROTATION  
METHODS —

F. Kusu, K. Yuasa, T. Mishima, H. Takayama, K. Takamura  
 Tokyo College of Pharmacy,  
 1432-1, Horinouchi, Hachioji, Tokyo 192-03, Japan

We have demonstrated the utility of specular reflection method in in situ observation of adsorption of organic compounds on metallic solid electrode surface[1]. By this method, monochromatic light polarized parallel or perpendicular to the plane of incidence is directed to the electrode surface from solution and we can measure the intensity of the reflected light at the electrode/solution interface. Because of high sensitivity toward state of the surface, this method can be applied to the study of the adsorption, although it lacks sufficient specificity for the determination of the molecular structure of adsorbed species. A long optical path length thin-layer cell (LOPTLC) also allows the study of adsorption of organic compounds on solid electrode[2]. Using the cell, of which solution layer is about 100  $\mu\text{m}$  in thick and about 1cm in length, the solution species in the cell are monitored spectrophotometrically by light beam travelled through the solution, in parallel to the electrode surface. Adsorption of solution species on the electrode surface causes a decrease in absorbance of the species.

We are under development of magnetic optical rotation method for the study of adsorption of organic compounds on an optically transparent electrode. In order to clarify the characteristics of these three methods, this paper reports the comparison of data on the adsorption of 5'-AMP (adenosine 5'-phosphate) on a gold electrode obtained by them. Experimental Specular reflection measurements were carried out in conjunction with conventional electrochemical methods. A polycrystalline gold plate, polished to a mirror-like finish was used as a working electrode. The light beam of 500 nm and perpendicular polarization, was directed to the electrode surface at an angle of incidence of  $15^\circ$ . Current-potential ( $i$ -E), relative reflectivity ( $R/R_0$ )-E, and  $R/R_0$ -time curves were recorded on XY recorders. The spectroelectrochemical system for LOPTLC method consists of a LOPTLC, a spectrophotometer, and a solution filling apparatus. A piece of 0.5 mm-thick polycrystalline gold plate was used as a working electrode. The geometric surface area of the gold plate was 0.6  $\text{cm}^2$ . The LPOTLC volume was 7.6  $\mu\text{l}$ . The  $i$ -E, absorbance (A)-E, and A-time curves and absorption spectra under controlled potential electrolysis were measured. Block diagram of the apparatus and the structure of electro-

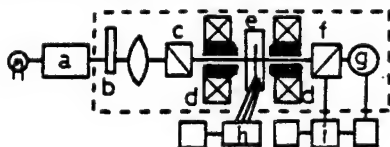


Fig. 1

Apparatus for MOR measurement

a:monochromator, b:chopper, c:polarizer,  
 d:magnet, e:electrochemical cell, f:analyzer,  
 g:photomultiplier, h:potentiostat, i:goniometer

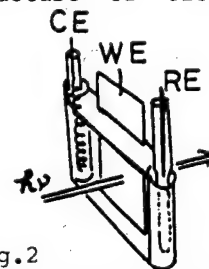


Fig.2

Electrochemical cell

chemical cell for the magnetic optical rotation ( MOR ) method are shown in Figs. 1 and 2. Evaporated gold on glass plate was used as a working electrode. MOR measurement were carried out with electrode/solution layer magnetized perpendicular to the electrode plane by an external magnetic field (  $\geq 12$  kG ) and polarized light beam parallel to the magnetic field. Angle of Faraday rotation,  $\phi$ , under controlled potential electrolysis was measured by a goniometer.

**Results and Discussion** No redox peak of 5'-AMP on its voltammogram obtained in 0.1 M NaClO<sub>4</sub> suggests that 5'-AMP is electroinactive at potentials between -1.0 and 0.5 V vs. Ag/AgCl. The presence of 5'-AMP in 0.1 M NaClO<sub>4</sub> caused a decrease in  $R/R_0$  of gold electrode surface at 500 nm in positive potential region on a  $R/R_0$ -E curve. The magnitude of reflectivity change,  $|\Delta R/R_0|$  varies with both the potential and the concentration (Fig. 3 ). This suggests that 5'-AMP adsorption takes place at the potentials positive than -0.6 V. A decrease in A at 260 nm was also observed at the positive potentials on an A-E curve obtained in 0.1 M phosphate buffer (pH 7 ) containing 5'-AMP using LOPTLC. The decrease indicates a loss of the solution 5'-AMP attributable to its adsorption on gold. Potential dependence of absorbance change,  $\Delta A_{ad}$ , due to adsorption was shown in Fig. 4. During electrolysis of 5'-AMP in 0.1 M NaClO<sub>4</sub> on an optically transparent gold electrode,  $\phi$  was measured ( Fig. 5 ). Although  $\phi$  value of gold and solution without 5'-AMP increases under magnetic field, furthermore increase in  $\phi$  appeared in the potential region where 5'-AMP is adsorbed. This  $\phi$  change may be ascribed to 5'-AMP adsorption on gold.

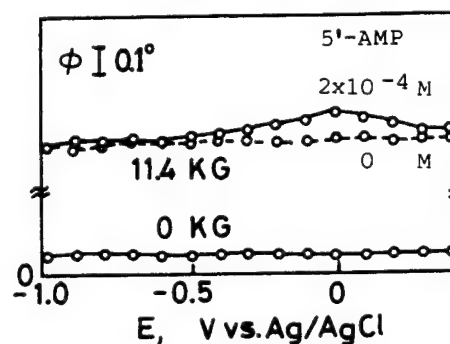
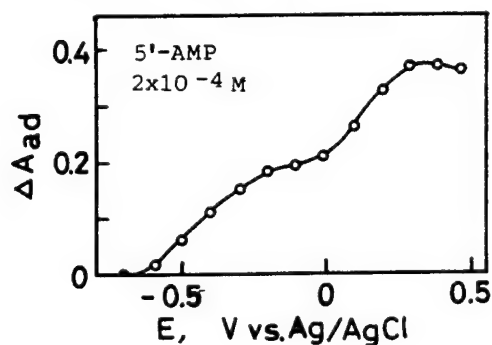
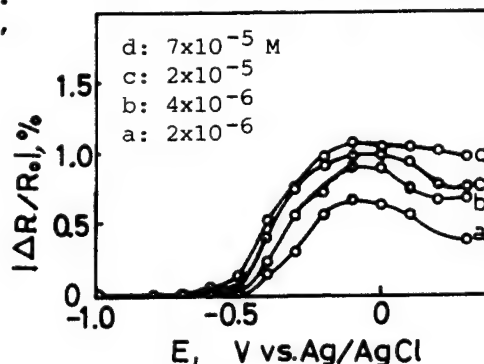
[1] K. Takamura and F. Kusu in "Methods of Biochemical Analysis", Vol.32, p.155, D.Glick Ed., Wiley, New York (1987).

[2] F. Kusu and T. Kuwana, Chem. Lett., 1988, 531.

Fig. 3 Potential dependence of  $|\Delta R/R_0|$  due to 5'-AMP adsorption on a gold electrode.

Fig. 4 Potential dependence of  $\Delta A_{ad}$  due to 5'-AMP adsorption on a gold electrode.

Fig. 5 Potential dependence of  $\phi$  observed for gold electrode/solution interface.





19-12-02-G

ELECTROCHEMICAL BIOSENSING OF Cu(II) AND Zn(II) IONS USING THE IMMOBILIZED APOENZYMES IN THE FIA SYSTEM

I.Satoh

Department of Chemical Technology, Kanagawa Institute of Technology,  
1030 Shimo-Ogino, Atsugi-shi, Kanagawa-ken 243-02 Japan

The author has been proposing a novel idea of "APOENZYME REACTIVATION ASSAY FOR HEAVY METAL IONS IN CONTINUOUS FLOW STREAMS" [1]. Metalloenzymes essentially need metal ions for playing their catalytic activity. Heavy metal ions in the metalloenzymes are generally coordinated in an active site of the enzyme and function as a cofactor in the catalytic reaction. Removing the metal from the cofactor-bound enzyme(holoenzyme) with strong chelating agents forms the corresponding cofactor-free enzyme(apoenzyme) lacking in its activity. The apoenzyme can be reactivated by exposure to the metal-containing sample so that metal ions can be taken up and trapped in the active site. Therefore, the amount of the metals coordinated in the catalytic center of the enzyme molecules may be related to the enzyme activity and in turn proportional to the added amount of the metals. Thus the trace metal content can be evaluated by measuring the enzyme activity of the reactivated apoenzyme. Alkaline phosphatase from *E.coli* was immobilized on oxirane-acrylic beads(Eupergit-C) and packed in a small polymer column. The flow-injection biosensing system was assembled with the immobilized enzyme reactor and an ion-sensitive field effect transistor (pH ISFET, from Shindengen Electric Co.) for monitoring the enzyme activity (Fig. 1).

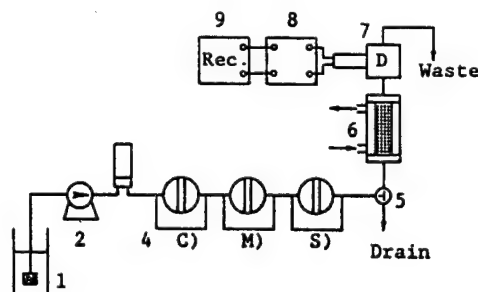


Fig. 1. SCHEMATIC DIAGRAM OF AN APOENZYME-ISFET SENSOR IN A FLOW INJECTION SYSTEM

- 1) Carrier reservoir( 5 mM Tris-HCl(pH 7.2), 1 M NaCl),
- 2) Plunger pump(flow rate 1.00 mL/min), 3) Damper, 4) Rotary injection valves; C) for cofactor-complexing agent, M) for standard zinc(II) or samples, S) for substrate, 5) Three way valve, 6) An immobilized enzyme reactor housed in a water-jacketed holder, 7) pH ISFET and Ag/AgCl equipped with a flow-through cell, 8) ISFET meter, 9) Recorder.

Zinc(II) was potentiometrically determined in a range of 0.01 - 1.0 mM through its activation of the immobilized metal-free alkaline phosphatase reactor. The activity was assessed by injection of a 0.5 mL of 0.1 M *p*-nitrophenyl phosphate solution and then the potential output of pH shift due to orthophosphate liberated in the hydrolytic reaction was displayed on a recorder through an ISFET-meter(Shindengen Electric Co.). Regeneration of the reactor was made by pumping a 2.0 mL of 2,6-pyridine dicarboxylic acid solution(pH 6.0) between successive samples.

Submicromolar level of copper(II) was amperometrically assayed through its activation of the apoenzyme(ascorbate oxidase from cucumber) immobilized onto glass beads with controlled-pore size[2]. The activity of the reactor was determined by introduction of a 0.1 mL of 10 mM L-ascorbate solution and then the consumption of dissolved oxygen by the oxidative reaction was monitored with a polarographic oxygen electrode. The immobilized apoenzyme-reactor was regenerated by injecting only a 1.0 mL of *N,N*-diethyldithiocarbamate solution(pH 8.0). The time required for one assay was 35 min or shorter. The system can be used repeatedly without any loss of the activity during one month observation.

- [1] I. Satoh, K. Ikeda, N. Watanabe; Proc. 6th Sensor Symp., p.203 (1986).
- [2] I. Satoh, R. Abe, T. Nambu; Tech. Digests 4th Int. Conf. Solid-State Sensors Actuators, p.789 (1987).

19-12-03-G

High Sensitive Immuno-Sensor with a Semi-Solid Electrolyte

H. Uchida, M. Hara and T. Katsube

Department of Electronics, Saitama University, Shimo-Okubo, Urawa 338, Japan

1. Introduction

Recently, extensive studies have been continued to develop a miniaturized solid-state immuno-sensor with micro-electronic technology. However, the practical application has not yet been achieved mainly because the sensitivity is still insufficient.

For the sensitivity improvement, we applied Langmuir-Blodgett (LB) method to immobilize immuno-globulin G (IgG) antigen combined with a charge detection type amplification system, which made it possible to detect the anti-IgG concentration of  $5 \times 10^{-8}$  M.<sup>(1)</sup>

In this paper, we report another approach for the sensitivity improvement by using a semi-solid electrolyte. Thin film electrolyte of solid state was applied instead of a usual liquid electrolyte.

Electro-polymerization technique was also discussed in this report for the application to the protein (IgG) immobilization technique.

2. Experimental details

Fig.1 shows the structure of the IgG immobilized electrode and measurement system.<sup>(1)</sup> On a metal electrode, IgG antigen was immobilized by both LB method and electro-polymerization technique.

Semi-solid electrolyte was prepared according to the following procedure : 0.7 wt% agar gel was dissolved in 25mM phosphate buffer (pH6.8) at an elevated temperature, and subsequently was cooled slowly to 40°C. In the solution, bovine serum albumin of the concentration of 1 mg/ml was dissolved. Then the solution was coated on the sensor electrode and cooled to room temperature until sufficient gelation was obtained. The thickness of the semi-solid electrolyte was measured to be approximately 2 mm.

After dropping an antibody solution on the semi-solid electrolyte, the surface potential change of the working electrode was detected in a constant temperature container with saturated vapor pressure.

3. Results

Fig.2(a) shows the output signal of the IgG electrode prepared by LB method. The result shows the time response of the output signal after 5  $\mu$ l of 8 mg/ml anti-IgG solution was dropped on the semi-solid electrolyte.

For the comparison, output signal measured in a usual liquid electrolyte was shown in Fig.2(b). The electrolyte was 25 mM phosphate buffer and the other condition was adjusted to those described in Fig.2(a). As shown in Fig.2(b), a large spike-like noise appeared in the signal immediately after the addition of sample solution. On the other hand, such noise did not appear in the signal measured with semi-solid electrolyte as shown in Fig.2(a).

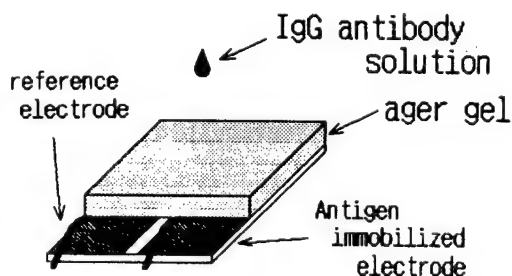


fig.1 Measurement system of an immuno-sensor

Another remarkable difference between these measurement systems is the magnitude of output signal voltage, i.e. 0.3 mV of output voltage was obtained with semi-solid electrolyte for the detection of  $10^{-8}$  M IgG antibody [Fig.2(a)], while the output voltage was about one order of magnitude smaller in the case of liquid electrolyte [Fig.2(b)].

These results suggest that the high sensitive detection system can be expected with semi-solid electrolyte.

Fig.3 shows an output signal of the electrode prepared by electrochemical polymerization method. In this measurement, a semi-solid electrolyte was used, and the IgG antibody concentration was  $10^{-8}$  M. It is noted that signal voltage in Fig.3 is considerably larger than that of Fig.2(a). Although the reason of the high sensitivity is not clear yet, it may be caused by the dense entrapment of IgG molecules in the polypyrrole film.

It should be also mentioned here about the possibility of a reversible reaction of antigen-antibody on the electrode prepared by electrochemical polymerization method, i.e. After the detection of the signal voltage described in Fig.3, a surface potential change was again observed in the repeated measurement process though the signal magnitude became gradually smaller, which suggests a possibility of reversible reaction at the interface between IgG electrode and electrolyte. The reversible signal was not seen with a electrode prepared by LB method.

Detailed discussions are now being carried out from both experimental and theoretical approaches.

#### 4. Conclusion

A semi-solid thin film electrolyte was successfully applied to obtain a high sensitive solid-state immuno-sensor. The intensity improvement of the signal was approximately one order of magnitude compared to that obtained with liquid electrolyte.

Electro-polymerizaion technique was also successfully applied to enhance the sensitivity.

Finally, a discussion was presented about the mechanism of sensitivity improvement and a possibility of reversible reaction of antigen-antibody.

#### 5. Reference

- (1) T. Katsube and M. Hara : Digest of Technical Papers, 4th Intern. Conf. on Solid-State Sensors and Actuators, (1987), C-10.4, p.816

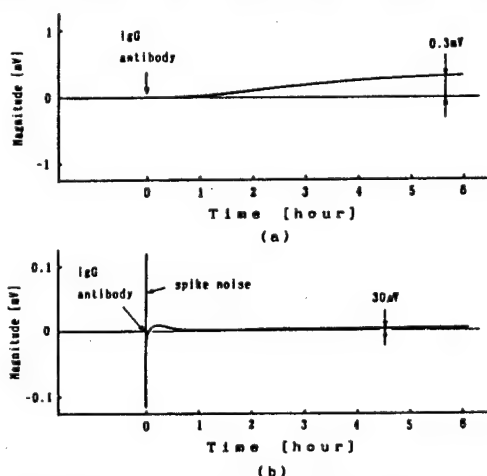


Fig. 2 Time response of the output signal (LB method)  
(a) Semi-solid electrolyte  
(b) Solution electrolyte

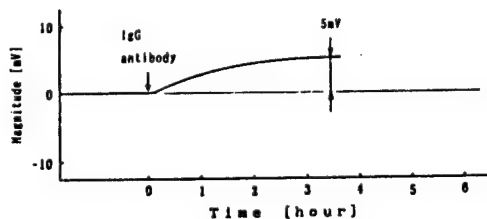


Fig. 3 Time response of the output signal (Electro-polymerization)

19-12-05-G

THE ELECTRODEPOSITION OF FILM OF H. HALOBIUM PURPLE MEMBRANE (PM) ONTO POLY(VINYL ALCOHOL) (PVA). FABRICATION OF AN OPTICALLY TRANSPARENT GOLD(Au)/PVA/PM/PVA/Au MULTI-LAYER SANDWICH CELL AND ITS PHOTOELECTRIC RESPONSE.

K. Uehara<sup>1</sup>, K. Kawai<sup>1</sup>, T. Kouyama<sup>2</sup> and M. Tanaka<sup>1</sup>

<sup>1</sup>Department of Applied Chemistry, University of Osaka Prefecture, 4-804 Mozu-umemachi, Sakai, Osaka 591;

<sup>2</sup>Institute of Physical and Chemical Research, 2-1 Hirosawa, Wako, Saitama 351, Japan.

Purple membrane (PM) fragments isolated from Halobacterium halobium contain 75 % single protein (bacteriorhodopsin, bR) and 25 % lipid by weight and bR functions as a light-driven proton pump[1]. Because PM has a large permanent electric dipole and a negative net charge, the electrodeposition is an effective technique to fabricate an oriented film of PM[2]. In the present study, PM fragments were sandwiched between two layers of wet poly(vinyl alcohol) (PVA) and proton movement in the PM film under illumination was investigated. Electrodeposition of PM was carried out with a bias voltage of +4 V onto a wet PVA film (Kurarey, VF-P, #7500); commercial PVA (Wako Pure Chemical Industries, Ltd., DP=1500) was cast; finally, gold (Au) was vacuum evaporated onto the PVA-film and the PVA-cast, and a sandwich cell Au(1)/PVA-cast/PM/PVA-film/Au(2) as shown in Fig. 1 was made. Upon irradiation of light, the cell showed a photovoltaic response that the Au(1) electrode was always positive, supporting uni-directional proton movement from the PVA-film to the PVA-cast. Action spectra for both the photovoltage and the photocurrent corresponded to the absorption spectrum of light-adapted PM.

At a constant relative humidity (R.H.), the cell showed an effective photocurrent even after prolonged irradiation (5 hours), suggesting that PVA serves as proton source and reservoir. Blue light effect [3] was observed for the photocurrent.

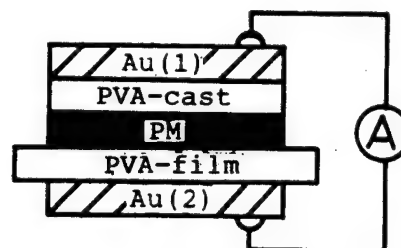


Fig. 1. The construction of the sandwich PM cell.

- [1] W. Stoeckenius, R. H. Lozier, and R. A. Bogomolni, *Biochim. Biophys. Acta*, 505, 215 (1979).
- [2] Gy. Varo, *Acta Biol. Acad. Sci. Hung.*, 32, 301 (1981).
- [3] P. Ormos, Zs. Dancshazy and B. Karvary, *Biochim. Biophys. Acta*, 503, 304 (1978).

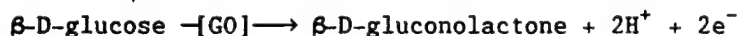
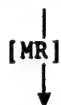
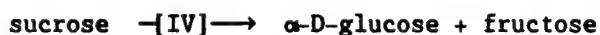
19-12-06-G

AMPEROMETRIC BIOSENSORS: RECENT ADVANCES

H.P. Bennetto, G.M. Delaney, S.J. Ford, A. Koshy, J.R. Mason,  
J.L. Stirling, R.J. Sutton and C.F. Thurston  
Bioelectrochemistry and Biosensors Group, King's College London,  
Campden Hill Road, London W8 7AH, United Kingdom.

The numerous advantages resulting from the use of heterogeneous platinised carbon paper as an electrode base represent a major advance in the development of amperometric biosensors. In particular, glucose biosensors constructed by immobilisation of glucose oxidase on this type of catalytic material are easily prepared, require no mediator, have a fast, rapid response over a wide concentration range, are highly reproducible, and have a remarkably long lifetime [1]. They are effectively insensitive to oxygen concentration, although the observation of a requirement for the presence of trace oxygen suggests that the electron transfer pathway may involve participation of adsorbed dioxygen species ( $O_2$ ,  $H_2O_2$  and radicals) which can form 'bridges' between the electrode and the 10a or 4a positions of the reduced flavin [2].

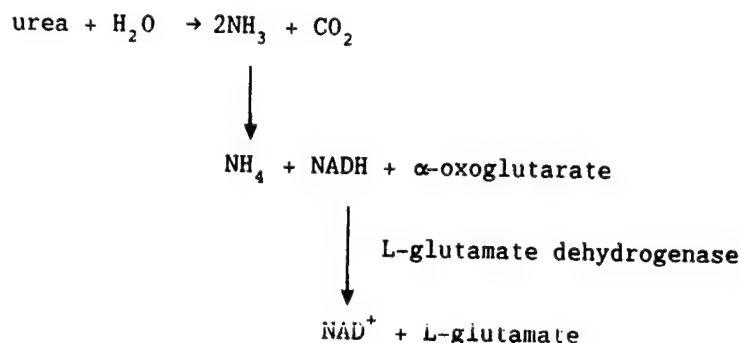
Similarly prepared electrodes for other analytes, using single enzymes, function satisfactorily, although the immobilized enzymes are less stable [3]. The feasibility of constructing multi-enzyme sensors, based on the glucose sensor, by co-immobilisation of appropriate enzymes is exemplified by a bi-enzyme sensor for glucosinolates [5] and a tri-enzyme sensor for sucrose [4]. Mechanistic studies on the latter show the rôles of invertase (IV), mutarotase (MR) and glucose oxidase (GO) in the following reaction sequence, where the final step is used for amperometric signal-generation:



Preliminary results from recent work show the potential applications of the sucrose sensor in the analysis of beverages and soft drinks.

An additional important area for application of activated carbon electrodes concerns the many enzymatic analyses which use specific dehydrogenases in conjunction with the cofactor  $\beta$ -nicotinamide adenine dinucleotide ( $NAD^+$ ) or its reduced form ( $NADH$ ). Conventional approaches to this type of analysis commonly employ spectrophotometric monitoring, and are necessarily limited with respect to the accessible range of  $NAD^+$  (or  $NADH$ ) concentration. Although this difficulty can be overcome, in principle, using amperometric determination of  $NADH$ , numerous previous attempts to devise amperometric  $NADH$  assays have met with only partial

success. We have discovered, however, that considerable improvements result from the use of heterogeneous carbon paper electrodes, since NADH is oxidised rapidly, efficiently and reproducibly at relatively low overpotentials on these materials [6]. The potential for application of this methodology in clinical analysis is illustrated with reference to an assay for urea, using urease and glutamate dehydrogenase according to the following scheme:



- [1] D.J. Anderton, H.P. Bennetto, D.R. DeKeyzer, G.M. Delaney, A. Koshy, J.R. Mason, G. Mourla, W.H. Mullen, L.A. Razack, J.L. Stirling and C.F. Thurston. Int.Ind.Biotech. 8, 5-10, (1988).
- [2] H.P. Bennetto, D.R. DeKeyzer, G.M. Delaney, A. Koshy, J.R. Mason, J.G.I. Ong, L.A. Razack, J.L. Stirling and C.F. Thurston. In Biotechnology Research and Applications, Abs.'Canbiocon', Montreal, April 1988, J. Gavora, D.F. Gerson, J. Luong, A. Storer and J.H. Woodley, eds., (Elsevier, London and New York, 1988) pp.185-194.
- [3] H.P. Bennetto, D.R. DeKeyzer, G.M. Delaney, A. Koshy, J.R. Mason, L.A. Razack, J.L. Stirling and C.F. Thurston. In Proc. SENSOR 88, Nürnberg, May 1988, (ACS organisations GmbH, Wunsdorf, 1988) sec A3, pp.131-44.
- [4] C.F. Thurston, H.P. Bennetto, D.R. DeKeyser, G.M. Delaney, A. Koshy, J.R. Mason, L.A. Razack, J.L. Stirling. In World Biotech Report 1988, Proc. 'Biotech 88', London, May 1988, (Online Publications, London, 1988) pp.307-16.
- [5] H.P. Bennetto, G.M. Delaney, A.J. MacLeod, J.R. Mason, J.L. Stirling and C.F. Thurston. Analyt. Letts. 21, 2177-95, (1988).
- [6] H.P. Bennetto, D.R. DeKeyzer, G.M. Delaney, J.R. Mason, W.H. Mullen, J.L. Stirling and C.F. Thurston. Europ.Pat.Appln. nos. 88303922.4; 88303921.6 (1988), and papers in press.

19-12-07-K

MULTI-GATE AND MULTI-ENZYME SENSORS

F. Scheller, R. Hintsche, I. Dransfeld, W. Moritz, M.T. Pham  
Academy of Sciences of the GDR, GDR-1115 Berlin-Buch, and  
Humboldt University Berlin

Starting from membrane covered Clark-type electrodes chip biosensors with direct enzyme fixation at the sensor surface have been developed. Their response time and functional stability are superior to that of the conventional biosensors. However, for the application in real samples the components - membrane, biolayer and transducer - have to be adapted to give the desired specificity and measuring ranges. Two alternative approaches of optimizing the analytical characteristics are presented:

(i) multi transducer biosensors

A two-functional FET containing pH and  $F^-$  sensitive gate regions is uniformly covered by a layer containing peroxidase and glucose oxidase or lactate oxidase. In the presence of a highly buffered solution of an organofluoro compound the  $F^-$  gate responds to the fluoride ions formed in the enzyme sequence whilst the constant output of the pH-FET acts as the reference. In this way, effects by variations of both the pH value and the buffer capacity of the sample are eliminated.

(ii) multi enzyme layers

The introduction of enzymes eliminating interfering substances, e.g., laccase, results in an improved specificity of amperometric biosensors. In order to extend the measuring range to higher concentrations, enzymes converting the analyte in parallel with the indicator reaction are coimmobilized. On the other hand, enzymatic regeneration of the analyte molecule overcomes the limits of sensitivity set by diffusional processes. Using highly effective enzymatic recycling systems nanomolar concentrations of lactate and hydroquinone may be determined. In this way the biosensors exhibit a higher sensitivity than the basic amperometric electrodes.



c3

19-12-08-G

ELECTROCHEMICAL IMMOBILIZATION OF ENZYMES  
AND CURRENT RESPONSE OF GOD ELECTRODES

Wu Huihuang    Zheng Zhimin  
(Chem, Dept, Xiamen Univ., Xiamen, China)

ABSTRACT

Glucose oxidase (GOD) was entrapped into poly pyrrole films by electropolymerization. The redox properties and catalytic activities of the immobilized enzymes were examined. Its application to amperometric enzyme electrodes was discussed both in the presence and in the absence of mediators.

19-12-10-G

Photochemical Control of Electrical Oscillations  
in Lipid Membranes

Hiroshi Nakanishi, Kanekazu Seki, and Yasushi Mori

Toshiba Research and Development Center, Toshiba Corporation,  
1 Komukai Toshiba-cho, Saiwai-ku, Kawasaki 210 Japan

The optical information processing in the retina is an excellent model to develop a new optical sensing system. In the retina, the light information is converted into the frequencies of the nerve pulses. At first, the initial photoreception occurs through the structure change in the bilayer membrane, and the nerve pulses are generated through the change of the functional character of the cell membrane.

In this paper, we will report a simple biomimetic functional system to convert the light information to the electric pulses using the artificial lipid membranes where the structure change is induced by the light.

An azobenzene amphiphilic derivative (4'-octylazobenzene-4-oxybutyric acid; AZ) was used as a photoresponsive molecule. This molecule is known to proceed the  $\text{trans} \rightleftharpoons \text{cis}$  photoisomerization as can be found in nature. The photoresponsive lipid membrane was prepared by the impregnation of the lipid mixture of AZ and monoolein to the porous ( $0.4\mu\text{m}$  in pore size) polyester filter of  $10\mu\text{m}$  thickness.

Experiments were carried out by the apparatus shown in Fig.1. A simple oscillating circuit was connected to the pair of platinum electrodes set at the both sides of the membrane. The cell was filled with 0.1M KCl solution. The membrane was irradiated by the monochromatized light from a 150W Xe lamp.

For the filter without the lipid mixture, the oscillation frequency was in the order of  $10^{-1}$  Hz. When the lipid was impregnated, the frequency was increased to the order of  $10^5$

Hz, and remained almost constant. Then, the irradiation was carried out at the membrane. In Fig.2, the change of the frequency in the membrane by the irradiation with two different wavelengths is shown. Each irradiation, 360nm and 450nm, corresponds to the photoisomerization, trans  $\rightarrow$  cis and cis  $\rightarrow$  trans reaction, respectively. A 360nm irradiation decreased the frequency, which was recovered by the 450nm irradiation. Such a change in frequency with regard to the irradiation wavelengths was not detected for the membrane impregnated with monoolein alone. Therefore, it was clarified that the frequency change induced by the irradiation was caused by the reversible change of the membrane structure, initiated with the trans  $\rightleftharpoons$  cis photoisomerization reactions.

These results indicates that this artificial lipid membrane system is a promising biomimetic model to convert the light signals to the electrical pulse signals.

This study was performed through Special Coordination Funds of the Science and Technology Agency of the Japanese Government.

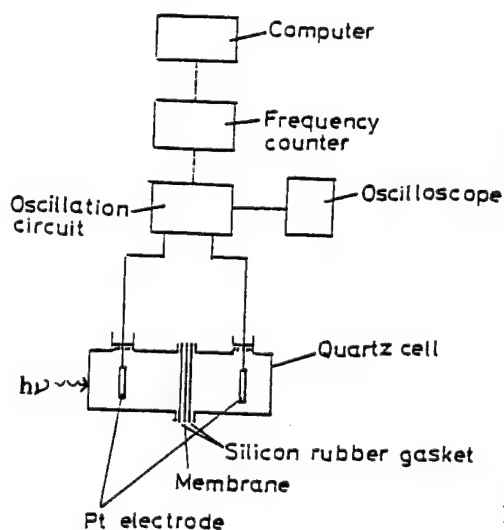


Fig.1 Schematic diagram of the experimental apparatus.

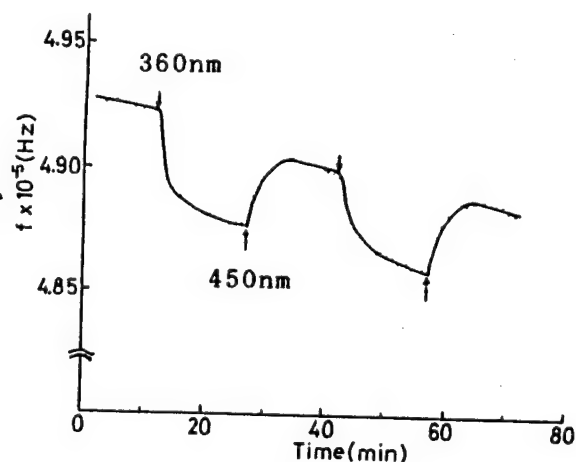


Fig.2 Light induced change in frequency,  $f$ , for the membrane containing AZ/monoolein mixture.

19-12-11-G

BIOELECTROCHEMICAL IMMUNOASSAY FOR HUMAN CHORIONIC GONADOTROPHIN

Lu Mingxang, Chen Kungming

Dept. of Applied Chemistry, Tianjin University, Tianjin, China

It is well known that the combination of electrochemical detection with immunoassay results in extremely sensitive assays. An immunosensor is an analytical device which principally depends on its immunochemical affinity and electrochemical sensitivity. Here we introduce a bioelectrochemical immunosensor for determination of HCG. It can be used in diagnosis of pregnancy.

The glassy carbon electrodes cleaned were treated with  $K_2Cr_2O_7$  and  $HNO_3$  solution under +2.2V (vs. SCE) for 15". After electrode was oxidized in strong oxidation medium, the carboxylic acid was formed on its surface. The reaction between the carboxylic acid and amino group of protein will occur when the electrode is immersed in the solution containing anti-HCG antibodies.

As resulting the anti-HCG antibodies have been chemically coupled to the surface of glassy carbon electrode. Then the electrode attached antibodies was placed into PB solution with different concentration of HCG antigen for 1h at 30 °C, then washing electrode with water, measuring cyclic voltammogram in 0.8% NaCl solution. As illustrated in figure there is a little cathode peak under -0.4V (vs. SCE). However its peak current associated with the concentration of antigen HCG, it will be decreased with HCG increasing. The reason is due to formation of antigen and antibodies complex on the electrode surface, then a reduction procedure of adsorbed oxygen on the electrode is repressed.

The relationship between the  $I_p$  and antigen concentration is obtained, here  $I_p$  express the difference of peak current between oxidized electrode and formed complex electrode. The theoretic function was obtained by computer:

$$y = 14.05 + 89.41x - 8.22x^2$$

where  $y$  is  $I_p$ ,  $x$  is concentration HCG. The sensitivity is  $5 \times 10^{-7} \text{g/ml}$ .

[1] N. Yamamoto; Kobunshi Kako, **33**, 6 (1984), 5

[2] M. Aizawa, A. Morioka, et al., Analytical Biochemistry, **94** (1979), 22

[3] G. A. Robinson, V. M. Cole, et al., Biosensors, **2** (1986), 45

19-12-12-K

ELECTROCHEMICAL PREPARATION OF ULTRA-THIN CONDUCTIVE ENZYME MEMBRANE AND ITS POTENTIAL-DEPENDENT ACTIVITY CONTROL

M. Aizawa, Y. Ikariyama, S. Yabuki and H. Shinohara  
 Department of Bioengineering, Tokyo Institute of Technology  
 O-okayama 2-12-1, Meguro-ku, Tokyo 152

There have been intensive researches on developing biofunctional synthetic membranes either after the model of biomembranes or in combination with biomolecules. Few synthetic membranes, however, are endowed with both electronic and biomolecular functions. To greater extent the development of new functional synthetic biomembranes depends on an efficient embodiment of conductive materials with biomaterials. The authors have been aiming at synthesizing a novel functional membrane, "Conductive Enzyme Membrane", in which the enzymatic properties are complexed with the electronic properties of the membrane matrix.

Therefore, we have carried out a series of experiments on the conductive enzyme membrane. In the first step, an electroconductive enzyme membrane was prepared on a platinum electrode surface by electrochemical polymerization of pyrrole in the presence of glucose oxidase (GOD). The membrane demonstrated smooth electron transfer between the enzyme and the electrode with retaining enzyme activity, since the conductive polymer seemed to serve as an interface between the enzyme and the electrode (Figure 1(a)). The FAD/FADH moiety was reversibly reduced/oxidized by the base platinum electrode in the absence of oxygen. The membrane demonstrated responses to glucose at an applied potential above the oxidation potential of FADH. The approach was then extended to a conductive dehydrogenase membrane where NAD (coenzyme) should be coexisted for the demonstration of its activity. For the smooth and efficient electron transfer, alcohol dehydrogenase (ADH), NAD and Meldola blue (a mediator for NAD) were mixed with pyrrole for the preparation of a conductive ADH membrane (Figure 1(b)). The conductive ADH membrane showed responses to alcohol at an applied potential above -0.2V where NADH is oxidized under the assistance of Meldola blue. Finally, ultra-thin conductive enzyme membrane was prepared. GOD was electrochemically absorbed on a platinum electrode surface, following which electropolymerization of pyrrole was performed by applying a pulsed potential for a short time interval (Figure 1(c)). By controlling electricity, an ultra-thin polypyrrole membrane with a thickness up to the GOD diameter was prepared. The membrane demonstrated GOD activity which was dependent on the applied potential. The approaches presented here will open up a new vista on intelligent devices such as output-controllable biosensors and oxygen-free oxidase biosensors.

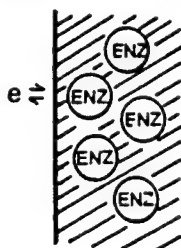


Fig.1

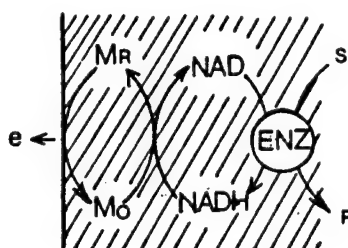


Fig. 2

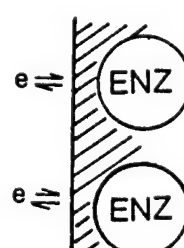


Fig. 3

19-12-13-G

ELECTROCHEMICAL IMMOBILIZATION AND CHARACTERIZATION OF ENZYME GOD

H. H. Wu, Z. M. Zhen, S. M. Zhou  
 Department of Chemistry, Xiamen University, Xiamen, Fujian, China

The immobilization of an enzyme by electropolymerization has recently been carried out and a number of advantages has shown for construction of enzyme electrodes<sup>(1,2)</sup>. In this work, the electrochemical immobilization of glucose oxidase GOD in polypyrrole film is discussed.

The immobilized GOD films were formed by potentiostatical polymerization at glassy carbon in a deoxygenated, buffered phosphate solution containing GOD and 0.05 mol dm<sup>-3</sup> pyrrole. The growth of polypyrrole in this solution is slower, but accessible to enzyme entrapment. The polymer films with or without GOD differentiate in IR spectra, particularly in the range of 1200 - 1755 cm<sup>-1</sup>. It was found that in pH<5.5 solution the immobilization was not successful.

A.C. impedance experiments show that Nyquist plot and Bode plot for the immobilized GOD films are similar with those for the polypyrrole films formed at same conditions except the absence of GOD. It indicates that the frame of polymer is not distorted in the presence of the enzyme.

As polypyrrole is electrically conducting, knowledge of the electron transfer between the enzyme and the polymer is desirable. On the cyclic voltammograms and differential pulse voltammograms for the GOD electrode in blank buffered solution, a peak was found characteristic of the enzyme films. By comparison, the peak was attributed to electron transfer of GOD in the polymer rather than that adsorbed on carbon. In the solutions containing O<sub>2</sub> or benzonquinone the GOD in the polymer exhibit enzymatic activity and respond to D-glucose. However, the enzyme films failed in constructing a mediatorless glucose electrode. The kinetic parameters were estimated for the enzymatic reaction in the polymer, and Michaelis constant for the immobilized enzyme is one order of magnitude higher than that for the free enzyme.

Simultaneous immobilization of GOD and mediators by electropolymerization has been attempted. When Fe(CN)<sub>6</sub><sup>3-/4-</sup> exists in the enzyme films, the sensitivity and operational potential of the enzyme electrode are improved.

- (1) N. C. Foulds and C. R. Love, J. Chem. Soc. Faraday Trans. 1, vol. 82 (1986), 1259
- (2) P. N. Bartlett and R. G. Whitaker, J. Electroanal. Chem., vol. 224 (1987), 27

## 19-12-14-G

Rectifying Function of Porphyrin-Flavin LB Monolayer-Junction  
on Gold Electrodes Derived from the Redox Properties of Proteins

Satoshi Ueyama, Satoru Isoda and Mitsuo Maeda

*Central Research Laboratory, Mitsubishi Electric Corporation  
8-1-1 Tsukaguchi-Honmachi, Amagasaki, Hyogo 661, Japan*

**Introduction** The biological electron transfer system, especially photo-synthetic system, has drawn a wide attention, since the electron transfer takes place very efficiently through prosthetic groups in one direction. This specific electron transfer is based both on the redox potential difference and on the steric factor of the groups. The mechanism of the one-way electron transfer is considered to be used for the construction of molecular rectifying devices [1]. Thus, we formed a porphyrin-flavin heterojunction by modifying gold electrodes with a porphyrin-LB film and a flavin-LB film, and studied the interlayer electron transfer rate between the porphyrin and flavin by cyclic voltammetry.

**Experimental** Hematoporphyrin(IX) bis (tridecanoyl ether) Ru(II) (pyridine)<sub>2</sub> complex (RuHP(Py)<sub>2</sub>) and 7,8-dimethyl-3,10-dinonylisoalloxazine (DNI) were used for the heterojunction formation (Fig.1). RuHP(Py)<sub>2</sub> and/or DNI were deposited on gold electrodes by the LB method at  $\pi=25$  mN m<sup>-1</sup>. Cyclic voltammetry was carried out after the starting potential of -0.6 V vs Ag/AgCl was applied for 1 hour to reduce all the deposited molecules.

**Results and Discussion** Firstly, a pair of head-to-head LB monolayers (Y type) of RuHP(Py)<sub>2</sub> were deposited on a gold electrode. The surface electron transfer rate ( $k''$ ) between the gold electrode and the one unit-layer of porphyrin (we treated a pair of LB monolayers as a unit-layer in the simulation) was determined to be about 10 s<sup>-1</sup> by analyzing the cyclic voltammograms (CV's) at  $v=0.05-64$  V s<sup>-1</sup> according to Daifuku et al.[2]. Secondly, the interlayer electron transfer rate ( $W_{PP}$ ) between the porphyrins was determined to be about 50 s<sup>-1</sup> by analyzing the CV's using 3 unit-layers of RuHP(Py)<sub>2</sub> according to Laviron [3]. Thirdly, a porphyrin-flavin heterojunction was formed by depositing a unit-layer of DNI on 3 unit-layers of RuHP(Py)<sub>2</sub> on a gold electrode (Fig.2). Figure 3 shows the CV's of the heterojunction electrode. It should be noted that the heterojunction has the following characteristics of CV: (1) no peaks due to DNI appeared at the redox potential (-0.40 V vs Ag/AgCl) of the DNI monolayers; (2) for the first cycle, only one anodic peak appeared near the anodic peak potential (0.27 V) of the RuHP(Py)<sub>2</sub> electrode; (3) the anodic peak current was much higher than that for the RuHP(Py)<sub>2</sub> electrode, while the cathodic peak current was much the same.

The flavin-to-porphyrin electron transfer rate,  $W_{FP}$ , was determined to be about 64 s<sup>-1</sup> by the simulation (Fig.4) using the differential equations listed below. The value of  $W_{FP}$  was much higher than the porphyrin-to-flavin transfer rate,  $W_{PF}$  ( $\leq 0.5$  s<sup>-1</sup>). This is considered to be due to the redox potential difference between the porphyrin and the flavin molecules according to the theory of the electron transfer [4]. The directional regulation of the electron transfer can be used for molecular electronic rectifying devices.

**Acknowledgment** This work was supported by the NEDO's Project of Basic Technology for Future Industries.

#### REFERENCES

- [1] (a) Isoda et al., US patent 4,764,415 (1988).  
(b) S.Ueyama et al., *J. Electroanal. Chem.*, in press.
- [2] Daifuku et al., *ibid*, 183, 1 (1984).
- [3] E.Laviron, *ibid*, 112, 1, 11 (1980).
- [4] R.A.Marcus, *Ann. Rev. Phys. Chem.*, 15, 155 (1964).

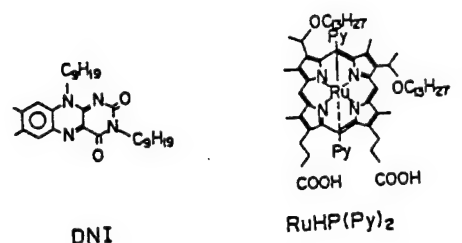


Fig.1 Electroactive LB compounds to form heterojunction.

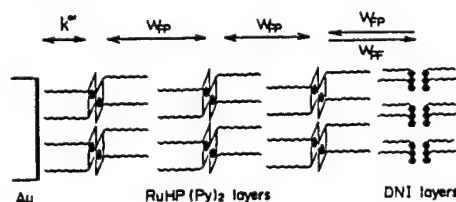


Fig.2 Schematic diagram of RuHP(Py)<sub>2</sub>-DNI Au electrode.

$$\begin{aligned}
 d\chi_{10}/dE &= (k''/v) \{ 2(1-\chi_{10}) \exp[\alpha_s \xi + (\Xi + \Delta \Xi^*)/2] (2\chi_{10}-1) \} \\
 &\quad - 2\chi_{10} \exp[\alpha_s \xi - (\Xi - \Delta \Xi^*)/2] (2\chi_{10}-1) \} \\
 &\quad + (W_{FP}/v) (\chi_{20} - \chi_{10}) \\
 \xi &= (F/RT) (E - E_3^*) \\
 d\chi_{20}/dE &= (W_{FP}/v) (\chi_{10} - 2\chi_{20} + \chi_{30}) \\
 d\chi_{30}/dE &= -(W_{FP}/v) (\chi_{30} - \chi_{20}) \\
 &\quad + (W_{FP}/v) (1 - \chi_{30}) \chi_{40} - (W_{FP}/v) \chi_{30} (1 - \chi_{40}) \\
 d\chi_{40}/dE &= -(W_{FP}/v) (1 - \chi_{30}) \chi_{40} + (W_{FP}/v) \chi_{30} (1 - \chi_{40}) (\Gamma_F/\Gamma_P) \\
 \Psi &= i / \{ F^2 v A N \Gamma_P / RT \} \\
 &= (d\chi_{10}/dE + d\chi_{20}/dE + d\chi_{30}/dE + (\Gamma_F/\Gamma_P) d\chi_{40}/dE) (RT/F) / N
 \end{aligned}$$

$\chi_{n0}$ : the surface mole fraction of oxidized form in n-th layer  
 $\alpha_s$ : transfer coefficient  
 $\Xi, \Delta \Xi^*$ : interaction parameters  
 $E_3^*$ : the conditional redox potential of 3-layer-RuHP(Py)<sub>2</sub>  
 $\Gamma_F, \Gamma_P$ : surface concentration of the RuHP(Py)<sub>2</sub> and DNI  
 $N$ : number of unit-layers of RuHP(Py)<sub>2</sub> (=3)

Differential equations to simulate CV of porphyrin-flavin heterojunction electrode. A pair of head-to-head LB monolayers (Y type) is treated as a unit-layer.

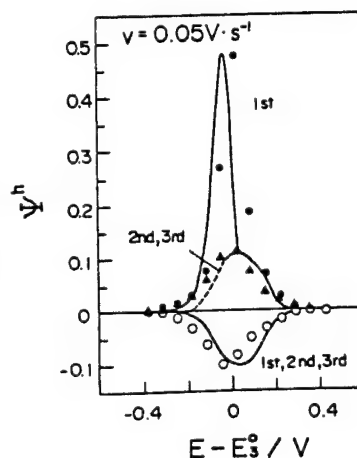
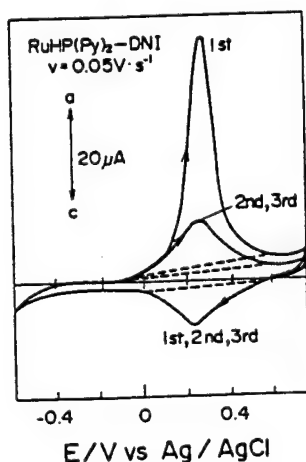


Fig.3 Cyclic voltammograms (1st, 2nd and 3rd cycles) of RuHP(Py)<sub>2</sub>-DNI Au electrodes.

Fig.4 Comparison of experimental and simulated CV's (1st, 2nd and 3rd cycles) of RuHP(Py)<sub>2</sub>-DNI Au electrodes. E<sub>3</sub><sup>\*</sup> is conditional redox potential of 3-layer-RuHP(Py)<sub>2</sub> (0.259 V vs Ag/AgCl).



Electrocatalytic Photolysis of Water at Photosystem II-Modified  
Carbon Paste Electrodes in the Presence of Electron Transfer Mediators

T. Ikeda, K. Amako, M. Senda

Department of Agricultural Chemistry, Kyoto University, Sakyo-ku,  
Kyoto 606

T. Shiraishi, K. Asada

The Research Institute for Food Science, Kyoto University, Uji,  
Kyoto 611

Biocatalyst electrodes, that is, modified electrodes carrying immobilized enzymes or proteins in which the electrode behaves as a substitute for a chemical electron acceptor or donor in the biochemical reaction can be used in such novel applications as biosensors, bioreactors and biofuel cells. We have constructed such biocatalyst electrodes using enzymes, oxidases and dehydrogenases. Here we use a multiprotein complex, photosystem II membrane complex (PS II) from chloroplast to construct a biocatalyst electrode which shows photocurrent response.

PS II-enriched membranes from spinach chloroplasts were immobilized on the surface of a carbon-paste electrode containing 2,6-dimethylbenzoquinone (DMQ) by covering it with a dialysis membrane. The PS II-modified electrode, PS II-DMQ-CPE, was immersed in an electrolysis solution and the voltammetric behavior of the electrode was studied. The PS II-DMQ-CPE produced cathodic and anodic cyclic voltammetric waves in the dark, which were attributable to the electrochemical redox reaction of DMQ dissolved in the immobilized PS II layer on the carbon-paste electrode surface. The anodic wave was increased by the illumination of the electrode. A PS II-modified electrode not containing DMQ showed no observable current response to the illumination. Steady-state anodic currents,  $I$ , were observed when measured at fixed electrode potential,  $E$ , under illumination.  $I$  increased with increasing positive potential to approach a limiting current,  $I_l$ . When dichlorophenyl dimethylurea, an inhibitor for the electron flow from  $Q_B$  site in the PS II complex to an electron acceptor, was added to the electrolysis solution,  $I_l$  decreased to almost zero. The results indicate that PS II membranes immobilized on the carbon-paste electrode surface remain active and that DMQ trapped in the PS II-membrane layer can mediate the electron transfer between the immobilized PS II and the carbon-paste electrode.  $I_l$  increased with increasing both the light intensity and the DMQ concentration to approach saturation. The results were interpretable by an equation obtained by assuming sequential electron transfer steps for the photoelectrocatalytic reaction. Several quinones other than DMQ were also found to serve as the electron transfer mediator, and the effect of these quinones on  $I_l$  and the  $I$ - $E$  curves were discussed from the point of the efficient energy conversion at the PS II-modified electrode.

19-12-16-G

## PLATINUM ELECTRODE POTENTIAL IN WASTEWATER TREATMENT

Alain Hédut\* &amp; Daniel R. Thévenot\*\*

\* Centre National du Machinisme Agricole, du Génie Rural, des Eaux et des Forêts (CEMAGREF), Unité Qualité des Eaux Pêche et Pisciculture, 14 avenue de Saint-Mandé, 75012 Paris (France).

\*\* Laboratoire de Bioélectrochimie et Analyse du Milieu (L.A.B.A.M.), U.F.R. de Sciences et de Technologies, Université Paris-Val de Marne, Avenue du Général de Gaulle, 94010 Créteil (France).

Various authors have recently demonstrated the practical importance of zero-current potential measurements in activated sludge in controlling nitrification and denitrification processes (Tanaka *et al.*, 1982, Fujii, 1983, Charpentier *et al.*, 1987, Charpentier *et al.*, 1989, Hédut *et al.*, 1988). Several patents have been taken out as a result of these studies (Hitachi Ltd, Kankyo Engineering Co Ltd, Meidensha Electric Mfg Co Ltd, Mitsubishi Heavy Industries, Nippon Steel Corp.).

Our work on pilot plants demonstrated that, when they are subjected to cyclic feed and aeration conditions, the  $E_H^*$  potential of polished platinum electrodes reached at the end of the aeration periods is related to the nitrification efficiency ( $R_n$ ) :

$$R_n = 100 - 8570 \exp(-0.0168 \cdot E_H^*) \quad r^2 = 0,97 \quad n = 12$$

(%) (mV/NHE)

The metal electrode potential in aerated sludge originates from several sources (Hédut & Thévenot, 1989). One of them is the oxygen reduction reaction. Full scale and pilot plant experiments showed that the  $E_H^*$  potential is closely related with the logarithm of the dissolved oxygen concentration :

$$E_H^* = a + b \log [O_2]$$

(mV/NHE) (mV/NHE) (mV/decade) (mg/l)

Experimental parameters  $a$  (in the range 200 - 500 mV) and  $b$  (in the range 50 - 200 mV/decade) differ significantly from the values calculated theoretically from oxygen reduction reaction (respectively 800 mV and 15 mV/decade at pH 7 and 20°C).

Although the equilibrium potential and the dissolved oxygen concentration are closely linked, they are not "equivalent". The platinum electrode potential in activated sludge is affected by other electroactive species in the interstitial water whose nature and concentration are mainly determined by the organic load, the overall oxygen input, the aeration sequence and the sludge concentration.

### References

CHARPENTIER J., GODART H., MARTIN G., MOGNO Y. (1989) Oxidation reduction potential (ORP) regulation as a way to optimise aeration and C, N and P removal : experimental basin and various full-scale examples. IAWPRC Conference (BRIGHTON), *Wat. Sci. Tech.*, 21, 1209-1223.

CHARPENTIER, J., FLORENTZ, M., DAVID, G. (1987) Oxidation reduction potential (ORP) regulation : A way to optimise pollution removal and energy savings in the low activated sludge process. IAWPRC Conference (RIO), *Wat. Sci. Tech.*, 19, 645-655

FUJII, M. (1983) Redox potential in control of activated sludge treatment of sewage of apartment development areas. *Mizu Shori Gijutsu*, 24 (9), 685-95.

HEDUIT, A. (1985) Mesure de potentiels d'équilibre dans les boues activées. *Mémoire de D.E.A. Sciences et Techniques de l'Environnement. Université de Paris Val de Marne - CEMAGREF* 25 pp.

HEDUIT A., LECLERC L.A., SINTES L., THEVENOT D.R. (1988) Perspectives de maîtrise des processus de nitrification et de dénitrification dans les boues activées à l'aide du potentiel d'oxydo-réduction. IAWPRC/AIDE Conference (BRUXELLES), *Wat. Supply*, 6, 275-285.

HEDUIT A., THEVENOT D.R. (1989) Relation between redox potential and oxygen levels in activated sludge reactors. IAWPRC Conference BRIGHTON, *Wat. Sci. Tech.*, 21, 947-956.

HITACHI, Ltd. (1983). Process control in biological denitrification of wastewater. *Jpn. Patent Kokai Tokkyo Koho JP 58/196891 A2 (83/196891)*, 16 Nov. 1983, 5 pp.

KANKYO ENGINEERING CO, Ltd. (1983). Activated sludge process control by redox potential. *Jpn. Patent Kokai Tokkyo JP 58/202094 A2 (83/202094)*, 25 Nov. 1983, 6 pp.

MEIDENSHA ELECTRIC MFG. Co, Ltd. (1980). Automatic control of wastewater treatment. *Jpn. Patent Tokkyo Koho JP 55/23678 (80/23678)*, 24 Jun. 1980, 7 pp.

MITSUBISHI HEAVY INDUSTRIES, Ltd. (1984). Wastewater treatment. Patent *Jpn. Kokai Tokkyo Koho JP 59/90695 A2 (84/90695)*, 25 May 1984, 4 pp.

NIPPON STEEL CORP. (1981). Activated sludge process control. *Jpn. Patent Tokkyo Koho JP 56/27096 (81/27096)*, 23 Jun 1981, 6 pp.

TANAKA, K., YASUE, K. et al. (1982) - Automatic control of biological denitrification process by use of redox potential. *Mizu Shori Gijutsu*, 23 (8) 689-95.

22-01-00-I

PROSPECTS AND PROBLEMS OF ELECTROCHEMICALLY INDUCED COLD  
NUCLEAR FUSIONJ.W. Schultze, U. König, A. Hochfeld  
Institut für Physikalische Chemie und Elektrochemie,C. van Calker, W. Kies  
Institut für Experimentalphysik

Universitätsstr.1, Heinrich-Heine-Universität, 4000 Düsseldorf, F.R.G.

Experiments by Fleischmann, Pons and Jones stimulated the imagination of electrochemists. Now, concepts have to be discussed in detail. At first, the correlation between hot fusion, muon catalyzed cold fusion and electrochemically and fracture induced cold fusion is explained. In Pd deuterons can be treated as delocalized bosons which are squeezed together in octahedral sites. The Coulomb barrier between the nuclei may be screened by the electron gas. Hence, deuteron tunneling may be enhanced.

Experiments are discussed with respect to deuteron concentration and current-potential curves of relevant processes, i.e. deuteron or water discharge. In various experiments the surface state of the electrode is modified. Electrochemical calorimetry has to be carried out only for the limiting cases of complete electrolysis and recombination, respectively. Difficulties arise for stationary electrolysis.

Radiochemical detection of fusion rates presumes careful elimination of background radiation, absorption phenomena (self and foreign), backscattering, etc. Experimental conditions to measure the tritium production, the  $\gamma$ -rays and neutrons are described.

Three months after the first paper various interesting experiments have been presented. But there is no certain evidence and many doubts occurred. Independent of the estimated fusion rates, most results are near to the background level (neutron rates of 0.04 n/s) or to the experimental error (fusion heats corresponding to  $10^{13}$  s<sup>-1</sup>, similar to chemical reaction enthalpies). Experiments are complex for various reasons. To compare results of different authors, more experimental data have to be checked in detail. A distinction between a volume- or surface phenomenon is not yet possible. Neutron production at grain boundaries is discussed.

22-01-02-G

Neutron Evolution from Palladium Cathode in  $D_2O$ -LiOD Solution

Tadahiko MIZUNO\*, Tadashi AKIMOTO and Norio SATO  
Faculty of Engineering, Hokkaido University  
(Kitaku North 13 West 8, Sapporo 060 JAPAN)

## 1 INTRODUCTION

In response to the recent reports of evidence(1,2) for room-temperature nuclear fusion in the electrolysis of  $D_2O$ , we have examined the evolution of neutrons from a cathodically charged palladium in  $D_2O$ -LiOD solution. This reports the results of our preliminary examination and confirms the evolution of 2.5 MeV neutrons which correspond to one of the reaction products of the nuclear fusion,  $D+D \rightarrow {}^3He+n$ .

## 2 EXPERIMENTAL

Experimental procedures were shown in previous paper(3). The cathode was a palladium rod of 99.9% purity with the dimension of 0.3 cm in diameter and 10 cm in length. The palladium rod was annealed at 800°C in vacuum( $2 \times 10^{-5}$  mmHg) for 20 hours. Followed by further annealing at 800°C in deuterium gas of 99.9% purity (760 mmHg) for 8 hours and cooled to room temperature in the deuterium gas. This annealing and cooling procedure of the palladium rod was repeated several times before the experimental measurements. A spiral wire of high purity platinum 0.5 mm in diameter and 30 cm in length was used as anode. The electrolyte used was 0.5 M LiOD which was prepared from analytical grade LiOD of 99.9% purity and  $D_2O$  of 99.75% purity.

A block diagram of experimental layout for neutron measurements is same as before. We employed a rise-time discrimination technique to eliminate the signals induced by gamma-rays and thermionic noises of the photomultiplier. A liquid scintillator of NE 213(proton recoil detector, 12.7cm  $\phi \times 12.7$ cm t) was used as a neutron detector.

The experiment was carried out in a dark underground room whose temperature remained constant at  $14.5 \pm 0.2^\circ C$ . The detector was shielded by lead brick (5 cm thickness) and borated polyethylene (10 cm thickness). Furthermore the front of the detector was covered with a cap of lead 1.0 cm thick.

## 3 RESULTS

Before the onset of electrolysis the background level of counting signals inherent in the experimental system was measured for seven days. Electrolysis continued being carried out for 1570000 seconds(18.2 days) at the current density of 100 mA/cm<sup>2</sup> with the palladium cathode of which the surface area of 7.00 cm<sup>2</sup> was always immersed in the electrolyte by supplying fresh deuterium oxide every hour. The signal measurements were continuously carried out during the whole period of electrolysis for 18.2 days and the count value was stored in memory. The neutron energy spectrum was obtained from the stored counting data by means of the FERDOR code.

Figure 1 shows the pulse amplitude distribution during the electrolysis (curve 1) and after the electrolysis was ceased (curve 2). The counts rises

above around channel 700 during the electrolysis. Figure 2 shows the neutron energy spectrum in term of foreground minus corresponding background counts obtained during electrolysis. The solid line at various energy levels indicates the estimated error bars due to counting statistics and other sources. It can be seen that there is a peak flux at the energy of 2.5 MeV in the neutron energy spectrum.

It may be concluded that the d-d nuclear fusion reaction takes place in or on the palladium electrode during cathodic charging in 0.5 M LiOD-D<sub>2</sub>O solution. An approximate estimate of the fusion rate  $\lambda$  for a d-d pair gives  $\lambda \sim 10^{-23}$  fusion/s, which is close to the value obtained by Jones et al.(2).

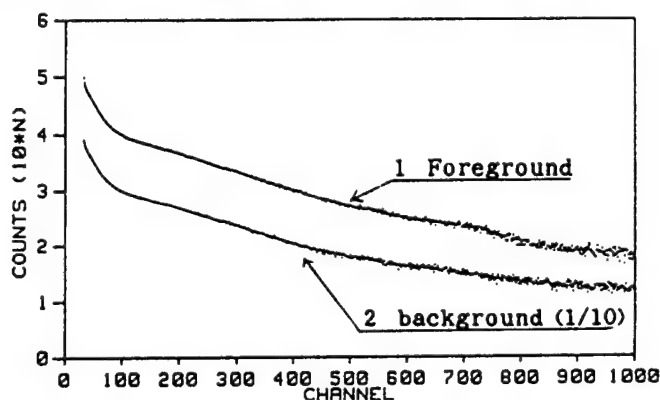


Fig.1 The pulse amplitude distribution during the electrolysis (1) and the electrolysis was ceased (2).

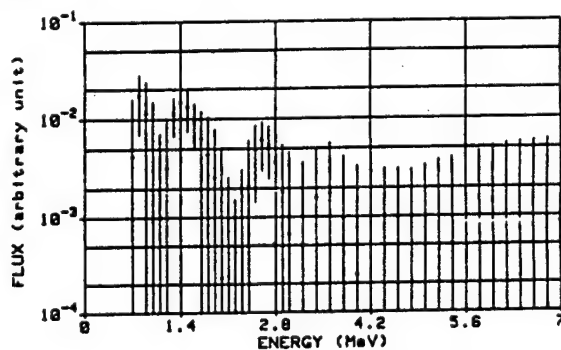


Fig.2 Neutron energy spectrum obtained by the cathodic polarization with Pd electrode in D<sub>2</sub>O-LiOD solution

#### REFERENCES

- 1) M.Fleischmann and S.Pons, J.Electroanal.Chem., **261** 301 (1989).
- 2) S.E.Jones, E.P.Palmer, J.B.Czirr, D.L.Decker, G.L.Jensen, J.M.Thorne, S.F.Taylor, and J.Rafelski, Nature, **338** 737 (1989).
- 3) T.Mizuno, T.Akimoto and N.Sato, Denki Kagaku, **57** No.7, 742(1989)

22-01-04-G

LOW TEMPERATURE FUSION OF DEUTERIUM IN ELECTROCHEMICAL PROCESSES

J. Zak, J.W. Strojek

The Silesian Technical University, Department of Chemistry  
44-100 Gliwice, Poland

Some preliminary results are reported from experiment proposed by Fleischmann and Pons. In the first series of experiments a small cell of 5 ml volume was used, which contained Pd cathode of  $4 \text{ cm}^2$  surface area, 0.1 mm thick and a similar Pt anode. The solution was 1 M  $\text{CF}_3\text{COOD}$  in heavy water. Deuterium evolution was carried out during the time approximately 8-10 longer than the calculated time corresponding to the charge necessary for saturation state of Pd. Then the flux of neutrons was detected near the cell, which was several times higher than the number of count recorded for background. In some experiments a series of short ejections of neutrons was monitored instead of continuous flux.

An evaluation of heat capacity of the system (16 J/deg) and temperature detection level (better than 0.1 deg) lead to conclusion that in the described system a power source of about 0.1 W could be detected. Under conditions of experiment such emission of heat did not occur so far. Nevertheless, the presence of neutrons proofs that nuclear fusion takes place in Pd charged by deuterium. More recent data are also reported in the communication.

el

## 22-01-05-G

### SOME EXPERIMENTS AND ANALYSIS OF POSSIBLE COLD FUSION

Noboru OYAMA, Takeo OHSAKA, Osamu HATOZAKI, Nobushige YAMAMOTO,  
Yuko KURASAWA, Seiichi KASAHARA, So TAKEOKA, Yuko IMAI  
Department of Applied Chemistry, Tokyo University of Agriculture and  
Technology, Naka-machi, Koganei, Tokyo 184, Japan

Yukio OYAMA, Tomoo NAKAMURA  
Japan Atomic Energy Research Institute, Tokai-mura, Naka-gun,  
Ibaraki 319-11, Japan

Tokushi SHIBATA, Mineo IMAMURA, Yoshitomo UWAMINO, Seiichi SHIBATA  
Institute for Nuclear Study, University of Tokyo, Tanashi, Tokyo 188, Japan

Since the announcement by Utah and Brigham Young Universities that "cold fusion" might be occurring in relatively simple electrochemical systems, we have been intensively endeavoring to verify these results[1,2]. Our experiments are mainly composed of two different approaches; (i) electrolysis experiments and (ii) high pressure loading experiments. The latter has been done to duplicate the work of Scaramuzzi and coworkers on the Ti-D system. The main experimental conditions and detection methods employed in these experiments are summarized in Table 1.

For the electrolysis experiments, several forms of Pd and Ti were investigated including rod, sheet, ball, and porous Pd as the cathode. Various kinds of "hydrogen-absorbing alloys (e.g., La-Ni, Ti-Nb)" were also used. Pt(wire, net) and Au(sheet) were used as the anode in most experiments. Both one-compartment and two-compartment glass vessels were used as electrolysis cells of two- or three-electrode systems. The 0.1 M LiOD (or 0.1 M LiOH) solutions were made by dissolving Li metal in 99.9% D<sub>2</sub>O (or H<sub>2</sub>O). The electrolysis was conducted galvanostatically with constant current densities on the cathode ranging from 20 to 500 mA cm<sup>-2</sup>; both cell voltages and currents were continuously measured with neutron emission measurement, calorimetry, tritium analysis, analysis of effluent gasses or gravimetric analysis of deuterium absorption into the Pd cathode. The redox reaction of deuterium at Pd cathodes in D<sub>2</sub>O solution was also examined using potential-step methods, hydrodynamic voltammetry, in situ quartz crystal microbalance method, etc.

On the other hand, for the high pressure loading experiments, a series of experiments has been carried out with powders of Ti, alloys, etc. in contact with various pressures of D<sub>2</sub> gas (1-40 kg cm<sup>-2</sup>) in which the samples have been thermally cycled several times between ca. 80 K and room temperature and observed for neutron emission. Neutron levels have been measured with liquid scintillators (NE 213).

The main results of these experiments may be summarized as follows:

1. No evidence has been obtained for production of neutrons above the level of 0.3 s<sup>-1</sup>.
  2. The content of He (<sup>3</sup>He and <sup>4</sup>He are not differentiated) in the effluent gas is less than the background level (i.e., ca. 1 ppm).
  3. Excess heat generation rates have been observed over a period of more than several days, depending on the pretreatment of the Pd cathode.
- Excess heating expressed as a percentage of break-even, estimated as



(excess rate of heating)/(input power), is typically 5-30%.

4. The deuterium content of the Pd lattice (i.e., D/Pd ratio) is in the range of ca. 0.6 ~ 0.93, depending on the pretreatment of the cathode, temperature, current density, etc.

The results of ongoing work concerning the detection of neutron bursts, tritium analysis of the electrolyte solution during and after electrolysis, surface analysis and the redox behavior of deuterium will also be presented and discussed.

[1] M. Fleischmann, S. Pons, M. Hawkins; J. Electroanal. Chem., 261, 301 (1989).

[2] S.E. Jones, E.P. Palmer, J.B. Czirr, D.L. Decker, G.L. Jensen, J.M. Thorne, S.F. Taylor, J. Rafelski; Nature, 338, 737 (1989).

Table 1 The Main Experimental Conditions and Detection Methods Employed in Our Cold Fusion Experiments

Experiments	Experimental Conditions	Detection Methods
Electrolysis Experiments	Cathode: Pd(rod, sheet, ball), Ti(rod), Pt(rod), Hydrogen-Absorbing Alloys(La-Ni, etc.), Electrodeposited Pd, Pd-Al Alloy, etc. Anode: Pt(wire, net), Au(sheet) Electrolyte: 0.1M LiOD/D <sub>2</sub> O, 0.1M LiOH/H <sub>2</sub> O, Jones' Electrolyte, etc. (volume = 20-100 ml) Electrolysis Mode: Galvanostatic Electrolysis (Two-Electrode System) (I = 50-500 mA cm <sup>-2</sup> )	Measurement of Neutron Emission Calorimetry Tritium Analysis Analysis of Effluent Gasses Surface Analysis Deuterium Absorption into Cathods Electrochemical Methods (Potential-Step Methods, Hydrodynamic Voltammetry, in situ Quartz Crystal Microbalance Method, etc.)
High Pressure Loading Experiments	Pressure: 1-40 kg cm <sup>-2</sup> Temperature: -190 ~ 23 °C Materials: Ti(powder, grain), Alloy, etc.	Measurement of Neutron Emission

e1

22-01-06-G

## ELECTROCHEMICAL PROPERTIES OF METALLIC HYDRIDES

Derek Lewis and Kurt Sköld

Studsvik Energy (DL) and Uppsala University Institute for Neutron Research (KS), S-61182 Nyköping, Sweden.

This paper reports an experimental study of metal hydride cathodes under conditions similar to those in the recent work of Fleischmann and Pons, on electrochemically induced nuclear fusion of deuterium.

The experiments have been concerned with measurements of changes of temperature and of neutron radiation in and around a cell in which mixtures of deuterium oxide and tritium oxide have been electrolysed using cathodes of metals, usually palladium, capable of forming metallic hydrides. For comparison, measurements have also been made of the changes in temperature occurring in similar cells in which common water has been electrolysed under essentially the same conditions. LiOD and LiOH, both at a concentration close to 0.1 molar, have been used for the electrolytes, as was appropriate. The cathodes were made from commercial bulk metals and carefully annealed to remove structural defects and occluded hydrogen.

In most of the experiments, the electrolysis current was kept constant with a conventional galvanostat and the cell voltage measured at the same regular intervals as the temperatures inside and outside the cell. A few experiments to explore the thermoneutral potential have been carried out potentiostatically.

With 200 ml of electrolyte in the cells, the limit of observation of the total thermal power of all processes occurring during the electrolyses was about 500 mW. The Dewar vessel that contained the cell was placed inside the central cavity of the neutron detection assembly, which had high sensitivity.

22-01-07-G

SEARCH FOR NEUTRON EMISSION ASSOCIATED WITH ELECTROLYSIS OF HEAVY WATER ON Pd AND Ti ELECTRODES

A. Kira, S. Nakabayashi, S. Yamagata, M. Aratani, M. Minami, K. Yoshida, M. Yanokura, T. Suzuki, T. Ichihara, H. Kumagai, and I. Tanihata.  
The Institute of Physical and Chemical Research (RIKEN)  
Wako-Shi, Saitama 351-01, Japan

Attempts were made to detect neutrons which may occur during the electrolysis of D<sub>2</sub>O. A pair of 8" diameter NE-213 liquid scintillators were set either side of an electrolytic cell. The signals for neutrons and gamma rays were separated by pulse shape discrimination and both monitored simultaneously. The scintillators were shielded against background radiations with lead, copper, iron, and polyethylene containing boron. A plastic scintillator is set as a veto counter above the main liquid scintillators inside the lead shielding. The background neutron rate was 0.06 cps.

The electrochemical systems examined were: (1) Pd plate electrodes in acidic D<sub>2</sub>O containing Pd ions, Fe ions, Ti ions, Na ions, and Au-CN ions, (2) Pd plate electrodes in acidic D<sub>2</sub>O containing PdCl<sub>3</sub> and Na<sub>2</sub>NO<sub>4</sub>, (3) a Ti-Pd mixture sponge electrode in D<sub>2</sub>O containing LiSO<sub>4</sub>, and (4) a Pd cylindrical electrode in D<sub>2</sub>O containing LiOD. In experiments for (3) and (4), electrodes were degassed at 420°C in vacuo and cooled in the D<sub>2</sub>-gas environment, and D<sub>2</sub>O was purified with respect to the H content by electrolysis with an H-abstracting Pd electrode. The ion-beam recoil analysis, mentioned later, indicated that these procedures are crucial for effective accumulation of D inside electrode. Typically, data for a run through a day were analyzed with reference to the background through another day. The data show that neutron generation rates are below 0.004 s<sup>-1</sup> in the systems examined.

Light atoms in a few-micron layer of the Pd-electrode surface were analyzed by the method of the forward recoil ion-beam analysis using a 61-MeV Ar ion from the LINAC at RIKEN. Light atoms recoiled by the energetic Ar ions were detected by a Si detector at a scattering angle of 30 degree. Particle identification is based on the total energy and the time of flight. The D atom ratio to Pd was 1 : 1 after treatment with D<sub>2</sub> gas and increased by 50 % after its electrolysis for 120 hours. After electrolysis at high voltage, penetration of Li into the electrode was observed. Pretreatment of electrodes with acids containing H led to the formation of a layer of adsorbed H which disturbed the penetration of D into the electrode.

e1

22-01-08-G

# CRITICAL ANALYSIS AND POSSIBLE EXPLANATION OF ELECTROCHEMICAL NUCLEAR FUSION

G. Kreysa, M. Schütze; Dechema-Institute, Frankfurt am Main  
G. Marx, W. Plieth; Free University, Berlin  
B. Zeitnitz, W. Heeringa, H.O. Klages; Nuclear Research Center, Karlsruhe

Recently two papers /1,2/ appeared claiming that in palladium or titanium electrodes cathodically loaded with deuterium cold nuclear fusion of deuterium occurs.



The neutron emission rate observed by Jones /2/ is about five orders of magnitude lower than those reported by Fleischmann /1/. Fleischmann additionally found  $\gamma$ -rays from the reaction,



tritium in the electrolyte and an excess heat production up to 27 W. We tried to confirm these results and came to the following conclusions /3/:

1. Neutron emission rate of  $4 \times 10^4$  n/s seems to be too high
2. The  $\gamma$ -rays are probably originated from the natural disintegration product Bi-214 (2.204 MeV).
3. Tritium measurements are not a fusion proof because  $D_2O$  contains already T which was not considered.
4. The "excess" heat production can be quantitatively explained by the assumption of a catalytic recombination between  $D_2$  and  $O_2$ .

The results obtained by Jones /2/ seem to be more reliable and could be confirmed by other authors, e.g. /4/. Klyuer /5/ did obtain excess neutrons from reaction (1) by producing fractures in LiD single crystals. This observation could be a key for the explanation of cold fusion in deuterated metal lattices. If one assumes as cathode reaction



with a standard potential of -1.580 V (for LiH), than LiD can be formed at the surface or inside the metal lattice. Cracks produced by hydrogen embrittlement can then produce some fusion neutrons according to the mechanism suggested in /5/. We have checked this hypothesis by trying to correlate the neutron emission rate with the occurrence of fractures detected by acoustic emission analysis. The results of these investigations will be reported.

## References

- /1/ M. Fleischmann, S. Pons; J. Electroanal. Chem. 261 (1989) 301; err. 263 (1989) 187
- /2/ S.E. Jones, E.P. Palmer, J.B. Czirr et al.; Nature 338 (1989) 737
- /3/ G. Kreysa, G. Marx, W. Plieth; J. Electroanal. Chem., in press
- /4/ D. Seeliger, K. Wiesener, A. Meister et al.; Electrochim. Acta, in press
- /5/ V.A. Klyuer, A.G. Lipson, Y.P. Toporov; Sov. Tech. Phys. Lett. 12 (1986) 551

22-01-09-G

Electrochemical Study on Cold-fusion Phenomenon  
 Sueki Baba 1), Kenji Kawamura 2) and Noboru Taniguchi 1)  
 1) Matsushita Electric Industrial Co., Ltd.  
 Central Research Laboratories  
 2) Matsushita Technoresearch, Inc.

### Introduction

In the certification of the phenomenon of cold nuclear fusion events, it is important to detect the fast neutrons from the D-D reaction in metal hydrides by electrolytic charging in solution of heavy water. But in natural environment, a large number of neutrons coming from the cosmos exists as the background. So, it is the problem to distinguish the fusion neutrons from the cosmic neutron.

The energy spectra of neutron from the cosmos is usually broad, on the other side, the energy spectra of neutron from the D-D reaction has a specific energy spectra. Then in this research, for the direct measurement of this 2.452MeV neutron caused by the D-D nuclear fusion, NE-213 liquid-scintillator neutron detector was developed and tried to detect the D-D reaction neutrons separating from the cosmic neutrons.

### Experiment

For the direct measurement of this 2.452MeV neutron caused by the D-D nuclear fusion, the recoil-proton detecting method using NE-213 liquid-scintillator with dual fast-photomultipliers (R329; Hamamatsu) was applied. The size of detector was determined for keeping 14 MeV neutron sensitivity. And shape of detector was the well type because of best detecting efficiency. Schematic diagram of this detector is shown in Fig.1. Output signals of each PMT were connected to the pulse-height-analyzer (PHA) and the pulse-rate-meter (PRM). This system was controlled by personal computer for measuring at fix intervals. And  $\text{BF}_3$ -neutron-counter was set over the well for measuring at same time. The block diagram of this system is shown in Fig.2.

The electrochemical cells used in this experiment were contained in 100 ml glass bottles. The electrodes for the electrolysis of heavy water were consist with the cathode made of palladium (0.5cc clod) and the anode made of platinum. The constant current of the electrolysis was  $10\text{mA}/\text{cm}^2$  in  $\text{LiOD}$  (0.1N) electrolyte. The pre-treatment of palladium was a continuous electrolysis in heavy water over 12 weeks.

### Results

Typical spectra and count-rates from the well-type NE-213 liquid-scintillator and output from the  $\text{BF}_3$  neutron counter is shown in Fig.3(a),(b). Fig.3(a) is a typical result of the electrolysis of heavy-water and (b) is the one of light-water. There is no difference between two data.

Back-ground of this system (about 10cps) is very high because of the large detector size. And energy-resolution is not enough to separate the neutron from natural radiation.

### Reference

1. S. E. Jones et al. Nature **338**, 737 (1989).
2. M. Fleischmann, S. Pons, J. Electroanal. Chem., **261**, 301 (1989).
3. M. Gai, S. L. Rugari et al. Nature **340**, 29 (1989).

e1

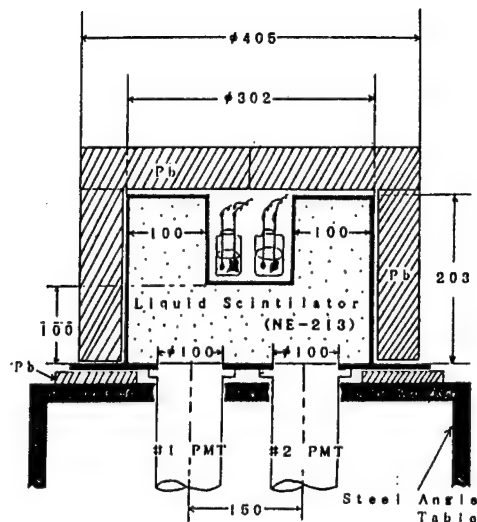


Fig.1 Cross-sectional view of the well-type NE-213 liquid-scintillation detector with dual fast-photomultipliers(R329; produced by Hamamatsu Photonics).

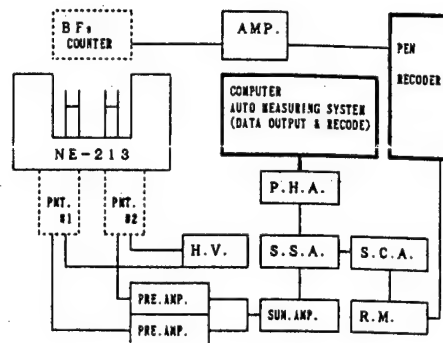


Fig.2 Block diagram of dual PMT-neutron measurement system for cold-nuclear-fusion.  
PMT:Photomultiplier-tube, P.H.A.:Pulse-Height-Analyzer, H.V.:High-Voltage-sup., S.C.A.:Single-Channel-Analyzer, S.S.A.: Spectro-Scopic-Amp., R.M.:Rate-Meter

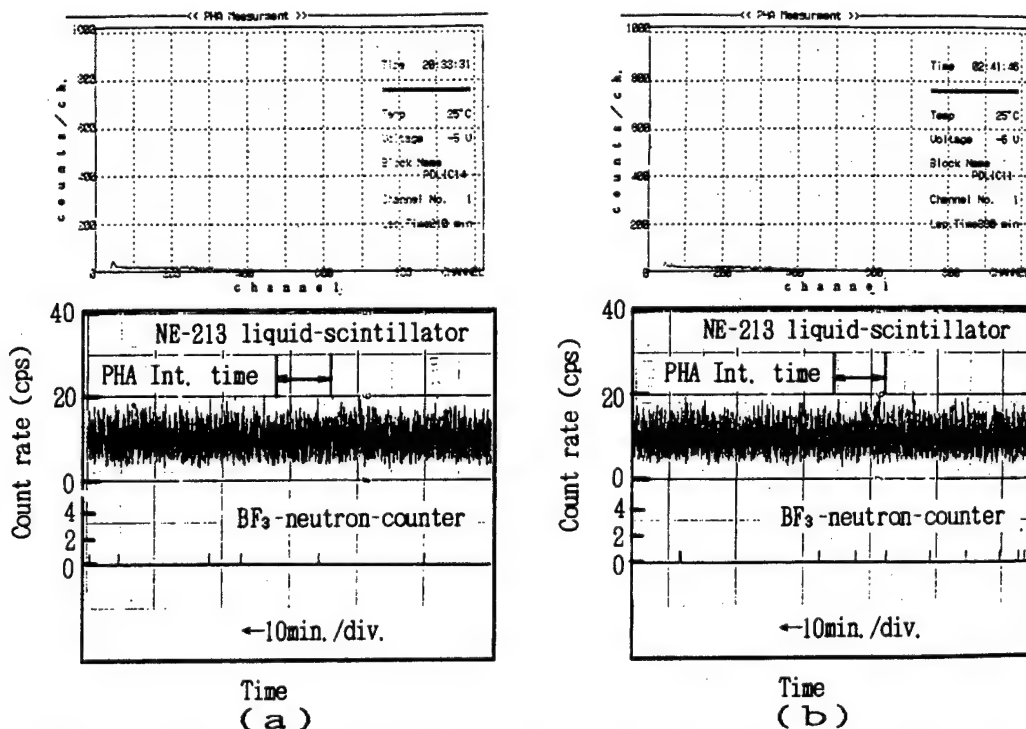


Fig.3 Typical energy-spectra and count-rate-curves from the well-type NE-213 liquid-scintillator and the output from the BF<sub>3</sub>-neutron-counter(NSM-410;Fuji Electric).  
(a) is a typical result of the electrolysis of heavy water, (b) is of light water.

22-01-10-G

CHARACTERISTICS OF Pd CATHODE IN D<sub>2</sub>O

K. Ota\*, N. Kamiya\*, F. Shiraishi\*\*\*, Y. Ishizuka\*\*, M. Yamaguchi\*,  
H. Matsui\*, S. Watanabe\* and H. Tanaca\*

\* :Faculty of Engineering, Yokohama National University  
Tokiwadai, Hodogaya-ku, Yokohama 240 Japan

\*\* :Faculty of Education, Yokohama National University  
Tokiwadai, Hodogaya-ku, Yokohama 240 Japan

\*\*\*:Institute for Atomic Energy, Rikkyo University  
Nagasaka, Yokosuka-shi, Kanagawa 240-01 Japan

The electrochemically induced nuclear fusion has been reported to occur at the electrolysis of heavy water utilizing Pd or Ti cathodes<sup>1,2</sup>).

In this study the electrode characteristics of Pd cathode have been measured at first in several solutions. Generally Pd has been considered to be one of the most electrocatalytically active material for the hydrogen evolution reaction. The hydrogen overpotential, however, increases drastically, when Pd cathode adsorbed hydrogen. The hydrogen overpotential of Pd was higher in alkaline solution than in neutral or acid solution. In the alkaline solution (light water) such as LiOH, KOH and NaOH there were no much differences in the hydrogen overpotential when the alkaline concentration was 0.1M. Although the hydrogen overpotential was independent of the alkaline concentration in NaOH and KOH solution, the hydrogen overpotential depended on the concentration in LiOH solution. The hydrogen overpotential increased at higher concentrations of LiOH.

The neutron emission and the tritium production have also been measured during the constant current electrolysis of D<sub>2</sub>O solutions where the current density was from 50 to 400mA/cm<sup>2</sup>. D<sub>2</sub>SO<sub>4</sub> and NaClO<sub>4</sub> solutions were utilized as the electrolyte as well as LiOD. Pd rods of 0.5-4mm $\phi$  were utilized as the cathodes. The neutron emission was continuously monitored by BF<sub>3</sub> counters during the electrolysis from 2 weeks to 2 months. The reaction cell and the monitoring system was settled in the cave 30m underground where the background neutron was reduced to 4-6counts/hour. The tritium was measured by the liquid scintillator before and after the electrolysis where deuterium and oxygen that were produced during the electrolysis was recovered by the catalyst. The experimental results will be presented and discussed.

Ref. 1)M.Fleischmann, S.Pons & M.Hawkins, J.Electroanalyt. Chem., 261, 301(1989) 2)S.E.Jones et al, Nature, 338, 737(1989)

e1

## 22-01-11-G

### ONE MONTH LOADINGS OF PALLADIUM : DEUTERIUM CONTENT, NEUTRON DETECTION

R.DURAND , R. FAURE , D. ABERDAM  
CREM.GP/ENSEEG and Spectrometrie Physique 38402 ST-MARTIN D'HERES  
FRANCE

The announcement of "cold fusion" by Fleischmann and Pons [1] was the starting point of a large number of experiments, in which palladium samples were electrochemically loaded with deuterium for relatively long times, but none of these experiments reported the actual amount of D absorbed by the samples.

In the course of experiments designed to check a possible neutron emission [2], we obtained an unexpected result relative to the amount of D absorbed by a Pd rod (4 mm in diameter, 60 mm in length, elaborated in a graphite crucible under argon atmosphere). The electrochemical conditions, similar to those used by Fleischmann and Pons [1], were as follows :

electrolyte : 0.1 M LiOD from 99.8 % D<sub>2</sub>O and 99.9 % Li metal ;  
current density : 50 mA.cm<sup>-2</sup> ; temperature : 20°C.

After a loading time of 34 days, during which no neutron emission was detected, the open circuit overvoltage was - 160 to - 170 mV/RHE (equivalent pressure of 3 to 6.8 x 10<sup>5</sup> atm). Unloading took place in two successive steps :

- spontaneous evolution of D<sub>2</sub> after switching off the cell current (≈50 cm<sup>3</sup> after 7 hours),

- potentiostatic oxidation at + 0.45 V/RHE (corresponding to 400 cm<sup>3</sup> of D<sub>2</sub>), during which a few burst of gas occurred at random times and produced 3500 cm<sup>3</sup> of gas which was found to be H<sub>2</sub> or D<sub>2</sub> by gas phase chromatography. At the end of the experiment the sample exhibited a lot of cracks.

In conclusion, with a sample loaded in conditions similar to those disclosed [1], we obtained a much smaller overpotential, but an amount of absorbed deuterium 4.7 times larger than the limit generally accepted (PdD). How much is actually absorbed in the metal lattice, how much is accumulated in defects and closed pores (pre-existing or produced by loading) has to be elucidated. Others experiments, with carbon and pore free samples, will be presented.

[1] M. FLEISCHMANN and S. PONS  
J. Electroanal. Chem., 261 (1989) 301.

[2] Experiments performed in the Frejus Tunnel Laboratory with a detector of the Bugey/ISN neutrino group.



el

22-01-13-G

IN SEARCH OF RADIOACTIVE EMISSIONS FROM THE Pd ELECTRODES OF THE Pd-D AND Pd-H SYSTEMS

H.Uchida, Y.Matsumura, T.Hayashi, Y.Ohtani and M.Kawachi  
Department of Applied Physics, Faculty of Engineering, Tokai University,  
1117 Kita-Kaname, Hiratsuka, Kanagawa 259-12, Japan.

The presence of any radioactive emission except neutrons from the Pd electrodes being electrolytically deuterided and hydrided has been examined in order to confirm whether the cold nuclear fusion reaction(CNFR) takes place or not. In our experiment consisted of over 100 runs since April 7, 1989, the measurement of radioactive emissions has been made using GM-counters to detect any sign of the CNFR from the electrolytic cell where the electromagnetic radiations such as  $\gamma$  - or X-rays and/or the emissions of charged particles such as neutrons(n), protons(p), deuterons(d) or tritons(t) are supposed as the results of the CNFR or their secondary effects.

Electrolytic Deuteriding and Hydriding

Two different types of electrolytic cells with Pd cathodes combined with Pt-plate or Pt-solenoid anodes were used to deuteride or hydride the Pd-wire cathodes annealed or cold worked in 0.025-0.1N KOH, KOD or LiOD solutions. The current density and electrode potential were changed from 60 to 1500 mA/cm<sup>2</sup> and 10 to 40 V, respectively. The deuteriding or hydriding of Pd was made at a constant current, or the reaction rates were intentionally fluctuated by changing applied current and /or voltage.

Measurement of Radiations

Three GM-counters and a scintillation(NaI) counter were used to measure the radiations from the electrolytic cell and to monitor the realtime background near the cell and at remote places from the cell: laboratory and another rooms. The temporal fluctuation of background due to cosmic ray and from surrounding materials is marked even for a short period experimental run. Therefore, it was very important to measure every minute the change in the realtime background in order to detect the excess counting rate compared to background. The comparison of measured data with statistical background obtained for a long period over one hour seems quite invalid because of the marked temporal fluctuation of background radiations. In this work, the counting rate, cpm, was recorded and each 10 min long count was adopted to the data analysis. The electric mains to the cell and counters were chosen isolatedly from different sources in order to avoid occasional noises increasing the counting rate.

MAIN OBSERVATIONS

① On boiling D<sub>2</sub>O(99.8-99.9 % purity) and KOD solution without any electric current, no increased counting rate was measured. The measured rate was identified with that of background.

② About 10 to 80 % excess counting rates compared to background were measured on deuteriding of the cold worked Pd-wire in the 0.025 to 0.1N KOD solutions at current densities and voltages higher than 600 mA/cm<sup>2</sup> and 20 V, respectively whereas no excess counting rate was measured from the cell in which the Pd electrode was being hydrided in the KOH solution at similar current and voltage input.

③ The excess counting rates could be much more frequently and clearly observed when the applied current and voltage were intentionally fluctuated.

④For the annealed Pd electrode, almost no excess radiations were observed whereas the cold worked Pd electrode exhibited distinct excess radiations during deuteriding.

#### DISCUSSIONS

The observed phenomena are implying the presence of the CNFR accompanied by the production of  $\gamma$ - or X-rays whatever these electromagnetic radiations are produced from the primary CNFR or as the result of the secondary effects of the n or charged particles emissions from Pd in the electrolytic cell. The emission of electromagnetic radiations is strongly supposed in the CNFR requiring energy lower than 1MeV where the fusion rate of the d-p pair reaction may become superior to those of d-d or d-t fusion reaction<sup>1,2/</sup>. The presence of H in the cold worked Pd electrode and also the minglement of H<sub>2</sub>O in air into the alkaline electrolytes should be assumed in our experimental results.

The fact that the fluctuating or oscillating deuteriding/deuteriding of Pd yields marked excess radiations is suggesting the the CNFR may take place rather near the surface region of the negative electrode where D and/or H atoms are being absorbed or desorbed at a markedly fluctuated deuteriding rate. This unsteady deuteriding condition seems very crucial to obtain the reproducible CNFR phenomena.

In addition, based on the obtained results, more improved measurements should be made from the viewpoint of surface reaction kinetics in the hydriding of metals<sup>3/</sup> in order to obtain much more readily reproducible evidence for the CNFR.

#### REFERENCES

- /1/S.Engstler, A.Krauss, K.Neldner, C.Rolfs, U.Schröder and K.Langanke, Phys. Letters B, vol. 202(1988), 179.
- /2/J.Rafelski, University of Arizona, private communication at the joint discourse "Cold Nuclear Fusion" by S.E.Jones and J.Rafelski, held by the Japan Creativity Society, June 16, 1989, Kasumigaseki-Bldg., Tokyo, Japan.
- /3/H.Uchida, K.Terao and Y.C.Huang, invited lecture "Current Problems in the Development and Application of Hydrogen Storage Alloys" at the 1st Int.Symp. Metal-Hydrogen Systems, Stuttgart, F.R.Germany, Sep.1988:Z.Phys.Chem.N.F. in press.

#### ACKNOWLEDGMENT

The authors are very grateful to the following colleagues of Tokai University for their useful discussions, kind instrumental arrangement and cooperation in the measurement: Prof.T.Hirayama, the head of Research Planning & Coordinating Division, Prof.K.Takayama, Institute of Technology Development and Associate Prof.Y.Nishi, Department of Materials Science.

- END -

This is a U.S. Government publication. Its contents in no way represent the policies, views, or attitudes of the U.S. Government. Users of this publication may cite FBIS or JPRS provided they do so in a manner clearly identifying them as the secondary source.

Foreign Broadcast Information Service (FBIS) and Joint Publications Research Service (JPRS) publications contain political, economic, military, and sociological news, commentary, and other information, as well as scientific and technical data and reports. All information has been obtained from foreign radio and television broadcasts, news agency transmissions, newspapers, books, and periodicals. Items generally are processed from the first or best available source; it should not be inferred that they have been disseminated only in the medium, in the language, or to the area indicated. Items from foreign language sources are translated; those from English-language sources are transcribed, with personal and place names rendered in accordance with FBIS transliteration style.

Headlines, editorial reports, and material enclosed in brackets [ ] are supplied by FBIS/JPRS. Processing indicators such as [Text] or [Excerpts] in the first line of each item indicate how the information was processed from the original. Unfamiliar names rendered phonetically are enclosed in parentheses. Words or names preceded by a question mark and enclosed in parentheses were not clear from the original source but have been supplied as appropriate to the context. Other unattributed parenthetical notes within the body of an item originate with the source. Times within items are as given by the source. Passages in boldface or italics are as published.

#### SUBSCRIPTION/PROCUREMENT INFORMATION

The FBIS DAILY REPORT contains current news and information and is published Monday through Friday in eight volumes: China, East Europe, Soviet Union, East Asia, Near East & South Asia, Sub-Saharan Africa, Latin America, and West Europe. Supplements to the DAILY REPORTs may also be available periodically and will be distributed to regular DAILY REPORT subscribers. JPRS publications, which include approximately 50 regional, worldwide, and topical reports, generally contain less time-sensitive information and are published periodically.

Current DAILY REPORTs and JPRS publications are listed in *Government Reports Announcements* issued semimonthly by the National Technical Information Service (NTIS), 5285 Port Royal Road, Springfield, Virginia 22161 and the *Monthly Catalog of U.S. Government Publications* issued by the Superintendent of Documents, U.S. Government Printing Office, Washington, D.C. 20402.

The public may subscribe to either hardcover or microfiche versions of the DAILY REPORTs and JPRS publications through NTIS at the above address or by calling (703) 487-4630. Subscription rates will be

provided by NTIS upon request. Subscriptions are available outside the United States from NTIS or appointed foreign dealers. New subscribers should expect a 30-day delay in receipt of the first issue.

U.S. Government offices may obtain subscriptions to the DAILY REPORTs or JPRS publications (hardcover or microfiche) at no charge through their sponsoring organizations. For additional information or assistance, call FBIS, (202) 338-6735, or write to P.O. Box 2604, Washington, D.C. 20013. Department of Defense consumers are required to submit requests through appropriate command validation channels to DIA, RTS-2C, Washington, D.C. 20301. (Telephone: (202) 373-3771, Autovon: 243-3771.)

Back issues or single copies of the DAILY REPORTs and JPRS publications are not available. Both the DAILY REPORTs and the JPRS publications are on file for public reference at the Library of Congress and at many Federal Depository Libraries. Reference copies may also be seen at many public and university libraries throughout the United States.